Gamma Strength from Quasi-Continuum Lifetimes using ^{56}Fe(p,p')

by

Leo Edward Kirsch

A dissertation submitted in partial satisfaction of the

requirements for the degree of

Doctor of Philosophy

in

Engineering – Nuclear Engineering

in the

Graduate Division

of the

University of California, Berkeley

Committee in charge:

Karl Van Bibber, Chair
Lee Bernstein
Wick Haxton
Augusto Macchiavelli

Fall 2017

Gamma Strength from Quasi-Continuum Lifetimes using ^{56}Fe(p,p')

Abstract

Gamma Strength from Quasi-Continuum Lifetimes using ^{56}Fe(p,p')

by

Leo Edward Kirsch

Doctor of Philosophy in Engineering – Nuclear Engineering

University of California, Berkeley

Karl Van Bibber, Chair

A new experimental method is presented to normalize the Gamma Strength Function (GSF) using proton-γ coincidences from ^{56}Fe(p,p'γ) with an excitation dependent variation of the Doppler Shift Attenuation Method where lifetimes of quasi-continuum states delay low-lying γ-ray transitions by an amount inversely proportional to the GSF magnitude. The E-ΔE scintillator array Phoswich Wall measures proton energies which designate initial nuclear excitation energy. The γ-ray tracking spectrometer GRETINA measures signature γ-ray transitions which designate the fed low-lying level. Doppler shift indicates γ-ray cascade time if comparable to the nuclear stopping time. Results provide the first ^{56}Fe GSF normalization.

To my parents Ronald and Jacqueline Kirsch
For their love and dedication to helping me thrive as a scientist.

Contents

Acknowledgments

First and foremost a special thanks to my thesis committee. A special thanks to my research and thesis advisor Lee Bernstein for being there every step of the way – from first touring me and my family around the National Ignition Facility, to giving nuclear physics lectures, to hosting productive group meetings, to training me to perform experiments, to casually discussing science, death, and taxes at happy hours, to introducing me to many intelligent people, to authoring and reviewing papers with me, to providing experimental, analytical, and theoretical insight. Thanks to my academic advisor Karl van Bibber for luring me to UC Berkeley and guiding me on career paths. Thanks to Augusto Macciavelli for lecturing on campus which first got me interested in GRETINA and also for encouraging me and helping me with data analysis and interpretation. Thanks to Wick Haxton for asking good fundamental physics questions and providing an excellent reference point to doctoral procedures outside nuclear engineering.

A big thanks to the Nuclear Structure group at Lawrence Berkeley National Lab for bringing me on to help with their project, especially Augusto Macchiavelli, Heather Crawford, and Michael Jones – I have learned a lot from you all: running experiments, debugging code, and interpreting data. Also thanks to other group members Chris Campbell, Mario Cromaz, I-Yang Lee, Paul Fallon, and Rod Clark for answering difficult questions about GRETINA and making insightful suggestions.

Thanks to Argonne National Laboratory for hosting the experiment presented in this work, providing beam, maintaining GRETINA, and engaging in a couple days of great discussion. Thanks to other staff at Lawrence Berkeley National Lab, especially Aaron Hurst, Rick Firestone, and M. Shamsuzzoha Basunia for working extensively with me. Thanks to collaborators at the University of Oslo, especially Magne Guttormsen and Cecilie Larson for constructive suggestions and encouragement and hosting a fantastic conference from which I learned so much. Thanks to collaborators from Washington University in St. Louis, especially Demetrios Sarantites for assistance with the Phoswich Wall.

Thanks to the Nuclear Science and Security Consortium for a year of funding, sending me to a conference, training me on a workshop, and supporting my work. Thanks to the Stewardship Science Graduate Fellowship for two and a half years of funding, bringing me to incredible labs around the country, sending me to conferences, and compelling me to pursue a career in national security. Specifically, this work was performed with the support of the DOE NNSA Stewardship Science Graduate Fellowship under cooperative agreement number DE-NA0002135.

Thanks to the nuclear engineering department as well as other departments at the University of California Berkeley and the University of Illinois at Urbana-Champaign for providing a high level of educational formation. Thanks to Lincoln Way East High School and Noonan Elementary Academy for being patient with me during my early years, showing me the thrill of math and science, and preparing me for college.

Thanks to my coworkers who have become my some of my closest friends: Cory Waltz, Mauricio Unzueta, Andrew Voyles, Amanda Lewis, Eric Matthews, Nnaemeka Nnamani,

Austin Lo, Sami Lewis, Bella Urdinarian, and especially Maria Simanovskaia. Your friendship has kept me so joyful so far during my time in Berkeley. Thanks also to Robert Crabbs who contributed an excellent thesis that I could use as a template.

Thanks to my mother, father, brother, younger sister, older sisters, niece, nephew, aunts, uncles, cousins, brother-in-law, future sister-in-law, and all those who have joined or will join our growing family. I am grateful for your loving support and care. I know that I will always have a home to which I can return.

Chapter 1

Introduction

1.1 Motivation and Problem Statement

When most quantum systems accumulate a vast sum of energy, the density of available levels can become intractably large. Inherently complex interactions can prohibit a full description of even a single level. The strong force that binds nucleons together in the atomic nucleus is an example of such a chaotic interaction, and certain nuclei possess an enormous number of levels below the particle evaporation energy. Physicists resort to using two continuous functions to characterize the *average* behavior of the complex nature of nuclei: Nuclear Level Density, $\rho(E_x)$ (or NLD), describing the exponential rise in the number levels with excitation energy, E_x, and the Gamma Strength Function, $f(E_\gamma)$ (or GSF), describing the transition probability between levels via emission of a γ-ray with energy E_γ. A statistical application of these average functions is most appropriate in the energy region where level width approaches level spacing, forming a quasi-continuum.

Accurate descriptions of NLD and GSF are essential to obtain reliable results from reaction modeling. These reaction calculations provide cross sections that are critical to a wide range applications such as nuclear reactors, astrophysics, and homeland security.

The number nuclear fission reactors is likely to increase in the coming decades to meet the energy demands of a growing population while minimizing the emissions of greenhouses gases from other dwindling natural resources. As noted in Reference [1], designers of the next generation of these reactors [2] must simulate the reactor core over short and long timescales to address fuel depletion, waste production, and accident scenarios. These simulations rely on a wealth of nuclear reaction cross section data. While the measurement community has extensively researched long-lived nuclei, it cannot practically measure isotopes with short half-lives due to fabrication and radioprotection concerns. Therefore, some cross sections in the actinide region rely on theoretical calculations, extrapolations, and measurements using the surrogate method [3]. The greatest uncertainty in the models is the NLD as a function of excitation energy in the actinide region. These uncertainties cause cross sections to vary by a factor of two or more. Moreover, neutron reactions with elements such as iron, nickel,

and zirconium produce hydrogen and helium via (n,p) and (n,α) reactions which modifies the chemical composition and structural integrity of the core walls and fuel cladding. Hence, there is a compelling argument to measure the NLD of these materials prior to building a costly prototype reactor. Projects such as the $680 million MAPLE reactors at Chalk River Laboratories have already suffered termination [4] due to technical problems potentially related to nuclear data.

The rapid neutron capture process, or r-process, is responsible for the formation of half the nuclei heavier than iron. Although the astrophysical site of the r-process is still unknown, it would require a sufficiently high neutron capture rate such that the nucleus does not have time to decay before another neutron capture occurs, thus producing neutron rich isotopes. These environments likely have (n,γ)–(γ,n) equilibrium governing relative isotopic abundances. Simulations require reliable neutron capture and photodisintegration data to accurately predict these abundances. Unfortunately there is not a great supply of data on the neutron rich side of the valley of stability. Theoretical calculations are necessary to determine missing cross sections because a poor estimate is preferable to a non-existent value. The GSF is an indispensable model input for γ-ray emission and absorption channels. Recently, an unexpected low-energy enhancement in the GSF was discovered in certain mid-mass nuclei such as ^{56,57}Fe and ^{96,97}Mo [5]. Currently, this enhancement is not theoretically well understood, but it changes the predicted abundances of neutron rich isotopes by more than an order of magnitude [6].

There are many other applications that require accurate knowledge of the properties of highly-excited nuclear states near the particle separation energy. A survey of these applications include fusion reactor designs, transmutation of radioactive waste, medical isotope production, single-event upsets in microprocessors, geophysics, oil-well logging, counter-proliferation, homeland security, and stockpile stewardship. Furthermore, the more mathematical fields of complexity, deterministic chaos, and quantum indeterminacy can marginally benefit from the study of nuclear structure.

The nuclear physics community has constructed several tools to measure the NLD and GSF. The Oslo Cyclotron Laboratory's MC-35 Scanditronix cyclotron, γ-ray detection scintillator array CACTUS [7], and coupled charged particle detector SiRi [8] provide the experimental means for simultaneous extraction of the energy dependence of NLD and GSF for a wide range of ions and energies via the Oslo method [9]. The pulsed neutron sources and long flight path lengths at the LANSCE [10] and n_TOF [11] facilities with 4π scintillator detector arrays DANCE [12] and TAC [13] enable simultaneous measurement of the absolute magnitude of NLD and GSF at the neutron separation energy for nuclei one neutron off stability. With the advent of the powerful high-purity germanium arrays GRETINA [14] and AGATA [15] for use in low energy nuclear structure, one may wonder if it is possible to extract useful NLD and GSF information from high resolution γ-ray spectroscopy. If so, it would be worthwhile to reanalyze these rich data sets with a reactions-oriented objective.

This work proposes a new method to use high resolution particle and γ-ray detectors, GRETINA and the Phoswich Wall [16], to determine the absolute magnitude of the GSF in mid-mass nuclei. The particular nucleus explored is ^{56}Fe, which cannot benefit from the

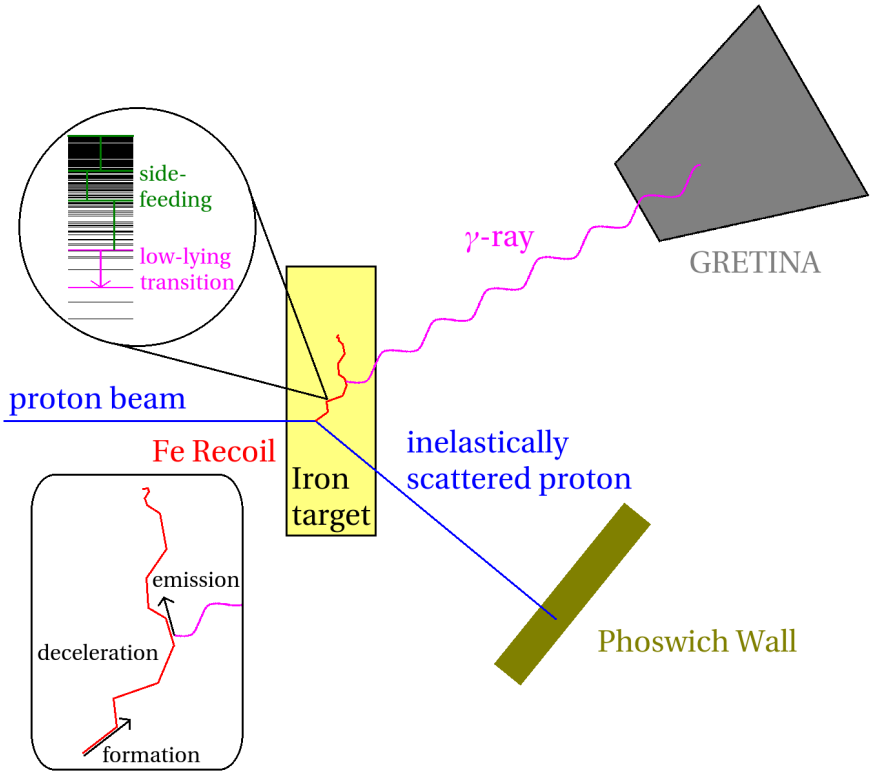

Figure 1.1: The quasi-continuum lifetime method. A proton inelastically scatters off an ^{56}Fe nucleus into the Phoswich Wall. The recoiling nucleus decelerates in the iron target while high-lying states feed a low-lying γ-ray transition. The nucleus is in motion during the transition and GRETINA absorbs the emitted Doppler shifted γ-ray.

traditional (n,γ) experiments at LANSCE and n_TOF since ^{55}Fe is radioactive. The new technique utilizes Doppler shifted low-lying γ-ray transitions of recoiling ^{56}Fe after proton inelastic scattering. The sidefeeding from highly excited states delays γ-ray emission during the deceleration of the nucleus, thus reducing the Doppler shift. This sidefeeding has been neglected or corrected for in prior nuclear structure literature; however, the quasi-continuum lifetimes involved in the sidefeeding are indirectly related to the coveted NLD and GSF via the following equations:

$$\tau_I = \hbar \left(\sum_{F,XL} \Gamma^{XL}_{I,F} \right)^{-1} \tag{1.1}$$

$$\bar{\Gamma}^{XL}(E_I, E_\gamma) = \frac{f_{XL}(E_\gamma) E_\gamma^{2L+1}}{\rho(E_I, J_I, \Pi_I)}, \tag{1.2}$$

where τ_I is lifetime of initial state I; $\Gamma^{XL}_{I,F}$ is the partial transition width to possible final state F; E_I, J_I, and Π_I are excitation energy, angular momentum, and parity of the initial state, respectively; and E_γ is the energy emitted in the transition of electromagnetic character X

and multipolarity L. Figure 1.1 briefly illustrates the essential experimental components. The goal of this work is to establish this quasi-continuum lifetime technique and determine if it has the capability to extract the GSF magnitude.

1.2 Chapter Overviews

Chapter 2 introduces the experiment which was a pioneering effort to test out the capabilities of two new detectors: GRETINA and the Phoswich Wall. In an attempt to keep the rest of the experiment familiar, the well-studied ^{56}Fe(p,p') reaction was chosen and performed at a dependable low-energy beam facility. I made the point to put the experiment chapter early on in this document because there are numerous paths this work could have taken. High resolution multivariate data sets are incredibly rich. There is a certain beauty to the depth and scope achievable with such physically large, mechanically intricate, and computationally powerful devices. In fact, this particular experiment was designed in order to confirm a previously observed anomaly in the low-energy behavior of the GSF, which is not the main topic of this work; Reference [17] presents these results. I was fortunate to take an experimental shift and I was given the opportunity to study some of the unanalyzed portions of the data. I felt that it would have been misleading to put a theory chapter first, suggesting that the newly introduced method flows naturally from theory alone; it does not. In fact, the recognition of the quasi-continuum lifetime effect was quiet serendipitous: I was trying to correct for broad peak shapes of the experimental γ-ray spectra. Therefore, Chapter 2 covers the following prerequisite tasks that were necessary before a more theoretical topic could be studied:

- obtaining a detailed understanding of the geometric configuration
- an inspection of the prominent reaction channels
- weighing the pros and cons of the different layers of signal processing
- recalibration of gain drifts and coincident detector timing
- an optimization of the algorithms used in γ-ray tracking

Chapter 3 describes the theoretical infrastructure supporting the data analysis. When a complete derivation is not possible within reasonable space constraints, at least give a cursory outline is provided. For example, it is feasible to fully derive two-body reaction kinematics, but it is only possible to glimpse the history and modern formalism of stopping power theory. Furthermore, the introduction of nuclear properties begins with quark level complexities and describes why it is necessary to treat nucleons as individual particles. Nuclear theory approximations proceed from the many-body nucleon level, to the shell model level, ending at the level of statistical mechanics. This chapter concludes with the formal presentation of the quasi-continuum lifetime method to determine the absolute magnitude of the GSF.

Equipped with the theory of Chapter 3, Chapter 4 explores concepts beyond the initial experimental calibrations by delving into physics-based interpretations. This chapter fully investigates the quasi-continuum lifetime effect in 16 MeV ^{56}Fe(p,p'γ). Certain quasi-continuum lifetime probes are superior to others: the parent level needs to have a lifetime on the order of the slowing down time and the γ-ray transition energy needs to be isolated from other peaks. It is shown that the angular momentum distribution is important in the population of low-lying levels. Systematic uncertainty are addressed. Detailed simulations are compared with experimental results to normalize the GSF. Neighboring nuclei accessible via (n, γ) measurements are compared to the final measurement of the ^{56}Fe GSF normalization.

Chapter 5 offers conclusions. Limitations of the quasi-continuum lifetime method can be reduced with improvements in either experimental equipment or simulation. A suggestion is made as to how the method might be extended to include the actinide region of the nuclear chart. Finally, this chapter hypothesizes what impact this method may have on applications.

Chapter 2

Experiment

This chapter contains the necessary information to understand the equipment in this experiment, the output data one can expect, the various calibrations that make the data reliable, and the quality of the measurable quantities.

Here, I am greatly indebted to my group members who facilitated the proposal and setup of the experiment as well as the Argonne National Lab staff members who operated the accelerator and hosted our team. Also, I cannot forget my engineering predecessors who set the stage by achieving the immense technological progress to make this experiment a possibility. Nor can I disregard the decades of theorists who made this work comprehensible, interesting, and applicable.

2.1 Argonne National Lab: ATLAS at a Glance

Argonne National Lab located in Darien, Illinois is home to the nation's premier stable beam facility, the **A**rgonne **T**andem **L**inear **A**ccelerator **S**ystem (ATLAS) [18]. Commissioned in 1978, ATLAS was the first to provide the world with heavy ions from a superconducting accelerator. ATLAS currently consists of 62 superconducting split-ring resonators that boost the beam energy to as high as 17 MeV/nucleon. The facility supports users in the fields of nuclear reactions and structure with beams of any stable ion. The resultant nuclear data primarily supports applications in astrophysics and basic nuclear science, but also contributes to developments in nuclear energy, medical physics, non-proliferation, and national defense by extension.

ATLAS supports many types of experiments. Figure 2.1 shows a stripped down diagram of ATLAS containing only the parts relevant to the experiment in this work. The **CA**lifornium **R**are **I**sotope **B**reeder **U**pgrade (CARIBU) [20], the **HELI**cal **O**rbit **S**pectrometer (HELIOS) [21], the **F**ragment **M**ass **A**nalyzer (FMA) [22], the 4π high purity germanium spectrometer Gammasphere, and the **C**anadian **P**enning **T**rap (CPT) [23] were not utilized in this experiment.

The **P**ositive **I**on **I**njection system (PII) [24] delivers the initial pulsed beam for the AT-

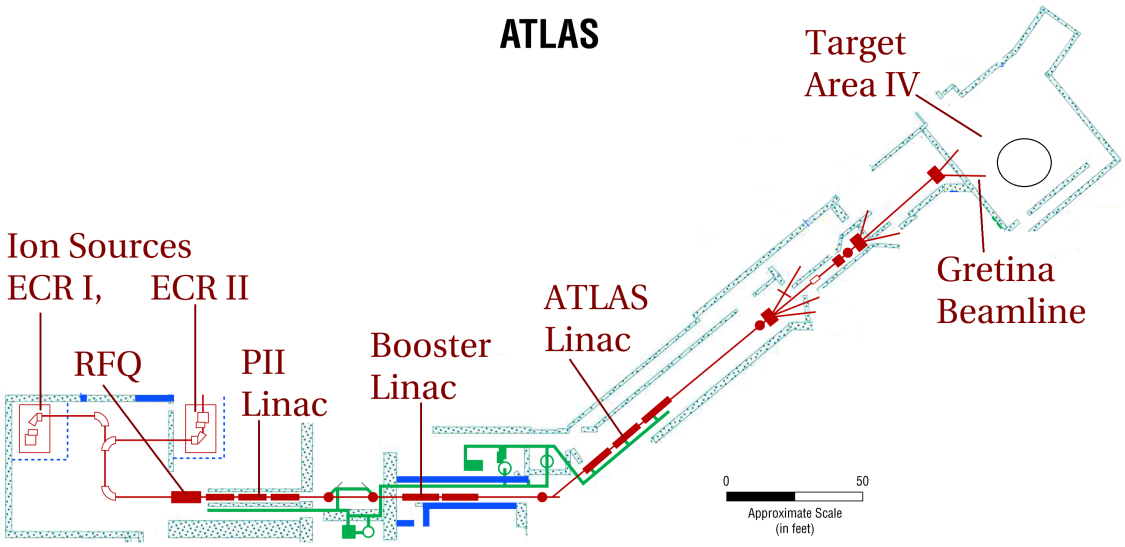

Figure 2.1: Experimentally relevant components of ATLAS. [19]

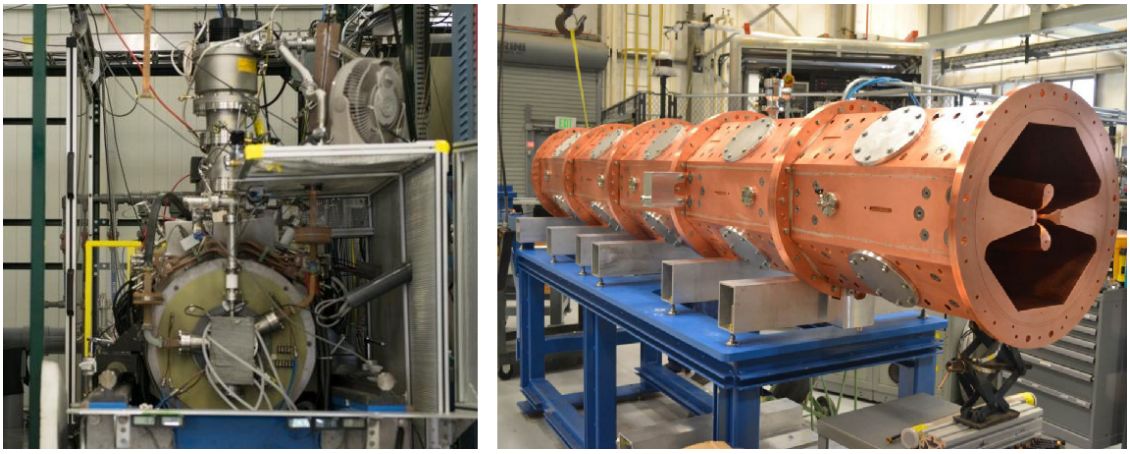

Figure 2.2: The Electron Cyclotron Resonance ion source (left) and Radio Frequency Quadrapole (right). [26]

LAS Linac. The left panel of Figure 2.2 shows the first stage of the PII: the 14 GHz **E**lectron **C**yclotron **R**esonance (ECR) ion source [25]. The ion source utilizes double frequency heating to maintain a high plasma density confined within a NdFeB hexapole magnetic field and a strong solenoid axial field. Typically the ECR produces high charge state ions, but this experiment used only a proton beam with a charge state of +1. Beam pulse bunching first occurs directly outside the ECR following initial beam diagnostics before transferring to the Radio Frequency Quadrapole accelerator.

A staple in ATLAS's modern accelerator design is its **R**adio **F**requency **Q**uadrapole (RFQ) [27] which is responsible for establishing the beam bunch shape, emittance, and per-

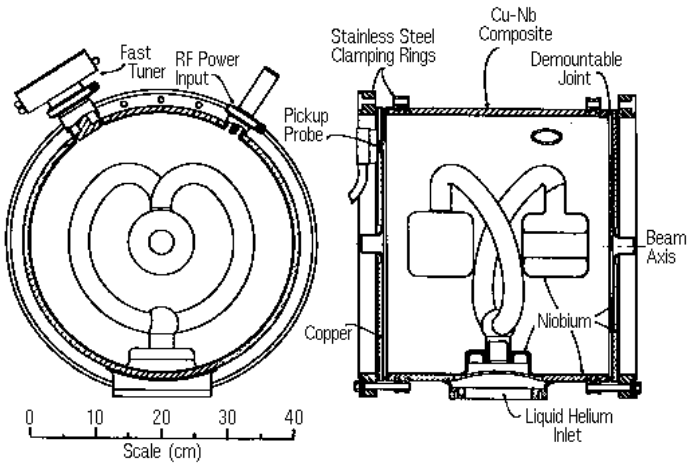

Figure 2.3: A schematic of one of the split-ring resonators. [29]

forming a portion of the acceleration. The right panel of Figure 2.2 shows the fabrication stage of the RFQ with its multisegment split-coaxial 4 meter long structure. In the accelerating section of the RFQ, the trapezoidal vane tip modulation increases the shunt impedance by 60% compared to conventional sinusoidal modulation, allowing the radio frequency eigenmode to interact more strongly with the charged particles. The RFQ impedance matches the initial beam to the superconducting section of ATLAS. Figure 2.3 shows one of the core accelerating units: the split-ring resonator [28]. ATLAS operating staff independently adjust each of these 62 variably sized split-ring resonators to synchronize with the increasing velocities of passing bunches.

For this experiment, the incident proton energy was 16 MeV, the current on target ranged from 0.5 to 1.0 nA, the beam pulsed every 40 ns with a 0.5 ns width, and the beam diameter was 2 mm. Approximately 80 hours of ^{56}Fe(p,p') data collection was useful for analysis.

2.2 The ^{56}Fe(p,*) Reaction and Detector Array Overview

This section highlights the important reaction products and introduces the detectors that will be sensitive to the ejected particles. Further descriptions of these detectors are given in greater detail in following sections.

Protons from ATLAS impinged upon a self supporting 1 mg/cm^2 thick layer of sputtered iron (Fe) target enriched to 99.7% in ^{56}Fe. Collaborators from Washington University in St. Louis provided these targets and targets of similar stature used for the carbon calibration runs shown in Figure 2.4.

The inelastic scattering ^{56}Fe(p,p')^{56}Fe* was used to generate excited ^{56}Fe nuclei for this

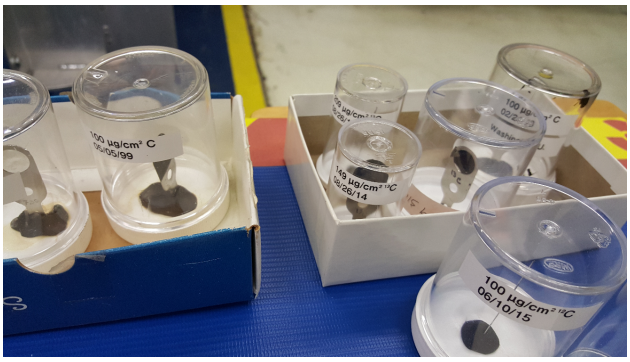

Figure 2.4: Some of the targets used for calibrations in the experiment.

experiment. The recoiling ^{56}Fe nuclei typically do not have enough energy to escape the thin foil target material and usually go undetected. Scattered protons emerge from the target into the chamber at all angles. The Phoswich Wall particle detection array [16] measured the angle and energy of the protons. In ^{56}Fe(p,p')^{56}Fe*, p' indicates that the proton deposited a fraction of its energy as an internal excitation in the ^{56}Fe nucleus denoted by *. The excited ^{56}Fe* nucleus decays via γ-ray emission. The γ-ray spectrometer GRETINA [14] measured the angle and energy of the emitted γ-ray's. GRETINA uses γ-ray tracking to determine the entire energy of an incident photon including deposition via both the photoelectric and Compton scattering processes. Any γ-ray with energy greater than twice the rest mass energy of the electron can produce a positron and electron pair through electromagnetic interactions with matter. This pair production can occur inside GRETINA or on nearby detector or structural material. Recoiling positrons and electrons created inside GRETINA will deposit their recoil energy and generate a signal, while those escaping the detectors will result in an inaccurate determination of the total energy of the incident γ-ray. After positrons lose most of their kinetic energy to scattering, they annihilate with nearby electrons and emit two 511 keV γ-ray's nearly back to back. GRETINA detects many of these 511 keV γ-ray's.

16 MeV protons on ^{56}Fe can induce 11 other kinematically allowed non-elastic reaction channels. The left pane of Figure 2.5 shows these allowable channels. These reactions almost always produce the heavy nuclei in excited states that subsequently γ-ray decay. Despite there being many allowable exit channels, GRETINA data only reveals γ-ray's from five of these reactions: (p,n)^{56}Co, (p,d)^{55}Fe, (p,pn)^{55}Fe, (p,α)^{53}Mn, and (p,pα)^{52}Cr. The remainder of the reactions have low cross section and occur infrequently. The right pane of Figure 2.5 shows the observed reactions on the National Nuclear Data Center's (NNDC) chart of the nuclides [31].

The Phoswich Wall detection array has the capacity to detect the angle and energy of the deuterons (d) and alphas (α) from these reactions. The Phoswich Wall can detect ^{3}H and ^{3}He ejectiles as well, but the production cross section is several order of magnitude lower. Reactions other than (p,p') are left unanalyzed in this work. The Phoswich Wall and

Reaction Q-values for ^{56}Fe + ^{1}H(E_{lab}=16 MeV)

Reaction Products	Q-value (keV)	Threshold (keV)
^{57}Co+γ	6027.5 *0.45*	0.0 *0.0*
^{56}Fe+p	0.0 *0.0*	0.0 *0.0*
^{53}Mn+α	-1053.32 *0.47*	1072.293 *0.478*
^{56}Co+n	-5348.971 *0.411*	5445.319 *0.418*
^{52}Cr+p+α	-7613.25 *0.744*	7750.384 *0.757*
^{55}Fe+d	-8972.533 *0.23*	9134.151 *0.234*
^{55}Mn+2p	-10183.67 *0.16*	10367.104 *0.163*
^{49}V+2α	-10206.33 *1.01*	10390.17 *1.02*
^{55}Fe+n+p	-11197.1 *0.23*	11398.788 *0.234*
^{54}Fe+t	-12013.391 *0.28*	12229.783 *0.285*
^{54}Mn+^{3}He	-12692.14 *1.08*	12920.76 *1.1*
^{52}Mn+n+α	-13106.83 *1.95*	13342.92 *1.99*
^{55}Co+2n	-15430.827 *0.34*	15708.776 *0.346*

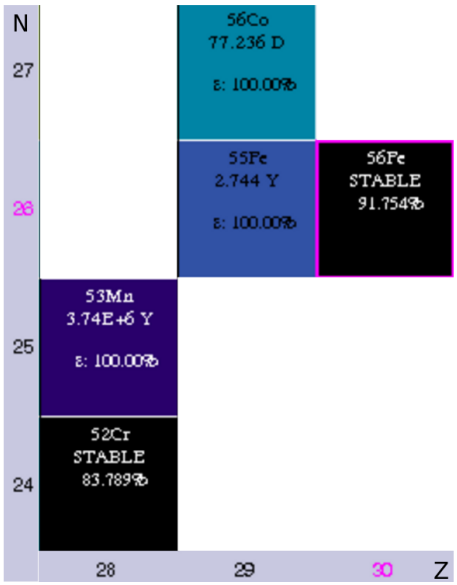

Figure 2.5: Kinematically allowable and observable reactions in ^{56}Fe(p,p') at 16 MeV. Output from the web program QCalc [30] and Chart of the Nuclides [31].

GRETINA are not designed to detect the neutrons (n) from the (p,n) and (p,pn) reactions, but features from these neutrons do appear in the data. The heavy ejectiles ^{56}Co, ^{55}Fe, ^{53}Mn, and ^{52}Cr like ^{56}Fe typically do not have enough recoil energy to exit the target material and are undetected.

As seen in the right pane of Figure 2.5, ^{56}Co is unstable to decay via electron capture (81%) and positron emission (19%) with a half-life of 77 days. The average emitted positron kinetic energy is 610 keV which is enough to escape the 1 mg/cm^2 target. The Phoswich Wall is not optimal for detecting positrons but some events appear in the data: GRETINA detects a significant number of annihilation 511 keV γ-ray's in a narrow coincidence time window with the Phoswich Wall positron events. Electron capture does not frequently generate high enough energy Auger electrons to escape the target. The experimental chamber is thick enough to prevent GRETINA from detecting any of the X-Rays from electron capture. ^{56}Co decays back into ^{56}Fe and produces the same γ-ray's as (p,p').

In summary, the Phoswich Wall detects the angle and energy of the outgoing protons while GRETINA detects the angle and energy of the emitted γ-ray's for analysis of the ^{56}Fe(p,p'γ) reaction. The unintended (p,α), (p,d), (p,n) reactions and ^{56}Co β^+ decay are ignored in this data analysis. The remaining ^{56}Fe(p,p'γ) data contains a host of information on the nuclear structure of ^{56}Fe. Multiple γ-ray emission provides information on the ^{56}Fe level scheme, γ-ray Doppler shifts provide information on lifetimes of ^{56}Fe excited states, and angular distributions of both protons and γ-rays provide information on the spin and parity of ^{56}Fe levels as well as the multipolarity of the transitions between levels. These phenomena and analytical procedures will be discussed in Chapter 3.

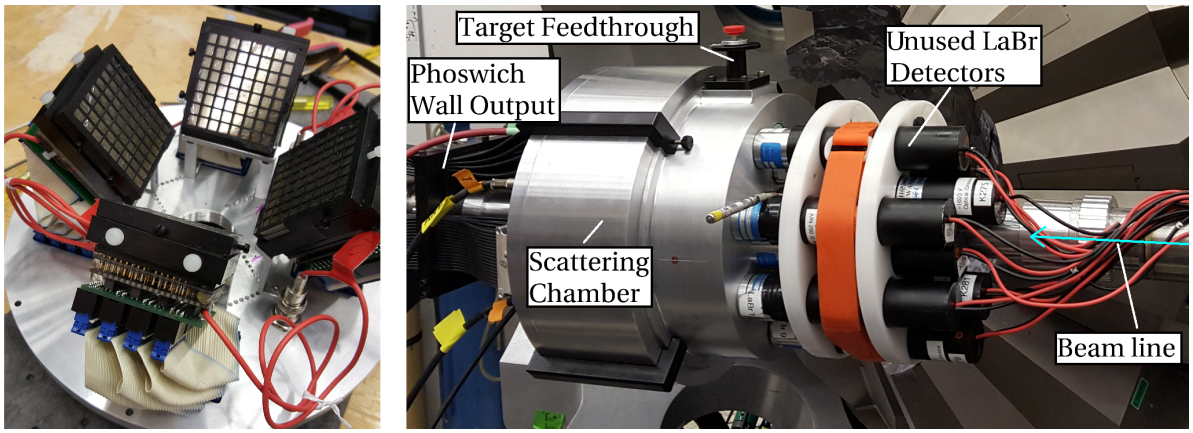

Figure 2.6: The Phoswich Wall charged particle detector arrays (left). Scattering chamber and feedthroughs (right)

2.3 The Phoswich Wall Array

This section further describes the Phoswich Wall and its location in the beam line. The Phoswich Wall's $E-\Delta E$ particle identification method is described. Calibrated energy spectra and particle identification spectra from experimental data are presented. Cross talk algorithms for enhanced energy resolution and sub-pixel position resolution are explained.

Geometric Configuration

The name "phoswich" is a contraction of "phosphor sandwich", where phosphors are defined as substances that exhibit the phenomenon of luminescence, and a stack of such phosphors is akin to a sandwich. The Phoswich Wall, shown in left panel of Figure 2.6, is a set of four 8×8 arrays of multianode photomultiplier tubes (PMTs) coupled to a "sandwich" of 2.2 mm thick CsI(Tl) and ∼12 μm thick BC400 fast plastic scintillating material. These arrays sit inside an evacuated scattering chamber connected to the ATLAS beam pipe, shown in the right panel of Figure 2.6. A target feedthrough connected to the scattering chamber supports the ^{56}Fe sample at the center of the chamber. The incident beam strikes the target and low-mass reaction ejectiles recoil into the phoswich arrays. Any unscattered beam exits the chamber and enters a beam stop a few meters past the scattering chamber.

A set of coordinate transformations are needed to relate the planes of the four 8×8 arrays to the beam coordinate system. In the beam coordinate system, the origin is the target center and the Z-axis is the beam direction. The transformations from the Cartesian coordinates of each detector array (x,y) to Cartesian coordinates of the lab (X,Y,Z) are the

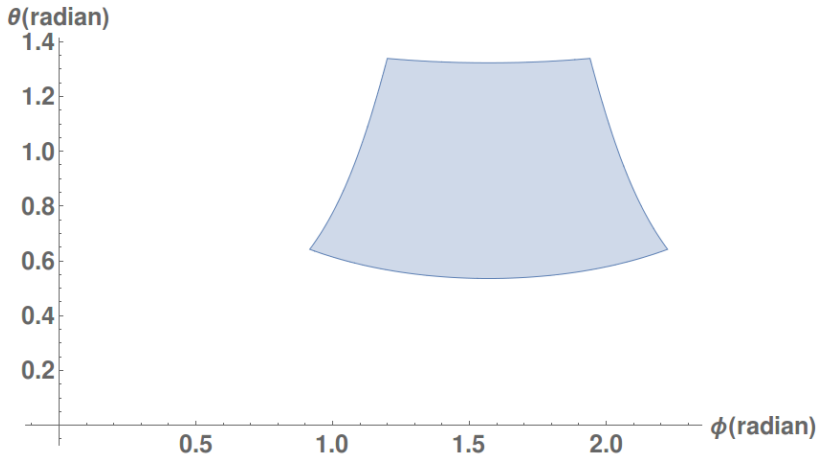

Figure 2.7: Angles covered by one of the four Phoswich Wall arrays. The other three detector arrays are each translated by $\Delta\phi = \pi/2$ with respect to the previous array.

following:

$$X(x,y) = L/2 + \delta \tag{2.1}$$
$$Y(x,y) = R_0 \sin\Psi - (L/2 - y)\cos\Psi - \delta + \alpha \tag{2.2}$$
$$Z(x,y) = R_0 \cos\Psi - (L/2 - y)\sin\Psi \tag{2.3}$$

where $L = 49$ mm is the length of one side of the square array, $\delta = 0$ mm is the linear displacement length, $\alpha = 10$ mm is the backset, $R_0 = 55$ mm is the maximum radius for $\delta, \alpha = 0$, and $\Psi = 50.6°$ is the angle between the normal to detector plane and the beam axis. The spherical polar coordinates of the beam coordinate system are

$$r(x,y) = \sqrt{X(x,y)^2 + Y(x,y)^2 + Z(x,y)^2} \tag{2.4}$$
$$\theta(x,y) = \cos^{-1}\left(\frac{Z(x,y)}{r(x,y)}\right) \tag{2.5}$$
$$\phi_1(x,y) = \tan^{-1}\left(\frac{Y(x,y)}{X(x,y)}\right) \tag{2.6}$$
$$\phi_n(x,y) = \phi_{n-1}(x,y) - \pi/2, \quad n = 2,3,4 \tag{2.7}$$

where r is the distance from the target origin, θ is the opening angle with respect to the direction of the beam axis (the Z axis), ϕ_1 is the azimuthal angle of array 1, and ϕ_n are the azimuthal angles of arrays 2, 3, and 4. Figure 2.7 shows the angular coverage of array 1 in spherical polar coordinates. The detector arrays are all situated at forward angles ($0 < \theta < \pi/2$) in this experiment (i.e. downstream of the beam).

The Phoswich Wall has the capability to study both inverse and normal kinematics reactions. In inverse kinematics, the projectiles in the beam are much heavier than the nuclei in the target. The ejectiles of inverse kinematics reactions are very forward focused by virtue of

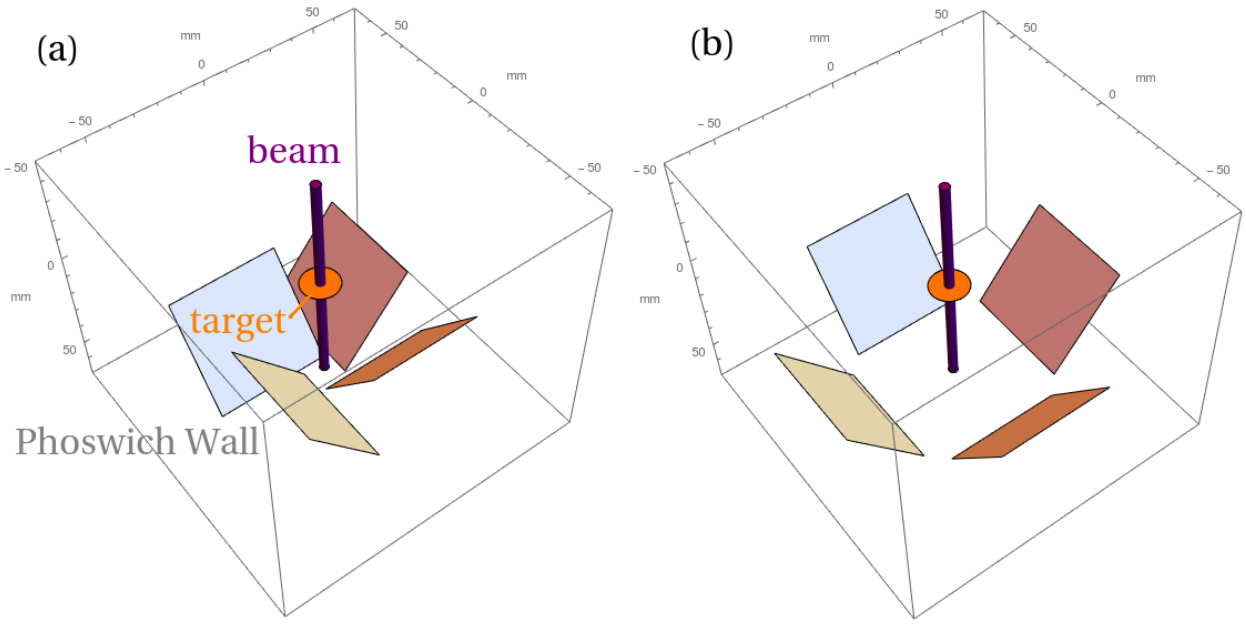

Figure 2.8: The Phoswich Wall configurations to scale. (a) Inverse kinematics configuration maximizing forward angle coverage ($\delta = 20, \alpha = 0$). (b) Normal kinematics configuration improving angular resolution while still covering a significant portion of the solid angle in the forward direction ($\delta = 0, \alpha = 5$). This experiment utilized the normal kinematics configuration for its high angular resolution.

the conservation of the large quantity of linear momentum along the incident beam direction. To accommodate inverse kinematics, Figure 2.8a shows the Phoswich Wall configuration that maximizes forward angle coverage without intercepting any of the unscattered beam. The forward tilt of the arrays with respect to the beam axis improves solid angle in the CM frame. In contrast, the experiment presented in this work was performed at normal kinematics: the proton projectile has a much smaller mass than the ^{56}Fe target. In normal kinematics, there is not as much linear momentum in the beam direction, but still a large portion of the cross section for direct reactions is forward focused. In normal kinematics reactions, the measured angle of the outgoing light ejectile provides a lot of information about the reaction and opens the possibilities for additional analysis. To accommodate a multitude of analyses in normal kinematics, Figure 2.8b shows the Phoswich Wall configuration used in this experiment that has an enhanced angular resolution in comparison to the inverse kinematics configuration without the forfeiture of a substantial amount of solid angle coverage. Figure 2.9 shows two examples of typical reactions.

The phoswich arrays have a $E-\Delta E$ structure for light charged particle identification. Ions deposit only a portion of their energy (ΔE) in the thin fast plastic, and deposit the remainder of their energy (E) in the thick CsI(Tl). According the Bethe formula [32], the mean energy loss of an ion traversing the fixed thickness of the fast plastic is proportional to the charge

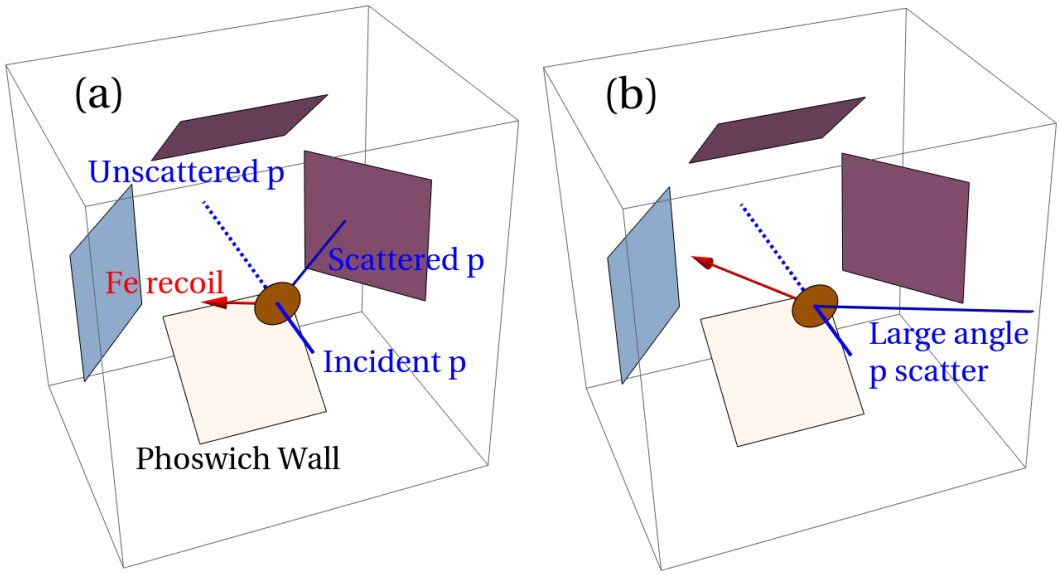

Figure 2.9: Examples of the Phoswich Wall's participation in and exclusion from detection. (a) An incident proton (blue) scatters off the ^{56}Fe target (orange) into one of the four the Phoswich Wall arrays, the recoil of the ^{56}Fe nucleus goes undetected since it does not have sufficient kinetic energy to escape the target but has an initial velocity vector (red) in a direction nearly opposite the proton. (b) An event where the proton recoils to an angle outside the detectable area of the Phoswich Wall.

of the projectile squared: $\Delta E \propto Z^2$. The waveform signal of decaying luminescence gives an indication of the charge Z of the deposited particle. Figure 2.10 illustrates proton and alpha output: energy deposited in the fast plastic (ΔE) decays away rapidly while energy deposited in the CsI(Tl) decays on a much longer timescale. A ratio of PMT output integrals at various times distinguishes the two types of particles on an event by event basis.

The energy resolutions of the phoswich scintillating materials are inferior to silicon particle detectors. The choice of fast plastic and CsI(Tl) scintillating material was chosen more for its radiation hardness, mechanical durability, and gain stability rather than its energy resolution. The fast rise time of the BC400 plastic and the large stopping power of the thick scintillator also were important considerations. The maximum energy proton that can be stopped by the 2.2 mm thick CsI is approximately 21 MeV, well below proton energies achieved in this experiment.

While the segmentation of the Phoswich Wall provides good angular resolution of the reaction products, light deposited above one PMT section can leak into a neighboring section. This "cross talk" allows sub-pixel resolution of the position hit. When two adjacent PMT pixels detect light, the true location of the energy deposition is a function of the ratio of the two signals. The angular resolution of fully isolated PMT pixels is around 7° FWHM, but it has been shows that analysis of cross talk can achieve up to a 2° resolution experimentally [16]. However, the analysis performed as part of this experiment did not include sub-pixel

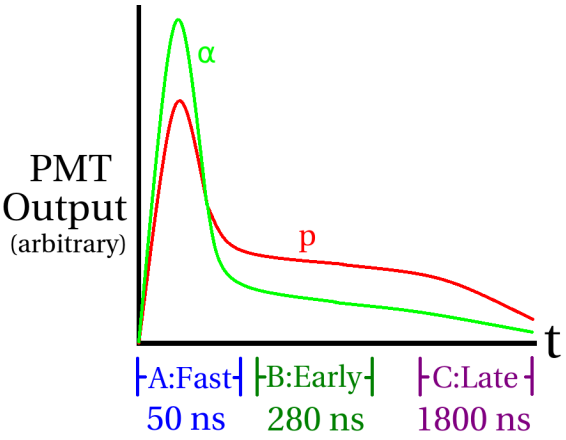

Figure 2.10: Schematic of the Phoswich Wall pulse shape discrimination time intervals (not to scale).

positioning.

As a final overarching design criteria, the Phoswich Wall has a small volume to fit inside the limited space at the center of 4 π γ-ray spectrometers. Similarly, the Phoswich Wall has a low overall mass of detector and structural material to minimize degradation of the γ-ray spectrum through Compton scattering. The attenuation of 511 keV γ-rays is 2.2% in the 1 mm aluminum chamber and 4.2% in the 2.2 mm CsI(Tl). The γ-rays studied in this work are primarily above 511 keV.

Calibration and Particle Identification

As introduced earlier, the Phoswich Wall has particle identification capabilities. Three separate integrals of PMT output are taken at separate times to capture the $E-\Delta E$ information. The early "A" gate captures the ΔE signal from the fast plastic and begins after a 15 ns delay with respect to the start of the pulse and has a 50 ns duration. The "B" gate captures some of the fast plastic ΔE signal and some of the E signal from the CsI(Tl); it has a 68 ns delay and 280 ns duration. The late "C" gate captures the remainder of the E signal; it has a 1000 ns delay and 1800 ns duration. These gates correspond to the illustration of Figure 2.10. Complete digitizer waveforms were not saved to disk.

Pulse shape discrimination requires knowledge of the PMT central hit location. However, since gains in neighboring PMT pixels vary by up to 25%, it is not always clear which pixel contains the central hit. The procedure of gain matching rectifies the situation by using a mask to prevent particles from hitting pixel *edges*, thereby isolating events where the majority of light enters only one PMT. In contrast, interactions near pixel *edges* produce scintillation light that enters both adjacent PMTs. With the mask in place the difference in light yield is greater than 25% between adjacent pixels. Gain are matched and thresholds are set at the beginning of the experiment with alpha particles from ^{252}Cf and ^{228}Th.

The B-gate of the largest hit pixel has the best energy resolution for protons. Resolution can be improved an additional 30% with face-neighbor add-back. Adding pulse heights of surrounding pixels typically doubles total pulse height, indicating that the central hit pixel does not capture a lot of the total scintillation light. Border pixels of the 8×8 arrays do not have the same number of neighbors which complicates add-back. For these pixels, it is necessary to multiply total pulse height by some function of the cross talk fractions of *available* face neighbors. The energy resolution of border pixels is not as good as pixels with 4 face-neighbors, but at least all pixels yield the same magnitude for a given energy deposition. Furthermore, some of the central PMT pixels are broken, and more complicated computational logic is required.

The energy add-back algorithm is similar to the sub-pixel hit positioning algorithm described by Sarantities *et. al.* [16]. An empirical function relates the sub-pixel hit location with cross talk fraction:

$$x(f), y(f) = a(2 - \frac{1}{f}) + b(f - \frac{1}{2}) + w \tag{2.8}$$

where f is the cross talk fraction between adjacent pixels, $w = 6.08$ is the width of each pixel, $a = 0.470$ and $b = 10.8$ are fitting parameters that vary among the phoswich arrays, and the coordinates x and y are in units of mm. For $f = 1/2$, the hit is located directly on the edge by definition since light enters both pixels equally: $x(1/2), y(1/2) = w$. For $f = f_{min} \approx 0.15$, the hit is located at the other edge: $x(0.15) = 0.0$. The face neighbor fractions that pinpoint the hit location inside the pixel are labeled f_L, f_R, f_U, f_D for left, right, up, and down, respectively. For example, if $f_L > f_R$ and $f_U > f_D$ the hit is located in the top left quadrant of the pixel. Equation (2.8) determines positions more accurately. There are two measurements of an axis coordinate when the pixel has two neighbors along that axis. Typically the larger cross talk fraction is more reliable. When a pixel on the corner or edge of the array is missing a neighbor pixel, the available neighbors determine how much light would have entered the missing pixel(s). The calculated energy(ies) of the missing pixel(s) is(are) added to the total energy of the event when performing add-back. Energy resolution is not as good when pixels are missing, but the pulse height has the same relative magnitude.

Several other corrections to the particle energy are necessary. The linearity of the B-gate proton energy is established with ^{12}C(p,p')^{12}C and ^{12}C(p,p')^{12}C*, where the two accessible excited states of carbon are at 4.439 and 9.641 MeV. Small corrections on a run-by-run basis correct for gain drift. Corrections for punch-through energy loss are angle dependent. Charged particles lose energy passing through the 1 mg/cm^2 iron target, the 7.28 mg/cm^2 tin absorber, and the varying thicknesses ($\sim$ 1.2 mg/cm^2) fast plastic ΔE layer before reaching the CsI(Tl) E detector. These corrections are not important in an absolute sense because the alpha particle calibrations establish the magnitude of energy deposition. However, the incident vectors of the particles are not all parallel to the normal vectors of the planes of the phoswich arrays. The particles pass through different amounts of material before entering the CsI(Tl) depending on which pixel they hit. These angle dependent corrections are as

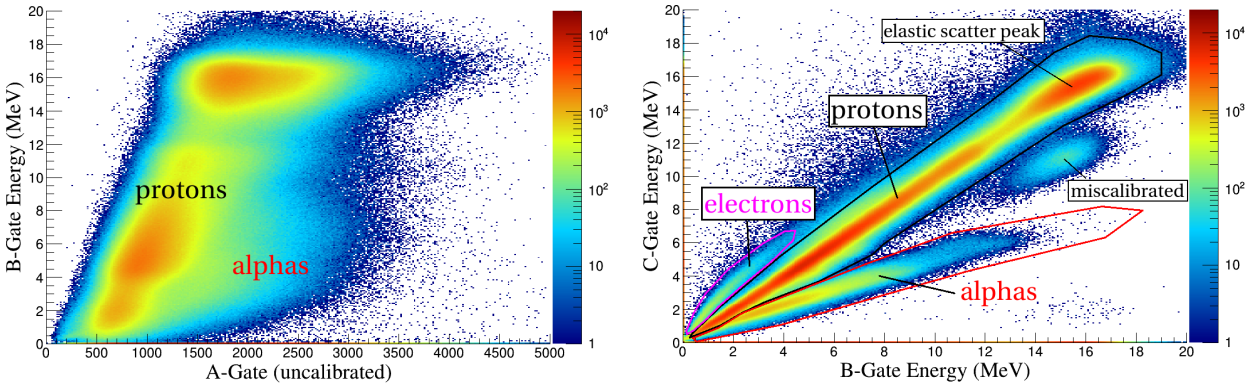

Figure 2.11: Experimental particle identification and energy calibration of the Phoswich Wall

large as 13% relative to one another. The calibrations and corrections in this experiment are only valid for protons. An entirely different set of calibrations would be necessary for alpha particles and electrons.

Figure 2.11 shows the Phoswich Wall A, B, C gate output from this experiment after energy calibration, drift correction, add-back, and energy-loss corrections. Recall that the A gate contains primarily ΔE information, the B gate contains both ΔE and E information, and the C gate contains primarily E information. As alluded to in previous sections, the Phoswich Wall detects multiple types of particles. At least three groups of particles are distinguishable: protons, alphas, and electrons/positrons. Since alpha particles have a larger Z than protons, the value of ΔE is larger for a given incident E. The Compared to ions, electrons and positrons have different energy loss parameters due to their small mass and large Bremsstrahlung losses. The positrons originate from the 19% positron emission decay branch of ^{56}Co and from γ-ray pair production in the detector material. Energetic electrons originate from target ionization, γ-ray pair production, Compton scatter, and photoelectric absorption.

Particle identification is much clearer for the B-C combination because the B and C pulse heights incorporate all the energy corrections described previously and have better resolution from a longer charge integral. The B gate likely contains more information on ΔE than it does on E because particle separation is clear in combination with C (which contains primarily E), but not A (which contains primarily ΔE).

2.4 GRETINA Array

This section begins with a brief overview of GRETINA including its segmented geometry, signal decomposition method, and concept of γ-ray energy tracking. Performance of crystal-level γ-ray energy, timing, and position resolution is summarized and supplemented with experimental data. Tracking parameters, performance, and suggestions are presented. Fi-

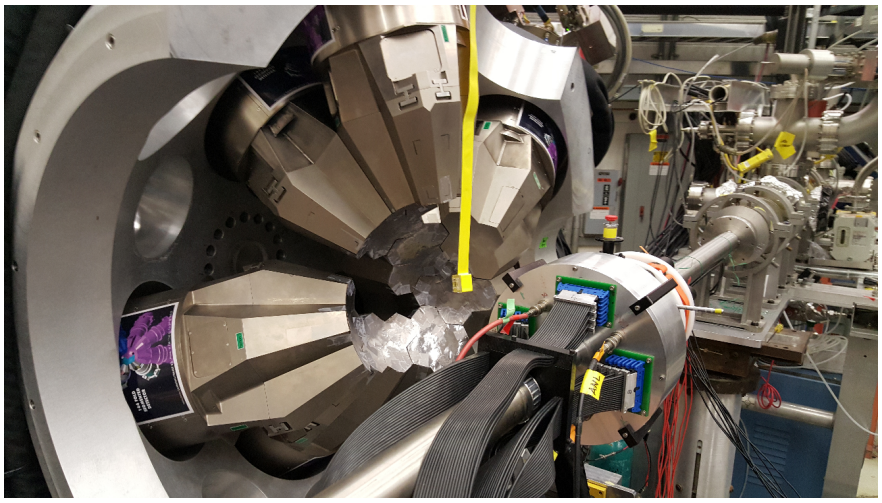

Figure 2.12: The Gamma-Ray In-beam Nuclear Array, GRETINA

nally, a new method to fix various energy/gain instabilities at the crystal level is shown to be useful.

Geometric Configuration

The **G**amma-**R**ay **I**n-beam **N**uclear **A**rray (GRETINA), shown in Figure 2.12, is the first stage in the construction of a high purity germanium (HPGe) array that covers 4π solid angle. The finalized version of the array will be called the **G**amma-**R**ay **E**nergy **T**racking **A**rray (GRETA). This detector currently covers over 1π solid angle in the use of 32 electrically segmented HPGe detectors. The segmentation of each of these crystals is 36-fold, allowing extraction of each γ-ray interaction point to great precision. Preceding large germanium arrays such as Gammasphere [33] in the United States, Euroball [34] in Europe, and various arrangements of clover detectors [35] relied on the Compton suppression method to improve resolving power.

Compton suppression consists of vetoing single scatter γ-ray escapes with exterior high density actively detecting shields such as Bismuth Germinate. This gives data analysts the ability to isolate events with complete energy deposition. GRETINA and its European counterpart AGATA [15], are the first of their kind to forgo the Compton suppression method entirely. The full 4π array GRETA will have the maximum coverage of germanium without bulky suppression shields that occupy a lot of valuable solid angle. This next generation of γ-ray detection is only possible with the energy tracking method [36]. Energy tracking utilizes the high degree of crystal segmentation to trace out multiple-scatter γ-ray paths.

The driving motivation for implementation of GRETINA is not its high photopeak efficiency nor good peak-to-total ratio. It is true these benefits will reduce the beam time necessary to achieve viable statistics per experiment, but the array was designed primarily

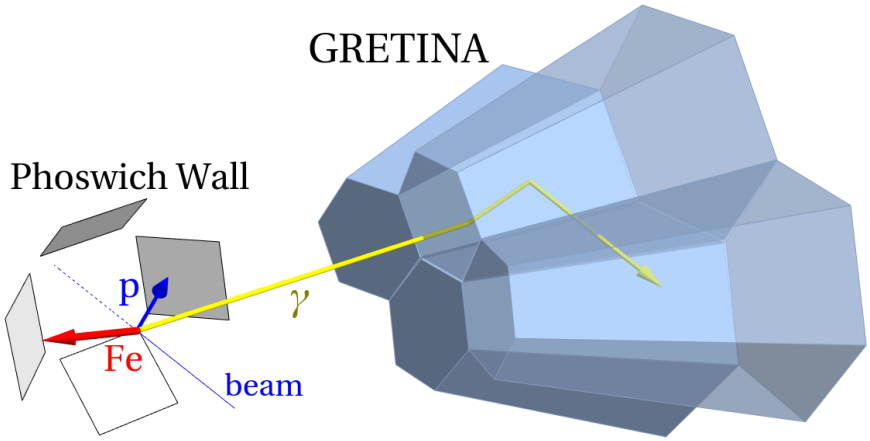

Figure 2.13: Location of GRETINA with respect to the reaction plane.

to meet the demanding requirements of nuclear structure. Frontiers of nuclear science involve studies of nuclei far from stability. It is rarely feasible to fabricate a target with a high purity of a *radioactive* isotope. Neither is it practical to place sensitive detection equipment nearby such high activity sources of radiation. Therefore, the optimal technique to access the limits of nuclear structure is in the production of radioactive ion beams (RIBs).

Particles in radioactive beams usually have a much larger mass than target nuclei and travel with large incident velocities. The reactions take place in inverse kinematics, where projectile-like fragments recoil at velocities typically $\beta \approx 0.07$. The emission of γ-rays from these nuclei are subject to significant Doppler broadening. Good angular resolution and segmentation correct for these effects through the means of event-by-event Doppler reconstruction. The precise determination of angle is not essential to normal kinematics experiments such as the present one, but the opportunity opens up new types of experimental analysis involving nuclear recoil. Figure 2.13 shows GRETINA's involvement in a typical reaction: the ^{56}Fe nucleus recoils away from a set of crystals and emits a γ-ray that scatters in the array.

The inner workings of GRETINA are quite complicated. Excellent bookkeeping is essential to keep all the digital output signals in order. The array is broken up into tiers of segmentation: GRETINA possesses 8 Quads, each Quad contains 4 crystals, each crystal has 6 vertical segments, each vertical segment divides into 6 hexagonal segments. The total segmentation of this experiment is 1152-fold. Each Quad has an identical design, but not all crystal within a Quad are interchangeable. Figure 2.14 shows the geometric division of GRETINA. The number of possible ways to tile the surface of a sphere limits the possible options of crystal configuration. The chosen configuration of the finalized GRETA has two types of hexagons, an A and B type, with 60 units each. The choice keeps a simple configuration for manufacturing purposes, limits the amount of germanium material necessary, maximizes solid angle coverage, and minimizes cost. Twelve untiled pentagonal spaces remain open for beam pipe and cabling.

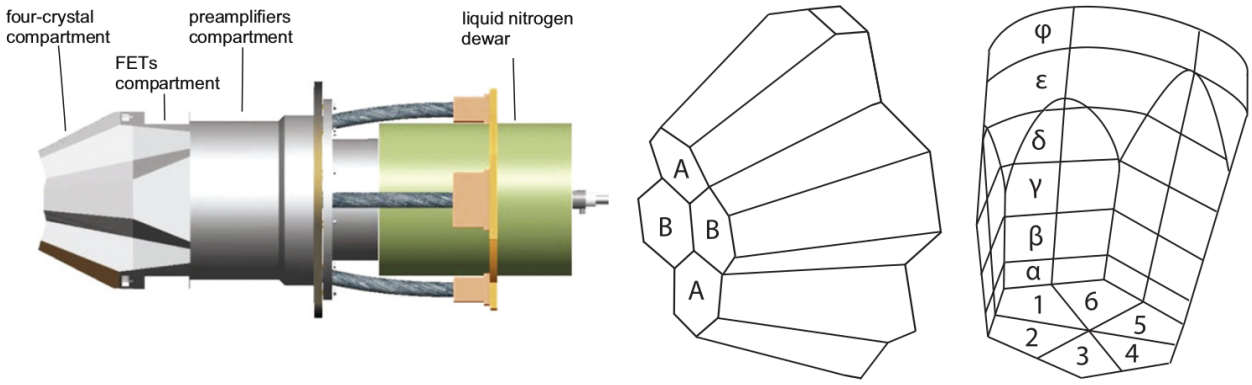

Figure 2.14: Quad, crystal, segment-level sectioning of GRETINA [14]

Each Quad stands at an 18.5 cm radial distance from target center to give space for an auxilary particle detector. Germanium inside each crystal is approximately 9 cm in thickness and 8 cm in diameter. The effective actively detecting volume is much less than the total volume of the spherical shell. Gaps and canister wall material create 9.2 mm of dead space between adjacent crystals in different Quads. Core holes 1 cm in diameter and 7.5 cm in length reduce the germanium volume, but facilitate semiconductor doping. It is not currently technologically practical to deplete a volume of germanium more than a few centimeters wide. Furthermore, the aluminum case and cryostat capsule cause scattering and absorption of γ-rays which interferes with energy tracking.

The crystals are n-type HPGe with less than 1.8×10^{10} cm^{-3} net impurity. Each Quad has a single liquid nitrogen cryostat. Quads contain 148 charge sensitive preamplifiers to readout the 37 signals from the four interior crystals. The Field-Effect Transistors (FETs) that measure the *total energy* deposited in each *crystal* are liquid-nitrogen-cooled. The FETs that measure energy deposited in each *segment* are outside the cryostat for ease of maintenance.

Signal Decomposition

Energy tracking requires a better position resolution, Δr, than the dimensions of the segment, which is on the order of 25 mm. Often, γ-rays interact multiple times in a single segment. An event that has two interactions in neighboring segments would have a 180° uncertainty without sub-segment position resolution. Fortunately, output signals depend on the position of γ-ray interactions allowing for the necessary sub-segment resolution. After Compton scattering or photoabsorption, the charge migration of electrons and holes through the main segment determines the shape of the waveform. Furthermore, induced signals in *neighboring* segments help pinpoint the location of energy deposition.

The signal decomposition process relies on prior simulation to provide basis signals [37]. A numeric solution of the Poisson equation determines the potential and electric field in each crystal. Charge trajectories depend on γ-ray interaction energy and location as well

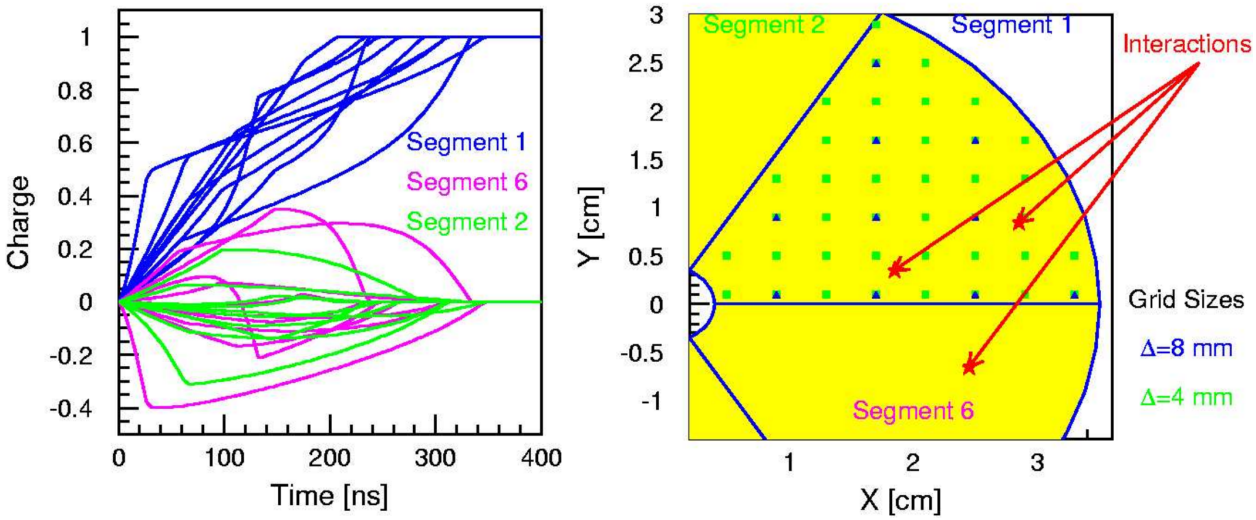

Figure 2.15: Basis signals for various interaction points in a grid spacing of 8 mm [39]

as detector geometry and applied voltage. Ramo's theorem determines the signal in nearby segment electrical contacts by calculating the induced instantaneous electric current [38]. The left panel of Figure 2.15 shows example basis signals for energy deposited at each of the 10 interaction locations in the $\Delta = 8$ mm grid spacing. An adaptive grid method further refines the sub-segment interaction position. An onsite computer farm calculates signal fits via brute force in a least χ^2 minimization. Currently, no other exotic fitting routines provide improvements in computational speed. Full waveforms are not saved; only more encompassing parameters like position, energy, and time of each interaction are stored on disk.

Position resolution is an important qualification for a γ-ray energy tracking array [40]. With poor resolution, unless interaction points are spaced a great distance, the uncertainty in scattering angle can be very large. To study position resolution, Paschalis *et. at.* [14] used a strong ^{60}Co source, lots of shielding, and an auxiliary scintillator detector [41]. The sharply collimated γ-rays scattered off a small volume of germanium inside the GRETINA crystal into the well shielded scintillator at various prescribed angles. The γ-rays imparted well defined amounts of energy to the electrons. These strongly constrained interactions produced a distribution of output signals. The signal decomposition process reconstructed the positions of the interactions as a spread of locations about the the known scattering points. They reported an average resolution of $\Delta r = 1.9$ mm with standard deviation 0.9 mm. Cross talk between signal channels was one of the major limiting factor in determining the locations of the energy deposition.

Tracking Algorithms

This analysis uses the energy tracking algorithm from Schmid *et. al.* [36]. The algorithm has several stages designed to maximize the resolving power of high multiplicity γ-ray events. The authors of the algorithm focused on their attention on the formation of superdeformed bands which decay with the emission of 20-25 γ-rays of 0.1-2.0 MeV. A scenario such as this would have around 100 γ-ray interaction points in a 9 cm thick germanium spherical shell. The reaction in this experiment, ^{56}Fe(p,p'), has much lower γ-ray multiplicities, typically 2-5. Therefore, not all stages of the tracking algorithm are useful for this low multiplicity purpose.

A single γ-ray has interaction points that localize in $\theta - \phi$ space as results of the forward peaked Klein-Nishina Compton scattering formula [42] and the decreasing average range of γ-rays with γ-ray energy E_γ. The first stage of tracking involves clustering of interaction points by angular separation angle, α, as viewed from the target origin. Angular separation is a variable parameter which produces different sets of clusters for different input values. A group of clusters will have good, fully absorbed γ-rays while other clusters will not. Often, two γ-rays are misidentified as one, one is misidentified as two, or one escapes out the back of the shell after partial energy deposition. These misidentified events require further processing.

A cluster is characterized as good or bad based on a calculated figure-of-merit, FOM. The FOM stems from a comparison between the two independent ways to calculate scattering angles: using deposited energies and interaction locations. The energy-angle relationship of Compton scattering provides the first way to calculate scattering angle:

$$\theta_c = \cos^{-1}(1 + \frac{m_e c^2}{E_\gamma} - \frac{m_e c^2}{E'_\gamma}), \tag{2.9}$$

where E'_γ is the scattered γ-ray energy, m_e is the electron rest mass, and θ_c is referred to as the Compton angle. The second way to calculate scattering angle is

$$\theta_m = \cos^{-1}(\hat{v} \cdot \hat{v}'), \tag{2.10}$$

where the $\hat{v}$ and $\hat{v}'$ are the unit vectors of the incident and scattered γ-rays, respectively, and θ_m is referred to as the measured angle. The reconstructed interaction locations from the signal decomposition process as well as the target origin determine these vectors. After computing these two quantities the FOM for a given three point combination is

$$\text{FOM} = \theta_m - \theta_c. \tag{2.11}$$

Early iterations of the algorithm have the FOM equal to the right hand side of (2.11) divided by $\Delta\theta$, the uncertainty in the difference of the two angles. However, the minor improvement from dividing by uncertainty does not justify its computational cost.

The algorithm first uses the target origin and all combinations of two interaction points in the cluster to determine the best 0-1-2 scattering sequence. The sequence is optimal for

the lowest FOM. Subsequent steps use the scattering location of the previous three-point sequence as the starting location of the next iteration. The procedure repeats for all points in the cluster, with the last assumed to be a photoabsorption. The total FOM for the cluster is an average of each individual sequence's FOM.

$$\mathrm{FOM}_{tot} = \frac{1}{N-1}\sum_{n}^{N}\mathrm{FOM}_n, \tag{2.12}$$

where N is the number of interactions.

Position resolution is the major limiting factor in FOM minimization. The fractional uncertainty of θ_m is on the order of $\Delta r/\lambda$, where Δr is the experimental position resolution and λ is the mean free path of the incident γ-ray. The fractional uncertainty of the Compton angle is on the order $\Delta E_\gamma/E_\gamma$, where ΔE_γ is the energy resolution of the detector. For $E_\gamma = 1.3$ MeV, $\Delta E_\gamma \sim 2$ keV making $\Delta E_\gamma/E_\gamma \sim 0.01$. On the other hand, typically $\Delta r \sim 1$ mm and $\lambda \sim 1$ cm making $\Delta r/\lambda \sim 0.1$, an order of magnitude larger in uncertainty.

The total FOM is an output parameter for event selection in offline analysis. For example, FOM might be used when creating histograms of total γ-ray energy. One may enforce a total FOM ¡ 0.8 for each accepted γ-ray cluster. This choice filters out events in which θ_c's and θ_m's disagree by more than 23° for the cluster. Ideally, histograms with this gate have improved peak-to-total ratios (P/T).

The FOM is undefined when the first and only interaction is photoabsorption. The tracking code assesses these events based on their interaction energy and depth d. A singles event is assigned a large FOM if $d \gg \lambda$, where λ is the mean free path of a γ-ray with incident energy equal to the interaction energy. Ideally, this process of singles rejection removes events where a γ-ray of a couple MeV scatters once in the crystal and escapes out the back of the germanium shell.

Additional algorithm modes are available in the tracking code. However, these modes are not always necessary for reactions with low γ-ray multiplicity. Tracking modes, such as those that attempt to split larger clusters, add significant computational time without much improvement of P/T.

Detector Performance

Figure 2.16 shows a ^{60}Co singles spectrum from this experiment using the central contact signal energies from GRETINA. The familiar features include:

1. two peaks at 1173.2 and 1332.5 keV due to the primary γ-rays
2. two corresponding Compton edges from backscatters in the germanium
3. a backscatter peak from backscatters outside the crystal
4. a 511 keV peak from pair production

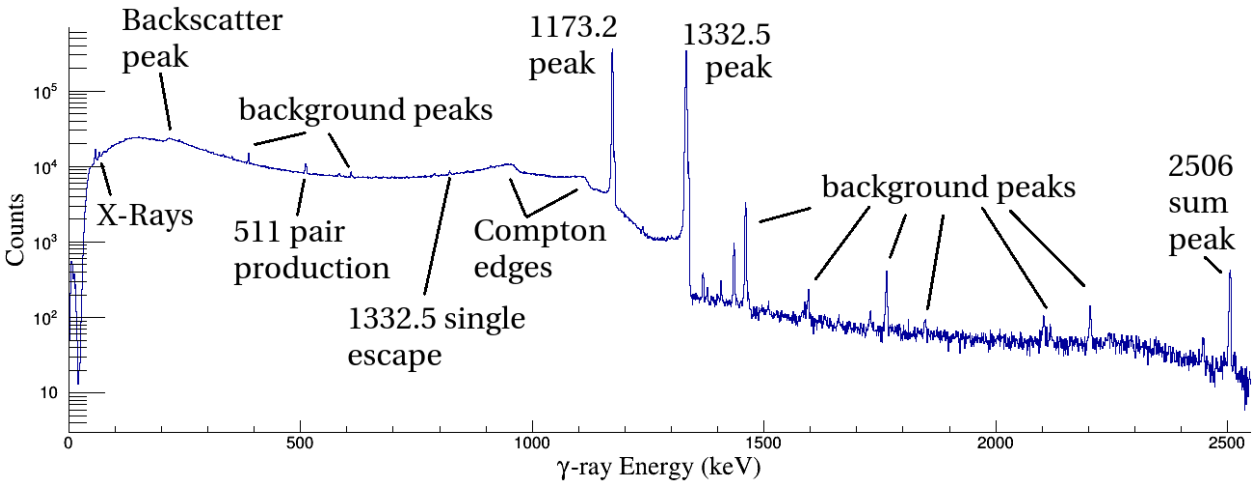

Figure 2.16: A simple GRETINA calibration spectrum with ^{60}Co prior to ^{56}Fe(p,p')

5. a sum peak at 2506 keV when both γ-rays deposit all their energy in one crystal
6. several low energy X-rays
7. multiple background peaks

The peak to total ratio (P/T) of a ^{60}Co source is often quoted as

$$\mathrm{P/T} = \frac{A(1173) + A(1333) + A(2506)}{A_{tot}}. \tag{2.13}$$

where $A(1173)$ and $A(1333)$ are the areas in the peaks of the source γ-rays of 1173.2 and 1332.5 keV respectively, $A(2506)$ is the sum peak, and A_{tot} is the number of counts up to just past the sum peak. There are many other ways to quote P/T [43], but equation (2.13) provides the simplest accounting of γ-rays and applies to both segmented and unsegmented detectors.

Calculation of P/T requires background subtraction. However, measurements in this experiment focus on in-beam data where background is assumed to have an empirical functional form. Also, the beam-induced background is completely different from pre-experiment background because the beam produces many short lived γ-ray emitters. Furthermore, post-experiment background is different from pre-experiment background because the beam produces many long-lived γ-ray emitters. Protons hitting the sides of the beam pipe are the largest producers of long- and short-lived beam-induced activity. Protons activating the iron target are also major producers of activity.

The photopeak efficiency, ϵ_p, is the probability that a single emitted γ-ray is measured in the photopeak of the spectrum. Calculation of ϵ_p involves angular correlations of γ-rays and a scattering factor C_S, the probability for γ-rays to scatter out of one crystal and fully absorb

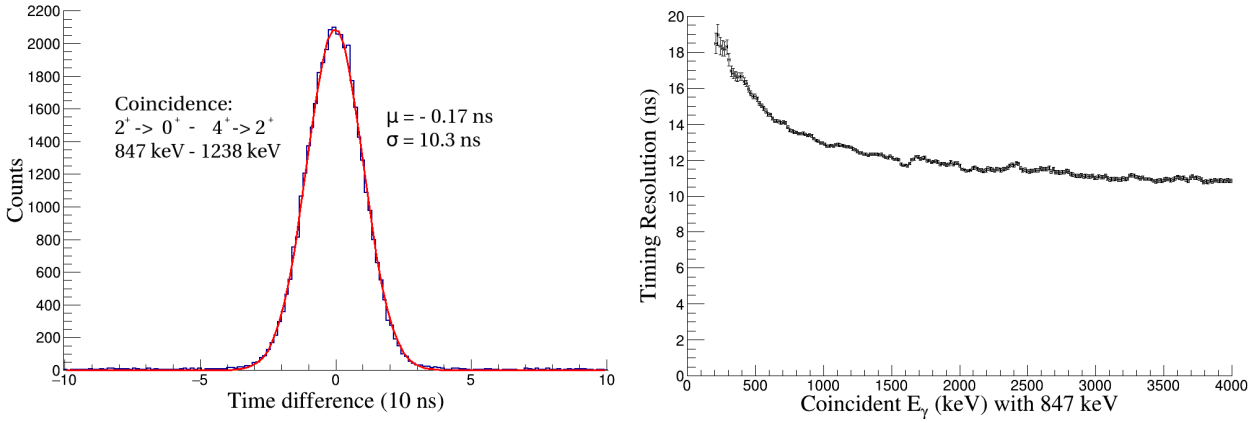

Figure 2.17: Experimental GRETINA $\gamma-\gamma$ timing resolution with the 847 keV ^{56}Fe $2_1^+ \rightarrow 0_1^+$ among all 32 crystals

in the remainder of the array. The P/T and absolute efficiencies were not investigated in this experiment due to the lack of a good background measurement. Lauritsen *et. al.* [43] report P/T = 0.381(5) and $\epsilon_p = 6.0(6)$ % using the central contact energies for 28 crystals. The 32 crystal configuration of this experiment has an extrapolated $\epsilon_p = 6.8\%$. In comparison, Gammasphere has $\epsilon_p = 7.8(8)\%$ for 100 active detectors.

GRETINA operates with purely digital electronics after the preamplifier stage. The timing of γ-ray interactions is determined at the software level from the digitized waveforms. A constant fraction discrimination (CFD) algorithm subtracts a time-delayed fraction of the waveform from the original pulse. The pulse height independent zero-crossing of the CFD output is resistant to walk effects. A polynomial fit to several points above and below the zero-crossing recovers the intrinsic germanium crystal timing from a 100 MHz sampling rate.

The left panel of Figure 2.17 shows in-beam data from this experiment of coincident ^{56}Fe 847 and 1238 keV γ-rays interacting in separate crystals. The centroid time difference, μ, between these two γ-rays is approximately equal to zero since they interact at nearly the same time and have no prescribed ordering in the array of data. The timing standard deviation, σ, for two crystals is approximately a factor of $\sqrt{2}$ larger than a single crystal's timing σ_{sing}. Therefore the collection of 32 crystals has an average of $\sigma_{sing} = 7.28$ ns around $E_\gamma = 1$ MeV, which is a bit larger than a typical single germanium crystal.

The right panel of Figure 2.17 shows in-beam data from this experiment of ^{56}Fe 847 keV γ-rays coincident with crystal interaction energies from 250 keV to 4 MeV. $\gamma - \gamma$ timing is nearly independent of the second γ-ray's energy above 1.5 MeV. However, $\gamma - \gamma$ timing severely worsens at low energy due to the small number of charge carriers migrating in the crystal.

Figure 2.18 shows this experiment's particle$-\gamma$-ray timing, $\Delta t_{p\gamma}$, with particles of all energies from the Phoswich Wall and γ-rays above 837 keV from GRETINA. The positive-valued centroid of the main peak indicates that the data acquisition systems register γ-rays before particle events. This may be due to the fact that the γ-rays have a shorter time-

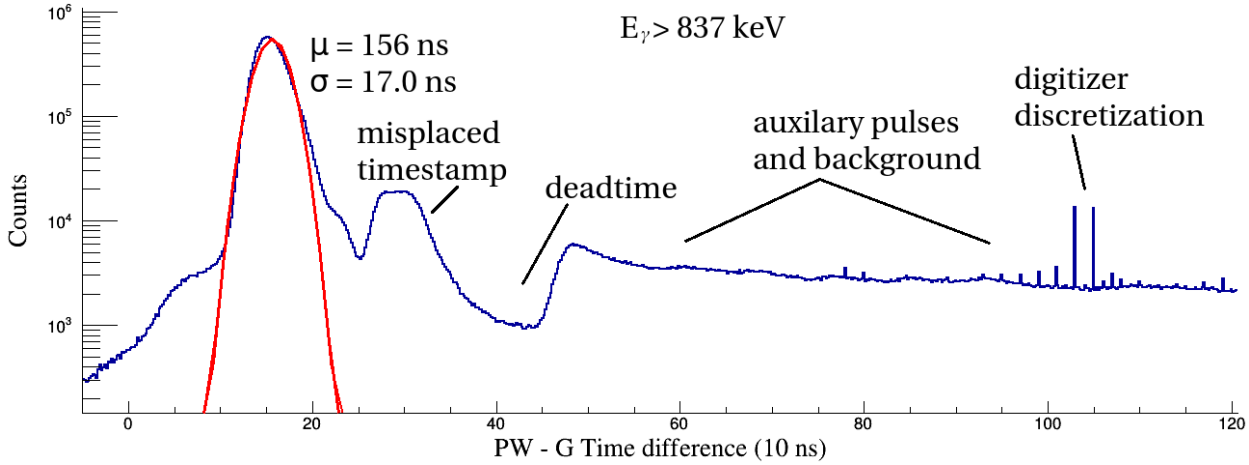

Figure 2.18: The Phoswich Wall (PW) and GRETINA (G) particle−γ-ray timing

of-flight (TOF) than heavy charged particles. However, there are many other factors that obfuscate an absolute TOF measurement including cable lengths and signal processing. The smaller $\Delta t_{p\gamma}$ peak at later times is not well understood and could be the result of a mis-recorded timestamp. The γ-ray energy spectrum of the $\Delta t_{p\gamma}$ second peak is nearly the same as the energy spectrum from the main $\Delta t_{p\gamma}$ peak, so the feature is likely a digitizer artifact. Additional digitizer artifacts are visible around 150 ns as sharp timing peaks, which are likely the result of digitizer discretization. Digitizer issues are on the Phoswich Wall side of signal processing since the problems were absent in γ-ray−γ-ray coincident timing as seen in the left panel of Figure 2.17. Since the second $\Delta t_{p\gamma}$ timing peak and other features are nearly two orders of magnitude smaller than the main $\Delta t_{p\gamma}$ peak, the events are not a large concern and data analysis is restricted to counts in the main peak.

Particle−γ-ray timing centroids and standard deviations are independent of particle energy deposition. This timing is in contrast to γ-ray−γ-ray timing which depends on energy as shown previously in the right panel of Figure 2.17.

Counts with $\Delta t_{p\gamma} > 500$ ns are primarily from neighboring pulses and partially from ambient room background activity. Beam pulses arrive roughly once every 40 ns, allowing several bunches to pass through the target before the timing window closes. The acquisition system has some inherent deadtime as there is a large drop in counts for $350 < \Delta t_{p\gamma} < 475$ ns. The Phoswich Wall events are global triggers for the acquisition system. GRETINA will only record waveforms within a prescribed timing window before and after each Phoswich Wall trigger. Digitizer banks can only readout approximately 15 MB/s per crystal, whereas a continuous waveform of one signal contact corresponds to 175 MB/s at 14-bit resolution and 100 MHz. Signal trace length is 1.6 μs, corresponding to about 14 kB for an entire crystal for one event, and limiting the crystal event rate to about 1.1 kHz. Local computational resources performed data processing during the experiment. The computer nodes reconstructed γ-ray interactions and saved only segment- and crystal-level energies and timing.

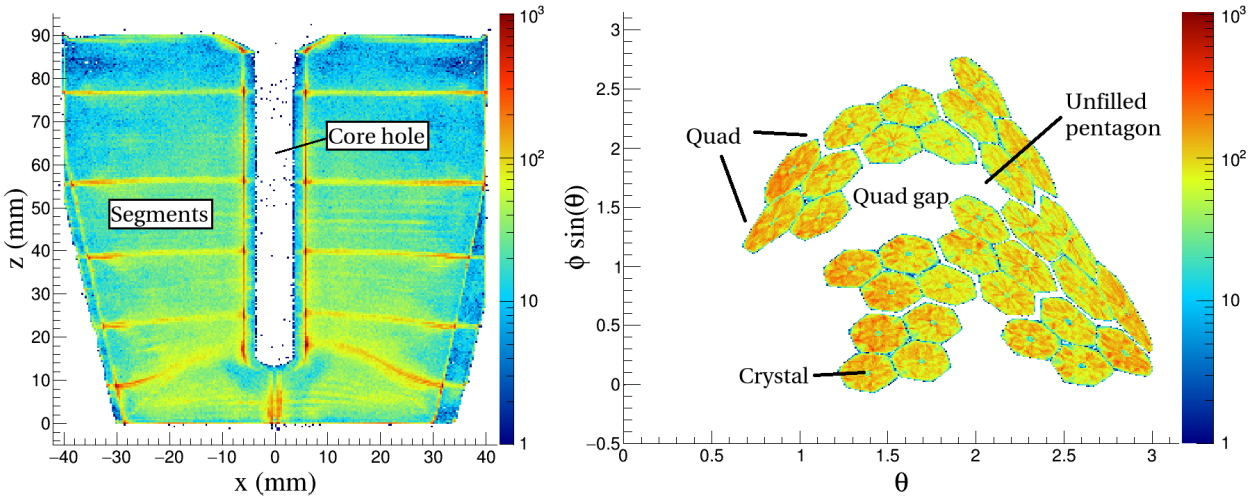

Figure 2.19: Crystal interaction locations in the XZ plane (left) and sinusoidal projection of the GRETINA array (right)

Figure 2.19 shows the results of the signal decomposition process for this experiment. The left panel shows a superposition of all crystals as a cut through the xz-plane in the crystal coordinate system. Position reconstruction of signal decomposition has a tendency to fault on segment edges and corners making segment boundaries visible. The core holes are necessary to uniformly dope the crystal volume during the fabrication process. The right panel of Figure 2.19 shows a map of the crystals in the lab polar coordinate system. The 8 Quad configuration at Argonne National Lab spans a large range of θ in contrast to the National Superconducting Cyclotron Lab (NSCL) configuration which primarily covers forward angles ($\theta < \pi/2$). The Argonne configuration is optimal for the stable beam facility which often provides reactions of normal kinematics. Covering back angles ($\theta > \pi/2$) allows access to a large range of Doppler shifts. The NSCL configuration is optimal for the fast beam facility which mostly provides reactions of inverse kinematics. The NSCL configuration maximizes solid angle coverage to account for an effect known as "Doppler focusing" in which γ-rays emitted isotropically in the frame of the heavy ejectile emit at forward angles in the lab frame.

Tracking Performance

In this experiment, the clustering algorithm used an angular separation parameter $\alpha = 15°$, regardless of the number of interaction points. The central contact signal has better energy resolution than the 36 segment contact signals because the FET for the central contact is inside the cryostat and the energy determination does not rely on the success of the signal decomposition process. Therefore, the tracking code used the central contact as normalization for individual interaction points inside a crystal to maintain stability. Tracking modes that recluster with a smaller FOM, split clusters, and try to match isolated singles

were turned off.

Clustering was only performed if the interaction points are coincident in time. Interactions points with timing difference $|\Delta t|$ less than 30 ns are automatically deemed coincident, otherwise further investigation is necessary. The second check deems interaction points i and j as coincident if their time difference satisfies the following energy dependent equation:

$$\frac{|\Delta t|}{10} < \sqrt{f(E_i)^2 + f(E_j)^2}, \tag{2.14}$$

where

$$f(E) = \begin{cases} \frac{b}{E-c} + d & E > E_{st} \\ a - E \cdot s & E < E_{st} \end{cases}, \tag{2.15}$$

and

$$s = \frac{b + (a-d)\cdot(c - E_{st})}{(c - E_{st})E_{st}}, \tag{2.16}$$

with empirical parameters

$$a = 4, \quad b = 1600, \quad c = 250, \quad d = 1.5, \quad E_{st} = 400\,\text{keV}. \tag{2.17}$$

This check includes low energy γ-ray interactions that have poor timing resolution and excludes high energy γ-ray interactions from different pulses.

Since a lot of attention is paid to high energy γ-rays in this experiment, the angular separation parameter might be too small when the mean free path is large. Furthermore, there are a lot of holes in GRETINA compared to the future GRETA, so a γ-ray might escape one crystal and pass through a gap to a different part of the array. To reconcile this fact, the "combinecluster" algorithm was turned on. The combinecluster mode takes a base cluster that has a FOM > 0.4 and loops through including other clusters to try to reduce the base cluster's FOM. Modifications were made to the original code to include singles hits among loop candidates but not base candidates. Two clusters or singles hits are only candidates for the combinecluster mode if the mean positions of the two clusters are within a maximum distance of 25 cm from one another. The value of 25 cm is approximately the size of a missing Quad gap plus a few cm mean free path. The combinecluster mode does not combine more than 2 clusters. In this data set, the combinecluster mode improved the FOM of 7% of clusters with FOM > 0.4.

The "singles rejection" algorithm was turned on and it used interpolated values of max hit depths d_{max} from Table 2.1. These values put the photoabsorption probability at 0.5% past the given depth. For example, a 1750 keV γ-ray has a 0.5868% chance to photoabsorb as its 1st interaction in an infinite volume of solid germanium. The probability that a 1750 keV γ-ray transmits through 6.9 mm of germanium without interacting is 85.2%. Therefore, the probability for an incident 1750 keV γ-ray to first pass through 6.9 mm of germanium then subsequently photoabsorb is $0.852 \times 0.005868 = 0.005$. Compton scattering, photoabsorption, and pair production values were taken from the NIST mass attenuation database [44]. The algorithm mode assigns a FOM of 0.05 if $d < d_{max}$ and 1.9 otherwise.

E_γ (keV)	d_{max} (cm)	E_γ (keV)	d_{max} (cm)
0	0.0	500	4.95
50	0.29	600	4.5
60	0.49	800	3.7
80	1.0	1000	3.0
100	1.65	1250	2.15
150	3.4	1500	1.4
200	4.6	1750	0.69
300	5.4	16300	0.0
400	5.25		

Table 2.1: Max Hit Depths for Singles Rejection

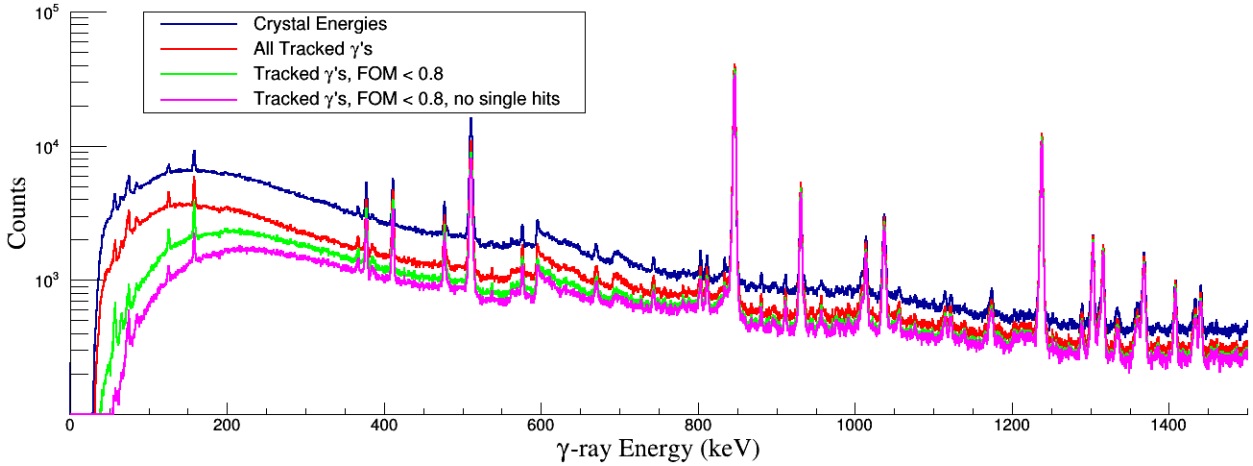

Figure 2.20: GRETINA singles spectrum for different restrictions on γ-ray energy tracking

Figure 2.20 compares crystal energies and tracking modes for this experiment. Tracking reduces the Compton background at low energy ($\sim$200 keV) by a factor of 2, the requirement that FOM < 0.8 further reduces the Compton background by a factor of 2, and all singles elimination reduces the Compton background by a factor of 1.5. The left panel of Figure 2.21 shows that tracking *increases* the number of counts in the 1238 keV ^{56}Fe $4_1^+ \rightarrow 2_1^+$ peak since the tracking process recovers Compton scatters in adjacent crystals. The FOM < 0.8 requirement and the elimination of all singles hits lower the Compton background but not the total area of the peak.

The right panel of Figure 2.21 shows a broad tracking FOM distribution. Finite interaction energy and position resolutions cause Compton escape events to have comparable FOM values to events of multi-scatter full energy deposition. The FOM cut of 0.8 means that a measured scattering angle off by 23° is acceptable for 2-point interactions.

Another way to estimate the quality of measured scattering angles is by constraining the Compton angle. If the ^{56}Fe $2_1^+ \rightarrow 0_1^+$ 846.7 keV γ-ray scatters with energy deposition 600 ± 5

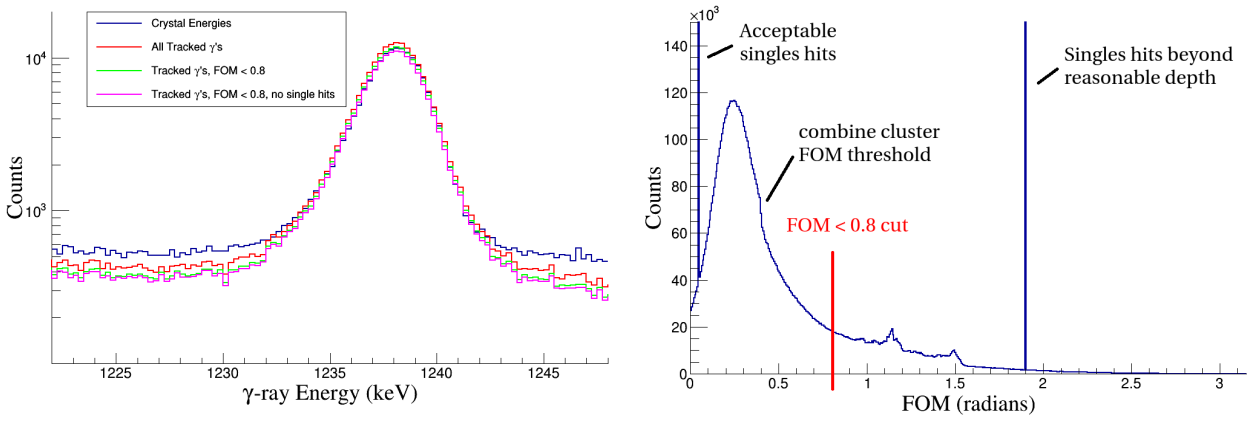

Figure 2.21: The effect of tracking on a mid-energy peak (left) and the tracking FOM distribution (right)

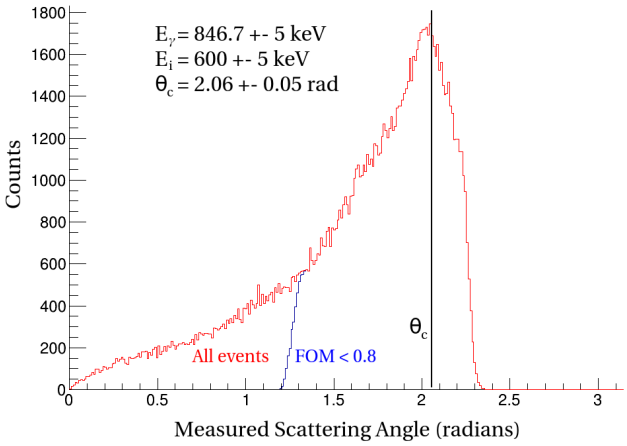

Figure 2.22: Quality of measured scattering angle after tracking

keV, the scattering angle is 2.06±0.05 radians according to Equation (2.9). Figure 2.22 shows experimental data of this scenario: events with $E_\gamma = 846.7 \pm 5$ keV and first interaction point energy 600 ± 5 keV. The measured scattering angle has a much larger uncertainty than the 0.05 radian uncertainty on the Compton angle. The resulting uncertainty of the measured scattering angle is approximately the centroid value of the previous FOM distribution: 0.25 rad.

GRETINA mainly has Compton escapes out crystal sides, whereas GRETA will mainly have escapes out crystal ends. For a source of 1.3 MeV γ-rays at the center of a 9 cm thick complete germanium spherical shell, 30% of the emitted γ-rays will leak out with at least a portion of their energy. The broad FOM distribution will not go away even with the development of GRETA as the probability for γ-rays to escape out the back is too high and the tracking algorithm accepts Compton scattering angles discrepant up to 23°. In contrast, Gammasphere had partial Compton suppression at the back of each crystal. If the GRETA

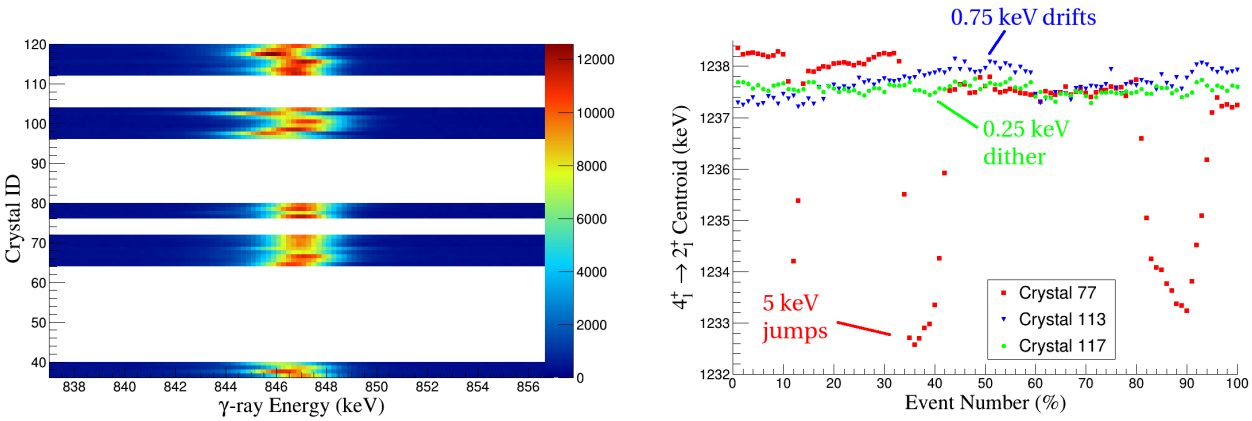

Figure 2.23: Crystal-level centroid mismatch (left), and time dependent gain fluctuation (right)

had at least some coverage of high density scintillator material at the back of each Quad, it might be possible to significantly reduce the Compton background.

Linear Event-By-Event Energy Correction and Recalibration

The analysis in Chapter 3 relies on precise values of γ-ray energy. Therefore, this section devotes a lot of attention to deviations from the initial energy calibration. Crystals, FETs, amplifiers, analog-to-digital converters (ADCs) are sensitive to temperatures shifts. Paschalis *et. al.* [14] show that the drifting ADCs are the primary source of energy/gain instabilities and are on the order of 0.025%/°F. This experiment experienced gain fluctuations and mismatches on both the crystal-level and segment-level.

The left panel of Figure 2.23 shows the first indication of energy/gain instability for this experiment: the photopeak centroids of the ^{56}Fe 846.7 keV γ-ray do not match among the crystals. Despite initial calibrations with ^{56}Co, ^{60}Co, and ^{152}Eu, centroid energies disagree by up to 2 keV because the ADC gains independently move away from initial values. The right panel of Figure 2.23 further investigates the gain fluctuations by displaying the centroid energy time dependence of a few crystals over the course of the experiment. The several types of gain fluctuation include:

1. short timescale, small magnitude "dither" on the order of 0.25 keV
2. long timescale, medium magnitude "drift" on the order 0.75 keV
3. short timescale, large magnitude "jumps" on the order 5 keV

Not all crystals experience all three effects.

Figure 2.24 shows an energy dependent gain mismatch at the segment-level for this experiment. The left panel shows modest agreement in gains for the medium energy ^{56}Fe

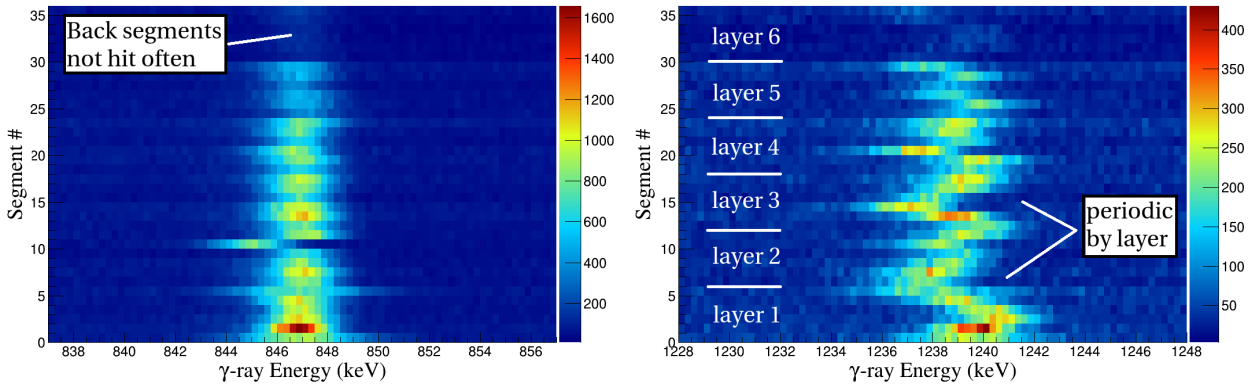

Figure 2.24: Segment-level γ-ray photopeak centroids for Crystal ID 69

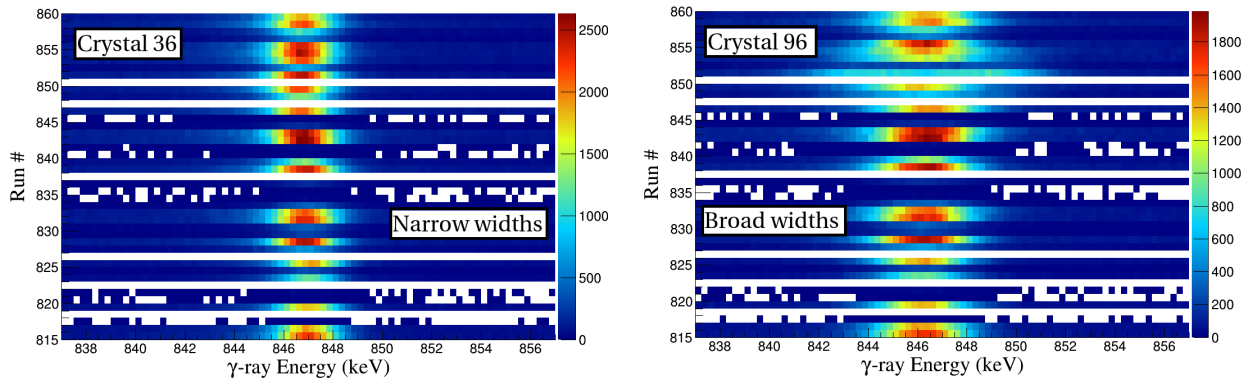

Figure 2.25: Run dependent crystal widths

846.7 keV γ-ray. The right panel shows disagreement in gains for the higher energy ^{56}Fe 1238.3 keV γ-ray. The disagreement is periodic every 6$^{\text{th}}$ segment because of the hexagonal geometry of the six crystal layers as described in Section 2.4. This periodic behavior may be the result of non-uniform cryostat refrigeration, temperature deviations in the warm FETs, or a temperature gradient in the ADC digitizer board.

Energy resolutions are not identical among the crystals. The left panel of Figure 2.25 shows that certain crystals have a narrow 2.4 keV full width at half maximum (FWHM) for $E_\gamma = 847$ keV. The right panel of Figure 2.25 shows that other crystals have a broader FWHM which increases and decreases from run to run to as much as 5 keV. Poor energy resolution is not likely attributable to gain fluctuations: broad width appear with as little as 100 counts in a peak.

It is not possible to deal with all the problems of energy/gain instabilities from a post-experiment analysis standpoint. Therefore, a simple algorithm was developed to correct the data on an event-by-event basis with the focus of eliminating short timescale jumps and long timescale drifts without introducing any gain issues at high energy. The corrections were made at the crystal-level before being used in tracking. During the data sorting, two

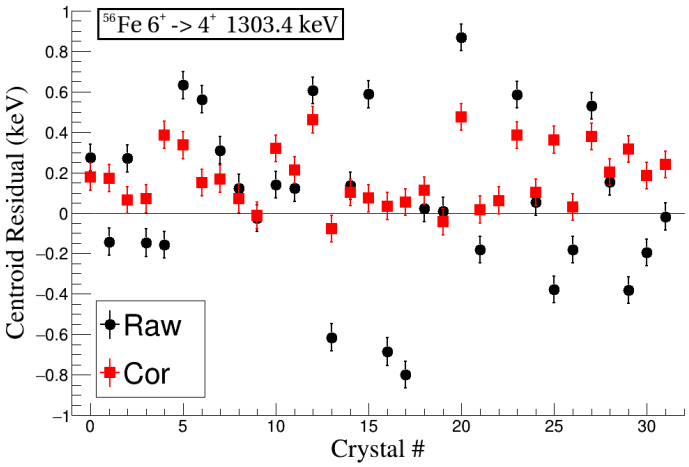

Figure 2.26: Residual ($E_\gamma - E_{true}$) distribution before and after event-by-event correction. (Note: Crystal # is not the same as Crystal ID)

windows surround the two major γ-ray transitions in ^{56}Fe: the 846.7 keV $2_1^+ \rightarrow 0_1^+$ and the 1238.3 keV $4_1^+ \rightarrow 2_1^+$. The gain *offset* is increased (decreased) a small amount if the lower half of the 846.7 keV window has 2 more (fewer) counts than the upper half. The gain *slope* is increased (decreased) a small amount if the lower half of the 1238.3 keV window has 2 more (fewer) counts than the upper half. After adjustments to gain slope and offset are made, window tallies are reset and data sorting resumes. The gain offset increment is 0.02 and the gain slope increment is 5×10^{-5}. These values are large enough to respond to large fluctuations in gain, yet small to maintain good energy resolution. The event-by-event correction is merely linear so as not to disrupt high energy photopeaks; a quadratic correction with three windows proved disadvantageous.

There are not enough statistics for each individual segment to adjust to rapid changes in gain. The data rate at the segment-level is a factor of 36 lower than the crystal-level and full energy deposition of a γ-ray in a single segment is more rare than in an entire crystal. Warm segment FETs add further unreliability in comparison to cryostat-cooled central contact FETs. Furthermore, tracking algorithms of Section 2.4 place more emphasis on central contact energy than individual segment energies.

Figure 2.26 shows the results of the event-by-event correction for the ^{56}Fe 1303.4 keV $6_1^+ \rightarrow 4_1^+$ transition, a γ-ray different from the two used to perform the correction. Event-by-event corrected data, "cor", has lower centroid standard deviation σ_μ in comparison to the uncorrected, "raw", data:

$$\sigma_{\mu,\text{raw}} = 0.45 \text{ keV}, \quad \sigma_{\mu,\text{cor}} = 0.15 \text{ keV}. \tag{2.18}$$

where

$$\sigma_\mu = \frac{1}{n}\sum_i^n (\mu_i - \mu_\mu)^2, \tag{2.19}$$

Source		$t_{1/2}$ (ps)	E_γ (keV)	Neighbor E_γ (keV)
^{56}Co	3^+_1	< 100	158.38 ± 0.03	-
^{55}Fe	$\frac{1}{2}^-_1$	6^{+6}_{-3}	411.42 ± 0.21	398, 405.5, 426
^{56}Fe	2^+_1	6.07 ± 0.23	846.7638 ± 0.0019	834.5, 843.7, 847.4
^{55}Fe	$\frac{5}{2}^-_1$	8 ± 3	931.25 ± 0.013	935.5
^{56}Fe	6^+_1	2.9 ± 5	1303.44 ± 0.06	1289.8, 1312, 1316.4
^{55}Fe	$\frac{7}{2}^-_2$	37.9 ± 17	1408.45 ± 0.14	1387, 1417

Table 2.2: Recalibration Source γ-rays

$n = 32$ is the number of crystals, and μ_μ is the mean of the means. This shows that after event-by-event drift corrections, GRETINA contends with typical germanium crystals which can achieve 100-200 eV peak centroid accuracy at 1.3 MeV.

In general, the event-by-event correction algorithm does not put the photopeak centroids at their true energies. This is realized in Figure 2.26 where $\mu_\mu = 0.175\,\text{keV} \neq 0$. The following phenomena can skew the number of counts in a particular half of a given window and cause an energy shift in the event correction algorithm:

1. Neighboring peaks
2. Non-flat Compton background
3. Doppler shift from nuclear recoil
4. Incomplete charge collection due to trapping of charge at dislocations in the germanium crystal lattice
5. Photoelectron escape from the germanium crystal
6. Compton scattering of the γ-ray off external material *into* the detector

The magnitude of these effects differ among the 36 crystals and are too complicated to account for on an absolute energy scale. Therefore, a second round of calibration is necessary for event-by-event corrected data.

The recalibration procedure performs a linear fit to experimental versus database values of γ-rays from Table 2.2. The Evaluated Nuclear Structure Data File (ENSDF) [45] provides comparison values. Recalibration is acceptable using external, background, or beam-induced γ-ray sources. The major restriction on an acceptable recalibration γ-ray is the half-life ($t_{1/2}$) of the parent level. Unless the nucleus comes to a full stop before emitting the γ-ray, there will be an angle-dependent Doppler shift. The slowing down time inside the target is a few hundred fs for recoil energies of a few hundred keV and $A \sim 56$. Therefore, the requirement for beam-induced recalibration γ-rays is $t_{1/2} > 1$ ps of the parent level.

There are not many fully-slowed γ-ray transitions available from the ^{56}Fe(p,*) reaction products. Nuclei typically emit high energy γ-rays quickly, since transition rates scale as

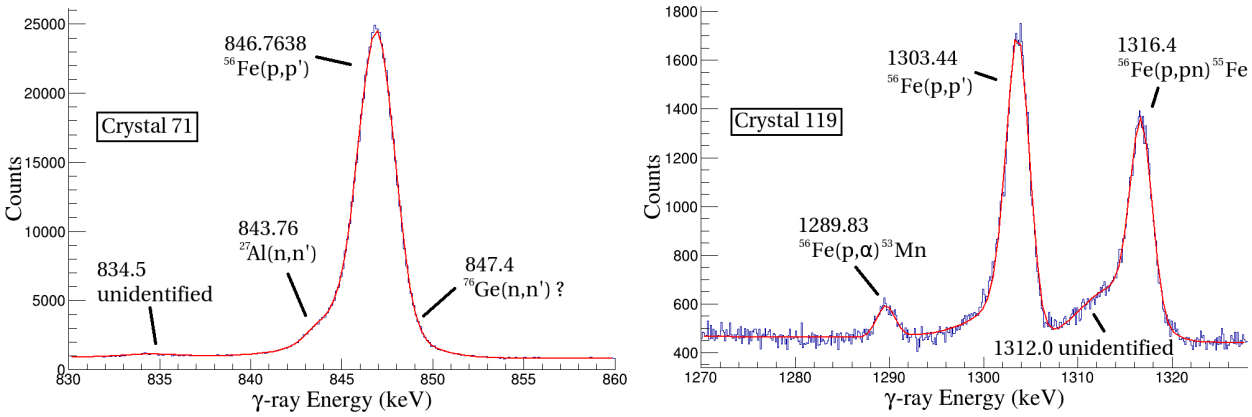

Figure 2.27: Multipeak recalibration fits

$\sim E_\gamma^3$. Level density rises exponentially with nuclear excitation energy E_x, providing more options in the decay of a highly excited level. These options speed up the transition, making highly excited levels unlikely candidates for recalibration. Therefore, Table 2.2 includes *all* available γ-rays that satisfy the parent half-life requirement.

Figure 2.27 shows that the few unshifted γ-rays that are available often have many neighboring peaks. Neighboring peaks do not always have the same intensity in different crystals, so a lot of computational logic is necessary. Fits to main peaks of Table 2.2 have the following form:

$$y = C_1 \cdot \exp\left[-\frac{1}{2}\left(\frac{x-\mu_1}{\sigma}\right)^2\right] + C_2 \cdot \exp\left(\frac{x-\mu_1}{\beta}\right) \operatorname{erfc}\left(\frac{x-\mu_1}{\sqrt{2}\sigma} + \frac{\sigma}{\sqrt{2}\beta}\right) + C_3 \cdot \operatorname{erfc}\left(\frac{x-\mu_1}{\sqrt{2}\sigma}\right) \tag{2.20}$$

$$C_1 = H_1(1-R), \quad C_2 = \frac{H_1 R}{\operatorname{erfc}\left(\frac{\sigma}{\sqrt{2}\beta}\right)}, \quad C_3 = \frac{H_1 S}{2} \tag{2.21}$$

where x is the energy channel number, y is the number of counts in that channel, μ_1 is the energy centroid, σ is the standard deviation, β is the skewedness, H_1 is the height of the peak, R is the incomplete charge collection fraction, and S is the background step factor. The first term in (2.20) is a standard Gaussian distribution which accounts for complete charge collection of full γ-ray energy deposition. The second term is a skewed Gaussian which accounts for incomplete charge collection due to trapping of charge at dislocations in the germanium crystal lattice. The third term is a step function which accounts for photoelectron escape from the germanium crystal and Compton scattering of γ-rays into the detector. During the fitting routine, $S = 0.005$ and $R = 0.1$ are fixed to source calibrated values, but β is allowed to vary. Neighboring peaks are fit with standard Gaussians of independent heights H_i and centroids μ_i. All peaks are fit on top of a linear Compton background.

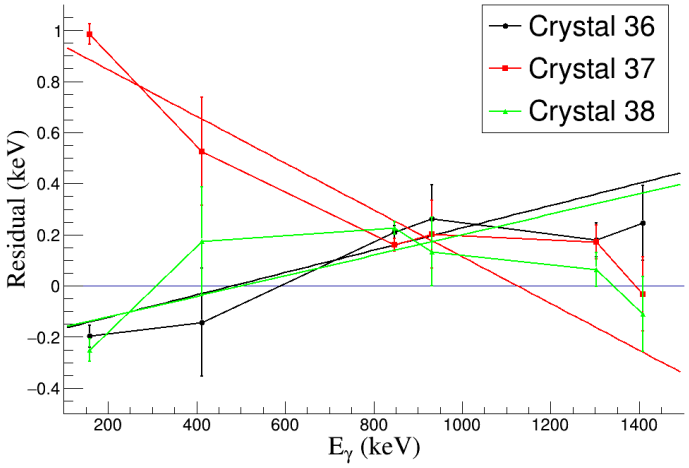

Figure 2.28: Residuals ($E_\gamma - E_{true}$) after event-by-event correction but before recalibration

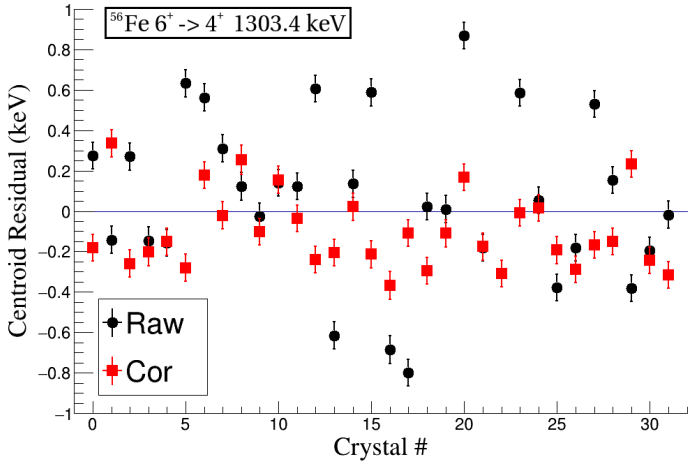

Figure 2.29: Before and after the combination of event-by-event correction and recalibration

Figure 2.28 shows the results of the fitting routine for three of the crystals. The largest soure of centroid uncertainty is the shape of the main peak, which often has a more complex shape than Equation (2.21). Most of the crystals have residuals that are linear with E_γ, so a linear recalibration was applied to each crystal in addition to the event-by-event correction. An attempt was made at quadratic recalibration but it worsened agreement among the crystals at high E_γ.

Figure 2.29 shows the results of recalibration for the ^{56}Fe 1303.4 keV $6_1^+ \rightarrow 4_1^+$ transition. In comparison to data with only the event-by-event correction, and for this particular E_γ, the mean of the means has improved at the cost of a slight deterioration of the centroid variance.

$$\mu_\mu = -0.10\,\text{keV}, \qquad \sigma_{\mu,\text{recal}} = 0.185\,\text{keV}. \tag{2.22}$$

No external or background sources were used during this experiment. However, it would

be worthwhile to include nearby high energy γ-ray sources for future experiments with GRETINA. Since there is no beam axis, the parent level requirement $t_{1/2} > 1$ ps is unnecessary. Sources could even be placed outside of the target chamber, allowing access to the back layers of the crystal. Tracking would eliminate these γ-rays from further stages of analysis. It might be possible to do segment-level event-by-event correction and recalibration with this setup since the back crystal layer is exposed.

The drift correction algorithm and recalibration procedure provide modified inputs for γ-ray energy tracking. Tracking *success* is not greatly not greatly improved since position resolution is the limiting factor, not energy resolution. However, the energy corrections carry into the output of the tracking algorithms providing enhanced sensitivity for angle dependent Doppler shifted energies by a factor of $\sigma_{\mu,raw}/\sigma_{\mu,recal} = 2.5$ and $\sigma_{\mu,raw}/\sigma_{\mu,cor} = 3.0$.

Chapter 3

Theoretical Basis

This chapter contains the foundations for all the dominant physical mechanisms occurring in this experiment. This material describes the principles governing nuclear reactions and the subsequent motion of reaction ejectiles through the target material. The structure of the nucleus and its emission properties are condensed from through successive levels of approximation and placed in the framework of thermodynamics. The chapter concludes with the introduction of a new method for determining an important nuclear property: the absolute magnitude of the Gamma Strength Function.

3.1 Kinematics

This section provides the energy and momentum relationships between the reactants and products in a general binary reaction.

Consider the following binary reaction:

$$a + X \rightarrow Y + b \quad \text{or} \quad X(a,b)Y, \tag{3.1}$$

where a is the projectile, X is the target nucleus, b is the ejectile, and Y is the residual nucleus. In normal kinematics $m_X >> m_a$, where m_i denotes the mass of particle i; however, the following equations apply to reactions of inverse kinematics as well where $m_a >> m_X$. For 16 MeV ^{56}Fe(p,p')^{56}Fe*, a and b are protons, X is ^{56}Fe and Y is ^{56}Fe*.

The conservation of relativistic energy before and after the reaction is the following

$$m_X c^2 + T_X + m_a c^2 + T_a = m_Y c^2 + T_Y + m_b c^2 + T_b, \tag{3.2}$$

where T_i is the kinetic energy of particle i. The reaction Q-value is defined as the initial mass energy minus the final mass energy:

$$Q = (m_X + m_a - m_Y - m_b)c^2. \tag{3.3}$$

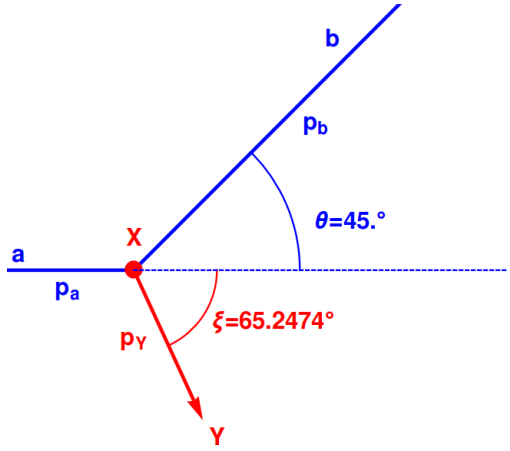

Figure 3.1: To scale, reaction energetics for proton elastic scattering on ^{56}Fe: a 16 MeV incident proton (a) scatters off target ^{56}Fe nucleus at rest (X) resulting in outgoing proton (b) exiting at angle θ and recoiling ^{56}Fe (Y) exiting at angle ξ.

Conservation of linear momentum along and perpendicular to the beam axis before and after the reaction give

$$p_a = p_b \cos\theta + p_Y \cos\xi \tag{3.4}$$
$$0 = p_b \sin\theta - p_Y \sin\xi, \tag{3.5}$$

where p_i is the momentum of particle i, and θ and ξ are the opening angles of ejectiles b and Y, respectively. Figure 3.1 illustrates the reaction plane and identifies all the relevant variables. These equations are valid in 3D simply by rotating the system to the appropriate azimuthal angle.

Applying the assumption that the target is at rest ($T_X = 0$) and combining Equations (3.2)-(3.5), the relationship between the outgoing kinetic energy and angle of the ejectile is dependent on the Q-value [46]:

$$T_b^{1/2} = \frac{(m_a m_b T_a)^{1/2}\cos\theta \pm \{m_a m_b T_a \cos^2\theta + (m_Y + m_b)[m_Y Q + (m_Y - m_a)T_a]\}^{1/2}}{m_Y + m_b}. \tag{3.6}$$

The threshold energy for reactions with negative Q-value is:

$$T_{th} = -Q\frac{m_Y + m_b}{m_Y + m_b - m_a} \tag{3.7}$$

which occurs at $\theta, \xi = 0°$. In 16 MeV ^{56}Fe(p,p'), the maximum excitation of ^{56}Fe is 15.72 MeV.

There is a one-to-one correspondence between T_b and θ above incident energy T'_a:

$$T'_a = -Q\frac{m_Y}{m_Y - m_a}. \tag{3.8}$$

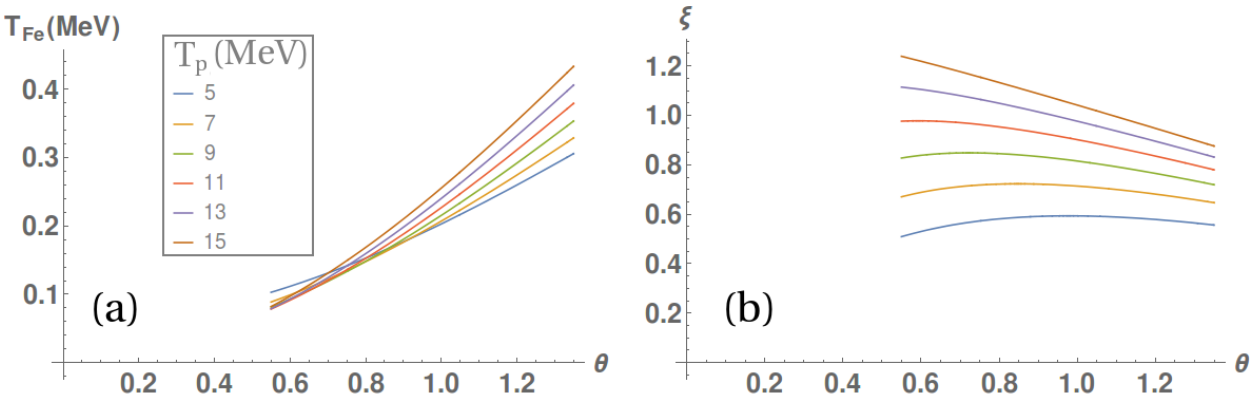

Figure 3.2: Recoil kinematics for 16 MeV ^{56}Fe(p,p')^{56}Fe. (a) Recoil kinetic energy, T_{Fe}, for a range of detected proton energies and angles. (b) Recoil opening angle, ξ, for a range of detected proton energies and angles. The Phoswich Wall can detect protons with angle $0.55 < \theta < 1.35$. Proton kinetic energies between $5 < T_p < 15$ MeV are relevant to this experiment.

For 16 MeV incident protons, only $|Q| > 15.7$ MeV poses the double-valued concern, otherwise measurements of T_b and θ uniquely determine Q:

$$Q = T_b\left(1 + \frac{m_b}{m_Y}\right) - T_a\left(1 - \frac{m_a}{m_Y}\right) - 2\left(\frac{m_a}{m_Y}\frac{m_b}{m_Y}T_aT_b\right)^{1/2}\cos\theta. \tag{3.9}$$

This work only investigates ^{56}Fe excitations below the neutron separation energy, $|Q| < S_n = 11.197$ MeV, thus avoiding the double-value issue. For reference, population of the first level in ^{56}Fe corresponds to $Q = -0.847$ MeV, the minimum energy that the Phoswich Wall can distinguish between a proton and an α-particle is approximately 2.5 MeV, and the maximum energy that the Phoswich Wall can fully stop a proton is approximately 21 MeV.

For energies considered in this work, measurements of T_b and θ also uniquely determine ξ and T_Y using the following rearrangements of Equations (3.2)-(3.5):

$$T_Y = Q + T_X + T_a - T_b, \tag{3.10}$$

$$\sin\xi = \frac{p_b}{p_Y}\sin\theta. \tag{3.11}$$

Again there is a one-to-one correspondence between angles θ and ξ in Equation (3.11) since $0 \leq \theta < \pi$ and $0 \leq \xi < \pi$. Since $T_i \ll 2m_ic^2$, the non-relativistic conversion of kinetic energy to momentum works to good approximation for protons and ^{56}Fe nuclei at the energies considered in this work:

$$p_i \approx \sqrt{2T_im_i}. \tag{3.12}$$

Figure 3.2 shows the ^{56}Fe* energies and angles spanned in this experiment. For the angular coverage of the Phoswich Wall configuration used in this experiment, the minimum and maximum ^{56}Fe* recoil kinetic energies are approximately 0.07 and 0.42 MeV, respectively.

3.2 Atomic Collisions

This section provides a brief overview to the theoretical framework of ions traversing matter. Various experimental questions related to the ion transport of the experiment in this work are answered using the stopping code SRIM.

Target design requires accurate knowledge of atomic collisions for the minimization of beam energy losses and maximization of the number of nuclear reactions. Charged particle detector design requires stopping power information to ensure a particle deposits the correct proportion of its energy in the various active detection layers. Data analysis requires the use a theoretical understanding of stopping to deduce fundamental quantities such as the lifetimes of excited nuclear states. Applications such as these have been the driving forces behind the development of the physics of atomic collisions for the past century. The new quasi-continuum lifetime method presented in this work also relies on the slowing down and angular deflection of ions in matter; therefore, it is instructive to provide a brief account of contemporary theory.

Lindhard Scharff Schiott Theory

Lindhard, Scharff, and Schiott (LSS) theory [47] is the backbone of current understanding of low energy ion penetration through matter. Appendix A outlines the important historical developments that led to this modern perspective. The primary motivation behind the establishment of LSS theory was the need for a tool to quantify ion ranges in matter resulting from previously unmeasurable nuclear reactions and decays, particularly fission. The improvement in techniques, which in 1960 allowed the measurement ion ranges to less than 100 Å[48], also provided a lot of new experimental validation. Futhermore, additional quantities such as range straggling, atomic sputtering, and ionization yields started to become instrumental in the determination of scattering parameters [49].

The major success of LSS theory was the unification of the competing processes of nuclear and electronic interactions into a single model. Prior literature on heavy particle transport theory [50] neglected electronic stopping and overcompensated with an increase in nuclear stopping [47]. On the other hand, prior literature on continuous slowing down theory [51, 52] focused on electronic stopping, treated nuclear stopping as a small perturbation, and attributed experimental discrepancies to incorrect Coulomb screening parameters [53, 54]. LSS theory combined the strengths of statistical and continuous approaches which proved difficult considering electronic and nuclear impact parameters differ by nearly four orders of magnitude.

To determine atomic deflection angles, LSS theory uses the Binet equation of central force motion derived in Appendix B:

$$\frac{d^2u}{d\phi} + u + \frac{F(u)}{u^2 \mu v_\infty^2 b^2} = 0, \tag{3.13}$$

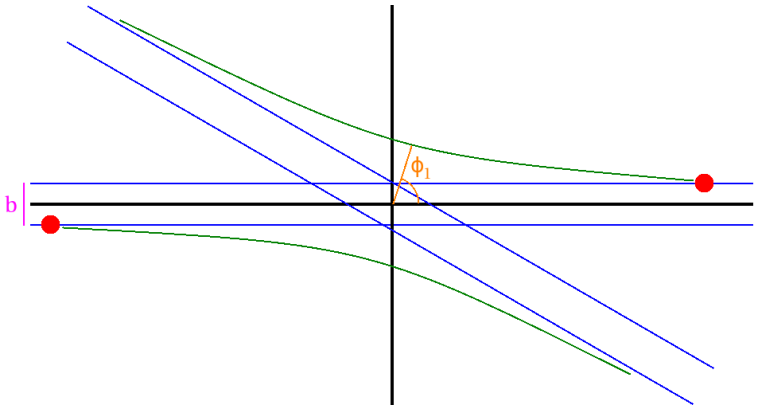

Figure 3.3: Scattering in the center of mass frame. The total deflection, θ, is equal to $\pi - \phi_1$.

where ϕ is the polar angle, $u = 1/r$ is the inverse distance of ion-atom separation, μ is the reduced mass, $F(r)$ is the interatomic repulsive force, b is the impact parameter, and v_∞ is the initial center of mass velocity. The point of closest approach occurs at angle ϕ_1 and the total deflection angle is $\theta = \pi - \phi_1$. Figure 3.3 depicts an ion-atom scattering event. The majority of the nuclear scattering portion of LSS theory focuses on an accurate determination and simplification of $F(r)$ and the procedure to solve Equation (3.13) for ϕ_1. For a force that depends on Z, Z_a, and r, the total deflection angle is a function of four variables:

$$\theta = \theta(Z, Z_a, T_\mu, b), \tag{3.14}$$

where $T_\mu = \mu v_\infty^2/2$ is the center of mass kinetic energy. A major goal of LSS theory is to achieve *similarity*, the concept that the dependent variable which characterizes scattering (such as θ) is a function of only one independent variable, such that any scattering calculation can apply the same equation. LSS attains similarity through the reduction and approximation of the interaction potential described in Appendix C

To obtain the functional dependence of the screening parameter a on Z and Z_a, LSS theory uses scaling laws of the Thomas-Fermi model. The Thomas-Fermi (TF) model [55] is a semiclassical theory developed in 1927 to approximate the distributions of electrons in atoms and molecules. The theory is a precursor to modern Density Functional Theory and is only valid in the limit of infinite nuclear charge, but it can reproduce general features in electron density. Appendix D provides an introduction to the Thomas Fermi model and applies the theory to ion scattering screening parameters.

In LSS theory, the electronic portion of stopping occurs as a continuous process between nuclear collisions. Since minuscule deflections have some finite probability even at large distances, scattering calculations only consider collisions above a specified energy transfer threshold. In the high velocity regime LSS theory applies the Bethe formula of (A.1), and for the low velocity regime LSS theory applies a velocity proportional stopping from Thomas-Fermi calculations [56] where the electronic stopping acts as a frictional force between scattering events.

The remainder of LSS theory combines the nuclear and electronic components of stopping and goes about doing the following:

- the search for simpler power law forms of the interaction potential that have solutions of total deflection θ that are a function of only one independent parameter
- the extrapolation of momentum transfer small angle scattering to wider angles while maintaining similarity
- the evaluation of the accuracy of wide angle extrapolations of power law potentials compared to an assortment of exact solutions of the Thomas-Fermi, Lenz-Jensen, Rutherford, and Bohr potentials (which do not have similarity)
- the introduction of a general scattering formula which is applicable to a wide range of reduced energies and angles
- the comparison of experimental range and straggling data to corresponding calculations

For the sake of brevity, the mathematical formalism involved in these steps has been omitted but is implemented in modern stopping power codes. LSS theory prospers in situations where both electronic and nuclear scattering influence stopping power across a wide range of incident ion energy.

SRIM - The Stopping and Range of Ions in Matter

The Stopping and Range of Ions in Matter (SRIM) [57] is a package of computer codes that simulates the penetration of energetic ions into matter. It covers a wide range of energies, incident ion and target atom species, as well as target molecular compounds. SRIM calculates ranges, straggling, and target damage effects including ionization, lattice displacement, and the creation of phonon and plasmon excitations. While there is a lot of literature on the measurement of experimental stopping powers, direct interpolation to other ions, atoms, and energies is not always possible to the desired accuracy. Therefore, SRIM uses the unified theoretical concepts outlined in the previous subsection to calculate general scattering cross sections and stopping powers.

To demonstrate the capabilities of SRIM, consider some of scenarios encountered in this experiment in which ions penetrate matter:

1. Protons from the beam lose energy in the 1.3 μm thick ^{56}Fe target
2. Elastically and inelastically scattered protons deposit energy in the 2.2 mm thick CsI(Tl) back layer of Phoswich Wall
3. Elastically and inelastically scattered ^{56}Fe nuclei escape the target and penetrate the 12 μm thick BC-400 front layer of the Phoswich Wall

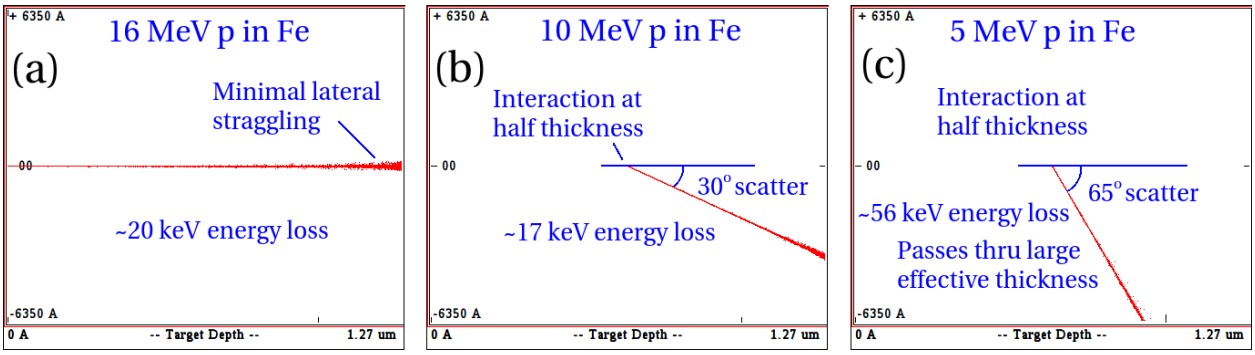

Figure 3.4: Proton penetration through the 12 μm thick iron target. (a) Incident 16 MeV beam passing through the full target thickness. (b) Protons after depositing 6 MeV via a nuclear reaction with outgoing angle 30°. (c) Protons after depositing 11 MeV via a nuclear reaction with outgoing angle 65°. There are 5000 incident protons in each simulation. Energy loss and angular deflection via electronic stopping are minimal in all cases $\lesssim 1\%$. Nuclear stopping power is three orders lower than electronic stopping for these energies.

4. Elastically and inelastically scattered ^{56}Fe nuclei recoil in the ^{56}Fe target

Basic SRIM output can answer questions such as:

- How much does the ^{56}Fe target thickness degrade the incident beam energy?
- At what maximum energy can the Phoswich Wall fully stop a proton?
- Will ^{56}Fe recoils trigger the Phoswich Wall data acquisition system?

Answers to these questions are crucial to comprehending the data analysis.

Figure 3.4 shows the penetration of 5, 10, and 16 MeV protons at various angles and depths in the 1.3 μm thick target of ^{56}Fe. The proton energy losses and angular deflections ($\lesssim 1\%$) are much lower than the energy and angular resolutions of the Phoswich Wall detector (~5–10%). Hence, the Coulombic interactions between the beam and target do not significantly interfere with measurements in this experiment.

Figure 3.5 shows the implantation of 21 MeV protons in the 2.2 mm thick CsI back layer of the Phoswich Wall. The CsI active detection layer is able to fully stop protons of ≤ 21 MeV. Although the Thallium dopant (Tl) is important for the scintillation mechanism, it has a small concentration and negligible effect on the stopping power. Proton energies do not exceed 16 MeV in this experiment, thus no proton can penetrate the back layer of the Phoswich Wall in this work.

Figure 3.6 shows the implantation of 400 keV ^{56}Fe in the 12 μm thick BC-400 fast plastic front layer of the Phoswich Wall. An incident kinetic energy of 400 keV is approximately the maximum recoil of an ^{56}Fe nucleus that can hit the Phoswich Wall front layer (cf. Fig. 3.2) under the assumption that the reaction occurred near the back surface of the target with

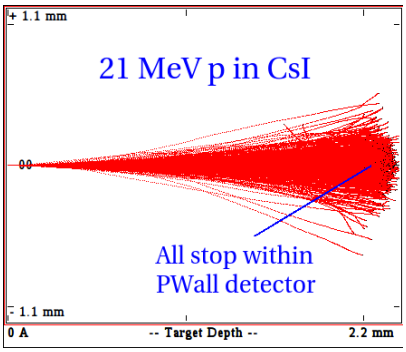

Figure 3.5: Proton implantation in the Phoswich Wall (PWall) back layer. There are 500 incident protons shown.

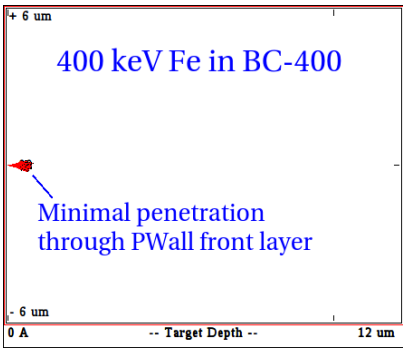

Figure 3.6: Iron nuclei stopping in the Phoswich Wall (PWall) front layer. There are 500 incident ^{56}Fe ions shown.

no energy loss. Since no ^{56}Fe ions can penetrate the BC-400 fast plastic front layer of the Phoswich Wall, they cannot deposit any energy in the CsI(Tl) back layer. Thus, any ^{56}Fe energy deposition generates only a fast signal. The Phoswich Wall data collection software will not save data to disk if there is no accompanying late signal (cf. Fig. 2.10). The higher atomic number Z and lower kinetic energy causes the ^{56}Fe ion range to be many orders of magnitude lower than the proton ranges in this experiment.

Figure 3.7 shows the recoil of 150 and 300 keV ^{56}Fe in the ^{56}Fe target. The slowing down time for 100–400 keV ions is on the order of 20–200 fs. For an initial spatially uniform distribution of ^{56}Fe recoils at these energies, most ions do not escape the target; typically, the few that do escape have low kinetic energy ($\lesssim$ 50 keV). Nucleon-nucleon Coulombic interactions dominate for Fe-Fe scattering in this energy range as seen by the wide angle scatters in Figure 3.7b. These complicated trajectories are useful for the Doppler Shift Attenuation Methods of Section 3.3.

Figure 3.8 shows plots from the SRIM scientific citation website [58] containing comparisons of theoretical and experimental stopping powers in the region of atomic number $Z, Z_a \sim 26$. Unfortunately, there is no data available for iron stopping in iron. According to

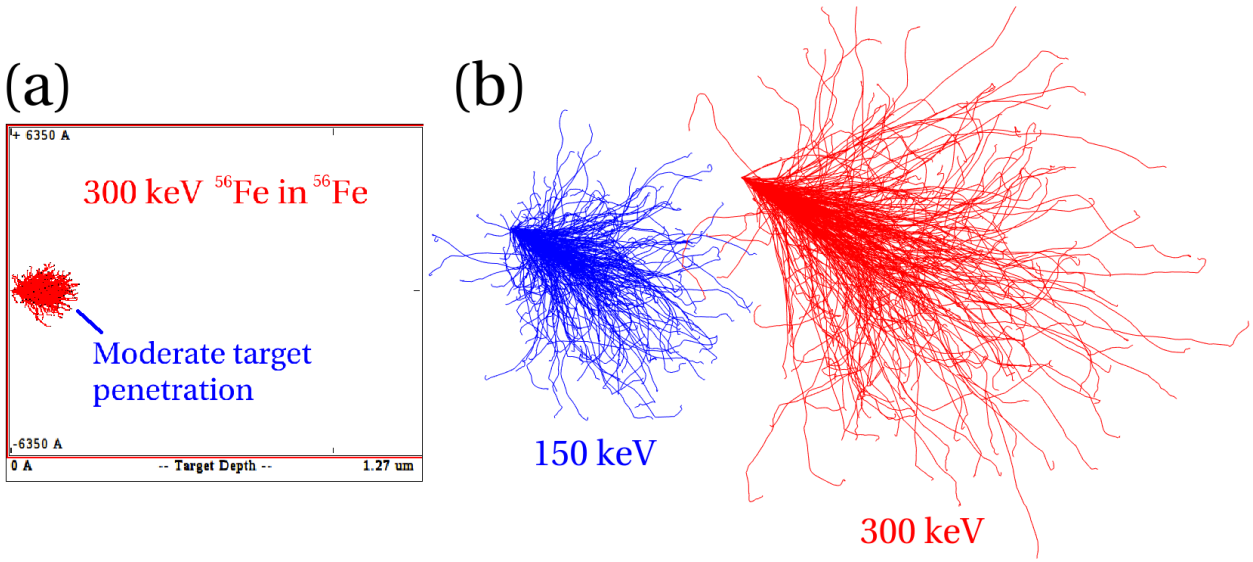

Figure 3.7: Iron nuclei recoiling in the iron target. (a) 2-dimensional projections of ^{56}Fe recoil show that the stopping range is on the order of 10% of the target thickness for 300 keV recoils. (b) ^{56}Fe recoil trajectories visualized at a different projection angle for two different initial recoil energies. Nuclear scattering is a dominant stopping mechanism and causes the wide angle deflections.

the similarity principle outlined in Appendix C, the interatomic potential is approximated by a function of Z/Z_a; therefore, the data with $Z, Z_a \sim 26$ give an estimate of the uncertainty for $Z, Z_a = 26$. For recoil energies of 2–20 keV/amu, the nickel and iron plots do not have much $Z, Z_a \sim 26$ data primarily due to experimental difficulties. Extrapolations of the data suggest that modern stopping power accuracy is approximately 5–8%, which is sufficient for the purpose of implementing the Doppler Shift Attenuation Method discussed in Section 3.3.

3.3 Doppler Shift Attenuation

This section provides derivations of the Doppler effect, the total angle between ion recoil and photon emission, and lifetime. The Doppler Shift Attenuation Method is outlined through the use of simulation.

Doppler Effect

Consider a photon source traveling along the x-axis with velocity $\beta = v/c$ emitting photons in the $x - y$ plane at angle Θ with respect to its velocity vector in the lab frame. In natural

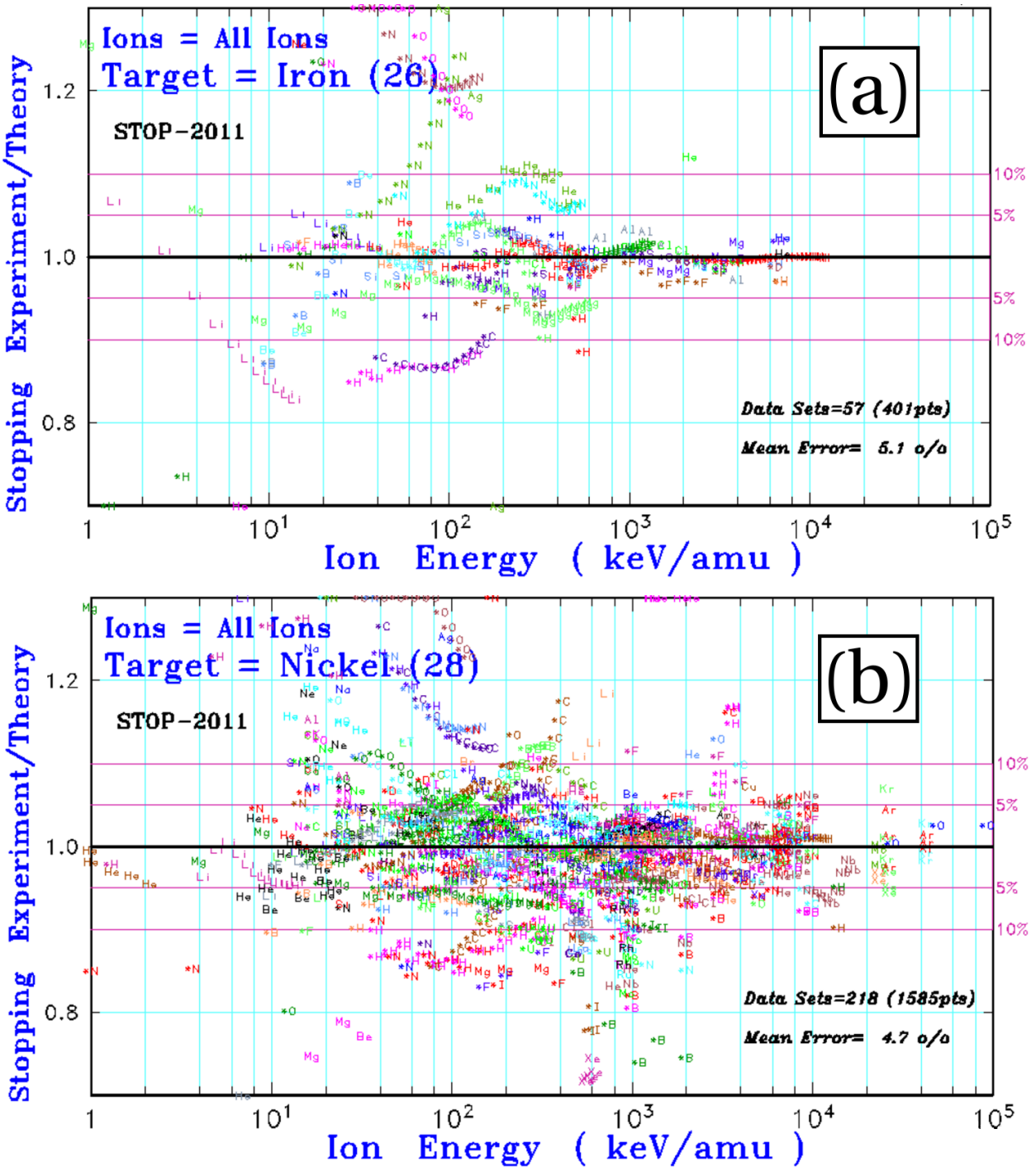

Figure 3.8: Relative error in the comparison of experiment and theoretical calculations of SRIM. (a) Ions stopping in Iron, $Z_a = 26$ [59]. (b) Ions stopping in Nickel, $Z_a = 28$ [60]. The full list of data sets and citations is available in Reference [58]. The SRIM scientific citation website states that discrepant points beyond 10% error are more likely due to systematic experimental error than theoretical issues.

units ($c = 1$), the lab frame 4-momentum of the emitted photon is

$$p_\mu = (E, p\cos\Theta, p\sin\Theta, 0), \tag{3.15}$$

where E and p are the emitted photon's energy and 3-momentum magnitude, respectively. For massless particles such as photons, momentum and energy are equivalent: $p = E$. The 4-momentum of the emitted photon in the rest frame of the photon source follows from a Lorentz transformation:

$$p'_\nu = p_\mu \Lambda^\mu_\nu = (\gamma E - \gamma\beta E\cos\Theta,\ -\gamma\beta E + \gamma E\cos\Theta,\ E\sin\Theta,\ 0), \tag{3.16}$$

where $\gamma = 1/\sqrt{1-\beta}$ is the Lorentz factor of the photon source and a Lorentz boost along the x-axis is given by

$$\Lambda^\mu_\nu = \begin{bmatrix} \gamma & -\gamma\beta & 0 & 0 \\ -\gamma\beta & \gamma & 0 & 0 \\ 0 & 0 & 1 & 0 \\ 0 & 0 & 0 & 1 \end{bmatrix} \tag{3.17}$$

The energy of the emitted photon in the frame of the photon source is

$$E' = \gamma E(1 - \beta\cos\Theta), \tag{3.18}$$

which provides a concise relationship between velocity and energy. For non-relativistic velocities (small β, γ) a series expansion of Equation (3.18) returns the familiar non-relativistic Doppler shift formula:

$$E = \frac{E'}{\gamma(1-\beta\cos\Theta)} \approx \frac{E'}{1-\beta\cos\Theta} = E'[1 + \beta\cos\Theta + (\beta\cos\Theta)^2 + \dots] \tag{3.19}$$

$$E \approx E'(1 + \beta\cos\Theta), \tag{3.20}$$

which is the appropriate form for the low velocities considered in this experiment in which all ^{56}Fe recoil velocities have $\beta < 0.0035$.

Total Angle

To determine the angle Θ between the direction of the moving photon source and the direction of photon emission, consider the two unit vectors in polar coordinates:

$$\hat{\boldsymbol{v}}_{\boldsymbol{i}} = (\sin\theta_i\cos\phi_i, \sin\theta_i\sin\phi_i, \cos\theta_i), \tag{3.21}$$

where θ, ϕ are spherical polar coordinates having identical axes and origins and $i = e, s$ denotes the directions of emission and source velocity, respectively. The dot product of the unit vectors is related to the total angle between source recoil and emission as follows

$$\cos\Theta = \hat{\boldsymbol{v}}_{\boldsymbol{e}} \cdot \hat{\boldsymbol{v}}_{\boldsymbol{s}} = \cos\theta_e\cos\theta_s + \sin\theta_e\sin\theta_s\cos(\phi_e - \phi_s). \tag{3.22}$$

Equation (3.22) provides a succinct formula for the Doppler shift angle Θ of Equation (3.20) in terms of experimentally determined quantities θ_i, ϕ_i.

Lifetimes

Consider a large ensemble of excited nuclear states. The decay rate of this ensemble is proportional to N, the number of excited nuclei in the ensemble:

$$\frac{dN}{dt} = -\lambda N, \tag{3.23}$$

where λ is the decay constant. The solution to this differential equation is an exponential decay function,

$$N(t) = N_0 e^{-\lambda t} = N_0 e^{-t/\tau} = N_0 2^{-t/t_{1/2}}, \tag{3.24}$$

where N_0 is the number of nuclei present at $t = 0$ and τ and $t_{1/2}$ are the lifetime and half-life of the excited nuclear state, respectively. The relationship between τ and $t_{1/2}$ is

$$\tau = \frac{t_{1/2}}{\ln 2} = \lambda^{-1}. \tag{3.25}$$

Note that Equation (3.24) is only applicable for a one-step transition. For a single excited nuclear state, the differential decay probability is similar to Equation (3.24),

$$P(t) = \tau^{-1} e^{-t/\tau} \tag{3.26}$$

where $P(t)$ is the differential probability that the state will decay near time t and the coefficient τ^{-1} ensures the probability distribution integrates to unity.

Stopping Time Simulation

The Doppler Shift Attenuation Method (DSAM) relies on precise simulations of slowing down and γ-ray emission time. Figure 3.9 shows an example SRIM simulation of 300 keV ^{56}Fe ions stopping in the iron target. The condition $\cos\Theta_I = 1.0$ signifies that the recoil and γ-ray detection angles are parallel, where the subscript I denotes the initial state. For reference, γ-rays detected antiparallel to the initial nuclear recoil vector have $\cos\Theta_I = -1.0$, corresponding to the maximum backward angle. Both recoil energy loss and angular deflection contribute to a reduction in average Doppler shift as in Equation (3.20).

A modern DSAM experiment typically has particle and γ-ray detectors at many angles to maximize the number of counts and enhance angular sensitivity. In these scenarios, the stopping simulation must also cover a wide range of initial total angles, Θ_I, and generate more complicated quantities for experimental comparison. For a fixed lifetime on the order of the slowing down time, t_{slow}, the Doppler shift is a approximately linear function of the quantity $v_I \cos\Theta_I$. The slope of this function is usually represented as $F(\tau)$,

$$F(\tau) = \frac{d(\Delta E)}{d(v_I \cos\Theta_I)}. \tag{3.27}$$

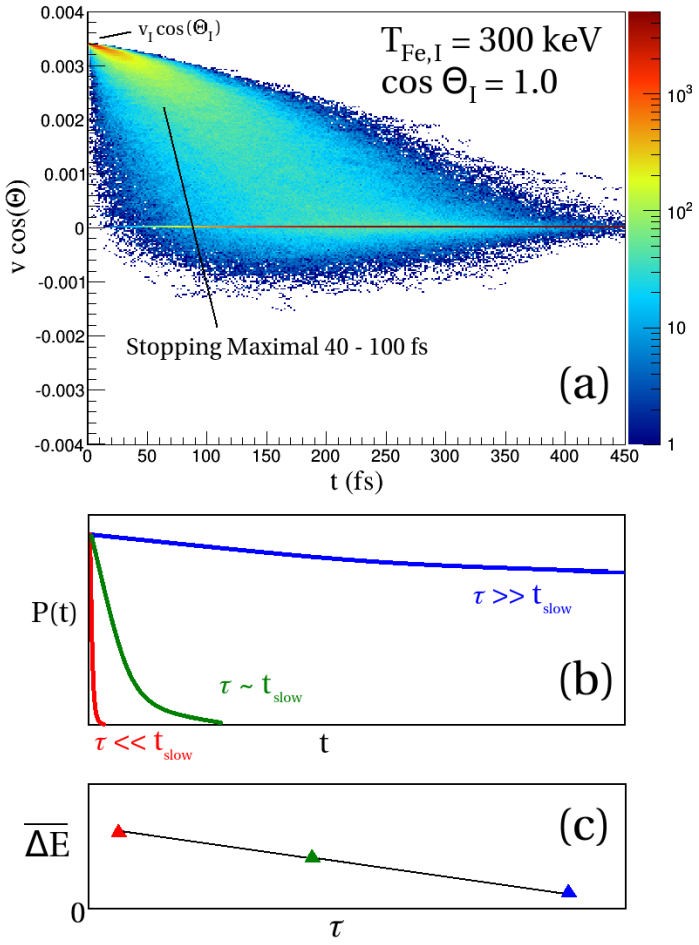

Figure 3.9: The stopping and decay of ^{56}Fe nuclei with parallel initial recoil and γ-ray emission vectors. (a) Component of velocity parallel to emission as a function of time. (b) Illustration of decay probabilities for several different lifetimes, where t_{slow} is the approximate slowing down time. (c) Illustration of average Doppler shifts in energy, $\overline{\Delta E}$, for the previously mentioned lifetimes values.

Figure 3.10 shows an example of a simulation of $F(\tau)$ using processed SRIM particle trajectories. An experiment can observe $F(\tau)$ by measuring the centroid energy of the γ-ray peak for various values of $v_I \cos\Theta_I$. The determination of the excited state lifetime involves a comparison between the experimentally measured and simulated $F(\tau)$'s as demonstrated in Figure 3.11. More specifically, this method is referred to as Centroid Shift DSAM (cf. Ref. [61] for another demonstration).

Experimental energy and angular resolution, as well as non-linearities in stopping power, tend to limit the accuracy of lifetime measurements. While resolutions are typically at their experimental limits, non-linearities in stopping power can be minimized by experimental modifications, such as using a target of a different thickness, or by using a different lifetime

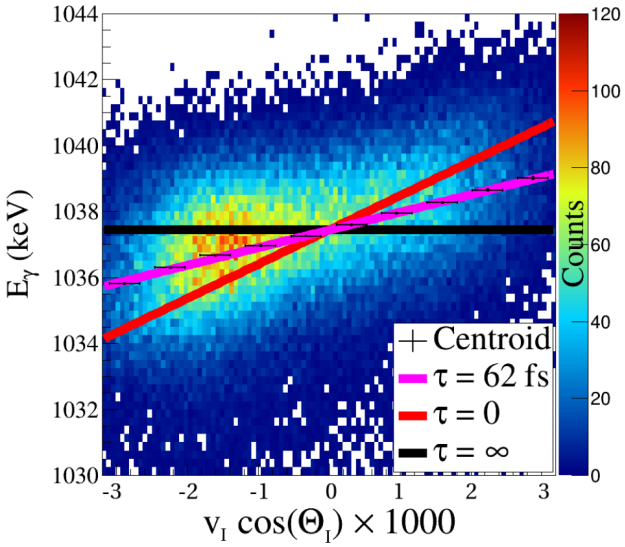

Figure 3.10: Simulated GRETINA detector response to Doppler shifted 1037.8 keV γ-rays at various initial recoil angles and velocities. The simulation uses the experimental solid angle coverage of the particle and γ-ray detectors as well as the initial recoil velocity distribution of the ^{56}Fe. The simulated lifetime of 62 fs produces a slope of $F(\tau) = 538$ keV, whereas very long and very short lifetimes produce no slope and maximum slope, respectively.

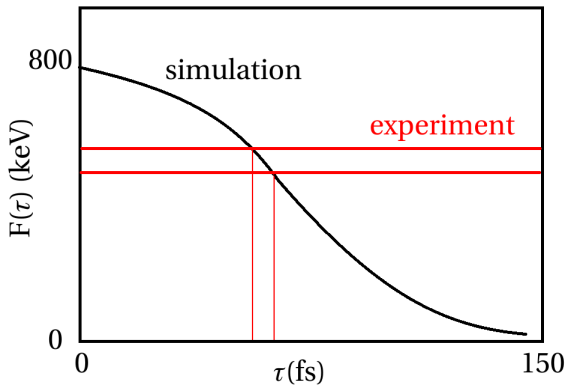

Figure 3.11: Illustration of an $F(\tau)$ curve. The intersection of the experimental and simulated $F(\tau)$ values determine τ. Error bars on the experimental $F(\tau)$ value translate to error bars on the lifetime measurement.

technique. Knowledge of stopping power is crucial to the DSAM technique; fortunately modern codes can calculate stopping powers to within 5% accuracy (cf. Fig. 3.8) thanks to the physics community's extensive study of slowing down theory (cf. Sec. 3.2). Therefore, theory is not the limiting factor in this experiment.

It is possible to measure lifetimes with other experimental techniques such as the Recoil Distance Method (RDM) [46, 62]. In RDM, reaction ejectiles escape from a thin target and travel downstream toward a secondary high density stopper. RDM γ-ray spectra have two peaks for most transitions: in-flight and stopped. Adjusting the target to stopper distance results in a change of these relative peak heights. The ratio modulation relates to lifetime information. No stopping simulation is necessary if the slowing down time in stopper is known to be much shorter than the lifetime ($t_{\text{slow}} << \tau$). However, RDM requires a larger fraction of recoils to escape the target than occurs in the 16 MeV ^{56}Fe(p,p') reaction explored in this work. RDM is more appropriate for experiments where ejectiles have higher initial recoil velocities and atomic number Z (for faster energy loss in the stopper) as typically occurs in reactions of inverse kinematics.

Another practical lifetime technique is Line Shape Analysis (LSA) [46, 63]. In LSA experiments, the γ-rays that are observed at one angle have a broadened peak shape due to target slowing. Slowing and decay time simulations generate peak shapes for comparison. A least-χ^2 fit of experimental data with the simulated peaks quantifies lifetime. LSA is appropriate for experiments that have Doppler shifts 5–10 times greater than the γ-ray detector energy resolution for the transition of interest. The Doppler shifts in this work are on the order of 2–3 times the detector resolution. Lifetime techniques with fewer detectors are naturally more susceptible to gain drift issues. An online calibration using unshifted γ-ray transitions can ameliorate gain drift issues as mentioned in Section 2.4. However, issues with gain differential non-linearities (DNL) can complicate the recalibration procedure and leave the analysis without additional consistency checks. The Centroid Shift DSAM technique is equally susceptible as LSA to gain drifts, but is more resilient to DNL due to the fact that the detector setup records γ-rays at many angles.

3.4 Nuclear Properties

This section describes the fundamentals of nuclear structure including models of Nuclear Level Density and the Gamma Strength Function. This section also covers the basics of nuclear reactions and introduces the reactions code TALYS.

Nuclear physics can seem like a "messy" field because many important details of internal nuclear structure are lacking and complete descriptions of nuclei are unavailable. However, not all problems in physics require explicit solutions. On the contrary, a completely microscopic approach to a simple situation may complicate rather than simplify results. For example, variables such as temperature and pressure better represent an expanding gas than would a complete quantum description of every individual atom. Thus, as is the case with

thermodynamics, nuclear physics relies on models and approximations that are mathematically tractable to explain experimental data and predict new properties.

The approximations begin with the nucleus's basic unit, the nucleon, which is itself not fundamental. Each nucleon is composed of three quarks which exchange gluon force carriers to bind the compound particle together. Quarks in separate nuclei do not exchange gluons due to color confinement, which naïvely seems as if the force between nucleons is absent. However, the pion exchange mechanism provides a residual binding force while obeying color confinement. This nucleon-nucleon interaction is not well understood. It is repulsive at distances shorter than 0.7 fm due to the Pauli exclusion principle, it is attractive with a maximum strength around 0.9 fm, and it has an exponential diminishing strength becoming negligible around 2.5 fm [64]. Currently there is no complete theory that can obtain the nucleon-nucleon interaction from the quark-quark interaction. Regardless, the existence of such a relationship in vacuum would be very different from the interaction in nuclear matter. To address the unknown interaction, the next approximation is the formulation of an effective mean nuclear field.

There are two main approaches to simplifying the potential of the mean nuclear field. The Hartree-Fock method iteratively solves the Schrodinger equation and variational principle of single particle orbitals starting from a trial nuclear wavefunction to self-consistently obtain the associated nuclear potential. This method involves adjusting the parameters in the functional form of the nucleon-nucleon interaction such that the calculated energies match experimental data. The second and more phenomenological approach parameterizes the function of the nuclear potential itself. Typically, mean field potentials contain terms corresponding to Coulomb repulsion, the centrifugal potential, a spin-orbit interaction, and a central force potential often cast into a Wood-Saxon form [65].

The shell model [66, 67] presupposes a set of basis state wavefunctions represented by quantum numbers to describe the arrangement of nucleons in terms of orbital fillings and energy levels. Arguably the biggest success of the shell model is its ability to explain differences between experimental nuclear binding energies and those calculated from a macroscopic model. Distinct deviations appear near $N, Z = 2, 8, 20, 28, 50, 82$, and 126; these are known as the magic numbers. These deviations are the result of orbital filling such that the binding energy of the first nucleon in an open shell is significantly less than the last one in the full shell. The first few magic numbers 2, 8, and 20 can be obtained by placing two groups of non-interacting Fermions into a potential that is a combination of a square well and three-dimensional isotropic harmonic oscillator while obeying the Pauli exclusion principle. Obtaining the remainder of the magic numbers requires breaking some of the degeneracy by adding an adjustable spin-orbit coupling term as seen in Figure 3.12.

The extreme independent particle version of the shell model assumes that little or no interaction occurs between individual nucleons and that each proton and neutron moves in its own orbit as if the other nucleons were absent. In this picture, nucleons can be independently promoted out of closed shells into the open orbitals to form excited states as long as the Pauli exclusion principle remains satisfied. The angular momentum and parity of these excited state corresponds to the orbital properties of unpaired valence particles and

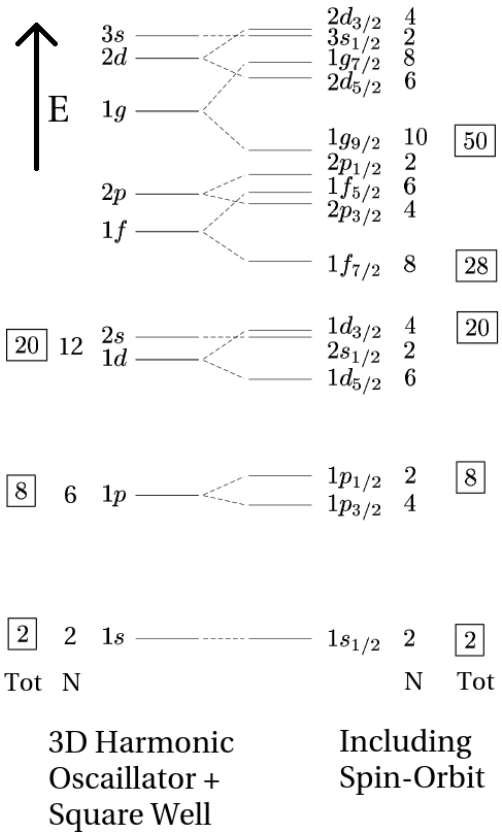

Figure 3.12: The first few orbitals of the shell model [68]. Left: the number of levels in each shell and the total number of cumulative levels for the Harmonic Oscillator and Square Well potential. Right: the addition of Spin Orbit to the potential yields the magic numbers beyond 20.

holes.

Modern shell model theory includes additional sophistication to describe excited nuclear states. The basis single-particle wavefunctions specified by quantum numbers are used to produce a fully antisymmetric product known as a Slater determinant. The Hamiltonian matrix elements include one- and two-body interactions. To confront the combinatorial difficulties associated with a large number of particles and orbitals, a division into core and valence spaces is necessary. The core is the inert set of low-lying orbitals that are completely occupied for all considered excitations and do not contribute to the Slater determinant. The valence space is the set of partially filled orbitals which do contribute to the Slater determinant. The excited state energies are the diagonal elements of the diagonalized Hamiltonian matrix of the valence basis. The two-body matrix elements are typically fit to experimental data, but another approach adjusts the mean field parameters of the potential or the microscopic interaction. Resultant energy levels are sensitive to the chosen nucleon-nucleon interaction and the division of core and valence spaces. Hamiltonian matrices have a very

large number of elements even for a modest valence space and require intense computational power. Due to these valence space limitations, the shell model has difficulty reproducing level properties at high excitation energies.

The Liquid Drop Model (LDM) [69] gives a more macroscopic picture of the collective behavior of nuclear matter. The LDM approximates the nuclear binding energy, E_B, from proton and neutron numbers by treating the nucleus as an incompressible spherical fluid:

$$E_B = a_V A - a_S A^{2/3} - a_C \frac{Z^2}{A^{1/3}} - a_A \frac{(N-Z)^2}{A} - \delta(A,Z), \tag{3.28}$$

where a_V, a_S, a_C, and a_A represent the coefficients for the volume, surface, Coulomb, and asymmetry terms, respectively. The asymmetry term arises from the Pauli exclusion principle and the $\delta(A,Z)$ term is due to pairing. The LDM provides the smooth reference function for the observation of shell structure in experimental binding energies.

Figure 3.13 provides a schematic of the levels of approximation used in nuclear structure physics. The quark-gluon level of detail is rarely useful in the comprehension of nuclear spectroscopy, whereas the LDM often oversimplifies matters. A good starting point for structure and reactions calculations is the mean field potential. However, there is not complete information about the basis state wavefunctions nor is it possible to calculate all combinations of wavefunctions with limited valence and core spaces. Thus, when extending theory to higher excitation energies, it becomes necessary to utilize continuous functions which are not mathematically present in discrete low-lying structure.

Nuclear Level Densities

To confront the issues of limited valence spaces in shell model calculations, it is necessary to use a more statistical approach by via the concept of a Nuclear Level Density (NLD). NLD is defined as the number of levels per unit energy at a certain excitation energy.

Levels at low excitation energy are experimentally accessible and resolvable. Nuclear structure describes the low-lying levels well and data evaluations confirm their complete physical descriptions. Reactions populate levels higher in energy than is typically experimentally resolvable. Especially in intermediate and heavy mass nuclei, there is incomplete knowledge of these high-lying levels and there is a significant chance of level overlap due to the finite energy width of each state. Above the particle separation energy, NLD becomes a continuous function due to the plane wave nature of particle unbound wavefunctions. In contrast, the states below the particle separation energy do not form a continuous function of accessible energies, but for mathematical convenience, a continuous description is used to describe these states. The term "quasi-continuum" is frequently used to describe this high density of bound nuclear states simplified in terms of continuous functions.

Figure 3.14 gives an example of experimental discrete level counting which shows that NLD increases rapidly with excitation energy. Results from s-wave neutron resonance capture experiments reveal an enormous number of levels near the neutron binding energy confirming that NLD continues to rise exponentially. Capture experiments also reveal that

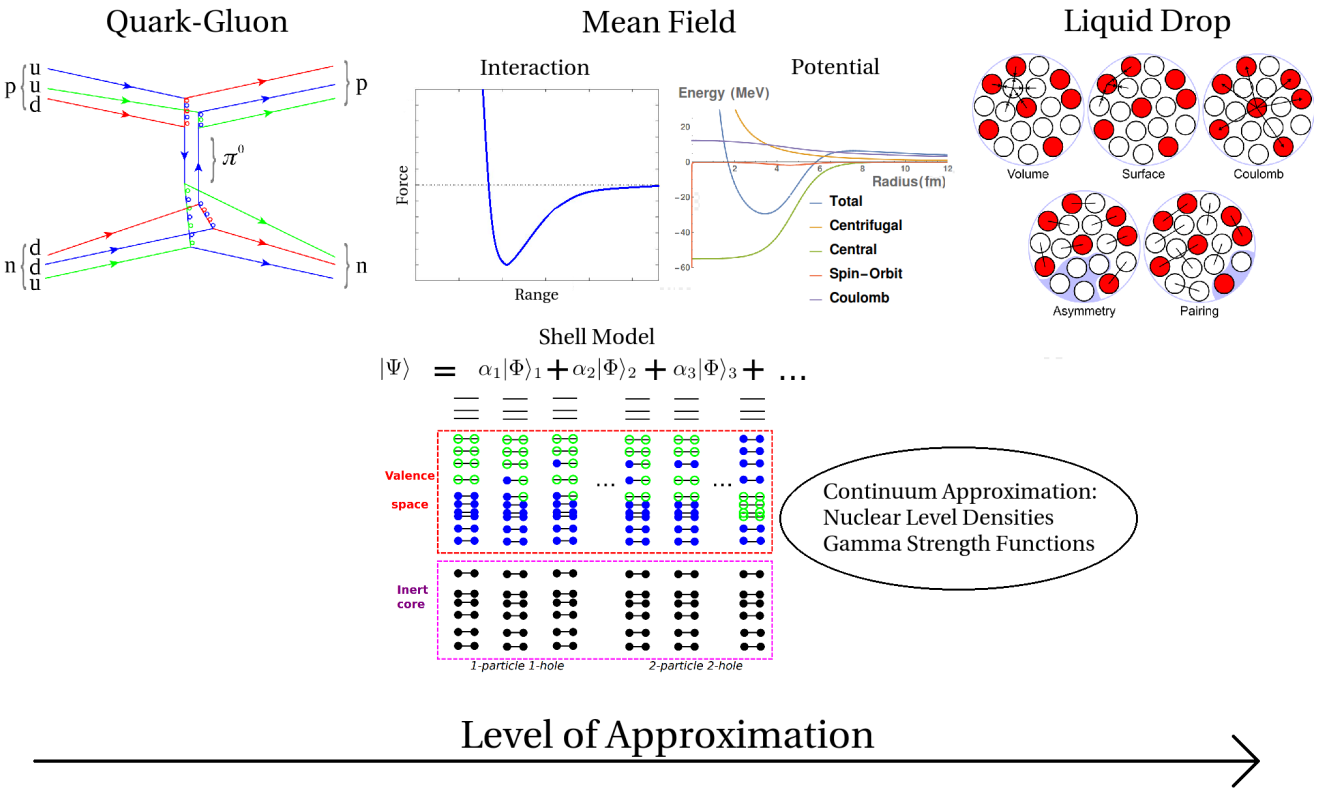

Figure 3.13: The evolution of approximation in nuclear structure theory from the quark-gluon level [70] to the mean field level [71] to the liquid drop level [72]. The shell model utilizes the mean field potential but is restricted by the use of valence and core spaces. The continuum approximation allows extensions of theory on level densities and transition widths to higher excitation energies.

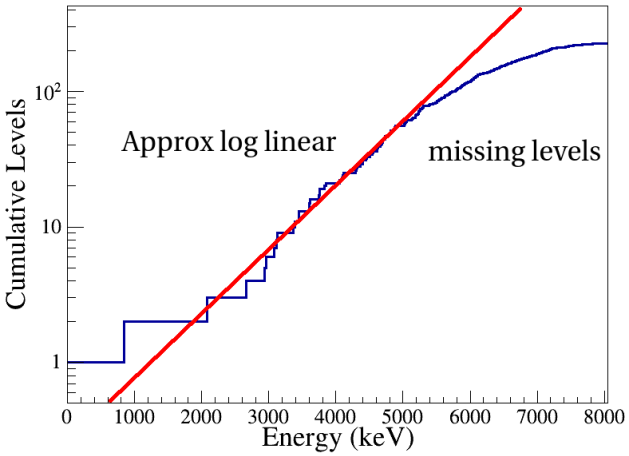

Figure 3.14: The number of cumulative levels in ^{56}Fe from ENSDF data [45]. The database starts missing levels around 5.5 MeV due to the limits of experimental energy resolution.

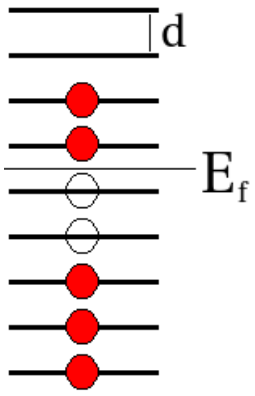

Figure 3.15: Single Fermion gas of equally spaced orbitals. The configuration shown has excitation energy $4d$ shared between two particles.

the NLDs in nuclei near a closed shell is several orders of magnitude smaller than the NLDs in nuclei far from a closed shell demonstrating that shell structure strongly influences NLD. Even-even nuclei have relatively few excited states at low excitation energies in comparison to odd-even and odd-odd nuclei; however, above a certain energy, the NLD of even-even nuclei increases rapidly which suggests that a nucleus must contain the energy necessary to break a nucleon pair before forming shell model configurations. A successful statistical NLD theory reproduces the above shell structure and pairing behavior and provides a function that can match experimental NLD data up to high excitation energies.

A Fermi gas model [73] can fulfill the criteria for a successful NLD theory. First consider a collection of one type of independent fermions that occupy one-particle orbitals that have equal energy spacing d. Excited states appear as multiples of d and are degenerate. The ground state has all orbitals occupied up to the Fermi energy. The first excited state has the fermion that was in the highest occupied orbital moved up to the lowest unoccupied orbital for a total energy of d. The second excited state of energy $2d$ has a degeneracy of two: either the highest occupied orbital Fermion moved up by two or the second highest occupied orbital moved up by two. At $3d$ there are three states, and at $4d$ there is the first possibility of simultaneously exciting multiple particles as shown in Figure 3.15. This simple model produces the desired exponential rise in NLD with excitation energy; in fact, any system described by elementary excitation degrees of freedom with additive energies possesses an exponential rise of NLD [73]. The residual interactions between valence nucleons break the degeneracies present in the simple model and change the nature of highly excited states with small spacings by mixing wavefunctions. Therefore, it becomes more appropriate to describe the NLD as a continuous function.

Due to the statistical nature of NLD, the literature on this subject borrows a lot of the vocabulary from thermodynamics. The partition function describing the system of eigen-

values $E_1, E_2, \ldots, E_i$ is defined as

$$Z(\beta) = \sum_i e^{-\beta E_i}, \tag{3.29}$$

and the NLD is a sum a Dirac delta functions for each level

$$\rho(E) = \sum_i \delta(E - E_i), \tag{3.30}$$

where an average over an energy interval containing many states will yield an approximately smoothly varying function. The partition function can be expressed in terms of $\rho(E)$ as

$$Z(\beta) = \int_0^\infty \rho(E) e^{-\beta E} dE. \tag{3.31}$$

Applying a Laplace transform and the method of steepest descent gives a minimum for β determined by

$$-\frac{d}{d\beta_0} \ln Z(\beta_0) = E \tag{3.32}$$

yielding a NLD of

$$\rho(E) = \frac{e^{\ln Z(\beta_0) + \beta_0 E}}{\sqrt{2\pi \frac{d^2 \ln Z(\beta_0)}{d\beta_0^2}}} \tag{3.33}$$

where the entropy S is given by

$$S = \ln Z(\beta_0) + \beta_0 E, \tag{3.34}$$

and $t = 1/\beta_0$ is the temperature of the system. The same relations of energy and entropy as in thermodynamics apply,

$$\frac{dS}{dE} = \frac{d}{dE}[\ln Z(\beta_0) + \beta_0 E] = \frac{d\beta_0}{dE}\frac{d}{d\beta_0} \ln Z(\beta_0) + \beta_0 + E\frac{d\beta_0}{dE} = \beta_0 = \frac{1}{t}, \tag{3.35}$$

and NLD becomes

$$\rho(E) = \frac{e^S}{\sqrt{-2\pi \frac{dE}{d\beta_0}}}, \tag{3.36}$$

where the NLD is now inherently a smooth function due to the application of the method of steepest descent. Thermodynamics usually neglects the variation of the denominator in

Equation (3.36), but in nuclear physics the excitation energy is not much larger than the temperature, so the denominator much be included. To keep the language of thermodynamics, the nuclear temperature, T, is defined as

$$\frac{1}{T} = \frac{d}{dE} \ln \rho(E). \tag{3.37}$$

To extend this formalism to describe a Fermi gas of two types of Fermions with a pairing interaction, one must include the grand canonical partition function considering all possible values of the available quantum numbers simultaneously. The details of the calculation [73] are omitted for brevity. The NLD for this system is [74, 75]:

$$\rho_{FG}(U) = g_0 \sqrt{\frac{g_0^2 d_n d_p}{4}} \frac{6^{1/4}}{12} \frac{e^{2\sqrt{\pi^2 g_0 U/6}}}{(g_0 U)^{5/4}}, \tag{3.38}$$

where $g_0 = 1/d_n + 1/d_p$ is the single Fermion density and $U = E - E_1$ is the effective excitation energy. The equidistant neutron and proton orbital spacings are d_n and d_p, respectively. The quantity E_1 is the backshift which is related to the pairing energy. This formula has the desired exponential increase in NLD with excitation energy, accounts for a shift due to pairing, and can incorporate the shell spacing effects into the level density parameter "a":

$$a = \frac{\pi^2 g_0}{6}. \tag{3.39}$$

To obtain the dependence of NLD on the projection of total angular momentum, M, one must apply the concept of random coupling to the sum of the z-axis projections of angular momentum, m, of the independent excited Fermions. The central limit theorem of statistics gives a Gaussian distribution for a large number of excited particles:

$$\rho(U, M) = \frac{\rho(U)}{\sqrt{2\pi\sigma^2}} \exp\left(-\frac{M^2}{2\sigma^2}\right), \tag{3.40}$$

with the mean square deviation

$$\sigma^2 = \nu \langle m^2 \rangle, \tag{3.41}$$

where ν is the average number of excited particles and holes. The NLD of a given total angular momentum, J, is then the difference in NLD of $M = J$ and $M = J + 1$:

$$\rho(U, J) = \rho(U, M = J) - \rho(U, M = J + 1) \simeq \frac{(2J+1)\rho(U)}{2\sqrt{2\pi}\sigma^3} \exp\left(-\frac{(J+1/2)^2}{2\sigma^2}\right), \tag{3.42}$$

where each value of total angular momentum has degeneracy $2J+1$ in the magnetic quantum number M.

For the purposes of this work, there is approximately an even distribution of postive and negative parities Π for any U, J:

$$\pi(U, J, \Pi) = 1/2. \tag{3.43}$$

Using the variables σ, a, and the approximation $g_0^2 d_n d_p/4 \approx 1$, the Fermi gas NLD of Equation (3.38) becomes

$$\rho_{FG}(U, J, \Pi) = \frac{1}{2} \cdot \frac{2J+1}{2\sqrt{2\pi}\sigma^3} \exp\left[-\frac{(J+1/2)^2}{2\sigma^2}\right] \frac{\sqrt{\pi}}{12} \frac{\exp(2\sqrt{aU})}{a^{1/4}U^{5/4}}. \tag{3.44}$$

The literature often refers to the mean square deviation, σ, as the "spin cutoff" parameter which is a bit of a misnomer. In the nucleus, σ refers to the distribution of *total angular momentum* which is the sum of orbital and spin components (not just the spin component itself). However, this work retains the name spin cutoff for consistency purposes. The precise value of σ is dependent on the details of the nuclear model under consideration.

The sum of the Fermi gas NLD in Equation (3.44) over J and Π yields

$$\rho_{FG}^{tot}(U) = \frac{1}{12\sqrt{2}\sigma} \frac{\exp\left(2\sqrt{aU}\right)}{a^{1/4}U^{5/4}}, \tag{3.45}$$

which depends only on energy. A further simplification of the energy dependence of total NLD is the Constant Temperature Model [76]:

$$\rho_{CT}(E) = \frac{1}{T_0} \exp\left(\frac{E - E_0}{T_0}\right), \tag{3.46}$$

where E_0 is backshift and T_0 is temperature which come from experimental fits to the data as in 3.14. The CTM reproduces the desired low energy linear exponential behavior, but begins to deviate from the Fermi gas model at high excitation energies ($\sim$15 MeV in ^{56}Fe). Additional NLD models not mentioned include the incorporation of an energy dependence into the parameter a and the parity distribution $\pi(U, J, \Pi)$.

Gamma Strength Functions

The Fermi gas formalism of the previous section describes the average distribution of levels, but cannot give much insight about the transitions between levels. These transitions are very important in the decay and reaction calculations pertaining to this work. This section outlines the theory and phenomenology surrounding nuclear transitions.

A partial transition width from some initial state I to final state F is defined as

$$\Gamma_{I,F}^{XL}(E, E_\gamma) = \frac{2\pi}{\hbar} |\langle \Psi_F | H^{XL} | \Psi_I \rangle|^2, \tag{3.47}$$

where $\langle\Psi_F|H^{XL}|\Psi_I\rangle$ is the matrix element connecting initial state wavefunction, Ψ_I, and final state wavefunction, Ψ_F which includes both the residual nucleus and emitted radiation. The energy of the initial state is E and the energy of the final state is $E-E_\gamma$, where E_γ is the energy of the emitted radiation, typically a γ-ray. The transition operator H^{XL} connecting the states has electromagnetic character X and multipolarity L. The total transition width out of an initial state is

$$\Gamma_{I,tot} = \sum_{F,XL} \Gamma^{XL}_{I,F}, \tag{3.48}$$

where the partial width sum includes possible transition types XL, to final states F below the initial energy. Decay widths incorporate both γ-ray emission width, Γ^{XL}_γ, and electron internal conversion width:

$$\Gamma^{XL}_{I,F} = \Gamma^{XL}_\gamma \cdot [1 + \alpha^{XL}(E_\gamma)], \tag{3.49}$$

where α^{XL} are relativistic internal conversion coefficients such as calculated from the evaluated $BrIcc$ tables [77]. Transition widths can be recast into other dimensionless forms such as branching ratios. The branching ratio to a specific final state is the ratio of a particular decay channel width to the total width of the state:

$$\mathrm{BR}_{I,F} = \sum_{XL} \frac{\Gamma^{XL}_{I,F}}{\Gamma_{I,tot}}. \tag{3.50}$$

Furthermore, total transition width is inversely proportional to the lifetime of the initial state:

$$\tau = \frac{\hbar}{\Gamma_{I,tot}}. \tag{3.51}$$

In real nuclei, partial widths are hypothesized to independently fluctuate about an average according to a width fluctuation distribution (WFD) commonly cast into a χ^2 distribution:

$$P(x,\nu) = \nu/2 \cdot g(\nu/2)^{-1} \left(\frac{\nu x}{2}\right)^{\nu/2-1} e^{-\nu x/2} \tag{3.52}$$

where $x = \Gamma^{XL}(E,E_\gamma)/\bar{\Gamma}^{XL}(E,E_\gamma)$ is the ratio of a given width to the average, g is the mathematical Gamma function, and ν is the number of degrees of freedom inherent to the system. By far the most widely used WFD is the Porter-Thomas Distribution (PTD) with $\nu = 1$ [78]:

$$P(x,\nu=1) = \frac{e^{-x/2}}{\sqrt{2\pi x}}, \tag{3.53}$$

which is equivalent to a Gaussian distribution squared. This form has a physical explanation [78]: the matrix element of Equation 3.47 is equal to an integral over a multipole operator between two wavefunctions which are presumably unrelated to one another due to the complexity of the residual nuclear interaction. Therefore one may expect the matrix element probability distribution to be Gaussian with zero mean. However, recent results

from Koehler *et. al.* [79] show that the WFD may be more akin to a distribution with $\nu \approx 0.5$, suggesting that there may be more symmetry in the system.

The individual partial widths of Equation (3.47) are numerous, difficult to measure absolutely, and subject to fluctuations. Fortunately, the inverse process of γ-ray decay, γ-ray absorption, provides a lot of insight about the *average* partial transition width. The cross section for the absorption of a γ-ray of energy E_γ by a nuclear ground state of angular momentum J_g to a single isolated level of index i, angular momentum J, and excitation energy E_i is [80]

$$\sigma_{\gamma,i}(E_\gamma) = \pi g \lambda\!\!\!^{-2} \frac{\Gamma_{0,i}}{\Gamma} \frac{1}{[(2/\Gamma)(E_\gamma - E_i)]^2 + 1}, \tag{3.54}$$

where $\lambda\!\!\!^{-} = \hbar c/E_\gamma$ is the γ-ray wavelength, Γ is the full width of the excited state, $\Gamma_{0,i}$ is the partial width for de-excitation to the ground state, and

$$g = \frac{2(2J+1)}{2J_g+1}, \tag{3.55}$$

is a statistical factor accounting for the angular momentum difference. The cross section integrated over the resonance is

$$\int \sigma_{\gamma,i}(E_\gamma) dE_\gamma = \frac{\pi^2 \lambda\!\!\!^{-2}}{2} g \Gamma_{0,i}. \tag{3.56}$$

The corresponding average cross section for an energy interval ΔE which contains n levels of the same spin J is

$$\langle \sigma_\gamma \rangle = \frac{1}{\Delta E} \sum_{i=1}^{n} \int \sigma_{\gamma,i}\, dE_\gamma = \frac{\pi^2 \lambda\!\!\!^{-2} g}{2} \frac{1}{\Delta E} \sum_{i=1}^{n} \Gamma_{0,i} = \frac{\pi^2 \lambda\!\!\!^{-2} g}{2} \cdot \frac{n \langle \Gamma_0 \rangle}{\Delta E} \tag{3.57}$$

where $\langle \Gamma_0 \rangle$ is the average partial transition width to the ground state near excitation $E = E_\gamma$. For large n, $\langle \Gamma_0 \rangle$ is independent of ΔE and n, and $\rho(E) = n/\Delta E$. Then

$$\langle \sigma_\gamma \rangle = \frac{\pi^2 \lambda\!\!\!^{-2} g}{2} \rho(E) \langle \Gamma_0 \rangle, \tag{3.58}$$

which corresponds to one particular J value. The energy dependence of the partial decay width to the ground state has a well known dependence on multipolarity. For dipole radiation,

$$\Gamma_{0,i} \propto E_\gamma^3 |\langle i|z|0\rangle|^2, \tag{3.59}$$

where $\langle i|z|0\rangle$ is the dipole matrix element connecting the nuclear excited state i to the nuclear ground state. The amount of dipole matrix element per unit excitation energy, $f(E_\gamma)$, is

$$f(E_\gamma) = \frac{\rho(E)\langle \Gamma_0 \rangle}{E_\gamma^3} \propto \frac{\langle \sigma_\gamma \rangle}{E_\gamma}. \tag{3.60}$$

The function $f(E_\gamma)$ will be referred to as the Gamma Strength Function (GSF).

The absorption of the γ-ray can be interpreted as resulting in a collective oscillatory motion of the proton and neutron clouds in the nucleus. According to the Brink hypothesis [81], the collective motion can be built equally on the ground and excited states independently of J and Π. Furthermore, the extreme statistical model postulated by Bohr [82] assumes the decay of a nuclear level is independent of the way in which it is formed and the reverse process has an equivalent matrix element. Thus, in general [83]

$$\bar{\Gamma}_\gamma^{XL}(E, E_\gamma) = \frac{f_{XL}(E_\gamma)E_\gamma^{2L+1}}{\rho(E, J, \Pi)}, \tag{3.61}$$

where now the individual components of the GSF are separated out by electromagnetic character and multipolarity.

Experimental and theoretical photoabsorption cross sections guide the energy dependence of GSF models as related in Equation (3.60). The Standard Lorentzian (SLO) form of GSF is [84, 80]

$$f_{XL}(E_\gamma) = K_{XL}\frac{S_{XL}E_\gamma G_{XL}^2}{(E_\gamma^2 - E_{XL}^2)^2 + E_\gamma^2 G_{XL}^2} \tag{3.62}$$

where S_{XL}, E_{XL}, and G_{XL} are the magnitude, centroid energy, and width of the giant resonance, respectively and

$$K_{XL} = \frac{1}{(2L+1)\pi^2\hbar^2c^2}. \tag{3.63}$$

There is also the Generalized Lorentzian (GLO) of the form of Kopecky and Uhl [85]:

$$\begin{aligned} f_{XL}(E_\gamma, T) &= K_{XL}S_{XL}G_{XL} \\ &\times \left[F_\ell \frac{G_{XL}4\pi^2T^2}{E_{XL}^5} + \frac{E_\gamma \widetilde{G}_{XL}(E_\gamma, T)}{(E_\gamma^2 - E_{XL}^2)^2 + E_\gamma^2 \widetilde{G}_{XL}(E_\gamma, T)^2}\right], \end{aligned} \tag{3.64}$$

where $F_\ell = 0.7$ is derived from the Fermi theory of liquids taking into account collisions between quasiparticles. The energy-dependent damping width is

$$\widetilde{G}_{XL}(E_\gamma, T) = G_{XL}\frac{E_\gamma^2 + 4\pi^2T^2}{E_{XL}^2}, \tag{3.65}$$

and nuclear temperature is

$$T = \sqrt{\frac{E - E_1 - E_\gamma}{a}}, \tag{3.66}$$

where E_1 is the backshift and a is the level density parameter as in the Fermi Gas model. Other forms include a single-particle states model of constant strength, the KMF model [86], the Kopecky and Chrien model [87], and the Enhanced Generalized Lorentzian (EGLO) model [88]. The common parameters of magnitude, width, and strength depend on the size of the nucleus and the relative number of protons and neutrons.

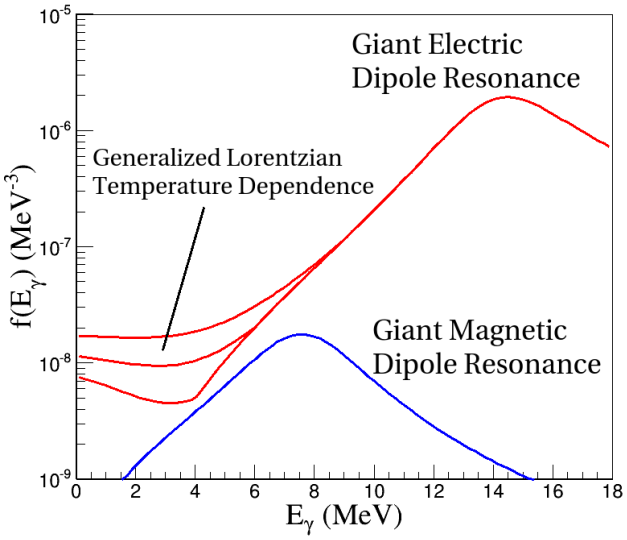

Figure 3.16: E1 and M1 Components of the Gamma Strength Function. The E2 GSF has a magnitude below the visible scale shown here. The excitation energy determines the low energy tail behavior of the giant electric dipole resonance as in Equation (3.64).

Nuclear matter possesses oscillation modes beyond dipole proton and neutron oscillation. The literature refers to these non-statistical GSF features below the giant dipole resonance as Pygmy resonances [83, 89]. For instance, some nuclei show an M1 scissors resonance when N>Z [90] which is hypothesized to correspond an oscillation of the excess neutron skin about the proton-neutron core [91]. Furthermore, recent results from the Oslo [92, 93] and Direct Reaction Two Step Cascade [94] methods show an enhancement in the GSF at low E_γ [5] which currently has no physical explanation. Figure 3.16 shows a few of the various GSF features.

A good representation and understanding of the GSF is important to nearly all reaction calculations because γ-ray emission is a universal decay channel. The GSF governs the balance between γ-ray and neutron emission and is therefore critical to many nuclear physics applications. Particularly, the overall magnitude of the GSF has the biggest impact on reaction rates since the average cross section scales with the average transition width as seen in Equation (3.60).

Reaction Mechanisms

Section 3.1 provided the details on the conservation of kinetic and rest mass energy in nuclear reactions, but it did not cover the more intricate processes that govern the internal reorientation of nucleons that occurs on very short timescales. This section aims to briefly outline the framework governing these reactions and provide some simulation examples relevant to the experiment in this work.

A nuclear reaction is the process in which two energetic nuclei collide to produce one or more nuclides that are distinct from the nuclides that began the process [95]. Scattering is the process where nuclides interact without changing the nature of either nucleus. A reaction could involve more than two incident nuclei, but because the timescale over which the reaction takes place is so short, the chance that three nuclei meet at the same location is very unlikely. Radioactive decay is the process of spontaneous emission of particles from an excited nucleus and occurs during or after the reaction.

There are numerous types of nuclear reactions including, but not limited to, the following:

- absorption - a heavy target nucleus absorbs an incoming light projectile and gives off γ-rays
- inelastic scattering - an energetic projectile induces an excited state in the target nucleus without changing the proton and neutron composition
- fusion - two nuclei join together to form a heavier nucleus in addition to γ-rays or other light particles
- fission - a very heavy nucleus splits into two fragments; can occur spontaneously or after absorption or inelastic scattering
- spallation - a very energetic particle strikes a nucleus and ejects many light particles

As mentioned in Chapter 2, the 16 MeV ^{56}Fe(p,p'γ) reaction studied in this experiment is considered a low energy proton inelastic scattering reaction, but many other reactions are also possible at this energy.

In this experiment, protons in the beam interact with ^{56}Fe target nuclei via Coulomb, nuclear elastic, and nuclear inelastic scattering. The Coulomb scattering only involves the electrostatic repulsion of the nuclear cores and does not involve strong nuclear forces. Coulomb scattering can result in large angular deflections especially for high Z and low center of mass energy. Section 3.2 on Lindhard Scharff Schiott theory gave a brief introduction to the formalism of this Coulomb scattering process.

Inelastic reactions can be broken down into direct and compound components. In a direct reaction involving a very high energy projectile and ejectile, the wavelength of the incident particle is small which causes the interaction to spatially localize on one single nucleon inside the target nucleus. Direct reactions transfer energy and nucleons in a single event, such as the knockout of a neutron, and leave the residual nucleus in one discrete excited state. Direct reactions occur on short timescales with no opportunity for the redistribution of internal energy during the transit of the incident projectile. On the other hand, compound reactions occur over long timescales in which the incident energy is fully absorbed and shared throughout the target nucleus. In compound reactions, low energy particle emission is akin to a statisical evaporation process: the amount of energy that randomly concentrates in one particle is enough to overcome the mutual attraction of the nucleus and escapes. The compound nucleus has no memory of how the initial compound nuclear state was formed

and emission is isotropic in the center of mass frame. Compound reactions favor emission of ejectiles with low Z, preferably neutrons. There is also the possibility for an intermediate process known as pre-equilibrium in which the struck nucleon makes a few collisions with other target nucleons before ejection. In this scenario, the nucleus retains information on how it was formed which effects subsequent decay. There are not clear divisions between compound, pre-equilibrium, and direct processes; rather, the coupling between entrance and exit channels decreases systematically with the number of intranuclear collisions.

The inner workings of reactions are extremely complex due to the copious number of initial, intermediate, and final state possibilities. Fortunately there has been a lot research in the way of general reaction modeling with codes such as EMPIRE [96], ALICE [97], GNASH [98], and TALYS [99]. I have relegated the reaction calculations in this work to TALYS for its completeness and user-friendliness. TALYS in turn relegates the integrated optical model and coupled-channels calculations to the code ECIS-06 [100].

TALYS aims for complete and accurate simulation of nuclear reactions involving photons, neutrons, protons, deuterons, ^{3}He, and alpha particles across the wide incident energy range of 1 keV to 200 MeV and for target nuclei of mass 12 or higher. The primary purpose of this code is as a nuclear physics tool for the analysis of nuclear reaction experiments, so that the intersection between experiment and theory can illuminate fundamental properties of nuclei and their interaction. Once the reaction models are sufficiently constrained, they have predictive power for future or unmeasurable data. TALYS can then generate nuclear data for simulations of radiation transport in new nuclear technologies.

TALYS developers take the general approach of dividing effort equally among all reaction types instead of investing in a perfect implementation of a complicated channel with a minuscule contribution to the output. The reaction calculation takes every energetically feasible binary reaction and evaluates every sequence of possible decay routes. Competing direct, compound, and pre-equilibrium production mechanisms determine the distribution of initial nuclear states, and the properties of the residual nuclei determine the decay paths. TALYS's primary contribution to the calculations of ECIS-06 is the convenient inclusion of separation energies, level densities, gamma strength functions, optical model parameters, and other nuclear properties as well as the implementation of modern reaction and decay models.

To see TALYS in action, consider the 16 MeV ^{56}Fe(p,p') reaction explored in this work. Figure 3.17a shows the initial state population of the residual nucleus after binary proton emission. This initial energy and angular momentum distribution is largely independent of γ-ray emission properties due to the differing orders of magnitude between particle and γ-ray emission widths. Figure 3.17b shows various discrete level population cross sections for protons outgoing at a certain angle. These angular distributions demonstrate that particle and γ-ray emission have non-trivial angular correlations. Figure 3.18 shows the total γ-ray emission spectra. As a result of the continuum approximation, TALYS's simulated nuclei have large energy bins which cannot provide high resolution particle emission spectra. This binning issue is fixed with the decay code RAINIER [101] which eliminates the continuum approximation in the γ-ray cascade. RAINIER will be described in the next section and

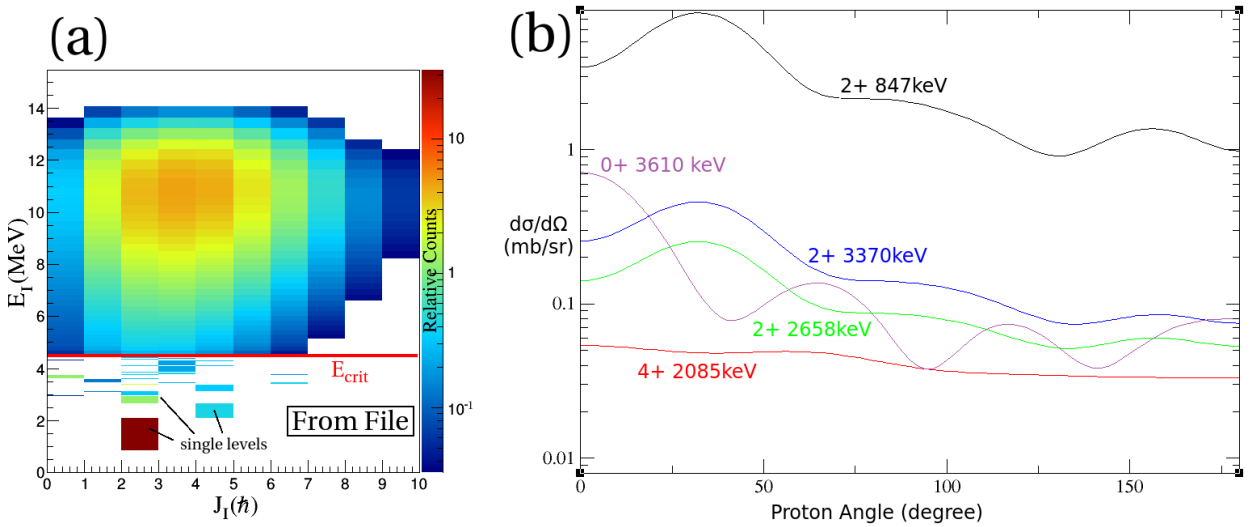

Figure 3.17: TALYS simulations of 16 MeV ^{56}Fe(p,p'). (a) $E_I J_I$ distributions; Π_I equipartition is assumed. The line $E_I = E_{\text{crit}}$ is the boundary between discrete and continuous approximations. (b) The angular distribution of protons after binary population of various discrete states. For reference, the Phoswich Wall in this experiment covers angles $32° < \theta < 77°$. Proton detection has a coincident nuclear angular momentum dependence since the angular intensity map is strongly correlated with J.

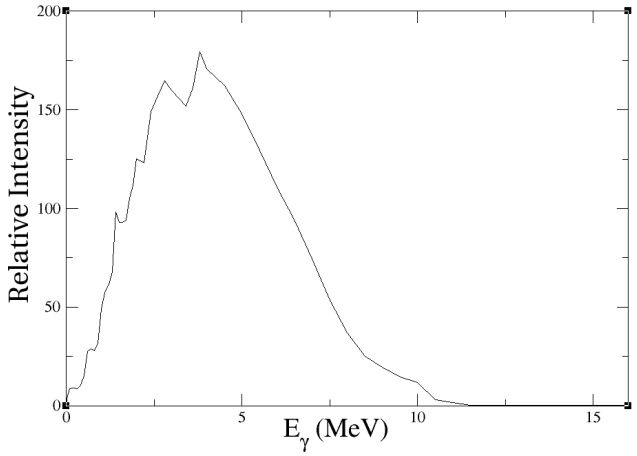

Figure 3.18: Low energy resolution in γ-ray emission spectra from TALYS simulations of 16 MeV ^{56}Fe(p,p'γ).

used extensively in Chapter 4.

TALYS does not determine the alignment of M-states, and cannot be used to determine the angular distribution or polarization of emitted γ-rays; TALYS's γ-ray output is assumed isotropic. Fortunately, an M-state distribution does not have a large effect on the method introduced in this work. An M-state distribution leads to a variation in γ-ray intensity as a function of angle, however, one of the main strengths of the novel method introduced in the next section is its independence of γ-ray intensity. Thus, no detector efficiency calibrations are necessary.

RAINIER

The **R**andomizer of **A**ssorted **I**nitial **N**uclear **I**ntensities and **E**missions of **R**adiation (RAINIER) [101] incorporates a Monte Carlo construction of nuclear level structure with the ability to populate a set of states spanning a wide range of $EJ\Pi$, thereby enabling the interpretation of discrete state population data to inform nuclear structure models in the quasi-continuum. A similar program, DICEBOX [102], uses the Monte Carlo method to simulate level and width fluctuations but is restricted to γ-ray decay from no more than two initial states such as de-excitation following thermal neutron capture. On the other hand, modern reaction codes such as TALYS and EMPIRE populate a wide range of states in the residual nucleus prior to γ-ray decay, but do not go beyond the use of deterministic functions and therefore neglect cascade fluctuations. This combination of capabilities allows RAINIER to be used to determine quasi-continuum properties through comparison with experimental data.

While RAINIER has many possible applications, it was specifically written to calculate feeding time distributions to low-lying levels from high-lying states that span a wide range of E, J, and Π. The experimental conditions in this work encouraged the development of such a code and this new capability will be beneficial for many experiments to come.

RAINIER's intended use is for modeling γ-ray cascades only (e.g., following emission of the last massive particle). RAINIER takes the following steps to simulate the complete, high-resolution γ-ray spectra from the residual nucleus:

- Build the low-energy portion of the level scheme from available information in structure databases
- Use NLD models to construct the upper portion of the level scheme. This set of artificially generated discrete levels is known as a nuclear "realization"
- Populate a user-specified distribution of initial levels
- Depopulate levels using GSF models
- Compute and histogram quantities such as emitted γ-ray energies, level populations, and decay times

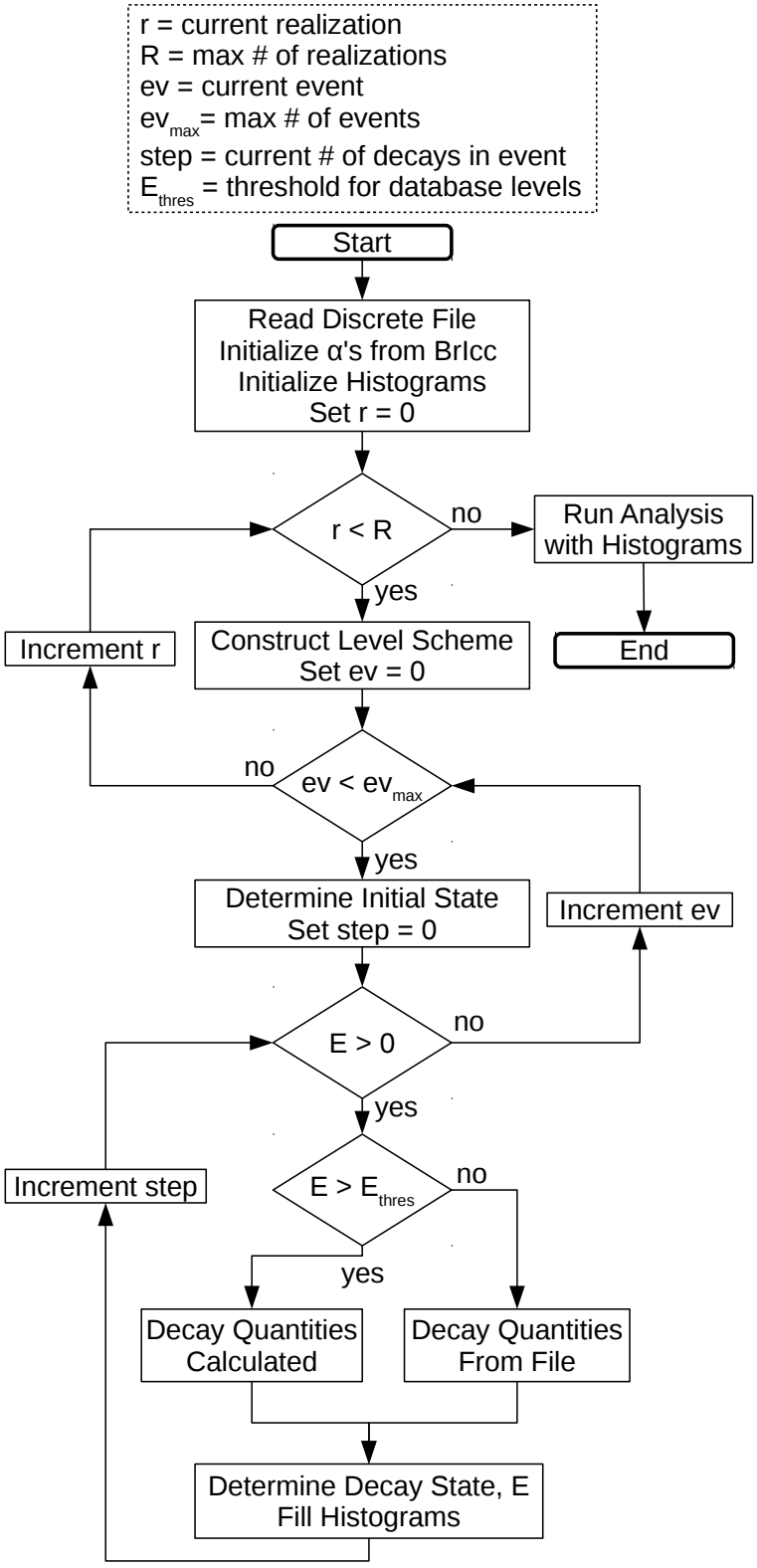

Figure 3.19: Program flow in RAINIER.

These steps are described in greater detail in Reference [101].

Figure 3.19 shows the execution order of RAINIER. To achieve low statistical uncertainty, users set the maximum number of events, $ev_{\max}$, large enough to obtain many instances of a desired observable. Users also set the maximum number of nuclear realizations, R, to track the influence of level spacing and width fluctuations on that observable.

3.5 Quasi Continuum Lifetimes

This section outlines the importance of Nuclear Level Densities and Gamma Strength Functions for reaction calculations, discusses the current techniques for measuring these quantities, and introduces a novel method for determining the absolute magnitude of the Gamma Strength Function.

Gamma-ray emission is a universal decay channel; reaction calculations are not reliable without an adequate quantification of the GSF. Nuclear Level Density is equally important because the number of γ-ray decay options is proportional to the number of levels below the excited state's energy. These two quantities determine the mission critical reaction rate cross sections such as neutron capture (n,γ) for medical isotope production [103], next-generation reactor design [2], and other applications. When a direct measurement of (n,γ) is not possible, an application's success depends on theoretical calculations and by extension GSF and NLD.

Level counting determines NLD at low energies. Many different types of reactions access levels at low excitation energy. Experimental data is tabulated, evaluated, and stored in the Evaluated Nuclear Structure Data File (ENSDF) [45]. A complete picture of a level scheme is only trustworthy up to a certain energy threshold, E_{thres}, beyond which there are either missing or misassigned levels. Researchers such as Von Egidy and Bucurescu [104, 105] analyze the completeness of these low-lying level schemes and fit NLD models (c.f. Sec. 3.4) to obtain extrapolations of low-lying levels to higher excitation energies. This procedure is effective with a level scheme complete up to about 50–100 levels and the extrapolation holds up to approximately the neutron separation energy. An estimate of the NLD near the neutron separation energy improves the quality of the extrapolation. Using the neutron Time Of Flight (nTOF) method [10, 11], researchers can count the number of s-wave neutron capture resonances [106] to determine the number of levels with angular momentum $J_g \pm 1/2$, where J_g is the ground state angular momentum of the target nucleus. A theoretical estimate of the spin cutoff parameter (c.f. Sec. 3.4) is necessary to relate the number of levels with $J_g \pm 1/2$ to levels with all J.

There are many experimental methods that probe the *energy dependence* of the GSF. The well-tested Oslo Method [9] uses light ion inelastic and transfer reactions, a procedure of detector response unfolding [93], and iterative subtraction [92] to obtain primary γ-ray spectra for simultaneous extraction of NLD and GSF. Recently, the Beta-Oslo method [107] extended the Oslo technique to nuclei further from the valley of stability by using fast ra-

dioactive beams and a γ-ray total absorption spectrometer in coincidence with β-decay. The well-established Two Step Cascade method (TSC) [108] analyzes γ-ray spectra following thermal neutron capture and compares γ-ray intensities to NLD and GSF simulation. Recently, an extension of the TSC method using direct reactions and particle-γ-γ coincidences [94] provided a model-independent confirmation of an anomalous low-energy enhancement in the GSF in ^{95}Mo [5]. These GSF methods observe *relative* γ-ray emission as a function of energy and thus rely on independent normalization.

Neutron capture experiments provide the major of GSF normalization data by using the previously mentioned nTOF method [10, 11]. These experiments quantify the average total radiative width $\bar{\Gamma}_\gamma$ near the neutron binding energy B_n through the use of high resolution transmission measurements [109]. However, many studies of important stable and unstable nuclei cannot benefit from (n,γ) measurements because short half-lifes or low isotopic abundances prohibit target fabrication. Photoabsorption experiments provide an alternative to measuring the GSF magnitude [85]. Section 3.4 and Equation (3.60) outline the definitional relationship between photoabsorption cross section and the GSF. The photoabsorption process probes collective excitations built on the ground state; unfortunately, levels are sparse at low excitation energies causing low energy γ-ray absorption data to be scarce. Furthermore, width fluctuations in the few existing low energy data points disrupt the ability to resolve the continuous nature of the GSF.

While outstanding features in the energy dependence of the GSF have profound theoretical implications, the GSF overall *magnitude* is the primary governing factor of practical applications. The GSF magnitude shapes the balance between γ-ray and neutron emission in thermal neutron reactions [99]. Hence, an independent method of GSF normalization is needed to address the gaps in neutron capture cross section data. The following section attempts to address this gap by proposing a new experimental technique to normalize the GSF. This technique extends the procedure of the Doppler Shift Attenuation Method (DSAM) [110] to infer quasi-continuum lifetimes which are fundamentally related to the GSF magnitude.

Statement of Method

Heavy ion fusion reactions populate a long chain of states along and slightly above the yrast band. In the determination of lifetimes using the Doppler Shift Attenuation Method, preceding decay from off-yrast states is an issue known as sidefeeding in the literature. Sidefeeding is typically corrected for by quantifying the γ-rays of interband transitions. To the knowledge of this author and collaborators, sidefeeding was never utilized to extract additional nuclear properties. Instead of using a small tangential distance off-yrast, the goal of this novel method is to populate unresolved states well above the yrast band. It is possible to access these states with light ion reactions. The lifetimes of these states depend on the NLD and GSF; therefore the Doppler shift of a low-lying transition following a γ-ray cascade yields information about global nuclear properties.

This method is intended for inelastic scattering or transfer reaction experiments using coincident particle and γ-ray spectrometers. Detection of the energy and angle of the light ejectile specifies the struck target nucleus's initial excitation energy and recoil velocity. The recoiling nucleus radiates its excitation energy via a γ-ray cascade while losing its kinetic energy via scatters with target atoms. Detection of a signature γ-ray from a low-lying transition specifies a particular emission excitation energy, angular momentum, and parity. The average Doppler shift of this γ-ray reveals information about the nuclear recoil velocity at emission time. The velocity reduction from initial excitation to γ-ray emission specifies the slowing down time (via sophisticated stopping simulations). This slowing down time is equivalent to a γ-ray cascade time. This cascade time depends on the intermediate quasi-continuum lifetimes which in turn depend on the magnitude of the GSF (via sophisticated cascade simulations). Proper recoil simulation requires refined slowing down theory and experiment. Proper cascade simulation requires prior knowledge of the NLD and the energy dependence of the GSF (e.g. via low energy level counting and Oslo Method experiments).

To further illustrate the concept of this method, Figure 3.20 depicts the reaction, particle detection, nuclear recoil, and γ-ray cascade of this method in the context of the 16 MeV ^{56}Fe(p,p'γ) reaction from this work. The Phoswich Wall detects the proton energy and angle providing the initial ^{56}Fe excitation energy E_I and initial recoil velocity vector $\vec{v}_{Fe,I}$. The ^{56}Fe nucleus can de-excite along many different decay paths while losing its kinetic energy via scattering with target iron atoms. GRETINA detects the signature $4_2^+ \rightarrow 4_1^+$ $E_\gamma = 1037.83$ keV γ-ray transition which specifies that the decay path traversed two well known states in ^{56}Fe: $E_B = 3.123$ MeV, $E_A = 2.085$ MeV, $J_{A,B} = 4$, $\Pi_{A,B} = +$, where A and B denote the 4_1^+ and 4_2^+ decay states, respectively. GRETINA detects many such $E_\gamma = 1037.83$ keV γ-rays and the average Doppler shift yields the average emission velocity. SRIM simulations use the average emission velocity to determine the average slowing down time. RAINIER simulations use the average slowing down time which is equivalent to an average cascade time to determine quasi-continuum lifetimes. These quasi-continuum lifetimes depend on the magnitude of the GSF via Equations (3.51) and (3.61).

There are additional nuances that factor into this method of exploiting quasi-continuum lifetimes to normalize the GSF. The primary experimental observables of this method are $F(E_I, L_B \rightarrow L_A)$, where F is the Doppler shift slope of the γ-ray emitted in the transition from level L_B to level L_A (c.f. Eq. (3.27)) and E_I is the initial excitation energy of the γ-ray cascade ($E_I \neq E_B$). A combination of SRIM, TALYS, and RAINIER provide simulated comparisons of $F(E_I, L_B \rightarrow L_A)$ in the following stages:

1. SRIM generates ^{56}Fe trajectories, $\vec{v}_{Fe}(t)$. To make this simulation as near to real experimental conditions as possible, the SRIM input initial recoil vectors are sampled from experimentally determined values. This prescription ensures the SRIM simulations incorporate the Phoswich Wall detector geometry. Example trajectories were shown in Figure 3.7.

2. TALYS generates the $E_I J_I \Pi_I$ distribution, $P(E_I, J_I, \Pi_I)$. In contrast to the γ-ray detector which fully specifies $E_B J_B \Pi_B$ of emission, the proton detector only speci-

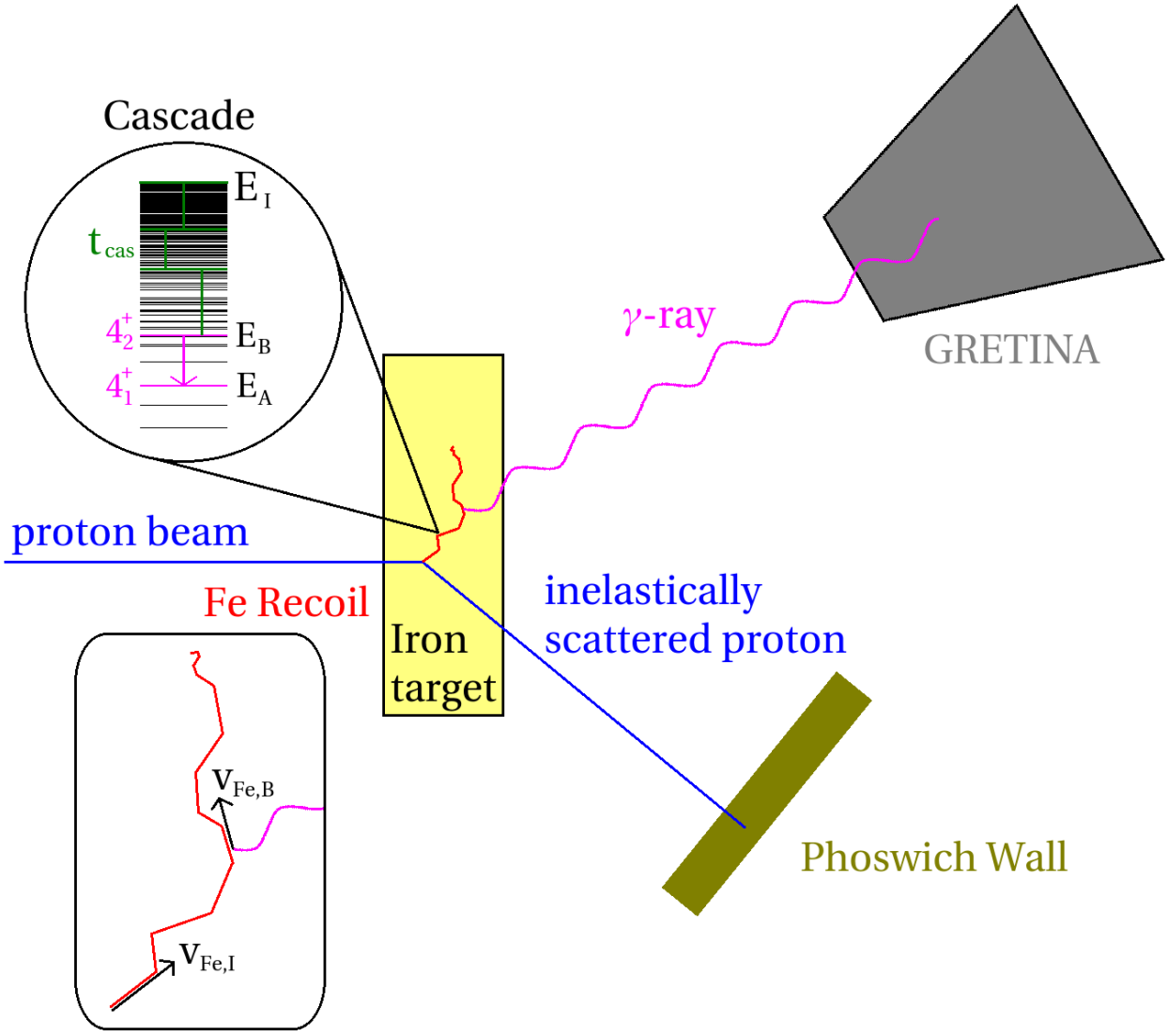

Figure 3.20: Energy exchange in a reaction that populates quasi-continuum states. A proton from the incident beam excites an ^{56}Fe nucleus. The proton detected by the Phoswich Wall specifies the intial ^{56}Fe recoil velocity, $v_{Fe,I}$. The recoiling nucleus slow downs in the iron target to velocity $v_{Fe,B}$ while de-exciting to energy E_B over the cascade time $t_{\rm cas}$. The nuclear transition from excitation energy E_B to E_A radiates a γ-ray while the nucleus still is in motion. GRETINA fully absorbs this Doppler shifted γ-ray.

fies E_I. TALYS provides the best estimate of J_I for a given E_I after binary proton emission through the use of the optical model and Distorted Wave Born Approximation. Equipartition of parity is assumed since the incident proton beam is unpolarized. Figure 3.21a shows the TALYS $P(E_I, J_I)$ distribution for this reaction.

3. RAINIER generates cascade times, t_{cas}. Due to fluctuations of level spacing and transition width, RAINIER takes the following steps to generate a *distribution* of cascade times:

   - NLD models are used to build a discrete level scheme.
   - The $P(E_I, J_I, \Pi_I)$ distribution is used to determine an initial discrete state as shown in Figure 3.21b. TALYS and RAINIER simulations have the same underlying models and parameters, but for level energies above E_{thres} TALYS uses a continuum approximation while RAINIER generates a discrete level scheme realization.
   - GSF models are used to determine branching ratios and decay times. Figure 3.22 shows RAINIER simulations of the $4_2^+ \rightarrow 4_1^+$ cascade time distribution for various E_I.

4. Remaining steps for $F(E_I, L_B \rightarrow L_A)$ determination:

   - Randomly sample t_{cas} and $\vec{v}_{Fe}(t)$ from their respective distributions to generate an emission time vector for each event, $\vec{v}_{Fe}(t_{\text{cas}})$.
   - Determine Θ (c.f. Eq. (3.22)) from $\vec{v}_{Fe}(t_{\text{cas}})$ and γ-ray emission angles θ_γ and ϕ_γ. To make this simulation as near to real experimental conditions as possible, θ_γ and ϕ_γ are sampled from experimentally determined values in conjunction with the initial recoil vectors. This prescription ensures the Doppler shifts incorporate the GRETINA detector geometry.
   - Use $|\vec{v}_{Fe}(t_{\text{cas}})| \cos\Theta$ to determine the event by event Doppler shifted γ-ray energies, $E_{\gamma,Dopp}$ (c.f. Eq. (3.20)).
   - Create histograms of $E_{\gamma,Dopp}$ vs. $|\vec{v}_{Fe}(t_{\text{cas}})| \cos\Theta$ separated into group of initial excitation E_I. Figure 3.23 shows $E_{\gamma,Dopp}$ vs. $|\vec{v}_{Fe}(t_{\text{cas}})|$ for the $4_2^+ \rightarrow 4_1^+$ and 1 MeV wide initial excitation gates of $E_I = 3.12, 5.4, 10.4$.
   - Determine the Doppler shift slopes $F(E_I, L_B \rightarrow L_A)$ from the $E_{\gamma,Dopp}$ vs. $|\vec{v}_{Fe}(t_{\text{cas}})| \cos\Theta$ histograms.
   - Fit $F(E_I, L_B \rightarrow L_A)$ to experimental observations. Minimize the difference between experiment and simulation by modifying the GSF normalization. Figure 3.24 shows $F(E_I, 4_2^+ \rightarrow 4_1^+)$ for $E_I = 3.12, 5.4, 6.4, 7.4, 8.4, 9.4, 10.4, 11.4, 12.4$ and two GSF normalizations.

Chapter 4 presents experimental comparisons of $F(E_I, L_B \rightarrow L_A)$ for three transitions in ^{56}Fe and explains the fine tuning of simulation parameters for the nuclear models. Known

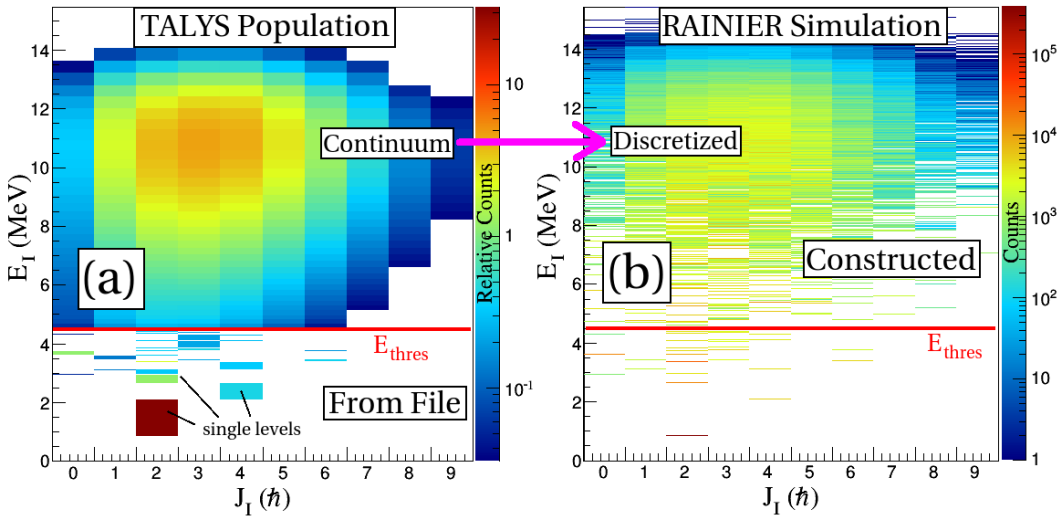

Figure 3.21: Population of ^{56}Fe initial states from 16 MeV (p,p'). (a) TALYS calculation. (b) RAINIER randomly samples the continuous distribution of TALYS output above E_{thres} and selects the nearest discrete level of the constructed level scheme.

to this author, the result is the first recorded measurement of the magnitude of the GSF for ^{56}Fe.

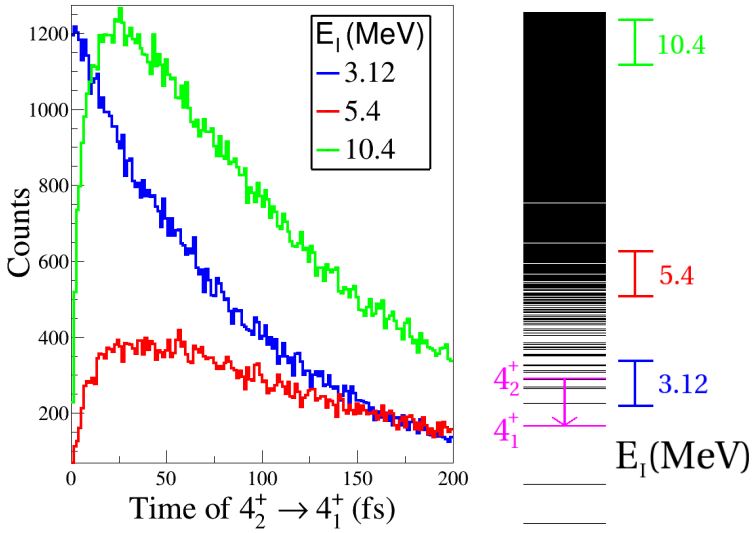

Figure 3.22: Left: RAINIER simulation of the decay time distribution of the $4_2^+ \rightarrow 4_1^+$ with different initial excitation energies E_I. Direct population of the 3.12 MeV 4_2^+ results in a simple exponential decay distribution, but indirect feeding from higher excitations results in time delay. Right: Schematic of the initial excitation energy gates that feed the $4_2^+ \rightarrow 4_1^+$ transition. The $E_I J_I \Pi_I$ intensity distribution of Figure 3.21 is implied.

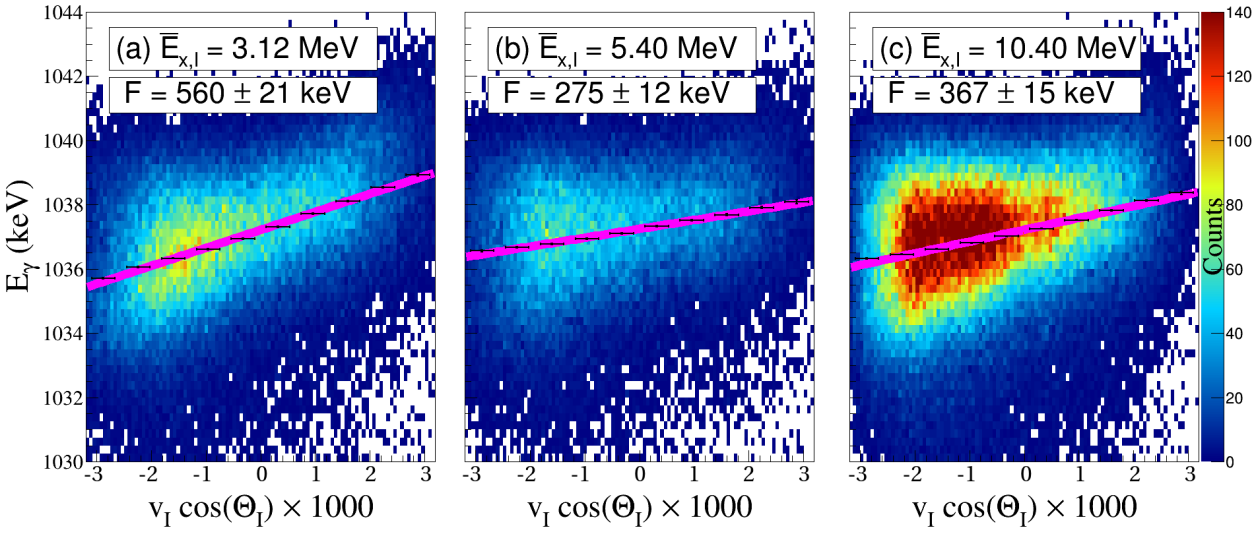

Figure 3.23: Doppler shifts of the $E_\gamma = 1.037$ MeV, $4_2^+ \rightarrow 4_1^+$ in ^{56}Fe. (a) Direct population with largest Doppler shift slope, F. (b) Initial population slightly above the 4_2^+ with smallest F. (c) Initial population at high exicitations with intermediate F.

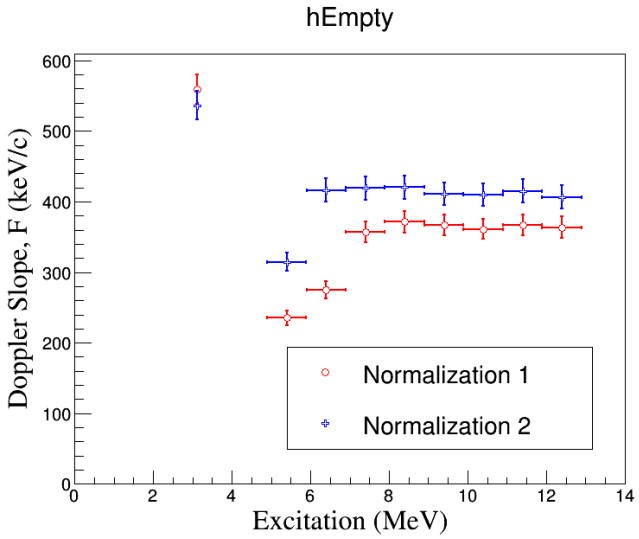

Figure 3.24: Doppler shift slopes of the $4_2^+ \rightarrow 4_1^+$ at various initial excitation energies. The only remaining free model parameter is the magnitude of the GSF; the Oslo method can determine the NLD and GSF energy dependence. Normalization 1 of the GSF is taken from mass table extrapolations of neighboring nuclei. Normalization 2 is a factor of three larger as suggested by Algin *et. al.* [111] to match ^{57}Fe.

Chapter 4

Analysis and Interpretation

4.1 Observation of Quasi-Continuum Lifetimes

This work involves measurements of additional slowing due to the time spent decaying through quasi-continuum states; we will refer to this as quasi-continuum lifetimes. This section presents the first indications of quasi-continuum lifetimes by unraveling the ^{56}Fe(p,p') data.

It should be possible to observe quasi-continuum lifetimes in many experiments that have energetic light ions incident upon a heavy target. A first observation may not require additional sort code if the energy and angle of light ejectiles and coincident γ-rays are already available. As done in the following paragraphs, displaying the existence of quasi-continuum lifetimes is straightforward. Perhaps this section will inspire the interested reader to dig further into a past data set and put a bit of effort into extracting the GSF. To observe quasi-continuum lifetimes, perform the following:

1. Compare sealed source and in-beam γ-ray energy widths
2. Compare sealed source and in-beam γ-ray energy centroid dependence on emission angle
3. Compare in-beam γ-ray energy centroid dependence on angle as a function of initial nuclear excitation energy

Note that the γ-ray peaks should not be so broad that there is continuous overlap.

There are two data collection modes relevant to this work: a self-triggered mode to detect γ-rays with no external correlation and an externally-triggered mode to detect γ-rays in coincidence with some event. The self-triggered mode is typically used with γ-ray emitting sealed calibration sources, but it will cause large detectors such as GRETINA to pick up a lot of background radiation since any cosmic muon or terrestrial γ-ray that passes through the large volume of germanium crystal will trigger the whole device. The self-triggered

mode can also be used with a beam on target, but GRETINA will detect many unwanted beam-induced events such as interactions with the beam pipe or collimators. On the other hand, the externally-triggered mode is typically used in conjunction with a particle detector or a radio-frequency signal from the beam; GRETINA records and processes waveforms for approximately 1 μs before, after, or during the triggering event. The externally-triggered mode significantly reduces recorded background counts because the unfiltered background count rate is much lower than 1 μs^{-1}. The background rate is reduced even farther if the particle detector registers the correct particle and particle energy, thereby vetoing unwanted beam-induced radiation.

This experiment recorded data of both types:

- ^{56}Co electron capture decay with GRETINA self-triggering
- Beam-induced ^{56}Fe(p,*) with the Phoswich Wall externally-triggering GRETINA

These two scenarios conveniently produced identical excited states of ^{56}Fe, albeit with differing population intensities. Figure 4.1 compares γ-ray energy spectra near $E_\gamma = 1.037$ MeV corresponding to the ^{56}Fe $4_2^+ \rightarrow 4_1^+$ transition. Since the beam-induced ^{56}Fe* emits γ-rays in flight, the peak is much broader in energy than the same transition from the sealed calibration source. Note that the additional broadening is not due to gain drifts in the digital data acquisition system; the same phenomenon occurs within a short time interval. The sealed source produces ^{56}Fe via electron capture decay of ^{56}Co. Since the mass of the emitted neutrino is much smaller than the mass of the ^{56}Fe, the nuclear recoil kinetic energy is trivial. According to Figure 3.2a, the typical ^{56}Fe recoil kinetic energy after inelastic scattering is approximately 300 keV, corresponding to $v_{Fe} \approx 0.0034$c. The broadening due to this recoil velocity will be on the order of the maximum Doppler Shift, $E_\gamma \cdot v_{\mathrm{Fe}} \approx 3.5$ keV, which agrees with the magnitude of the additional broadening in Figure 4.1.

All ^{56}Fe in this experiment scatter in the forward direction; a light projectile is kinematically forbidden from causing a heavy target to recoil backward if the reaction has a negative Q-value. Figure 4.2 shows typical ^{56}Fe recoil angles with respect to the incident proton beam. According to Figure 3.2b, the nuclear recoil opening angle is confined to values $0.5 < \xi < 1.3$ for the proton energies and angles covered in this experiment. The GRETINA geometry is such that there is more active detection volume for $\theta > \pi/2$. Since γ-rays are mostly detected at backward angles, one can expect the average Doppler shift to be negative. Figure 4.1 confirms this expectation since the centroid of the beam-induced peak is lower in energy than the sealed source.

To further confirm that the additional peak broadening is the result of Doppler shift, Figure 4.3 shows how peak centroid depends on γ-ray detection angle. For the beam-induced spectrum, it is clearly visible that peaks at backward detection angles, $\theta_\gamma > \pi/2$, have lower centroid energies than peaks at forward angles, $\theta_\gamma < \pi/2$. For the sealed source spectrum, the peak centroids appear independent of θ_γ as anticipated. The beam-induced peaks retain a broad width because there is currently no restriction on ^{56}Fe recoil angle which can take on any azimuthal angle $0 < \phi < 2\pi$ in addition to the aforementioned range of opening angles,

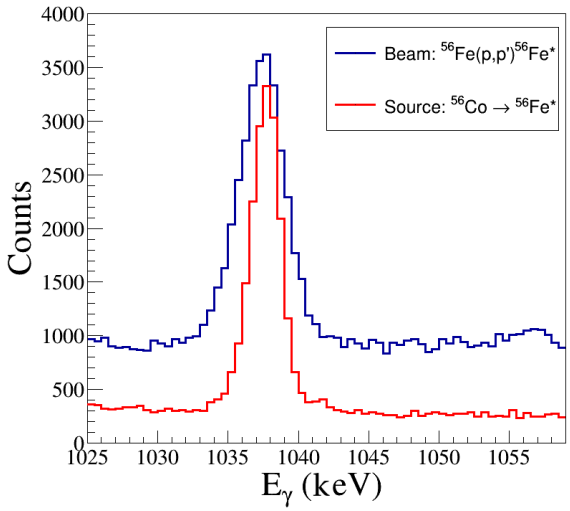

Figure 4.1: Peak broadening of the ^{56}Fe $4_2^+ \rightarrow 4_1^+$ γ-ray transition. Germanium detector resolution dominates the sealed source peak width. Doppler shift dominates the beam-induced peak width.

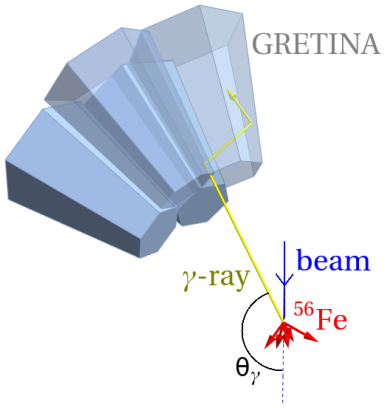

Figure 4.2: Typical angles of nuclear recoil and γ-ray detection.

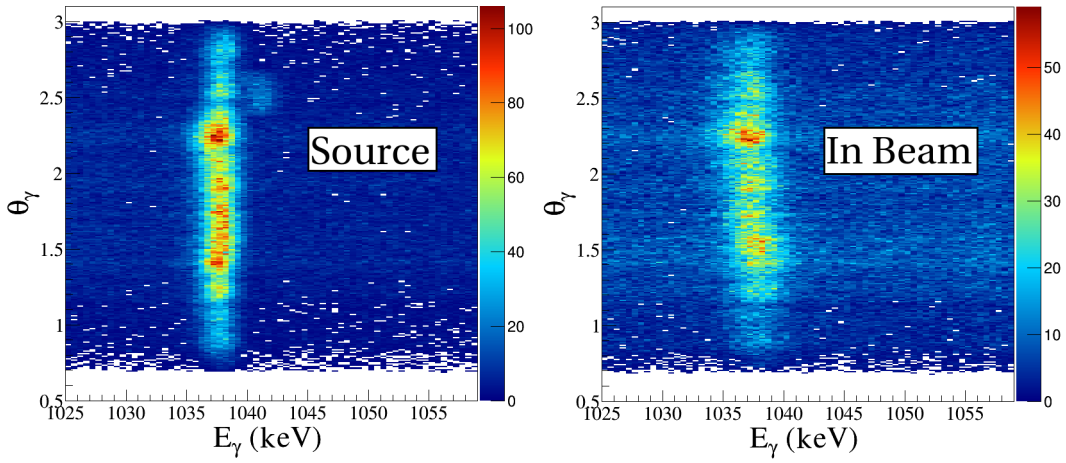

Figure 4.3: Angular dependence of centroid energies. The recoil momentum from γ-ray emission alone is a minor concern; therefore the sealed source spectrum is detection-angle-independent. The recoil momentum from proton bombardment is non-trivial; therefore the beam-induced spectrum is detection-angle-dependent. Note that GRETINA does not cover θ uniformly – there are more detectors at backward angles.

$0.5 < \xi < 1.3$. According to Equation (3.20), the total angle between recoil and emission, Θ, governs Doppler shift. Θ takes on a wide range of values if there is no restriction on the nuclear recoil angle apart from the fact that the nucleus generally recoils forward. For reactions of inverse kinematics where the mass of the projectile is much larger than the mass of the target, the projectile-like product travels in the forward direction with $\xi \approx 0$ with a recoil velocity nearly two orders of magnitude greater, $v_{\text{recoil}} \sim 0.3c$. In that case, the peak centroid energy depends much more strongly on θ_γ.

Not all beam-induced γ-rays have a slope. Figure 4.4 shows the beam-induced ^{56}Fe $2_1^+ \rightarrow 0_1^+$ $E_\gamma = 847$ keV transition with $\tau \approx 6$ ps. According to Figure 3.9, the slowing down time for a 300 keV recoil varies from 40-400 fs. The nucleus comes to a halt before γ-ray emission, resulting in no Doppler shift.

Since the nuclear recoil angle can take on such a wide range of values, the independent variable must be improved to enhance the sensitivity to Doppler shift. The independent variable is switched from "θ_γ" to "$v_{\text{Fe,I}} \cos\Theta_I$", where Θ_I is the initial total angle and the initial nuclear recoil velocity is

$$v_{\text{Fe,I}} = \sqrt{\frac{2\,T_{\text{Fe,I}}}{m_{\text{Fe}}}}, \tag{4.1}$$

where $m_{\text{Fe}} = 55.9$ amu is the nuclear recoil mass and $T_{\text{Fe,I}}$ is the initial nuclear recoil kinetic energy according to the kinematics of Equations (3.9) and (3.10). Note that particle detectors can only deduce nuclear recoil kinetic energy immediately after the reaction, whereas the Doppler shift depends on the kinetic energy at the moment of emission which may be very different due to slowing down in the target. Determination of Θ_I requires measurements from

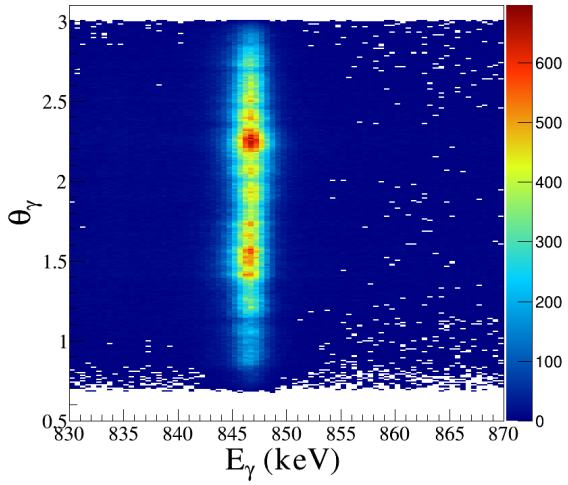

Figure 4.4: Fully stopped transition with no Doppler shift. Although the beam causes nuclear recoil before emission, the target material slows down the nucleus well before the nucleus emits a γ-ray

both particle and γ-ray detectors according to Equation (3.22). This angle also changes since the recoiling nucleus deflects off target atoms in flight.

The independent variable $v_{\mathrm{Fe,I}} \cos\Theta_I$ is a great improvement over θ_γ: there is now almost precise knowledge of the nuclear recoil velocity as opposed to knowing the fact that the nucleus generally recoils in the forward direction. Note that $v_{\mathrm{Fe,I}} \cos\Theta_I$ is a better independent variable than $\cos\Theta_I$ alone because according to Figure 3.2 the initial recoil kinetic energy varies from 70-400 keV corresponding to a velocity range of 0.001c-0.004c. The variable $\cos\Theta_I$ is only a good candidate for measuring Doppler shift when the initial nuclear recoil velocity does not vary much or there is sufficient data to produce multiple plots of specified initial velocity. The velocity stipulation is prevalent in lifetime literature, but there is not enough data in this experiment to make the additional cut. Figure 4.5 shows detected γ-ray energy as a function of the new independent variable $v_{\mathrm{Fe,I}} \cos\Theta_I$. The energy and angle resolution is much better than Figure 4.3.

According to Equation (3.20),

$$\Delta E = E_\gamma \cdot v_{\mathrm{Fe}} \cos\Theta, \tag{4.2}$$

where ΔE is Doppler shift. For $v_{\mathrm{Fe,I}} \cos\Theta_I = -0.002c$ and $E_\gamma = 1810.7$ keV, one may naïvely expect $\Delta E = -3.6$ keV. In contrast, Figure 4.5 shows $\Delta E = -2.2$ keV at $v_{\mathrm{Fe,I}} \cos\Theta_I = -0.002c$. This 38% reduction is attributable to lifetime. Recoiling ions encounter frictional target electrons and scatter off heavy, highly-charged target nuclei (c.f. Fig. 3.7). Since the recoiling nucleus slows down and changes angle, the quantity $v_{\mathrm{Fe}} \cos\Theta$ is on average lower at the moment of emission compared to initial formation, resulting in lower Doppler shift. For this transition the lifetime is $\tau \approx 40$ fs. For these recoil energies, the slowing down is a stochastic process on the order of 40-400 fs. Figure 4.6 shows several transitions of

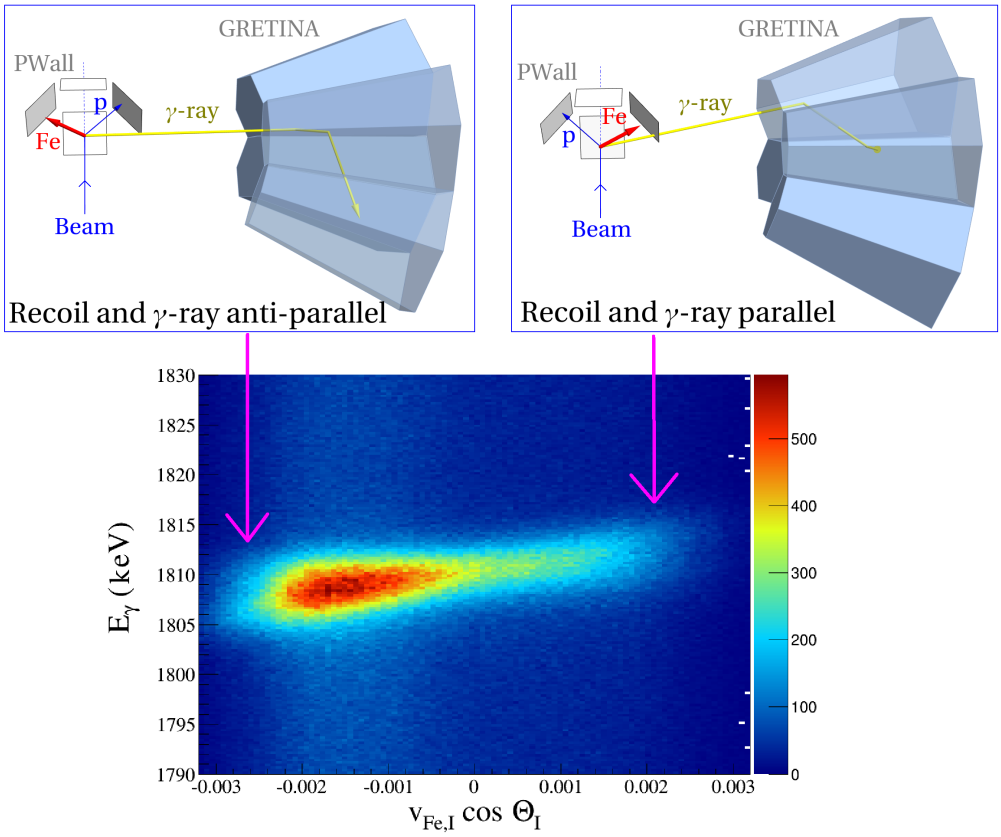

Figure 4.5: Doppler shifted ^{56}Fe $2_2^+ \rightarrow 2_1^+$ $E_\gamma = 1810.7$ keV transition. The variable $v_{\mathrm{Fe,I}} \cos\Theta_I$ uncovers a strong Doppler shift: when the nucleus emits a γ-ray in the forward direction of motion the lab frame energy is high; when the nucleus emits a γ-ray in the backward direction the lab frame energy is low.

varying slopes indicating differing lifetimes. Lifetime is a complicated fundamental nuclear quantity which depends on internal nuclear structure and is beyond the scope of the current discussion.

Quasi-continuum lifetimes are most apparent in a plot of Doppler shift slopes, F, as a function of initial nuclear excitation energy where F is the variation in Doppler shift as a function of $v_I \cos\Theta_I$. Consider the ^{56}Fe $4_2^+ \rightarrow 4_1^+$ $E_\gamma = 1037.8$ keV transition where the 4_2^+ level has an excitation energy of 3.123 MeV. There are a number of event scenarios in which GRETINA will detect a $E_\gamma \approx 1037.8$ keV γ-ray:

1. Direct Population: a proton inelastically scatters off ^{56}Fe to populate the 4_2^+ level; the $4_2^+ \rightarrow 4_1^+$ transition emits a $E_\gamma = 1037.8$ keV γ-ray; the Phoswich Wall absorbs the proton; GRETINA absorbs the γ-ray.

2. Quasi-Continuum Feeding: a proton inelastically scatters off ^{56}Fe to populate a level above the 4_2^+ level, likely among quasi-continuum states; the upper level decays to the

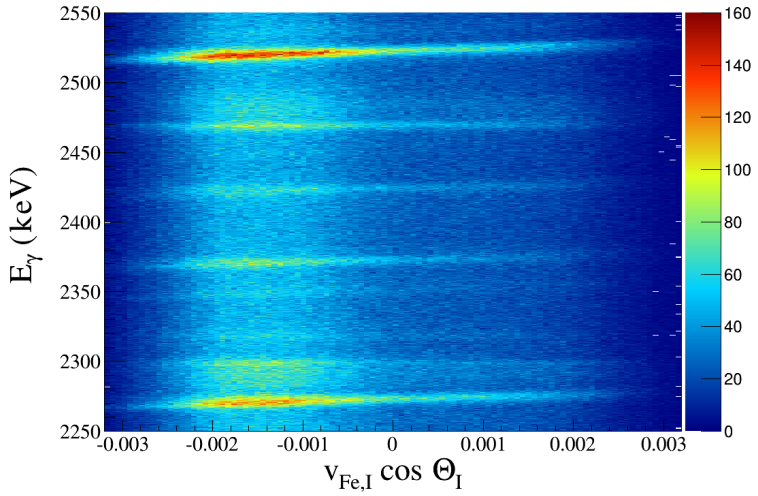

Figure 4.6: Doppler shifts of several ^{56}Fe γ-ray transitions. The differing slopes indicate differing lifetime, e.g. the 2523 keV transition has $\tau \approx 25$ fs, the 2470 keV transition has $\tau \approx 136$ fs, and the 2373 keV transition has $\tau \approx 38$ fs.

4_2^+ which then feeds the $4_2^+ \rightarrow 4_1^+$ transition; the Phoswich Wall absorbs the proton; GRETINA absorbs the $E_\gamma = 1037.8$ keV γ-ray.

3. Random Coincidence: a proton inelastically scatters off ^{56}Fe to produce the $E_\gamma = 1037.8$ keV γ-ray either directly or indirectly; a second proton from the same or neighboring beam bunch elastically scatters off another target nucleus; GRETINA absorbs the $E_\gamma = 1037.8$ keV γ-ray; the Phoswich Wall only absorbs the elastically scattered proton.

4. Compton Coincidence: a proton inelastically scatters off ^{56}Fe and populates a level which emits a γ-ray with $E_\gamma > 1037.8$ keV, this proton misses the Phoswich Wall, and the γ-ray Compton scatters in GRETINA depositing $\approx$1037.8 keV; a second proton inelastically scatters off ^{56}Fe and populates the 4_2^+ level, the Phoswich Wall absorbs the proton, and GRETINA misses any emitted γ-ray from the 2nd reaction.

Figure 4.7 illustrates each of these scenarios. Using initial nuclear excitation energy $E_I = -Q$ (c.f. Eq. (3.9), (3.10)), Figure 4.8 shows the number of counts yielding the $E_\gamma \approx 1037.8$ keV γ-ray. The first three phenomena from the aforementioned list are evident. The initial excitation energy resolution is poor ($0.4 < \sigma_{E_I} < 1.0$ MeV) due to the poor proton energy resolution of the Phoswich Wall. Figure 4.9 shows evidence of the fourth phenomenon, Compton coincidence. These Compton coincidences contribute about 14% of the events within $E_\gamma = 1037.8 \pm 7$ keV. I present an algorithm for removing these erroneous events in Section 4.2.

Quantifying the four previously mentioned phenomena is necessary for later stages of analysis, but quasi-continuum lifetimes are evident with only rough E_I gates in Doppler

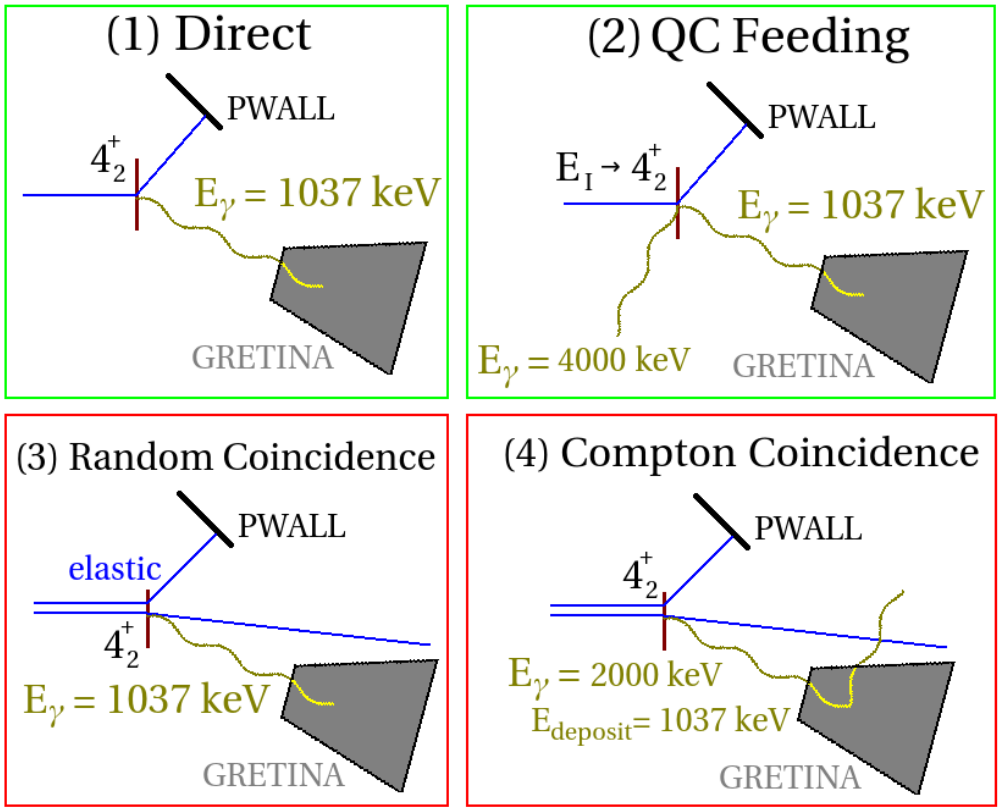

Figure 4.7: Four types of events with the Phoswich Wall and GRETINA. The top two panels show events useful in the analysis: the direct events are used to determine lifetimes of discrete states while the quasi-continuum (QC) feeding events are used to determine the GSF. The bottom two panels show false coincidence events that need to be addressed in the analysis: random coincidences are primarily due to high Rutherford scattering cross section while the Compton coincidences are due to γ-rays scattering out of the germanium detectors.

shift slope plots. Figure 4.10 shows Doppler shift slopes of the $4_2^+ \rightarrow 4_1^+$ transition for three E_I gates: direct, indirect, and quasi-continuum. Results are similar to the simulation of Figure 3.23 from Chapter 3. The Doppler shift is much smaller with an E_I gate just above the 4_2^+ level: a preceding transition adds slowing down time. The Doppler shift is not as small with an E_I gate in the quasi-continuum: the large factor of E_γ^3 makes large energy transitions proceed faster (c.f. Eq. (3.61)).

After an assessment of the systematic uncertainties, details of how quasi-continuum lifetimes are used to extract the GSF absolute magnitude will be discussed in Section 4.3.

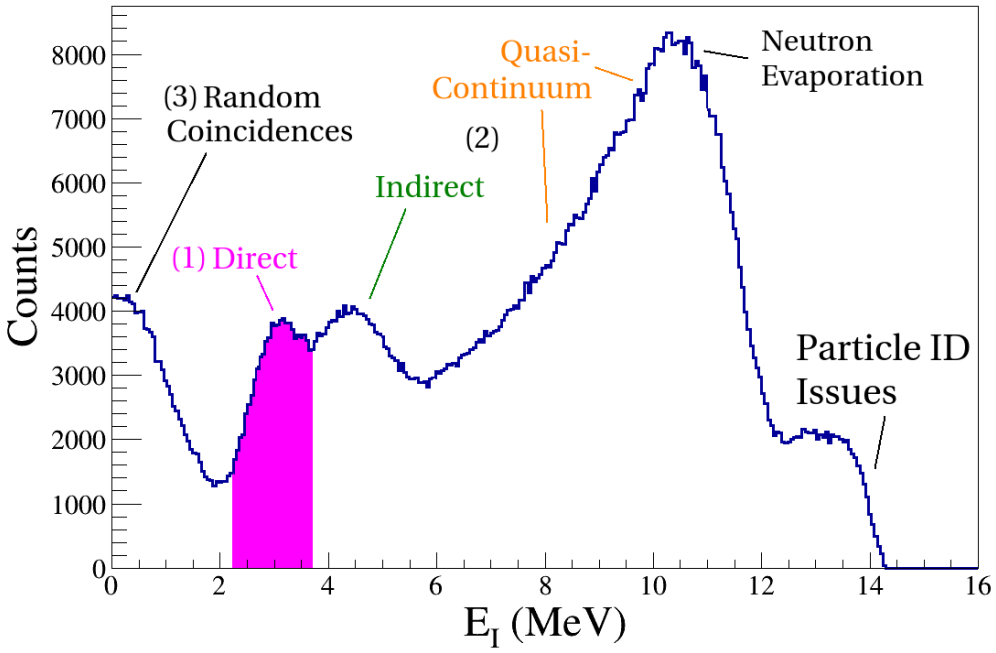

Figure 4.8: Events yielding $E_\gamma = 1037.8 \pm 7$ keV as a function of nuclear excitation energy. See text and Figure 4.7 for more details on the various features. The particle identification issues are the result of intersecting C- vs. B-Gate cuts in the Phoswich Wall data analysis (c.f. Fig. 2.11).

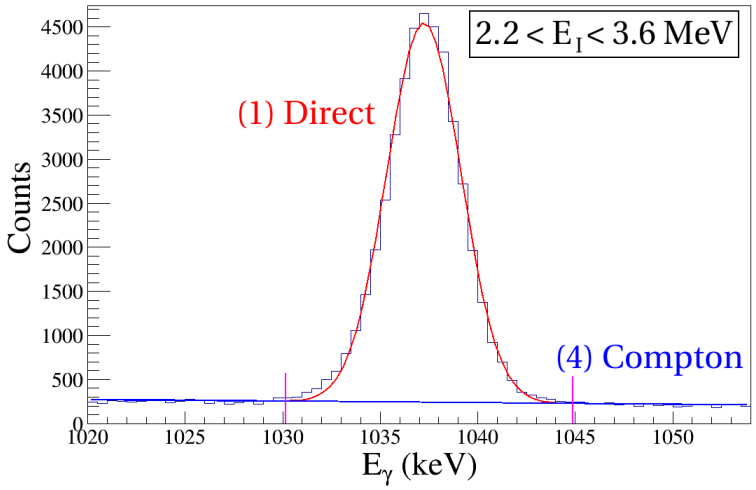

Figure 4.9: Evidence for the Compton Coincidence in the data. An excitation energy gate of $2.2 < E_I < 3.6$ MeV preferentially selects events that directly populate the 4_2^+ level. However, the incident proton beam bunches are dense and inelastic coincidences generate γ-rays that Compton scatter in GRETINA. Note that the gate width of 7 keV used in Figure 4.8 adequately captures all 1037.8 keV γ-rays.

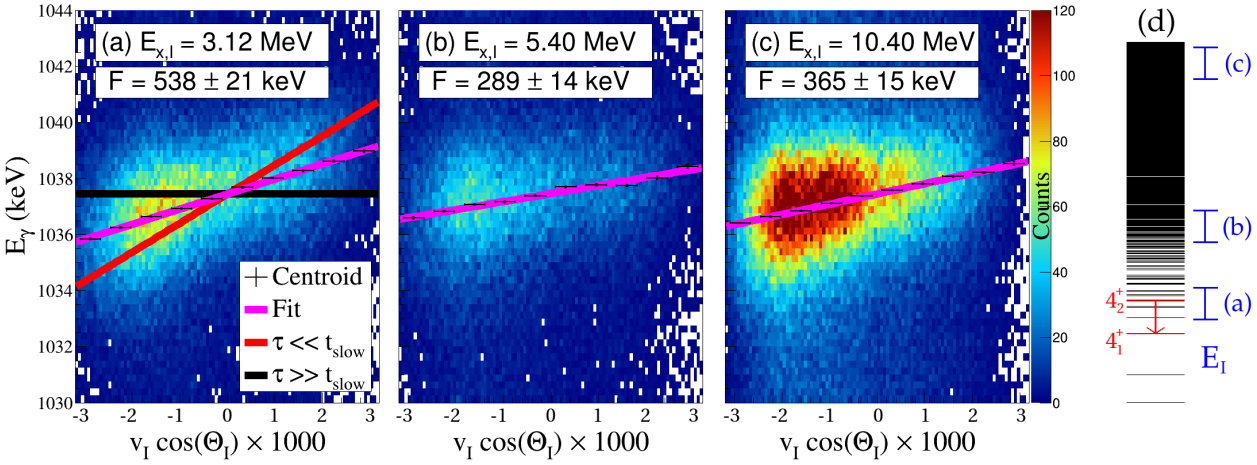

Figure 4.10: Doppler shifts of the $E_\gamma = 1.037$ MeV, $4_2^+ \rightarrow 4_1^+$ in ^{56}Fe. The lifetime of this transition, τ, is on the order of the nuclear slowing down time, t_{slow}, causing lifetime effects. (a) Direct population with largest Doppler shift slope, F. (b) Initial population slightly above the 4_2^+ with smallest F. (c) Initial population at high excitations with intermediate F. The changing slope is evidence for quasi-continuum lifetimes. (d) Schematic of the excitation gates relative to the $4_2^+ \rightarrow 4_1^+$ transition.

4.2 Systematic Uncertainties

This section explores the possible systematic errors that may arise in obtaining Doppler shift slopes, presents results for three γ-ray probes, and offers interpretations of the various features.

Quantifying Contaminants

The large random coincidence peak in Figure 4.8 is burdensome because its 1 MeV half-width overlaps the direct population peak. From a comparison of peak areas, a proton which populates the 4_2^+ level has a smaller chance of scattering into the Phoswich Wall than another proton in coincidence elastically scattering into the Phoswich Wall. The elastic coincidence probability is so immense because the Rutherford scattering cross section is so high:

$$\frac{d\sigma}{d\Omega} = \left(\frac{Z_1 Z_2 \alpha \hbar c}{4 E_K \sin^2(\Theta/2)} \right)^2 \tag{4.3}$$

where $Z_1 = 1$ and $Z_2 = 26$ are the charges of the incident proton and target ^{56}Fe, respectively, $\alpha \approx 1/137$ is the fine-structure constant, $\hbar c \approx 197$ MeV fm, and $E_K = 16$ MeV is center of mass kinetic energy. This formula neglects electron screening, but it gives a good estimate of the magnitude of scattering. Figure 4.11 shows that the differential cross section for

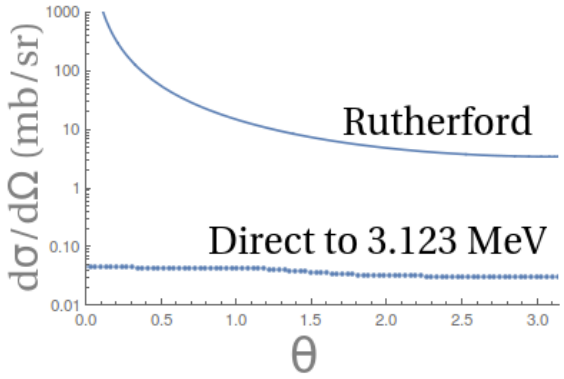

Figure 4.11: Rutherford and direct cross sections for ^{56}Fe(p,p) and (p,p'). Direct cross sections to other levels are of the same order as the 3.123 MeV level.

Table 4.1: Levels that feed the 3.123 MeV 4_2^+

E (MeV)	$J\Pi$	τ (fs)	BR (%)	E_γ (keV)
3.388	6+	4200(300)	1.3	265.5
3.755	6+	180(30)	<2	632.6
3.856	3+	36(4)	1.1	733.5
4.100	4+	62(7)	11	977.4
4.120	3+	200(60)	1.2	996.9
4.298	**4+**	**160(70)**	**61**	**1175**
4.395	3+	50(25)	9.3	1271
4.458	**4+**	**38(14)**	**58**	**1335**
4.509	3−	120(40)	9	1386
4.554	4+	140(50)	17	1432
4.608	2+	70(40)	10	1486
4.683	(2+)3+	100(60)	12	1560
4.692	4+	50(10)	7	1569
5.131	3+,4+,(2+)	100(30)	24	2009

Rutherford scattering is more than two orders of magnitude greater than that of inelastic scattering directly to the 3.123 MeV 4_2^+ level. Note that compound elastic scattering to the 4_2^+ is negligibly small; if the incident kinetic energy disperses evenly among all nucleons, there is only a small chance that all the energy will localize back into one proton and evaporate.

The large indirect population peak in Figure 4.8 is also burdensome because it overlaps the direct population peak. Table 4.1 lists many of the known neighboring levels that feed the 4_2^+. Assuming an excitation energy uncertainty of 0.5 MeV, the levels in bold in the table are the biggest contaminants to the direct level peak. The magnitude of contamination of these peaks can be deduced from a fit of the *Counts vs.* E_I curve with several Gaussian functions. Figure 4.12 shows the results of the fit using peaks at 0 MeV for elastic coincidence, 3.123

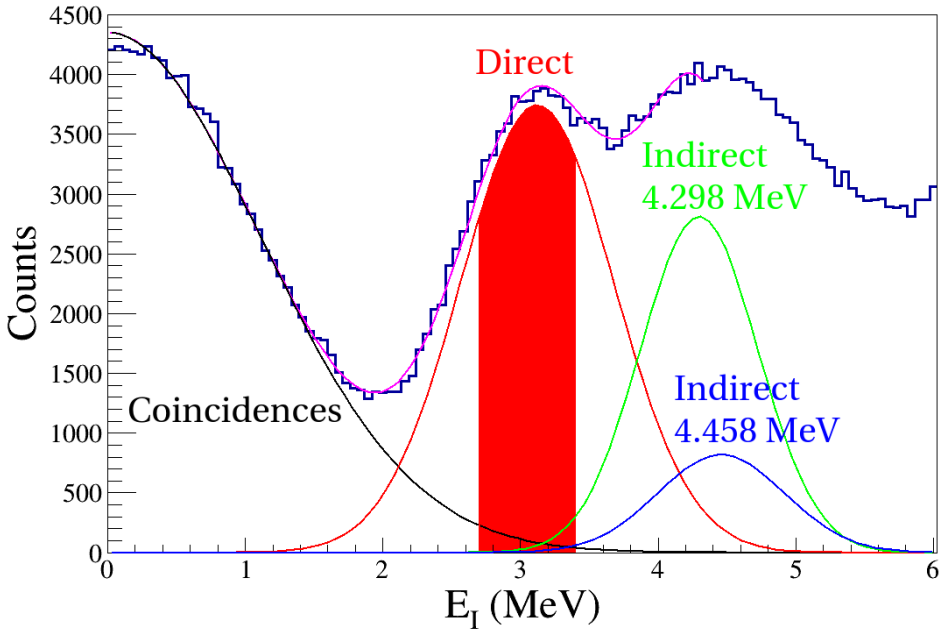

Figure 4.12: Events yielding $E_\gamma = 1037.8 \pm 7$ keV as a function of nuclear excitation energy. Counts in the range $2.7 < E_I < 3.4$ MeV have contributions from direct population, elastic coincidences, and indirect population.

Table 4.2: Fraction of the $E_\gamma = 1037.8 \pm 7$ keV counts in the range $2.7 < E_I < 3.4$ MeV

Peak Type	E (MeV)	Contribution (%)
Elastic Coincidence	0	3.1
Direct Population	3.123	94.5
Indirect Population	4.298	2.0
Indirect Population	4.458	0.4

MeV for direct population, and two indirect population peaks. The fitting range is 0–4.35 MeV; a higher E_I range would require an additional Gaussian function for each additional level. Two indirect peaks are flexible enough to account for minute contributions from the remaining contaminants of Table 4.1. A good direct population excitation window is $2.7 < E_I < 3.4$ MeV which minimizes the coincidence and indirect contaminants while keeping a large number of direct populations. Table 4.2 lists the integral of the peaks in this E_I range. Direct population always has approximately a 94.5% contribution regardless of the number of indirect peaks and the maximum fit range E_I. Figure 4.13 shows that the γ-rays from the two indirect populations appear in the 1D spectrum with excitation gate $2.7 < E_I < 3.4$ MeV. The magnitude of the contaminant peaks is within a factor of two of the expectations of Table 4.2; the differing inelastic scattering cross sections make up the difference.

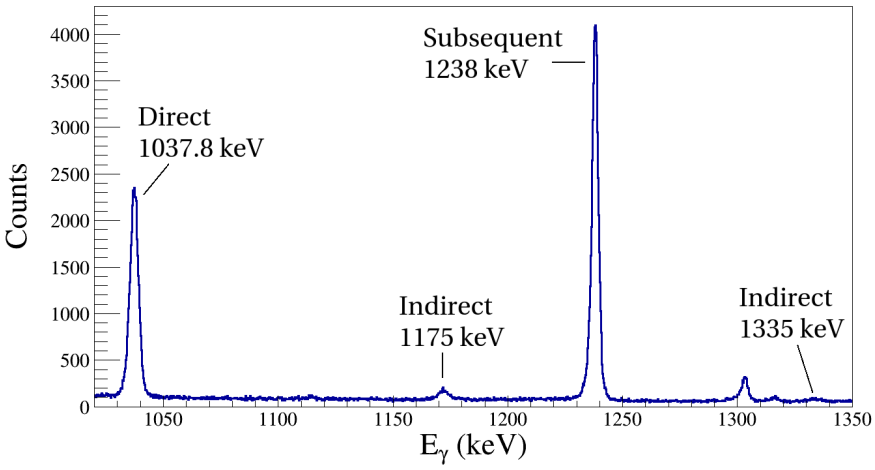

Figure 4.13: γ-ray spectra for the excitation range $2.7 < E_I < 3.4$ MeV. The $4_1^+ \rightarrow 2_1^+$ $E_\gamma = 1238$ keV transition follows 1037.8 keV γ-ray emission with 100% intensity.

For higher excitation gates, the elastic coincidence peak is not an issue since the tail has a negligible contribution for $E_I > 3.5$ MeV. Furthermore, the indirect contribution is no longer a contaminant but precisely the subject of study when measuring quasi-continuum lifetimes. In fact, the direct population peak is the contaminant for higher E_I gates. The tail of direct contamination has negligible contribution for $E_I > 5$ MeV. For quasi-continuum lifetimes at higher excitations, the inclusion of multiple indirect peaks is acceptable. Quasi-continuum lifetimes depend on the GSF which is an average quantity in the first place. Therefore, the 0.5 MeV excitation energy resolution provides a built-in averaging when determining the GSF with quasi-continuum lifetimes.

The elastic coincidence and indirect contaminants are not detrimental to direct lifetime determination. An algorithm in a following subsection negates the uncorrelated elastic coincidences. Since the indirect contaminants are quantifiable, they propagate into the lifetime uncertainty, as described in the following subsection.

Recoil Accuracy

This section discusses average $v_I \cos\Theta_I$ uncertainty which is used to bin the data when measuring Doppler shift slopes.

The Phoswich Wall's proton energy and angle uncertainties have approximately constant values of $\sigma_{T_p} = 0.5$ MeV and $\sigma_\theta = 3°$, respectively. According to Equation (3.9), the reaction Q-value is roughly independent of θ such that the nuclear excitation energy uncertainty is nearly equal to the proton kinetic energy uncertainty. In contrast, the nuclear recoil velocity and angle have a more complicated dependence:

$$T_{Fe} = \frac{m}{M}\left(T_p' + T_p - 2\cos\theta\sqrt{T_p' T_p}\right) \tag{4.4}$$

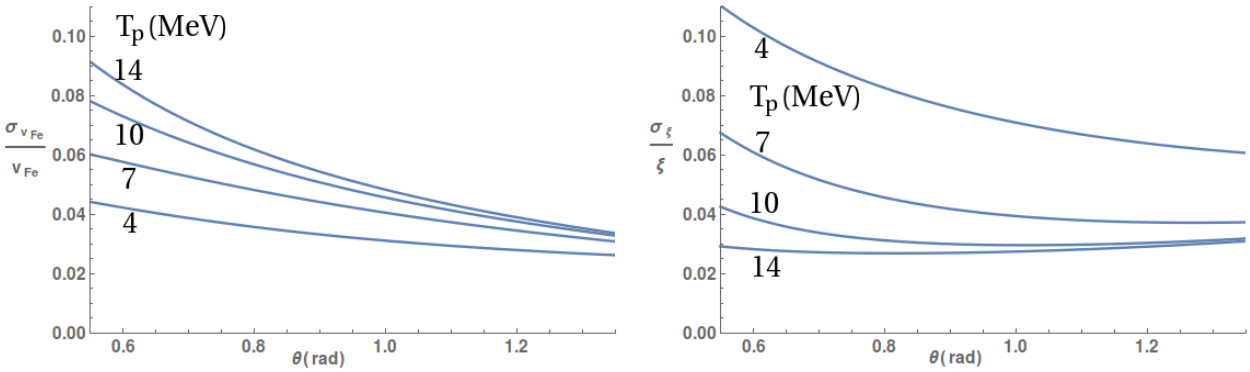

Figure 4.14: Uncertainties in ^{56}Fe recoil velocity and angle as a function of detected proton energy and angle.

$$v_{Fe} = \sqrt{2T_{Fe}/M} \tag{4.5}$$

$$\sin\xi = \sin\theta \left(1 + T_p'/T_p - 2\cos\theta\sqrt{T_p'/T_p}\right)^{-1/2}, \tag{4.6}$$

where m and M are the proton and ^{56}Fe masses, respectively, T_p and θ are the detected proton energy and angle, T_{Fe} and ξ are the undetected ^{56}Fe recoil energy and angle, and $T_p' = 16$ MeV is the incident proton energy. Figure 4.14 shows results of linear uncertainty propagation:

$$\sigma_f = \sqrt{\left(\sigma_x \frac{\partial f}{\partial x}\right)^2 + \left(\sigma_y \frac{\partial f}{\partial y}\right)^2 + \dots}\ , \tag{4.7}$$

where σ_f is the uncertainty of the function f, σ_x is the uncertainty of variable x, σ_y is the uncertainty of variable y, and so forth. The uncertainties in the recoil velocity and angle are approximately 5% and 6%, respectively. These uncertainties help determine bin width for histogram projections when measuring Doppler shift slopes. As an example, Figure 4.15 shows the Doppler shift of the ^{56}Fe $4_2^+ \rightarrow 4_1^+$ $E_\gamma = 1037.8$ transition after direct population, $E_I = 3.123$ MeV. When measuring the γ-ray centroid energy at various values of $v_I \cos\Theta_I$, it is not yet clear how wide to make the projection bins. The $v_I \cos\Theta_I$ bin widths should be as big as or larger than the uncertainty in $v_I \cos\Theta_I$, but they must be small enough to measure the variation in γ-ray centroid energy. A higher number of projections gives a better estimate of the Doppler shift slope.

Linear propagation of uncertainty in total angle σ_Θ diverges when ^{56}Fe emits a γ-ray at 90°; hence a purely analytical approach to uncertainty breaks down. An uncertainty Monte Carlo simulation could map out the standard deviations of |Detected–True| values of $v_I \cos\Theta_I$ for the 5 correlated variables and the specific geometry of this experiment. However, this statistical approach is even more complicated and defeats the event-by-event

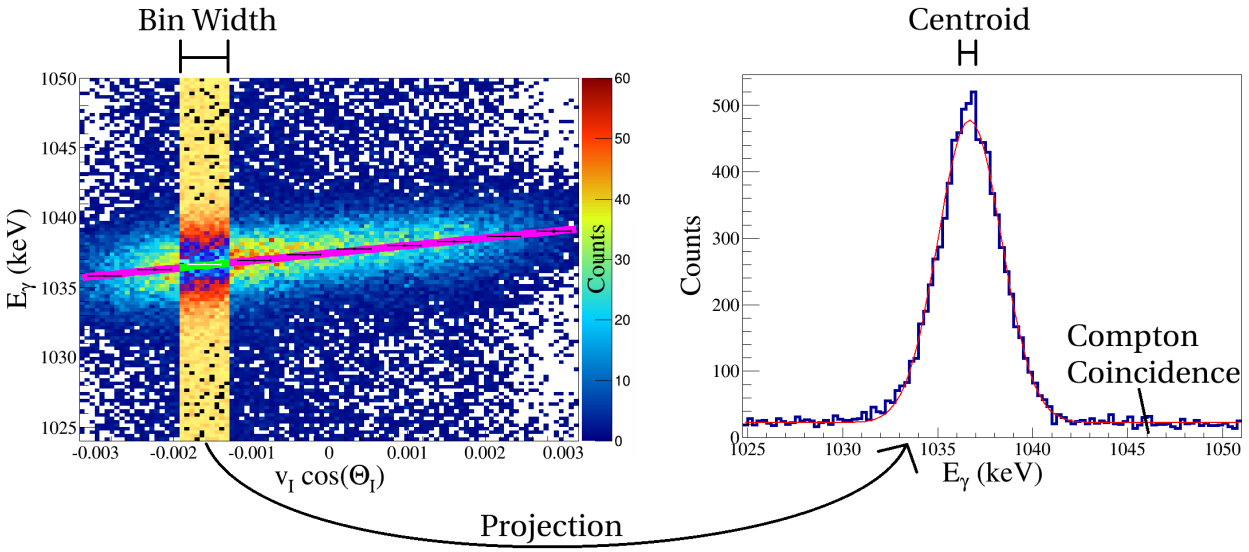

Figure 4.15: Projections of $v_I \cos\Theta_I$ γ-ray spectra. The projection bin width must be as big as or larger than the uncertainty, but small enough to map change in the γ-ray centroid energy. Compton Coincidences are noticeable in the projection and must be addressed by fitting a Gaussian function with a constant background.

histogram technique already in motion. Instead, an overestimate of the uncertainty suffices when setting a projection bin width. The coefficient $\cos\Theta_I$ is of order unity or smaller, and so v_I dominates the maximum $v_I \cos\Theta_I$ deviation of poorly resolved γ-ray and proton measurements. A good estimate for bin width is twice the maximum v_I deviation, which according to Equations (4.4)–(4.5) and Figure 4.14 is $2 \cdot \sigma_{v_{Fe},max} = 0.0003c$. Hence, the projection bin width of $0.00064c$ in Figure 4.15 was an overestimate and can be reduced to $0.0003c$.

Tracked γ-ray data has high angular resolution. A typical angular acceptance of a germanium crystal might be on the order of 15° in comparison to GRETINA's ≈2° tracked resolution. The Phoswich Wall ∼1 MeV proton energy resolution is the dominant factor in the $v_I \cos\Theta_I$ uncertainty. Silicon particle detectors can achieve as good as 20 keV resolution if cooled, but are have other technical issues such as fabrication, gain drifts, and radiation hardness. The large energy resolution of the Phoswich Wall is acceptable for quasi-continuum lifetime measurements which aim to measure the GSF which is an average quantity.

Centroid Algorithms

Projections of $v_I \cos\Theta_I$, as in Figure 4.15, have approximately a Gaussian form on top of a constant background. The centroid parameter from a χ^2-minimization of the following

function is used to determine the Doppler shift slopes:

$$y(x) = H \cdot \exp\left[-\frac{(x-\mu)^2/\sigma^2}{2}\right] + B, \tag{4.8}$$

where H is the height of the peak, μ is the centroid, σ is the standard deviation, and B is the constant background. The independent variable x is the detected γ-ray energy and the dependent variable y is the number of counts within the energy bin. There are a few drawbacks to using a χ^2-minimization technique to determine the centroid:

- Lineshape defects from the statistical slowing down process skew the peak toward the rest frame γ-ray emission energy.
- Incomplete charge collection skews the peak toward the low energy side.
- The goodness-of-fit of a Gaussian function is not simple to define, nor does it have a lot of physical significance.

However, the χ^2-minimization is a more stable technique than the use of the arithmetic mean of a γ-ray energy window, defined as,

$$\bar{E}_\gamma = \frac{\sum_{i=1}^{N} n_i E_{\gamma,i}}{\sum_{i=1}^{N} n_i}, \tag{4.9}$$

where $\bar{E}_\gamma$ is the mean γ-ray energy of the projection, N is the number of γ-ray bins in the projection, n_i is the number of counts in bin i, and $E_{\gamma,i}$ is the energy of the γ-ray bin. Unfortunately, Compton coincidences interfere too much to use the arithmetic mean. These events are not correlated with $v_I \cos\Theta_I$ and add a constant background of counts which tends to shift the arithmetic mean toward the center of the window. The Compton coincidence contamination is on the order of 10-15% of the counts in the projection window (c.f. Fig. 4.9). The source of these Compton coincidences was described in previous section (c.f. Fig. 4.7). To address this issue, a fit using the function of Equation (4.8) could get the underlying quantity of background counts. However, experience has demonstrated that eradication of Compton coincidences is extremely sensitive to the width of the γ-ray energy window: fluctuations in counts near window edges tend to make the arithmetic mean fluctuate greatly.

On the other hand, random coincidences have no correlation with $v_I \cos\Theta_I$ and add counts uniformly underneath the γ-ray peak alone and not outside the peak boundaries. For direct population, random coincidence contamination is on the order of 3-4% of counts in the projection window (c.f. Fig. 4.8). Reduction in Doppler shift slope is proportional to fractional contamination and persists regardless of centroid algorithm. This additional sub 5% uncertainty is manageable in the grand scheme of the total Doppler shift slope uncertainty. These random coincidences are only an issue for direct population since the tail of the elastic coincidence curve does not reach past $E_I \approx 3.5$ MeV.

In contrast to random coincidences, indirect population *does* have a correlation with $v_I \cos\Theta_I$. Indirect contamination is on the order of 1-2% of the counts in the projection window (c.f. Fig. 4.8). Similar to random coincidences, indirect contaminants necessarily reduced slope. However, the indirect reduction is smaller in magnitude than the elastic reduction since indirect γ-rays retain a $v_I \cos\Theta_I$ correlated Doppler shift just with a later emission time. Instead of absorbing the indirect contamination into the Doppler shift slope uncertainty, the simulation mechanisms of Section 4.3 account for indirect population. Knowledge of the approximate nuclear recoil velocity makes this treatment possible since the recoil velocity is not very sensitive to the reaction Q-value. The simulation uses the proton energy uncertainty, $\sigma_{T_p} \approx 0.5$ MeV, when assigning particle energy. Simulations allow for an indirect population to be mistaken for a direct population. As mentioned previously, when measuring Doppler shift slopes of quasi-continuum feeding, the indirect population events are no longer contaminants but the object of study. Therefore, it is acceptable that indirect population E_I gates contain many peaks because the GSF is an average quantity.

Finally, the corresponding uncertainty in the $v_I \cos\Theta_I$ value is $\sigma_{v_{Fe},max}$ as described in the previous subsection. This uncertainty is on the conservative side since it suggests that all bin entries have nearly the maximum recoil velocity. In principle, this particular uncertainty is more statistical than systematic because the spread of values is not the result of calibration offset errors, but rather the result of fluctuations in the readings of a measurement apparatus.

Doppler Shift Slope

Now with an established technique for determining the centroid and its uncertainty, a linear regression determines the Doppler shift slopes at various initial nuclear excitation energies. A minimum of 1500 entries in a γ-ray projection window ensures an accurate estimate of the centroid and its uncertainty, otherwise the point is discarded. Figure 4.16 shows results of linear fits to the centroids from direct and quasi-continuum population. Note that roughly 2/3 of the error bars on the points pass through the fit line as expected with statistics-limited uncertainty. Note that Doppler shift is not necessarily linear with $v_I \cos\Theta_I$. There may be peak shape defects associated with the statistical slowing down process. However, some quantification of Doppler shift that has few parameters is needed; a linear fit to the aforementioned centroids performs well.

Since all uncertainties have been kept as near to their statistical limits as possible, the uncertainty returned from the linear regression is assigned to the uncertainty in the Doppler shift slope. Reference [112] explains how uncertainties in the independent and dependent variables propagate into the χ^2-statistic.

Figure 4.17 shows the Doppler shift slopes of the $4_2^+ \rightarrow 4_1^+$ transition at various values of initial excitation energy. Listing from low to high excitation energy, the important features in the Doppler shift slope data are the following:

(a) Direct population has the largest Doppler shift slope, F.

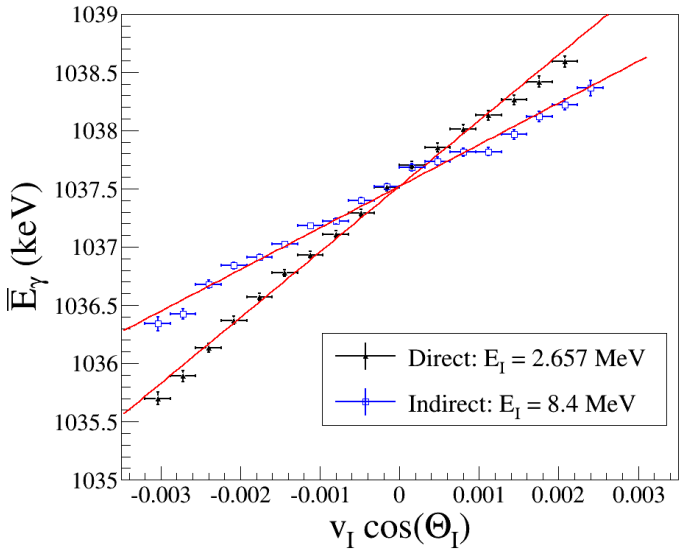

Figure 4.16: Measured γ-ray centroids as a function of $v_I \cos\Theta_I$ for direct and quasi-continuum population of the ^{56}Fe 4_2^+ $E = 3.123$ MeV level. Quasi-continuum feeding results in later γ-ray emission time, additional slowing in the target, a smaller emission velocity, and reduced Doppler shift slope.

(b) A decrease in F just above direct population at $E_I = 4.4$ MeV. Precursor γ-rays add a lot of time when the energy gap between levels is small. The extra time allows the nucleus to slow down more before making the $4_2^+ \rightarrow 4_1^+$ transition. The lower velocity results in a reduced γ-ray emission Doppler shift. This point at $E_I = 4.4$ MeV is not the minimum Doppler shift slope likely due to the anomalous low-energy upbend in the GSF. However, this inflection feature could also be the result of direct population contamination of the indirect excitation energy bin.

(c) An increase in F as E_I goes from 5.4 to 9.4 MeV. According to Equation 3.61, the average dipole transition rate is proportional to E_γ^3. The precursor transition rate increases as the energy gap grows larger. Furthermore, the precursor has a larger number of decay options to non-4_2^+ levels. More decay options increase the total transition rate, reducing the average precursor lifetime. The smaller precursor lifetime results in a larger Doppler shift.

(d) A decrease in F as E_I goes from 9.4 to 11.4 MeV. There are now many decay options to levels above the energy of the 4_2^+, $E = 3.123$ MeV, which potentially decay to the 4_2^+ and emit the $E_\gamma = 1037.8$ keV γ-ray. Multistep precursor transitions add additional time for the nucleus to slow down and reduce Doppler shift. Here the large number of multi-step decay paths outweigh the increasing partial transition rates. In contrast, below $E_I = 9.4$ MeV the precursor decays were mostly one-step due to the fact that the NLD is low in light, even-even, non-deformed nuclei with few valence particles. Note that

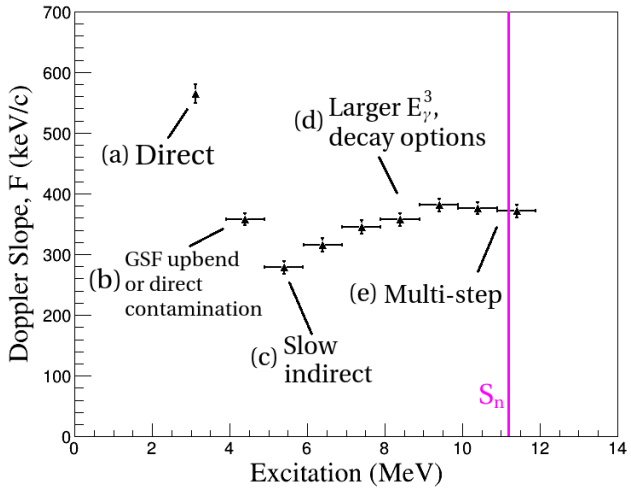

Figure 4.17: Doppler shift slopes of ^{56}Fe $4_2^+ \rightarrow 4_1^+$, $E_\gamma = 1037.8$ keV as a function of initial nuclear excitation energy. The ^{56}Fe neutron separation energy is $S_n = 11.197$ MeV. See text for interpretation of the many features.

this behavior may be different for different values of angular momentum, e.g. if instead the γ-ray emitting level was 2^+ instead of 4^+ since the intrinsic angular momentum distribution governs the number of possible decay paths.

One might expect an increase in F above the neutron separation energy, S_n. Neutron evaporation is a very fast process, on the order of 100 times the amount of time it takes for a nucleon to traverse the nucleus $\sim 10^{-7}$ fs. However, the ground state of ^{55}Fe has a low value of angular momentum, $J = 3/2$ whereas the most likely populated value of J_I is approximately 3–4$\hbar$ according to Figure 3.21. Emitted neutrons would need a lot more energy than is available in the compound nucleus to leave with an orbital component of angular momentum. There is not a sufficient number of counts to measure the Doppler shift slope beyond the ground state energy of ^{55}Fe: $E_1 = 0.411$ MeV, $J_1 = 1/2$; $E_2 = 0.931$ MeV, $J_2 = 5/2$.

Candidates

Up to now the $4_2^+ \rightarrow 4_1^+$ transition has demonstrated quasi-continuum lifetimes. The $4_2^+ \rightarrow 4_1^+$ transition was selected after careful assessment of all possible γ-ray probes because this extended Doppler shift attenuation method does not work well for all transitions. This subsection presents quasi-continuum lifetimes in two other ^{56}Fe γ-ray emissions and attempts to devise good selection criteria for future experiments.

The second useful γ-ray probe is the $2_2^+ \rightarrow 2_1^+$, $E_\gamma = 1810.8$ keV. Figure 4.18a shows that the 2_2^+ level has more direct population contamination than the 4_2^+ because the neighboring levels have higher population intensity. Figure 4.18b shows that the $2_2^+ \rightarrow 2_1^+$ has less statisti-

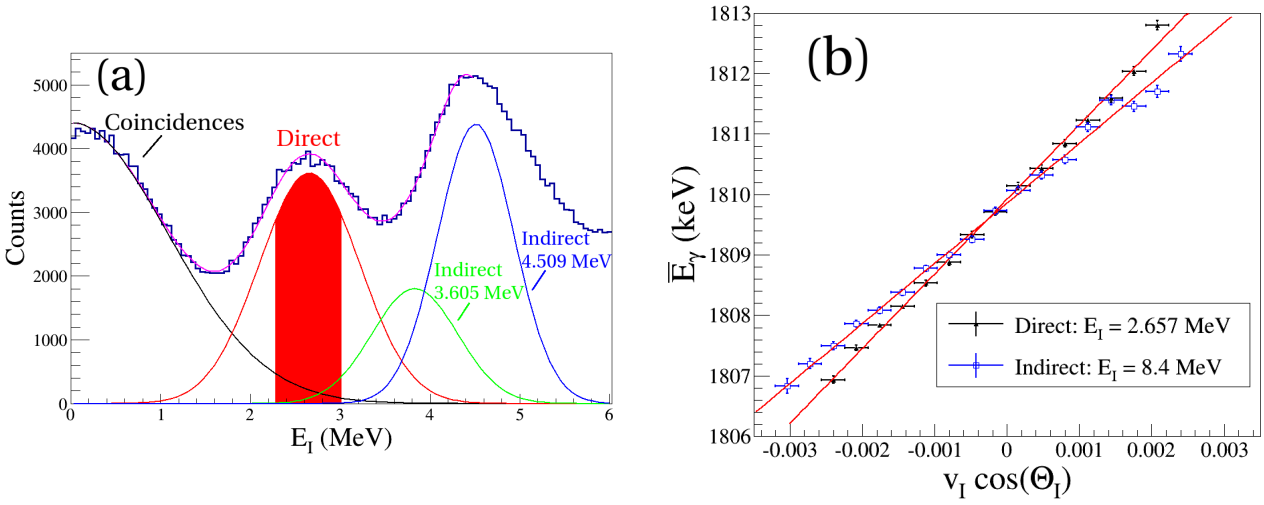

Figure 4.18: ^{56}Fe $2_2^+ \rightarrow 2_1^+$ $E_\gamma = 1810.8$ keV γ-ray probe. (a) Events yielding the $E_\gamma = 1810.8 \pm 12$ keV as a function of nuclear excitation energy. (b) Measured γ-ray centroids as a function of $v_I \cos\Theta_I$ for direct and quasi-continuum population.

cal fluctuation in the γ-ray centroids than the $4_2^+ \rightarrow 4_1^+$ because there are more γ-ray counts. There is a trade-off using this γ-ray transition: the contaminants make it more difficult to measure the direct 2_2^+ lifetime, but the larger number of counts make it easier to measure quasi-continuum Doppler shift slopes. The short lifetime of the 2_2^+ makes the Doppler shift non linear with $v_I \cos\Theta_I$, so only section from -0.002–0.002c is used to determine the Doppler shift slopes for this transition. Figure 4.19 shows the Doppler shift slope of the $2_2^+ \rightarrow 2_1^+$ as a function of initial nuclear excitation energy. The features of the Doppler shift slope of the $2_2^+ \rightarrow 2_1^+$ are similar to that of the $4_2^+ \rightarrow 4_1^+$ with the exception of overall scale and small indirect fluctuations.

The third useful γ-ray probe is the $2_3^+ \rightarrow 2_1^+$, $E_\gamma = 2113.1$ keV. Figure 4.20 shows the Doppler shift slope of this transition as a function of nuclear excitation energy. There are not as many counts for this γ-ray transition since the level is slightly off-yrast. The Doppler shift centroid and excitation contamination plots are omitted for brevity.

For the quasi-continuum lifetime analysis, there were two other γ-ray probes considered but not studied extensively:

1. The $E = 3.370$ MeV, $2_4^+ \rightarrow 2_1^+$, $E_\gamma = 2523.1$ keV. The quasi-continuum does not populate this level as frequently since it is further off-yrast. The γ-ray energy of the transition is slightly outside of the recalibration range of this experiment. Since the level is higher in energy and the level density increases with excitation energy, there are more direct population contaminants.

2. The $E = 4.100$ MeV $4_3^+ \rightarrow 2_1^+$, $E_\gamma = 3253.5$ keV. This γ-ray is also off-yrast and has low statistics. The γ-ray energy is even farther outside the recalibration range. The

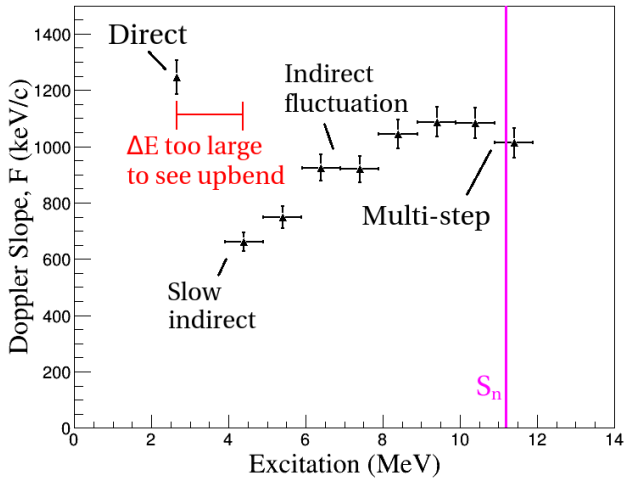

Figure 4.19: Doppler shift slopes of ^{56}Fe $2_2^+ \rightarrow 2_1^+$, $E_\gamma = 1810.8$ keV as a function of initial nuclear excitation energy. Note the increase in scale in the F-axis by a factor of two in comparison to Figure 4.17. The larger number of low-lying $J = 2$ states results in faster transitions and larger Doppler shifts. See text for further explanation of the differences.

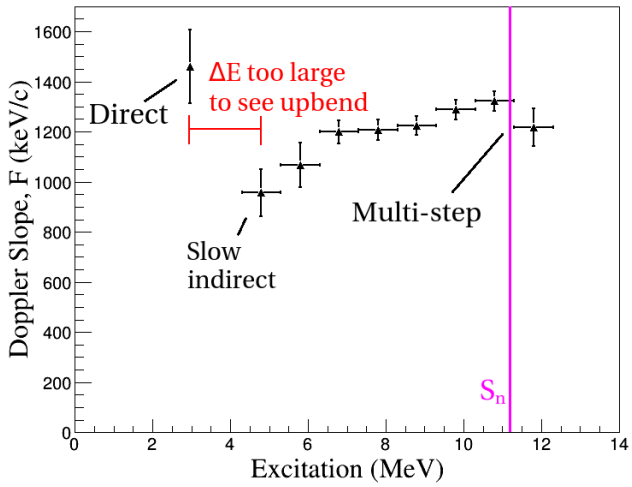

Figure 4.20: Doppler shift slopes of ^{56}Fe $2_3^+ \rightarrow 2_1^+$, $E_\gamma = 2113.1$ keV as a function of initial nuclear excitation energy. See text for further explanation of features.

Table 4.3: ^{56}Co γ-ray transitions used in the untracked relative efficiency calibration.

E_γ (keV)	Relative Intensity
977.4	1.439 ± 0.015
1037.8	13.99 ± 0.1
1175.1	2.279 ± 0.02
1238.3	67.6 ± 0.4
1360.2	4.33 ± 0.04
1771.4	15.69 ± 0.15
1810.8	0.64 ± 0.01
1963.7	0.72 ± 0.015
2015.2	3.08 ± 0.03
2034.8	7.88 ± 0.07
2598.5	17.28 ± 0.15
3009.6	1.049 ± 0.01

direct population has many more contaminants.

The best transitions that probe quasi-continuum lifetimes are usually between the first and second levels of the same angular momentum and parity, $J_2^\Pi \rightarrow J_1^\Pi$. This specification ensures that the γ-ray has sufficient statistics and fast transition rate. This first level off-yrast, J_2^Π, typically has $10 < \tau < 200$ fs, it is strongly populated directly, strongly fed at all E_I, and has a high branching ratio for $J_2^\Pi \rightarrow J_1^\Pi$. It is also important that the $J_2^\Pi \rightarrow J_1^\Pi$ γ-ray has no neighboring peaks at *any* E_I and that $E_\gamma \lesssim 2500$ keV so that it is easy to correct drifts with recalibration.

Low-Lying Population of Angular Momentum

As suggested in the previous subsection, the J_I distribution strongly influences the Doppler shift slopes. The low-lying level populations from a given nuclear excitation energy help determine the J_I distribution. First a tracked relative efficiency curve is needed to normalize the γ-ray peak areas. Figure 4.21 shows an untracked relative efficiency calibration using a ^{56}Co sealed source and the γ-ray transitions from Table 4.3. A simple fit to this untracked relative efficiency curve is

$$\epsilon_{\mathrm{u,r}}(E_\gamma) \propto (E_\gamma + 100)^{-0.660}, \tag{4.10}$$

where E_γ is the γ-ray energy in keV and ϵ is the efficiency in percent. Other authors present similar efficiency curves. Weisshaar *et. al.* [113] suggest the following untracked absolute efficiency curve for GRETINA singles spectra:

$$\epsilon_{\mathrm{u,a}}(E_\gamma) = 4.532(E_\gamma + 100)^{-0.621}. \tag{4.11}$$

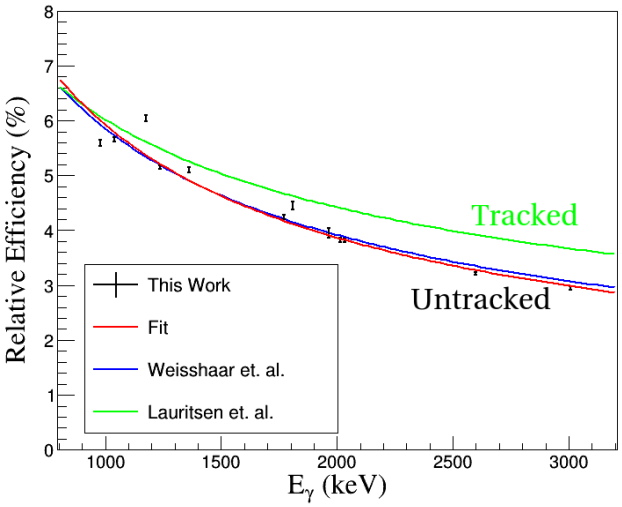

Figure 4.21: Untracked relative efficiency curve for GRETINA singles spectra using a ^{56}Co sealed source and the transitions mentioned in Table 4.3.

Lauritsen *et. al.* [43] present a plot with the following tracked absolute efficiency curve for GRETINA singles spectra:

$$\epsilon_{\mathrm{t,a}}(E_\gamma) = 1.70(E_\gamma + 100)^{-0.477}, \tag{4.12}$$

however the authors did not publish the full equation, so Equation (4.12) is a rough estimate.

The γ-ray peak areas of signature transitions are divided by their corresponding branching ratios and relative efficiencies to determine the low-lying relative populations as a function of E_I. Using the tracked efficiency curve of Equation (4.12), Figure 4.22 shows the low-lying relative populations of the ^{56}Fe levels from Table 4.4. To compare populations for

Table 4.4: ^{56}Fe low-lying levels.

Level	E (keV)	E_γ (keV)	BR (%)
4_1^+	2085.1	1238.3	100.0 ± 2
2_2^+	2657.6	1810.8	97.0 ± 0.3
0_1^+	2941.5	2094.9	100.0 ±
2_3^+	2960.0	2113.1	98.0 ± 2
1_1^+	3120.1	2273.2	95.4 ± 0.7
4_2^+	3123.0	1037.8	99.2 ± 0.4
2_4^+	3370.0	2523.1	85.5 ± 1
6_1^+	3388.6	1304.4	98.7 ± 4
3_1^+	3445.3	1360.2	20.1 ± 0.4
6_2^+	3755.6	1670.8	82.0 ± 5
3_2^+	3856.5	1771.3	91.8 ± 0.3

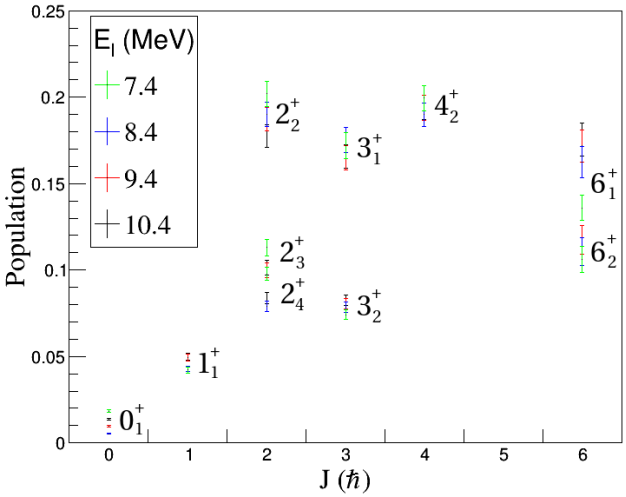

Figure 4.22: Populations of the low-lying levels from Table 4.4 relative to the 4^+_1.

different E_I, the population intensities of this figure are relative to the 4^+_1 population for the corresponding excitation window. Most of the transitions from the initial state are single step; therefore, to give a rough sense of J_I distribution, the abscissa in Figure 4.22 is the level's J value. Visually, the maximum relative population is between 2 and 5$\hbar$, hinting that the mean of the J_I distribution is between those limits.

TALYS estimates the J_I distribution through the use of the optical model, the Distorted Wave Born Approximation, and numerical integration of the Schrodinger equation; Figure 3.21a has already shown these results. This calculation averages the results for proton emission to any angle, but the Phoswich Wall in this experiment detected protons at specified angles. TALYS is currently not able to calculate the J_I distribution for proton emission to a specific angle due to limitations of its numerical Schrodinger equation integration program routine. However, reactions with low particle emission energy are mostly compound in nature, and therefore nearly independent of particle emission angle. Figure 4.23 shows TALYS calculations for differential angle cross section in terms of reaction components. From 7.4–10.4 MeV of nuclear excitation energy, the reaction is primarily compound with a small component of preequilibrium. Therefore, the J_I distribution of Figure 3.21a should work to good approximation for protons emitted at a specified angle. An experimental test confirms this hypothesis: Figure 4.24 shows relative low-lying populations for two different ranges of proton emission angle. If the J_I distribution was strongly correlated with the proton emission angle, the relative populations would disagree by more than just statistical scatter. Overall, the two angle relative populations are in good agreement; there may be some contribution from the preequilibrium reaction mechanism so further refinements of the angular momentum distributions may be necessary.

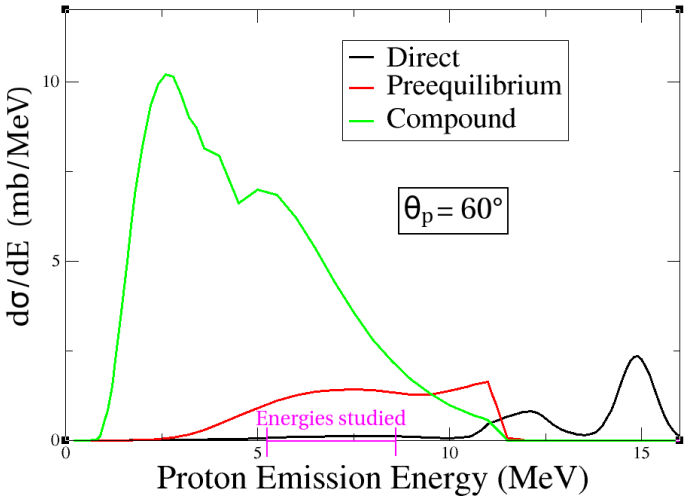

Figure 4.23: Differential cross sections calculated for the three reaction mechanisms. The compound reaction mechanism typically occurs at low particle emission energy and is independent of particle emission angle.

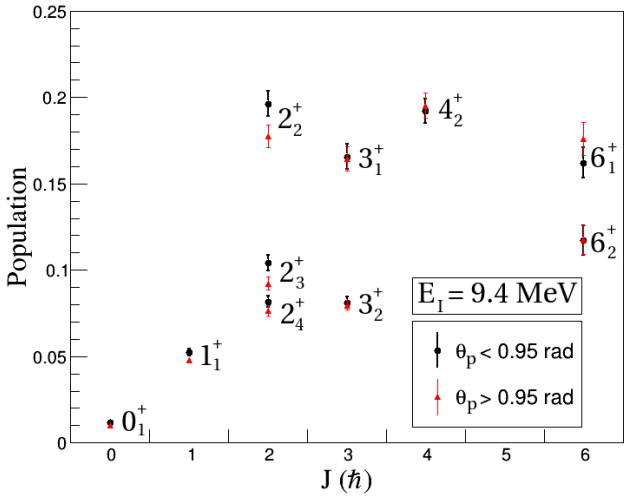

Figure 4.24: Relative low-lying populations of ^{56}Fe levels from excitation $E_I = 9.4 \pm 0.5$ MeV at forward and side proton emission angles. The strong agreement suggests that the reaction mechanism is mostly compound.

4.3 Comparison to Simulation

Chapter 3 briefly covered some of the γ-ray decay simulations, particularly Sections 3.3 through 3.5. That material illustrated the basic concepts but did not fully specify or fine-tune the parameters of the underlying nuclear models. This section aims to pick up where Section 3.5 left off by simulating Doppler shift slopes to determine the absolute magnitude of the Gamma Strength Function.

Models in Use

In the Back Shifted Fermi Gas (BSFG) model, the effective excitation energy is related to nuclear excitation energy by $U = E - E_2$, where the energy backshift E_2 is an empirical parameter related to the pairing energy which accounts for the fact that pairs of nucleons must break before each nucleon can be excited individually. When a level scheme is complete up to 50–100 levels and the level density near the neutron separation energy is known, one can fit the BSFG level density function to determine E_2. Von Egidy and Bucurescu [104, 114] tabulate E_2 from fits to experimental data and report a global phenomenological model:

$$E_2 = -0.477 + 0.5Pa' + 0.442\frac{dS(Z,N)}{dA} \tag{4.13}$$

where

$$Pa' = [M(A+2, Z+1) - 2M(A,Z) + M(A-2, Z-1)]/2 \tag{4.14}$$

is the deuteron pairing energy, $M(A,Z)$ are mass excess values [115], and

$$\frac{dS(Z,N)}{dA} = [S(Z+1, N+1) - S(Z-1, N-1)]/4, \tag{4.15}$$

where

$$S(Z,N) = M_{\text{exp}} - M_{\text{LD}} \tag{4.16}$$

is the difference between the nuclear mass from the liquid drop model and the observed experimental value (c.f. Eq. (3.28)). For ^{56}Fe, the level density at the neutron separation energy is not known experimentally so this global parameterization is used: $Pa' = 2.905$ MeV; $S = -3.731$ MeV; $dS/dA = -0.104$ MeV; and $E_2 = 0.5245$ MeV. TALYS uses a different global phenomenological parameterization:

$$E_2 = \chi\frac{12}{\sqrt{A}} + \delta, \tag{4.17}$$

where

$$\chi = -1, \text{for odd–odd}, \tag{4.18}$$
$$= 0, \text{for odd–even}, \tag{4.19}$$
$$= 1, \text{for even–even}, \tag{4.20}$$

and δ is an adjustable parameter to fit experimental data on a nucleus by nucleus basis. For ^{56}Fe, TALYS defaults to $\chi = 1$, $\delta = -1.24213$ MeV, and $E_2 = 0.3614$ MeV.

In shell model nuclei, the level density parameter "a" depends on the neutron and proton orbital spacings. In a rotational, vibrational, or transition nuclei, a characterizes the average energy spacing between excitation modes of the many independent degrees of freedom. However, the energy spacings in shell model orbitals and other independent degrees of freedom are not necessarily constant with excitation energy. For instance, in shell model nuclei there may be large energy spacings near a closed shell. For this reason, an energy dependent version of a is implemented:

$$a(E) = \tilde{a}\left[1 + W\frac{1 - \exp(-d \cdot U)}{U}\right], \tag{4.21}$$

where $\tilde{a}$ is the asymptotic value of a devoid of shell effects, d is the damping parameter which determines how rapidly shell effects disappear, and

$$W = S(Z, N) - 0.5Pa', \tag{4.22}$$

is the shell correction energy. Von Egidy and Bucurescu [104, 114] use $d = 0.06$ MeV^{-1} and tabulate $\tilde{a}$ from fits to experimental data and report a global phenomenological model:

$$\tilde{a} = A(0.127 - 9.05 \times 10^{-5} \cdot A). \tag{4.23}$$

For ^{56}Fe, the level density at the neutron separation energy is not known experimentally so a global extrapolation is used: $W = -2.279$ MeV and $\tilde{a} = 6.8282$ MeV^{-1}. TALYS uses a different global parameterization:

$$\tilde{a} = \alpha A + \beta A^{2/3}, \tag{4.24}$$

with $\alpha = 0.0722396$, $\beta = 0.195267$, and

$$d = \frac{d_1}{A^{1/3}} + d_2, \tag{4.25}$$

with $d_1 = 0.410289$ and $d_2 = 0$. For ^{56}Fe, TALYS defaults to $d = 0.10724$ MeV^{-1} and $\tilde{a} = 6.90358$ MeV^{-1} and uses the shell correction energy directly from its database: $W = -2.1515$ MeV. Figure 4.25a compares the various values of a for the excitation range of ^{56}Fe in this experiment.

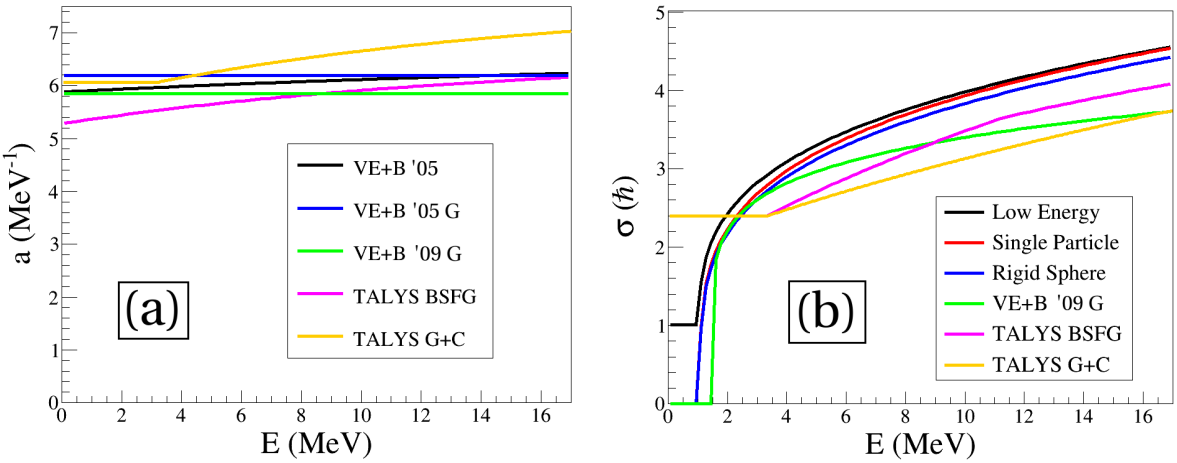

Figure 4.25: Nuclear model parameters. (a) Level density parameter a for ^{56}Fe. Von Egidy and Bucurescu (VE+B '05/'09 G) [104, 114, 105] also report two global constant values of a: 6.1959 and 5.854 MeV^{-1} with corresponding values of energy backshift, E_1: 0.939 and 1.071 MeV. (b) Spin cutoff parameter for ^{56}Fe. For the first three σ models, $a = 5.854$ MeV^{-1} and $E_1 = 1.071$ MeV. The σ models do not agree as well as the a models because it is more difficult to experimentally determine J than E; theoretical guidance is limited. TALYS also provides an interpolation between the Constant Temperature Model and the BSFG known as the Gilbert and Cameron Model (G+C).

The spin cutoff parameter σ represents the width of the angular momentum distribution. Theoretical versions of the energy dependent spin cutoff parameter include a low energy model [116]

$$\sigma^2_{LE} = 0.0146 A^{5/3} \frac{1 + \sqrt{1 + 4aU}}{2a}, \tag{4.26}$$

a single-particle states model [117]

$$\sigma^2_{SP} = 0.1461 \sqrt{aU} A^{2/3}, \tag{4.27}$$

and a rigid sphere model [118]

$$\sigma^2_{RS} = 0.0145 \sqrt{U/a} A^{5/3}. \tag{4.28}$$

Von Egidy and Bucurescu [105] provide a global phenomenological fit:

$$\sigma^2_{VB} = 0.391 A^{0.675} (E - 0.5 \cdot Pa')^{0.312}. \tag{4.29}$$

The spin cutoff parameter for a range of levels in the discrete level sequence is:

$$\sigma^2_d = \frac{1}{3 \sum_{i=N_L}^{N_U} (2J_i + 1)} \sum_{i=N_L}^{N_U} J_i (2J_i + 1), \tag{4.30}$$

where the lowest level in the range, N_L, has energy E_L and the upmost level in the range, N_U, has energy E_U. TALYS defaults to a slightly modified version of the rigid sphere model that retains the asymptotic energy dependence of a:

$$\sigma_T^2 = 0.01389 \frac{A^{5/3}}{\tilde{a}} \sqrt{aU}. \tag{4.31}$$

At low excitation energies, TALYS incorporates an interpolation method to determine σ when $U < 0$ by calculating the distribution of J of the low-lying discrete levels:

$$\begin{aligned} \sigma^2(E) &= \sigma_d^2 && \text{for} \quad 0 \le E \le E_d && (4.32)\\ &= \sigma_d^2 + \frac{E - E_d}{S_n - E_d}[\sigma_T^2(S_n - E_2) - \sigma_d^2] && \text{for} \quad E_d \le E \le S_n && (4.33)\\ &= \sigma_T^2(E) && \text{for} \quad E \ge S_n, && (4.34) \end{aligned}$$

where $E_d = (E_L + E_U)/2$. For ^{56}Fe, TALYS uses $N_L = 3$, $N_U = 20$, $E_L = 2.658$ MeV, $E_U = 4.049$ MeV, $E_d = 3.354$ MeV, $\sigma_d = 2.399$ $\hbar$, and $S_n = 11.197$ MeV. Figure 4.25b compares the σ models for the excitation range of ^{56}Fe in this experiment.

Equation (3.45) provides the energy dependence of the total level density in the Back Shifted Fermi Gas model:

$$\rho_{FG}^{tot}(U) = \frac{1}{12\sqrt{2}\sigma} \frac{\exp\left(2\sqrt{aU}\right)}{a^{1/4}U^{5/4}},$$

where a and σ are energy dependent parameters. Equation (3.46) provides the energy dependence of the total level density in the Constant Temperature Model:

$$\rho_{CT}(E) = \frac{1}{T_0} \exp\left(\frac{E - E_0}{T_0}\right). \tag{4.35}$$

TALYS interpolates between these two models to get the appropriate behaviors at low and high excitation energies. The literature refers to this procedure as the Gilbert and Cameron (G+C) model [119]; Figure 4.25 shows the values of a and σ for this model. Figure 4.26 compares the three most reliable NLD models.

The most difficult simulation inputs are the GSF energy dependence and low energy magnitude. References [120, 121, 111] use the Oslo method to extract data on the *energy dependence* of the GSF in ^{56}Fe for $E_\gamma = 2$–10 MeV. The Oslo method extracts the *sum* of all components of the GSF: E1, M1, E2, and so forth. The Oslo method does *not* independently provide GSF normalization since it relies on branching ratios such that the absolute magnitude of $f(E_\gamma)$ cancels out. The Oslo method typically uses the average total radiative width at the neutron separation energy, $\bar{\Gamma}_\gamma(S_n)$, to normalize its results. However, for ^{56}Fe there is no (n,γ) data to determine $\bar{\Gamma}_\gamma(S_n)$ due to difficulties with ^{55}Fe target fabrication. Algin *et. al.* [111] scale their ^{56}Fe Oslo method data to match the GSF of ^{57}Fe; however,

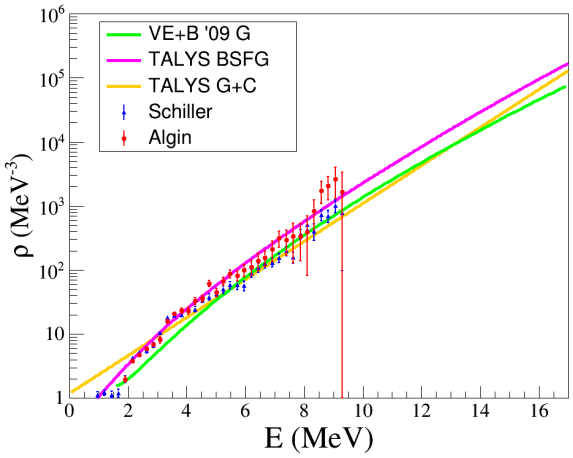

Figure 4.26: Level density models: TALYS Gilbert and Cameron (G+C); TALYS Back Shifted Fermi Gas (BSFG); and Von Egidy and Bucurescu (VE+B '09 G) with global extrapolations of a, E_1, and σ from Reference [105]. Level density data from Schiller *et. al.* [5] and Algin *et.a al.* [111] are shown for reference.

this may be misleading since ^{57}Fe is an odd-A nucleus with higher level density and higher total radiative width at equivalent excitation energies.

The (γ, n) reaction can probe the GSF for γ-ray energies around 20 MeV. Equations (3.58) and (3.60) provide a conversion from (γ, n) cross section to $f(E_\gamma)$. Unfortunately there are no ^{56}Fe(γ,n) experimental data available. Figure 4.27 shows converted (γ,n) data for neighboring nuclei in the $A = 48 - 64$ region [122, 123, 124, 125], but the magnitude and energy dependence of the resultant GSFs vary greatly. Typical GSFs possess a Giant Dipole Resonance (GDR) which is related to the oscillation of neutron and proton clouds. The character of the GDR depends strongly on the geometric shape of the nucleus. Split GDRs are indicative of oscillation modes parallel and perpendicular to the axis of deformation. The mass region $A = 48 - 64$ is transitional between several different nuclear structures: shell model, spherical, and vibrational. As shown in Figure 4.27, the shell model nuclei ^{54}Fe and ^{58}Ni do not have a split GDR, but off-shell ^{55}Mn, ^{59}Co, and ^{64}Zn do have a split GDR. ^{56}Fe is off-shell and likely has a split GDR; however, the problem of low energy magnitude is not resolved since the tails of neighboring split GDRs differ by a factor of 2 near 10 MeV. This variability is troublesome because reaction simulations rely on the GSF all the way down to 0 MeV. Often times, separate (γ,n) experiments of the *same* nucleus report GDR magnitudes differing by a factor of 2–3; the discrepancies indicate the difficult technical nature of (γ,n) experimental work. Even if the magnitude of the GDR at the resonance energy is correct, differing models of the GSF (such as SLO, GLO, EGLO, and KMF; c.f. Sec. 3.4) have low-energy tails which differ by more than an order of magnitude.

The TALYS database provides global values of the GSF which have been adjusted to fit an abundance of low energy nuclear data. Table 4.6 provides the TALYS global interpolation of the giant dipole resonance parameters for ^{56}Fe. Alternatively, a χ^2-minimization on the

Table 4.5: Phenomenological GSF Parameters for ^{56}Fe from Global Fits.

XL	E_{XL} (MeV)	G_{XL} (MeV)	S_{XL} (mb)
E1	18.687	6.976	91.52
M1	10.717	4.000	1.101
E2	16.467	5.438	0.075

Table 4.6: Split GDR fit of ^{55}Mn.

XL	E_{XL} (MeV)	G_{XL} (MeV)	S_{XL} (mb)
E1,A	16.648 ± 0.106	2.603 ± 0.474	18.440 ± 3.508
E1,B	20.790 ± 0.715	16.723 ± 2.828	48.723 ± 3.472

split giant dipole resonance of neighboring ^{55}Mn is used to model the GSF of ^{56}Fe. I use the Generalized Lorentzian (GLO) model for the giant electric dipole resonance and the Standard Lorentzian (SLO) model for the giant magnetic dipole and the giant electric quadrupole resonances. The Oslo method data show an anomalous upbend at low γ-ray energies which is modeled with a soft-pole form:

$$f_{up}(E_\gamma) = C_1 \exp(-C_2 E_\gamma) \tag{4.36}$$

where C_1 and C_2 are experimentally fit parameters. The nature of the upbend is assumed to be M1. Figure 4.27 shows the results of the fit using the function:

$$f(E_\gamma) = f_{E1,A}(E = 8.6\,\text{MeV}, E_\gamma) + f_{E1,B}(E = 8.6\,\text{MeV}, E_\gamma) + f_{M1}(E_\gamma) + f_{up}(E_\gamma) + f_{E2}(E_\gamma)/E_\gamma^2, \tag{4.37}$$

where A and B denote the two oscillation modes of the split GDR. The χ^2-minimization and the global extrapolations show that the normalization of the Oslo method data is too high. Figure 4.28 shows the Oslo method data rescaled down by a factor of 2.2 in order to match the fit. The best fit low energy upbend parameters of Equations (4.36) and (4.37) are $C_1 = 4.8 \times 10^{-7}$ MeV^{-3}, and $C_2 = 3.0$ MeV^{-1}; Table 4.6 shows the best fit split GDR parameters of ^{55}Mn.

The first 32 of the low-levels from the RIPL database [88] up to threshold excitation energy $E_{thres} = 4.510$ MeV are used. A Poisson level spacing distribution distribution is used to generate levels above E_{thres}; equipartition of parity is assumed. A Porter Thomas width fluctuation distribution [78] is used to model the variation in partial transition widths. TALYS is used to determine the E_I and J_I populations similar to Figure 3.17a. Population files corresponding to the VE+B '09 G, TALYS BSFG, and TALYS G+C models will be tested. For ^{56}Fe, the internal conversion coefficients, α, are negligible since Z is low and most decays have high transition energy.

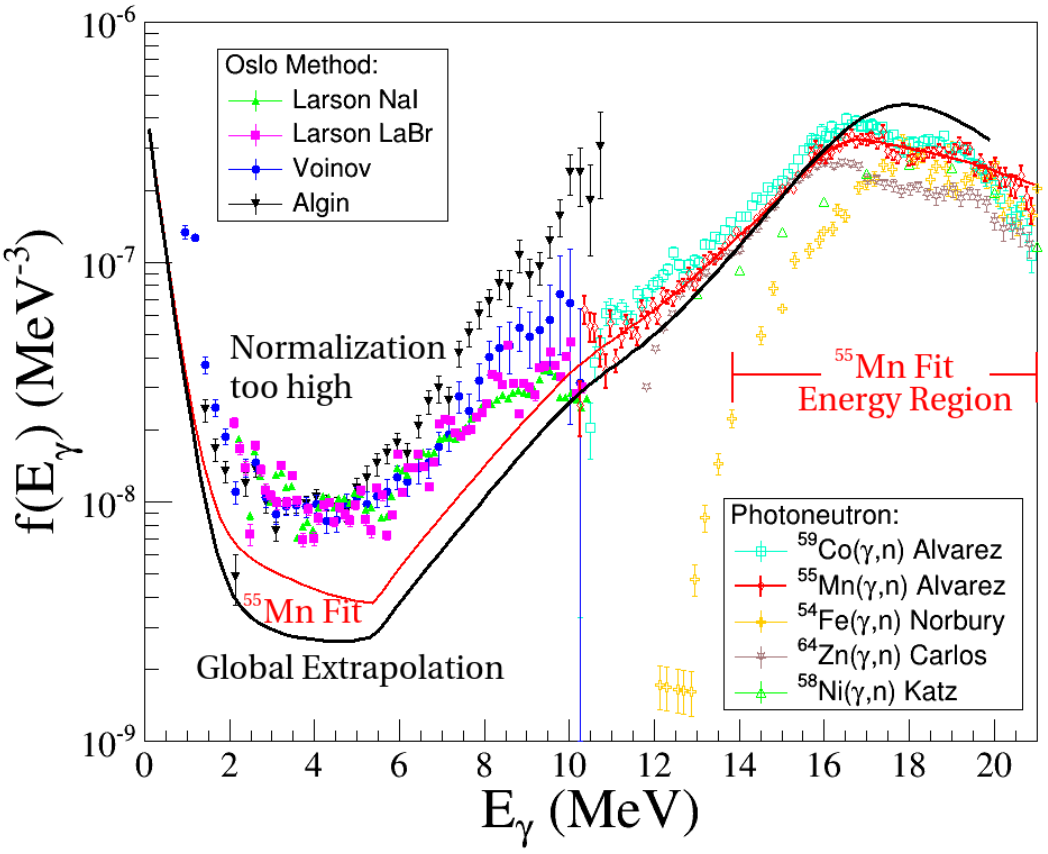

Figure 4.27: Oslo method data of the energy dependence of the GSF from Larsen *et. al.* [120], Voinov *et. al.* [121], and Algin *et. al.* [111]. Photoneutron data, (γ,n), converted into absolute GSF data from Katz *et. al.* [122], Carlos *et. al.* [123], Norbury *et. al.* [124], and Alvarez *et. al.* [125].

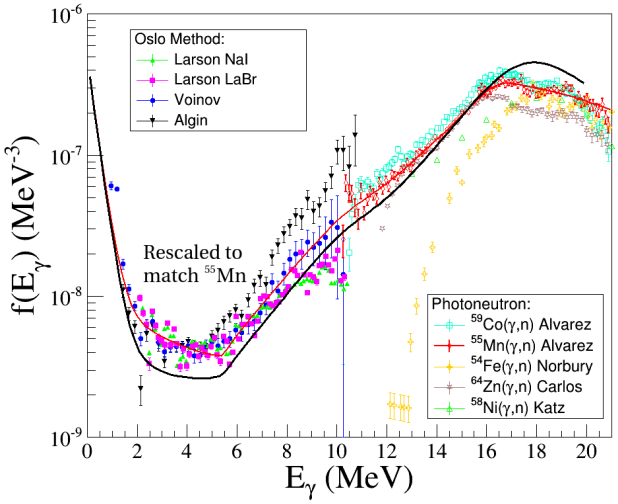

Figure 4.28: Rescaled Oslo Method data by a factor of 2.2 to align with the General Lorentzian split giant dipole resonance of ^{55}Mn.

Angular Momentum Distribution

Accurate assessments of the initial and intrinsic angular momentum distributions are indispensable in order to properly model γ-ray decay. Simulations of low-lying level populations help gauge whether models properly describe these distributions. Figure 4.22 displayed experimental results while the simulations that follow will use the computer program RAINIER [101].

RAINIER uses the "realization" concept to replicate the chaotic nature of nuclei. A nuclear realization is one ensemble of unchanging, yet randomly distributed set of level spacings and transition widths. In reality, each nucleus of a given isotope has an identical set of spacings and widths and is effectively a single realization. Unfortunately, the nuclear physics community can only build a complete level scheme up to a certain energy, above which experimental methods become unreliable. RAINIER generates several unique realizations of the unknown portion of the level scheme to demonstrate how statistical fluctuations influence observables. Furthermore, reactions populate levels psuedo-randomly which tends to further intensify statistical fluctuations. RAINIER is currently the only code available that can fully implement the extreme statistical model in reactions that populate and decay a wide range of E_I, J_I, and Π_I.

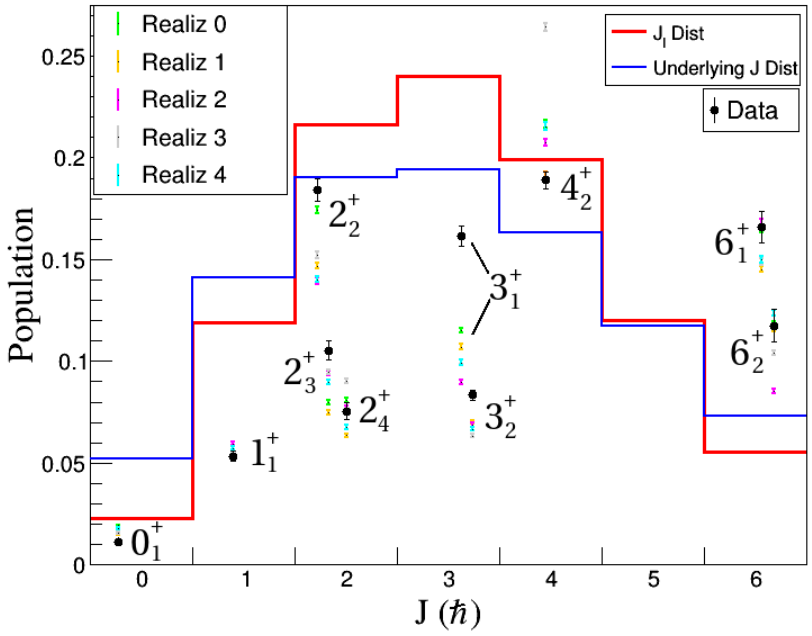

Figure 4.29: A comparison of simulation and experimental measurements of relative low-lying level populations after 16 MeV ^{56}Fe(p,p') with $E_I = 9.4 \pm 1$ MeV. These simulations use the TALYS G+C model to generate several nuclear realizations.

Figure 4.29 shows RAINIER simulations of low-lying level populations for multiple nuclear realizations. The agreement between simulation and experiment is promising: six

experimental points are within the realization spread, two are just outside, and the remaining two are off by a factor of 1.5 or less. The realizations alone have approximately 15–25% spread for a single low-lying population.

Low-lying populations depend not only on the angular momentum distribution, but also on the nuclear realization since the level density in ^{56}Fe is so sparse. There could be a realization that brings the simulation into perfect agreement with the data. However, it is more likely that other factors can better explain the lingering differences:

- Systematic experimental calibration error. The γ-ray tracking efficiency is not known perfectly and likely depends on γ-ray multiplicity. In multi-detector systems, γ-ray peak areas are hard to quantify since the independent gains drift at different rates. Doppler shifts further broaden the peak resolution depending on level lifetime and cascade time.

- Pre-equilibrium contamination. Employment of the TALYS J_I distribution assumed that the reaction was fully compound and did not depend on the fact that the Phoswich Wall detected protons at a specific angle. However, Figure 4.24 showed evidence that the populations of the 2_2^+ and 2_3^+ levels depend slightly on outgoing angle of the proton and Figure 4.23 showed that the preequilibrium differential cross section was non-trivial. Direct and preequilibrium reactions selectively populate J_I by ejectile angle.

- Missing physics. Collective behavior is not always well-characterized by extreme statistical models. Reaction dependent quantum numbers could be involved in the population of levels in the quasi-continuum. Rotation, deformation, vibration, and shell model phenomenon may be present at high excitation energies.

Gamma Strength Magnitude

To reproduce the experimental data in Figures 4.17, 4.19, and 4.20, TALYS, RAINIER, and SRIM plus the TALYS G+C, TALYS BSFG, and VE+B '09 G nuclear models are used to simulate Doppler shift slopes of γ-ray transitions as a function of initial nuclear excitation energy. Simulated slopes are analyzed with same analysis code as the data (c.f. Sec. 4.2). Note that Doppler shift slope simulations are not possible without the Monte Carlo method. Since the nucleus has a finite recoil slowing down time, the tail end of the γ-ray emission time distribution does not contribute Doppler shift. Deterministic codes such as TALYS or EMPIRE could be modified to output lifetimes and average cascade time, but cannot generate a statistical distribution, nor can they see the effect of variable realizations. RAINIER steps in at right time to provide the appropriate statistical capabilities.

Figure 4.30 compares experimental data to simulated Doppler shift slopes using the TALYS G+C model and the experimental fit of the GSF in Figure 4.28. The Doppler shift slope data of the $2_3^+ \rightarrow 2_1^+$ transition has been omitted due to suspected issues with the database value of the of 2_3^+ direct lifetime. These Doppler shift slope simulations fit the data better than the low-lying populations of Figure 4.29 which are likely hampered by erratic

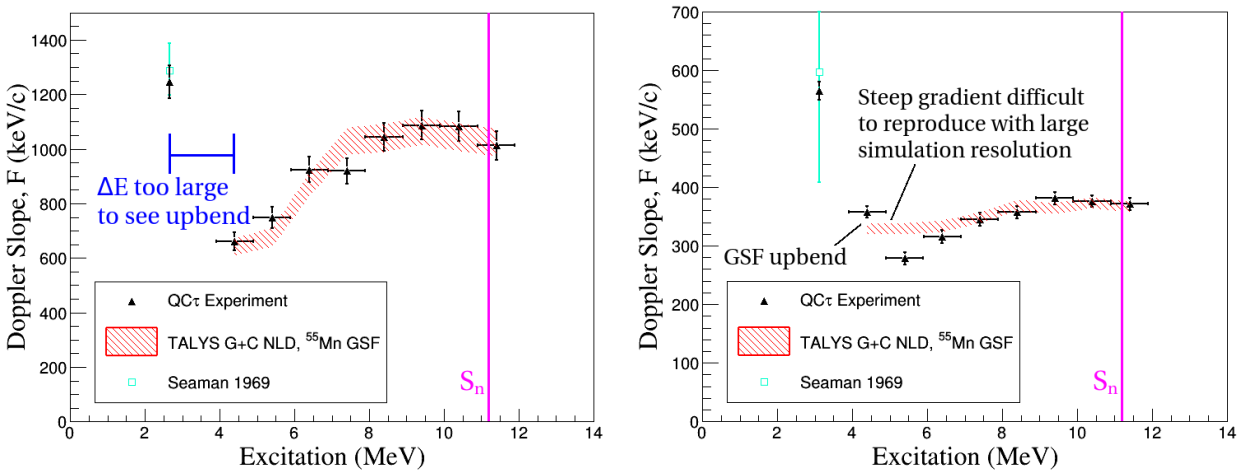

(a) $2_2^+ \rightarrow 2_1^+$ (b) $4_2^+ \rightarrow 4_1^+$

Figure 4.30: Doppler shift slopes as a function of excitation energy. Experimental data is compared to simulations using the TALYS G+C NLD model and the experimental fit of the GSF in Figure 4.28. Seaman *et. al.* in 1969 [126] measured the direct lifetime of ^{56}Fe; the values have been translated into Doppler shift slopes using $v_I \cos\Theta_I$ as the independent variable. The RAINIER simulation has difficulty reproducing the low-energy upbend in the GSF due to the steep gradient of the GSF and the large excitation energy resolution.

GRETINA detection efficiencies. Furthermore, low-lying populations are more sensitive to the more uncertain J_I distribution, whereas Doppler shift slopes are more sensitive to the NLD and GSF input parameters which have experimental support.

Figure 4.31 explores the statistical variations in the simulated Doppler shift slopes by testing three nuclear realizations and three NLD models: TALYS G+C, TALYS BSFG, and VE+B '09 G. Figure 4.31 also explores three normalizations of the GSF by scaling the ^{55}Mn GDR fit of Figure 4.28 by factors of 1.0, 2.2, and 0.3. The simulations show the following trends:

- The realization psuedo-random number generator parameters slightly affect the simulation's Doppler shift slope outcome. Lifetime is inversely proportional to the sum of the many partial exit channel widths. While individual partial widths fluctuate greatly, the central limit theorem dictates that their sum fluctuates much less. However, slight fluctuations remain since the level density in ^{56}Fe is sparse. The low excitation Doppler shift slopes have the most variability since the number of decay paths are few.

- Since the level densities and angular momentum distributions differ between models, the TALYS G+C, TALYS BSFG, and VE+B '09 G realizations are naturally distinct from one another. The TALYS G+C is likely the best fit to the Doppler shift slope data because this model is the default in TALYS and the global parameterization of

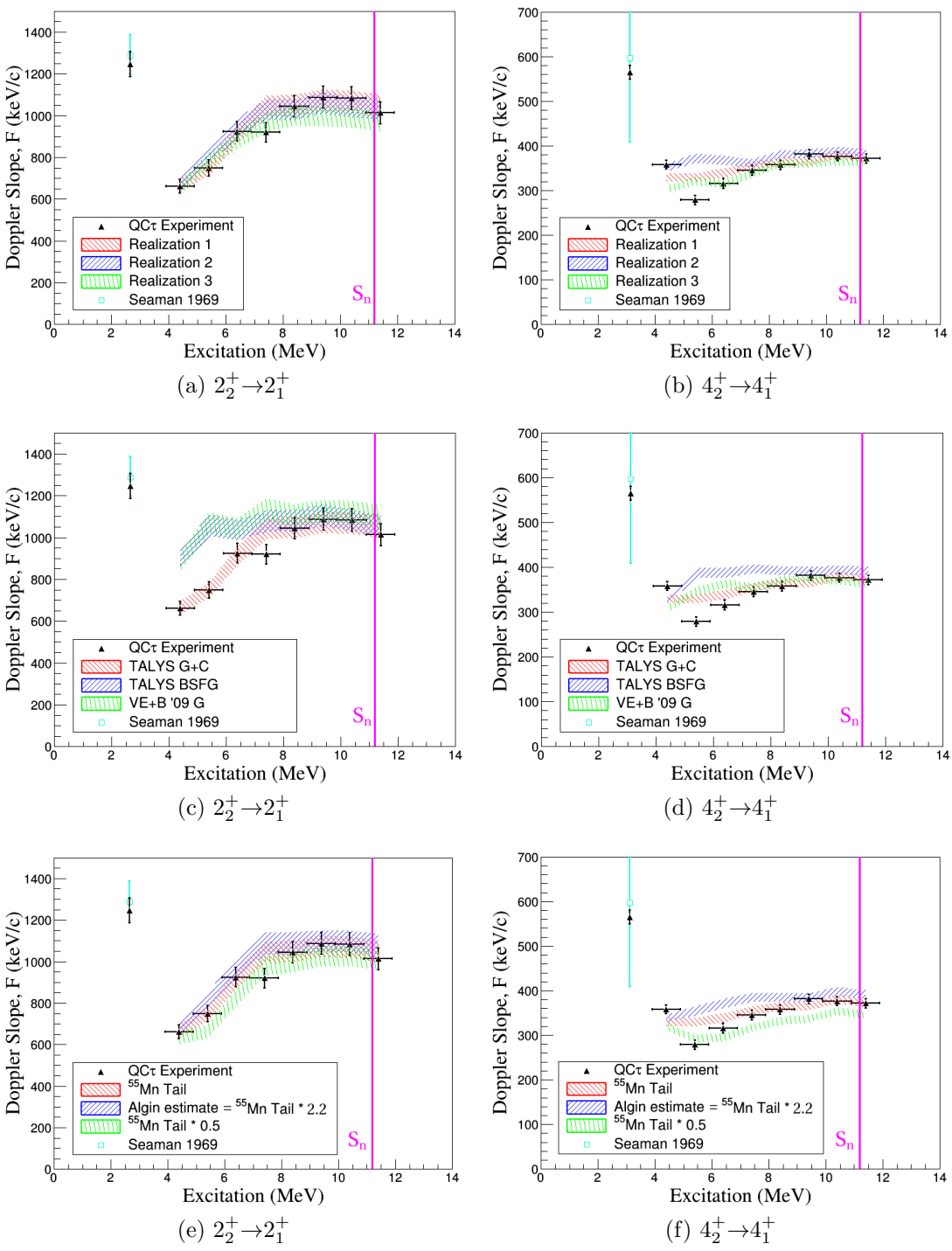

(a) $2_2^+ \rightarrow 2_1^+$ (b) $4_2^+ \rightarrow 4_1^+$

(c) $2_2^+ \rightarrow 2_1^+$ (d) $4_2^+ \rightarrow 4_1^+$

(e) $2_2^+ \rightarrow 2_1^+$ (f) $4_2^+ \rightarrow 4_1^+$

Figure 4.31: Doppler shift slopes as a function of excitation energy. Top: experimental data is compared to three realizations of the TALYS G+C NLD simulation model. Middle: experimental data is compared to simulations using the TALYS G+C, TALYS BSFG, and VE+B '09 G models of NLD. Bottom: experimental data is compared to three normalizations of the GSF. See text for interpretation.

Gilbert and Cameron NLD has been fit to an abundance of experimental data. Additionally, the TALYS G+C model uses interpolated values of the spin cutoff parameter determined from low-lying levels whereas the other models are more dependent on theory. The models align at high excitation energy.

- The simulations support the normalization of Figure 4.28 that uses the Generalized Lorentzian fit to the split GDR of ^{55}Mn with an extrapolation to the low energy tail. The estimate of Algin *et. al.* is factor of 2.2 higher in scale and gives Doppler shift slopes that are systematically high. A reduction in scale by a factor of 0.5 yields Doppler shift slopes that are systematically low in scale.

The low-lying population simulations take approximately 10 minutes each, but the Doppler shift slope simulations take approximately 10 hours because of the need to simulate many γ-ray emission angles and nuclear recoil velocities; therefore, the number of simulations in this work are limited. There could be more model fine tuning or introduction of new physics, but rapid testing would require a slight rework of RAINIER to harmonize with ROOT's PROOF parallel processing framework so as to be set up on a computer cluster. The experimental data, sort code, and simulation package can be made available for anyone up to the task.

The average total radiative width at the neutron separation energy, $\bar{\Gamma}_\gamma(S_n)$, is often an important component of the GSF normalization. Neutron time-of-flight experiments determine $\bar{\Gamma}_\gamma(S_n)$ by averaging the resonance widths of s-wave neutron capture. The $\bar{\Gamma}_\gamma(S_n)$ average is taken over levels with $E \gtrsim S_n$ and $J = J_{g.s.,N-1} \pm 1/2$, where $J_{g.s.,N-1}$ is the ground state angular momentum of the target nucleus. Table 4.7 shows the known $\bar{\Gamma}_\gamma(S_n)$ of nuclei in the $Z = 24 - 28$ region. The values of $\bar{\Gamma}_\gamma(S_n)$ in this region vary greatly due to differing values of S_n; the number of levels below S_n in the sum of partial widths depends on an exponentially increasing value of NLD with excitation energy.

For ^{56}Fe there is no (n,γ) data available to determine $\bar{\Gamma}_\gamma(S_n)$ since ^{55}Fe is radioactive. Instead, the best fit simulation model determines $\bar{\Gamma}_\gamma(S_n)$. Doppler shift slope data and simulation can arrive at the value of $\bar{\Gamma}_\gamma(S_n)$ only once the NLD and GSF are known; this order of events is the reverse of the Oslo method in which the value of $\bar{\Gamma}_\gamma(S_n)$ helps normalize NLD and GSF. Since $J_{g.s.,^{55}Fe} = 3/2$, the ^{56}Fe levels are averaged over $J = 1, 2$; the average is taken over the excitation range $E = 11.197$–11.297 MeV. Table 4.8 shows the $\bar{\Gamma}_\gamma(S_n)$ value determined for ^{56}Fe from experimental Doppler shift slopes of this work. The uncertainty in the ^{56}Fe $\bar{\Gamma}_\gamma(S_n)$ value is a combination of Porter-Thomas width fluctuations, statistical variation of separate simulated nuclear realizations, and a systematic 1σ overlap of uncertainties in the Doppler shift slopes from data and simulation. Assuming the capture state could have angular momentum of either $J = 1, 2$, the combined uncertainties yield $\bar{\Gamma}_\gamma(S_n) = 1100 \pm 500$ meV. Algin *et. al.* [111] estimate $\bar{\Gamma}_\gamma(S_n) = 2300 \pm 1200$ meV from global extrapolation systematics, but they do not specify in the text exactly how they arrive at this normalization. The largest $\bar{\Gamma}_\gamma(S_n)$ uncertainty in any nucleus with any measurement technique is the variation of total width. Neighboring levels near S_n can have vastly differing total width due to Porter-Thomas fluctuations of partial widths. If there were an infinite

Table 4.7: Average Total Radiative Width at the Neutron Separation Energy, $\bar{\Gamma}_\gamma(S_n)$ from the RIPL database [88].

Nucleus ${}^{A}_{Z}$X	$J_{g.s.,N-1}$	S_n (MeV)	$\bar{\Gamma}_\gamma(S_n)$ (meV)
${}^{51}_{24}$Cr	0	9.261	1100(400)
${}^{53}_{24}$Cr	0	7.939	2000(500)
${}^{54}_{24}$Cr	3/2	9.719	1400(500)
${}^{55}_{24}$Cr	0	6.246	1500(500)
${}^{56}_{25}$Mn	5/2	7.270	750(150)
${}^{55}_{26}$Fe	0	9.298	1600(700)
${}^{57}_{26}$Fe	0	7.646	920(410)
${}^{58}_{26}$Fe	1/2	10.044	1850(500)
${}^{59}_{26}$Fe	0	6.581	1130(110)
${}^{60}_{27}$Co	7/2	7.492	540(50)
${}^{59}_{28}$Ni	0	8.999	2030(800)
${}^{60}_{28}$Ni	3/2	11.388	2200(700)
${}^{61}_{28}$Ni	0	7.820	1120(200)
${}^{62}_{28}$Ni	3/2	10.596	2000(500)
${}^{63}_{28}$Ni	0	6.838	910(270)
${}^{65}_{28}$Ni	0	6.098	1400(700)

Table 4.8: $\bar{\Gamma}_\gamma(S_n)$ for ^{56}Fe determined with Doppler shift slope measurements and simulated comparisons. Width fluctuations (Wid.), experimental systematic error (Sys.), and realization variability (Real.) contribute separate uncertainties. Since $J_{g.s.,^{55}Fe} = 3/2$, the capture state angular momentum could be $J = 1, 2$.

J	$\bar{\Gamma}_\gamma(S_n)$ (meV)	Wid.	Sys.	Real.
1	1300	±700	±400	±70
2	960	±190	±300	±30
1,2	1100	±400	±300	±40

number of possible partial decay paths, the uncertainty in $\bar{\Gamma}_\gamma(S_n)$ would be non-existant; however, the number of levels with lower energy is not large enough for the central limit theorem to smooth out the fluctuations.

Chapter 5

Conclusions

5.1 Considerations

This section reviews the lessons learned and summarizes the optimal characteristics of the quasi-continuum lifetime analysis. This section condenses the relevant information that is necessary to perform a good experiment and lists certain pitfalls to avoid.

In this work I have outlined the experimental setups of ATLAS, GRETINA, and the Phoswich Wall for the ^{56}Fe(p,p'γ) reaction. The theory surrounding nuclear structure, reactions, and interactions with matter was instrumental to the understanding of the many features in the data analysis. The deficit in knowledge about the Gamma Strength Function inspired a new experimental method to measure its absolute magnitude using quasi-continuum lifetimes. Weaknesses of this method include the following:

- It requires sophisticated equipment that is capable of high energy and angle resolution. This requirement is achievable with highly segmented detectors which are in short supply. These detectors require a multitude of tedious gain calibrations and event-by-event drift corrections to maintain high energy resolution.

- The method requires independent simulation of recoil trajectories. The Stopping Range of Ions in Matter (SRIM) code provides sufficient accuracy only for a specific range of target atom species, incident ion species, and initial recoil kinetic energies. The target must be thin enough so as not to degrade the energies of the incident beam or outgoing ejectiles. The target must be thick enough to generate a high reaction rate and minimize recoil escape.

- The method requires independent simulation of γ-ray cascades. The Randomizer of Assorted Initial Nuclear Intensities and Emissions of Radiation (RAINIER) code provides this capability, but has long run times. It is difficult to incorporate NLD and GSF model uncertainties into simulation.

- This method requires independent simulation of the initial angular momentum distribution of the residual nucleus. The code TALYS provides good estimates of this distribution, but is limited in terms of ejectile emission angle.

- This method requires some knowledge of the NLD and energy dependence of the GSF. Techniques such as discrete level counting, the Oslo method, photoneutron, and neutron capture reactions provide a good starting point for these two functions. The spin cutoff parameter is an important model input, but knowledge on this topic is narrow.

- Not all nuclei have γ-ray probes of optimal transition rate. The recoil slowing down time needs to be on the same order as the lifetime of the parent level. These lifetimes need to be known accurately or measurable with the experimental setup. The uncertainties of many database lifetimes are on the order of 10–50%.

- The NLD must be high enough to average level spacing and width fluctuations. The code RAINIER can estimate these fluctuations before the experiment occurs or before data from a past experiment is reanalyzed using this method.

Highly segmented γ-ray detection is achievable with GRETINA and AGATA and perhaps other high purity germanium arrays. Gamma-ray energy tracking is not a requirement; overall uncertainty of this method is not at the limit of sub-centimeter γ-ray position resolution. Simulations are only an obstacle because they are tedious and the SRIM and TALYS softwares are not set up by default to provide the necessary output in a convenient manner. In comparison, understanding theoretical fits to cross section data requires the same complex reactions simulations; hence the nuclear physics community is familiar with such techniques. The prerequisite NLD and GSF knowledge need not be precise; we can fine tune models to match the quasi-continuum lifetime data.

Some of the strengths of this method include the following:

- The method does not require precise counting efficiencies. The low-lying level population data were not critical to the understanding of the Doppler shift slope data. The Doppler shift slope data are more sensitive to NLD and GSF, whereas the low-lying populations are more sensitive to the energy dependence of the spin cutoff parameter. Doppler shift slopes are primarily governed by the decay time of one-step transitions, whereas low-lying level populations are governed by fractional branching to all intermediate levels.

- This method can probe the low energy magnitude of the GSF. In contrast, (n,γ) and (γ,n) reactions only probe the GSF at high energies, near S_n and 20 MeV, respectively.

- This method can use multiple γ-ray probes in the same data set to verify measurements. In this work, the $2_2^+ \rightarrow 2_1^+$ and the $4_2^+ \rightarrow 4_1^+$ yielded comparable results.

The differences in nuclei, reactions, and detection equipment uniquely affect the quality of the quasi-continuum lifetime method. Some of the fortunate circumstances in this work include the following:

- The particle and γ-ray *angle* resolution was excellent. GRETINA has 1152 segmentation and the Phoswich Wall has 256 segmentation.
- The γ-ray *energy* resolution was excellent. High purity germanium crystals are a requirement for this procedure.
- The slowing down time of recoiling ^{56}Fe was on the order of the cascade times and the direct lifetimes of several low-lying transitions. It is high recommended that the low-lying transitions of interest are compared to stopping simulations before experimental execution.
- There was minimal recoil leakage from the target. The beam energy, target thickness, and recoil angles were well matched. In reality recoil leakage is not detrimental—one can easily incorporate target thickness into Monte Carlo simulations. Such a correction was estimated to be unnecessary. A high density stopper is not required if the code properly accounts for leakage.
- There exists a lot of good Oslo method data on the energy dependence of the GSF for ^{56}Fe. ^{56}Fe was the first nucleus for which the low energy upbend in the GSF was observed and there were many experiments that provided further confirmation and exploration.

All of these points serve to make this particular experiment well suited to obtain a good result. If other datasets lack many of these benefits, quasi-continuum lifetime analysis may be more difficult. However, the experiment in this work also had many downfalls. Some of the unfortunate circumstances include the following:

- The biggest frustration was the Phoswich Wall 1 MeV proton energy resolution. Many problems can be fixed with cooled, or even uncooled, silicon detectors. The ejectile energy resolution is the biggest source of systematic uncertainty since the outgoing particle determines the recoil angle and excitation energy of the residual nucleus.
- There were only 80 hours of beam time. A lot of the γ-ray peaks are statistics limited. Many γ-ray probes that have a lot of potential for their nuclear properties were unanalyzed.
- ^{56}Fe has a low level density. Partial width and level spacing distributions cause a lot of lifetime fluctuation. A nucleus with a larger level density such as that with an odd number of neutrons and protons or a larger mass altogether will have more possible decay paths and smaller fluctuations of total width.

- There was not much guiding (n,γ) and (γ,n) data. NLD extrapolations did have a normalization point at the neutron binding energy. The starting estimate of the GSF absolute magnitude relied on extrapolations of neighboring nuclei.

If some of these shortcomings are fixed in other experiments and datasets, the quasi-continuum lifetime analysis will perhaps be much easier.

To reiterate Section 4.2, the optimal γ-ray probe has the following properties:

- The best transition stems from the first level off yrast, J_2^{Π}, which typically has a decent transition rate, $10 < \tau < 200$ fs, it is strongly populated directly, strongly fed at all E_I.
- The γ-ray probe should have no neighboring peaks at *any* E_I. Neighboring peaks may interfere or complicate algorithms that determine the Doppler shifted γ-ray peak centroid.
- The γ-ray transition energy is $E_\gamma \lesssim 2500$ keV so that it is easy to correct drifts with recalibration. Higher energy γ-ray peaks drift proportional to their energy.

If there are more statistics, the quasi-continuum lifetime analysis may be possible with additional γ-ray probes that do not satisfy these criteria.

5.2 Validation

This section uses discrete lifetimes to validate the normalization of the Gamma Strength Function determined in this work. Other methods of validation are suggested such as photoneutron and neutron capture reactions.

Thanks to the suggestion of Guttormsen *et. al.* [127], many direct lifetimes of 1^+ and 1^- states are available in ^{56}Fe from the photoelastic data of Bauwens *et. al.* [128] and Shizuma *et. al.* [129]. These experiments use dipole transitions to bound states by means of the nuclear resonance fluorescence method. The photon scattering cross section integrated over a single resonance is proportional to $\Gamma_0\Gamma_i/\Gamma$, where Γ_0, Γ_i, and Γ represent the ground state decay width, the decay width to an intermediate level, and the total decay width of the considered excited state, respectively. For elastic transitions where the excited state decays back to the ground state ($\Gamma_i = \Gamma_0$), the observed cross section is proportional to Γ_0^2/Γ. If the total decay width is known, one can determine Γ, and with Γ one can determine lifetime. Figure 5.1 plots these derived lifetimes.

Similar to the average total radiative widths, RAINIER can determine lifetimes as a function of angular momentum, parity, and excitation energy. Using the NLD and GSF parameters that best fit the quasi-continuum lifetime Doppler shift slope data, Figure 5.1 shows the simulated lifetimes of 1^+ and 1^- states in ^{56}Fe as a function of excitation energy. The scatter and magnitude of the simulated lifetimes match experimental data well lending

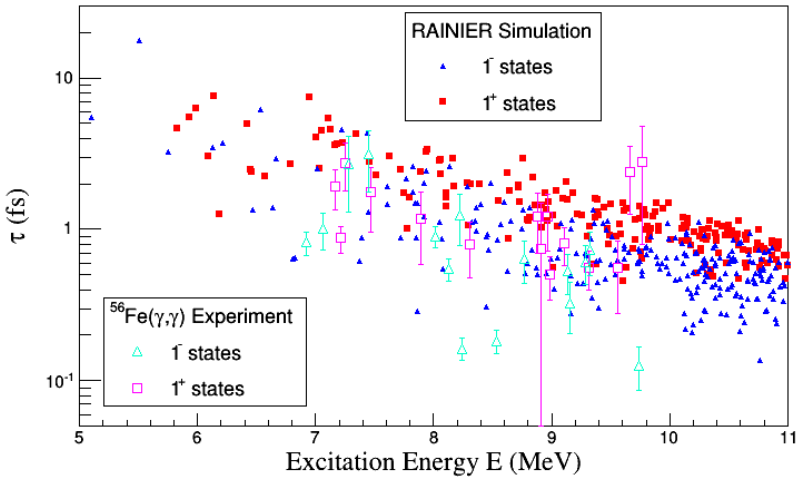

Figure 5.1: A comparison of ^{56}Fe lifetimes. Experimental points are derived from photoelastic data of Bauwens *et. al.* [128] and Shizuma *et. al.* [129]. RAINIER simulation points are calculated from the NLD and GSF parameters that best fit the quasi-continuum lifetime data in this work.

support to the measurements from this work and the work of both Bauwens and Shizuma. The RAINIER simulation does not include NLD or GSF model uncertainties; the scatter in lifetime is the result of width and level spacing fluctuations. The width fluctuations and large uncertainties in experimental lifetimes may be too large to determine the normalization of the GSF without other supporting measurements.

In order to fully validate this method it may be necessary to use different nuclei. Neutron capture experiments provide the best average total radiative width at the neutron separation energy. Since (n,γ) experiments catalog many total widths, both the average, $\bar{\Gamma}_\gamma(S_n)$, and the fluctuation, $\sqrt{\left\langle(\Gamma_\gamma - \bar{\Gamma}_\gamma)^2\right\rangle}$, are valuable validation tools. A high purity target is critical to the success of an (n,γ) experiment. A quasi-continuum lifetime experiment can utilize the same high purity target to study the same $N+1$ nucleus via the (d,p) reaction. In fact, a high purity target is not critical to the success of a quasi-continuum lifetime experiment since signature γ-rays indicate the participating nucleus. It might be possible to find an incident projectile and beam energy that is amenable to the quasi-continuum lifetime analysis for two or more nuclei provided that the particle detector can distinguish between ejectile species. Furthermore, quasi-continuum lifetime analysis may be possible with radioactive targets; one can easily veto events where the signature γ-ray is absent.

Photoneutron data would help guide the fitting procedures of the GSF. Split giant dipole resonances vary strongly as seen in Figure 4.28. The GSF derived from photoneutron cross section data of ^{59}Co, ^{55}Mn, ^{64}Zn, and ^{58}Ni do not align perfectly and it is challenging to extrapolate the magnitude of both peaks and both centroids in the split resonance. The neighboring nuclei of ^{56}Fe that have (γ,n) data are either odd-A or are on a closed neutron or proton shell. Shell model closures strongly influence the GSF and pairing might have

some effect. Similar to ^{56}Fe, the nucleus ^{54}Cr has one valence neutron pair off a shell closure and is not on a closed proton shell. The cross sections of ^{56}Fe(γ,n) and ^{54}Cr(γ,n) would help guide the low energy behavior of the GSF in ^{56}Fe. The isotopic abundances of ^{54}Cr and ^{56}Fe are 2.4% and 91.2%, respectively; therefore, target fabrication is feasible.

The nucleus ^{57}Fe may be a good candidate to attempt a full validation. There is a lot of available data on ^{56}Fe(n,γ)^{57}Fe, the NLD and GSF has been measured many times via the Oslo method [5, 111, 121], and the level scheme is nearly complete up to the neutron separation energy [130]. The lifetimes of the $1/2^-_2$, $3/2^-_3$, and $3/2^-_4$ are in the $10 < \tau < 100$ fs range and emit γ-rays within a good energy recalibration range. There may be a possible issue with γ-ray doublets separated by 14.41 keV due to the low first excited state energy, but this should not be a problem so long as the nuclear recoil velocity is kept low.

5.3 Impact on Cross Sections

This section uses the Gamma Strength Function determined in this work to simulate the neutron capture cross section of ^{55}Fe. The quasi-continuum lifetime method can be used to determine the Gamma Strength Function of many other important nuclei for a wide range of applications.

Section 4.3 used quasi-continuum lifetime measurements to estimate the ^{56}Fe average total radiative width at the neutron binding energy, $\bar{\Gamma}_\gamma(S_n)$; Table 4.8 showed these results. Perhaps the most useful application of $\bar{\Gamma}_\gamma(S_n)$ is its importance to neutron capture cross sections. The ^{55}Fe(n,γ) capture reaction may have narrow practical application, but this proof-of-concept shows what one can expect quantitatively in more influential nuclei. Figure 5.2 shows ^{55}Fe(n,γ) cross sections using the $\bar{\Gamma}_\gamma(S_n)$ values determined from this work.

One application of the ^{55}Fe(n,γ) cross section is astrophysical nucleosysthesis. The isotopes of iron are at the end of the stellar fusion process since they have the highest binding energy per nucleon. The slow neutron capture process is responsible for the production of elements heavier than iron. A time dependent model for calculating the creation of these isotopes requires accurate boundary conditions of iron seed nuclei. The neutron capture rate at the beginning of the *s*-process, such as determined by the ^{55}Fe(n,γ) cross section, influences the entire chain of subsequent neutron captures. In a sense, ^{55}Fe may be considered as one of the first *s*-process branch points. Additionally, photoneutron ^{55}Fe(γ,n) may be an important intermediate process in the production of ^{54}Fe since this isotope cannot be produced via slow neutron capture.

The fission yield of ^{55}Fe is negligible. To have a ^{55}Fe neutron capture event in a nuclear reactor or weapon, neutrons would first need to induce ^{56}Fe(n,2n) or ^{54}Fe(n,γ) in the steel support structures. However, the production rate of ^{55}Fe in these environments is likely too low to have a significant influence on the overall uncertainty of either simulation.

The normalization of the ^{56}Fe GSF does not strongly influence neutron inelastic scattering in ^{56}Fe. Since the compound nuclear state in ^{56}Fe(n,n') is ^{57}Fe, the NLD and GSF of ^{57}Fe

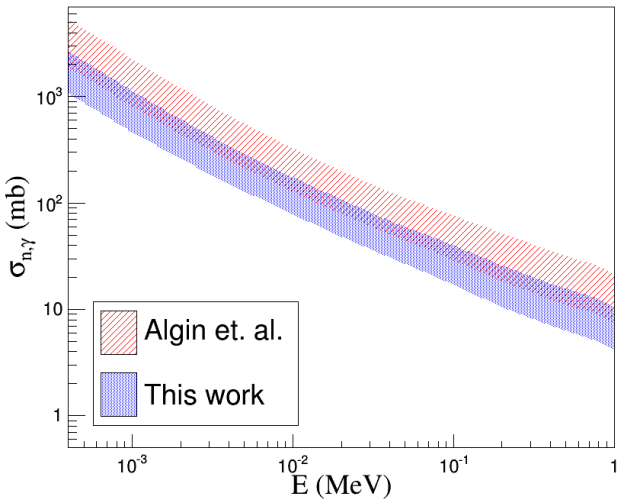

Figure 5.2: ^{55}Fe(n,γ) cross sections using the values of $\bar{\Gamma}_\gamma(S_n)$ from this work and the estimate of Algin *et. al.* [111].

and the NLD of ^{56}Fe determines the magnitude of the cross section. However, a different energy dependence of the ^{56}Fe GSF will result in different γ-ray production spectra.

The ^{56}Fe GSF normalization has a small influence on the ^{56}Fe(n,2n) cross section since there is a pre-equilibrium excited state of ^{56}Fe in the multiple compound emission process. The ^{56}Fe(n,2n) reaction is important to the neutron economy of both a nuclear reactor and a thermonuclear device. Validation of the quasi-continuum lifetime effect would not be easy with a measurement of the ^{56}Fe(n,2n) cross section. The intermediate ^{56}Fe excited state is short-lived and the ^{56}Fe GSF normalization contributes little.

If extension of the quasi-continuum lifetime method to higher mass regions proves feasible, the results may be useful to help constrain neutron capture cross sections of the actinides and fission product yields. These cross sections are valuable to nuclear forensics in the determination of the radiation history of a reactor, the fireball of a thermonuclear detonation, or the ground water transport of residual contamination. Knowledge of the cross sections of fission product yields relies on reaction calculations since the isotopes are mainly many neutrons above the valley of stability where target fabrication is difficult. When modeling the cross sections, one must infer the GSF; therefore a wealth of nuclear data is valuable to allow for global extrapolations.

5.4 Future Possibilities of the Quasi-Continuum Lifetime Method

This section discusses future possibilities for the quasi-continuum lifetime method. There are many nuclei where this method can be of use, including many nuclei not accessible via

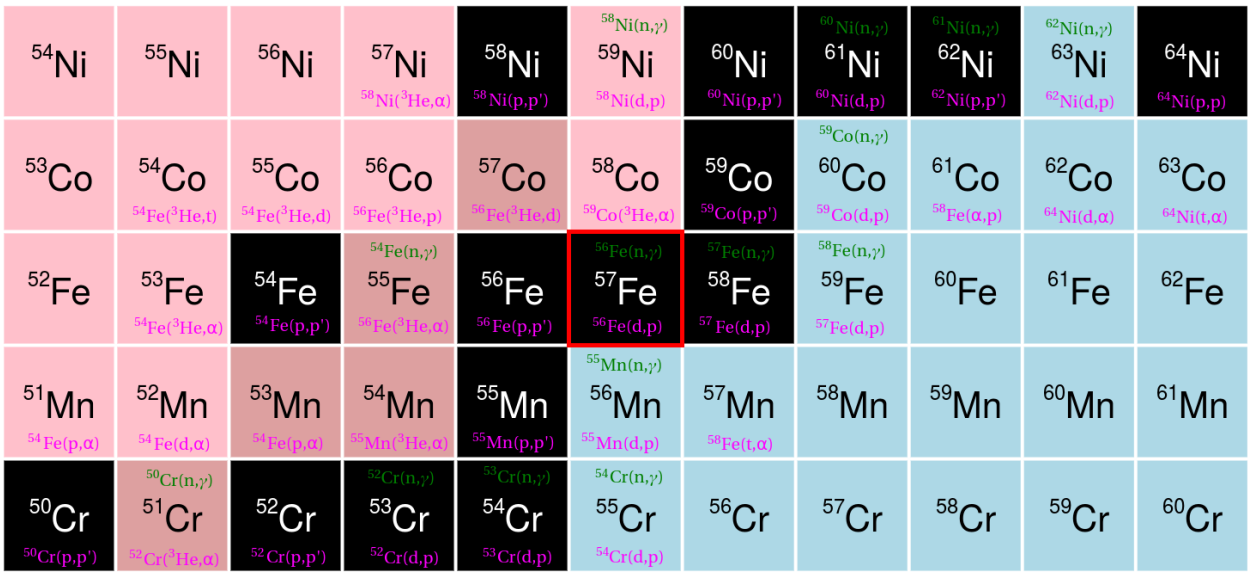

Figure 5.3: Nuclei accessible with the quasi-continuum lifetime method in the mass region near ^{56}Fe. The reactions below the chemical symbol identify which reaction is optimal for the method. If the nucleus is accessible with neutron capture, the (n,γ) reaction is listed above the chemical symbol. In this range, the quasi-continuum lifetime method can access 40 nuclei via light-ion reactions whereas neutron capture experiments can only access 14 nuclei. The highlighted ^{57}Fe nucleus is the best candidate for further validation of the method. Chart of the nuclides taken from Reference [131].

neutron capture. It is difficult to say whether this method will be extendable to the actinide region, but this section outlines a potential roadmap to such a goal.

Neighboring Nuclei

Section 5.2 outlined ways to further validate the quasi-continuum lifetime method. The procedure should be valid for nuclei in the mass region near $A = 56$ provided that there are low-lying levels with lifetimes on the order of 10–100 fs. Figure 5.3 shows the nearby nuclei that are accessible with the quasi-continuum lifetime method. The best nuclei to apply the quasi-continuum lifetime method are those with available (n,γ) data. Once the nuclear physics community perfects the method, there will be enough confidence to make estimates of $\bar{\Gamma}_\gamma(S_n)$ without supporting (n,γ) data.

The quasi-continuum lifetime method can access approximately three times the number of nuclei feasible with neutron capture experiments because of the flexibility of reaction mechanism. This method vastly expands the scientific capability to model neutron capture environments outside the valley of stability.

Relevance to Applications for Nuclei with Higher Masses

National security motivations might pave the way forward in the development of the quasi-continuum lifetime method. Fission fragments are key to the assessment of weapons performance. The simulation of reactions on unstable radioactive nuclei following a thermonuclear detonation require good inputs such as the NLD and GSF. For instance, in the low mass region of the fisson yields (FYs), zirconium is an important radiochemisty diagnostic that is subject to high neutron flux. Furthermore, zirconium is a fission reactor fuel cladding material; capture reactions on these stable nuclei influence the reactor's neutron economy. There is a lot of nuclear structure data available for ^{96}Zr; it will not be necessary to completely rebuild the level scheme and measure every lifetime. In contrast, there are few known J, Π, and τ for ^{94,95,97}Zr; a quasi-continuum lifetime experiment would require adequate particle energy and angle resolution to remeasure the important low-lying states.

In the high mass, high FY region, xenon and cesium both have high fission yields, but xenon is a noble gas and cesium is chemically reactive. Target fabrication may prove difficult and stopping power has larger uncertainties in chemical compounds. Barium might be the best candidate for extending the quasi-continuum lifetime method into the high mass, high FY region: ^{138}Ba has a ^{235}U FY of 4×10^{-5}, a natural abundance of 71.7%, and has many known J, Π, and sub-picosecond lifetimes. Neodymium is a good alternative in this mass region. There is a lot of (n,γ) data on these isotopes and the energy dependence of the GSF at low energy has been extensively studied by Bečvář *et. al.* [132]. For these heavier isotopes one may need to use the reaction (α,α') as an alternative to (p,p') to give the heavier recoil nucleus a larger initial kinetic energy. Longer slowing down time compensates for longer lifetimes.

The rare earth and heavy metals may require other lifetime techniques to apply the quasi-continuum lifetime method. An experiment may require particle detectors at backward angles with respect to the incident beam so that the backscatter imparts additional recoil momentum. The (α, α') reaction may not be sufficient to generate recoil slowing down times on the order of 1–10 ps, which is typical of low-lying lifetimes in this mass region. However, the quasi-continuum lifetime method may also be possible with the Recoil Distance Method [62] which would enable reactions of heavier projectiles such as (^{7}Li,^{7}Li') or higher. The level densities of these nuclei are high and overlap of γ-ray peaks may be cumbersome. In compensation, when the level density increases, Porter-Thomas width fluctuations become less of a concern since the total width includes many more decay paths. The highest mass, non-actinide, quasi-continuum lifetime candidates are $^{206-208}$Pb and ^{209}Bi. These nuclei do not have too high of level densities and they possess several low-lying lifetimes on the order of 10–100 fs.

The higher mass regions may require approximation techniques. Simulation of γ-ray cascades for every event is computationally intensive. RAINIER does not currently possess parallel processing capabilities, but extending its abilities should not require significant effort. Development of approximation methods may prove difficult considering that Porter-Thomas width fluctuations and multi-step γ-ray cascades have a large influence on results. Recoil

slowing down strongly depends on statistical nuclear scatter at low energies, but electronic slowing down is a continuous and more predictable process. Electronic stopping simulations may lift the computational burden of statistical scatter.

The feasibility of the quasi-continuum lifetime method in the actinide region is unclear. Thorium, uranium, and plutonium have important energy and homeland security applications. However, there is not an abundance of structure information in this mass region and the NLD of these nuclei are very high. The recoil distance method will need to be merged with the quasi-continuum lifetime method. As opposed to the wide angle nuclear scatter of ^{56}Fe in this work, electronic stopping power will be the dominant slowing down mechanism. One may wonder if the quasi-continuum lifetime method will work with radioactive beams and inverse kinematics. For residual nuclei traveling near $\beta \sim 0.3$, there is a large Doppler shift for in-flight decay. The lifetime effect would only be noticeable if the nucleus can lose a significant portion of its velocity. This rapid deceleration would require a high density stopping material, and the stopping times may be on the order of ns. For the quasi-continuum lifetime effect to be profitable, the cascade time, the low-lying level lifetime, and the slowing down time must all be within the same order of magnitude. First, the nuclear physics community must extend the quasi-continuum lifetime method into the higher mass regions before attempting a leap into the actinide region. However, a successful measurement of the average total radiative width using the quasi-continuum lifetime method would be very beneficial in actinide applications.

Bibliography

[1] Wilson, J.N. et al. "Nuclear Data for Reactor Physics: Cross sections and level densities in the actinide region". In: *EPJ Web of Conferences* 2 (2010), p. 12001. DOI: 10.1051/epjconf/20100212001.

[2] J. Serp, et. al. "The molten salt reactor (MSR) in generation IV: Overview and perspectives". In: *Progress in Nuclear Energy* 77 (2014), pp. 308 –319. ISSN: 0149-1970. DOI: 10.1016/j.pnucene.2014.02.014.

[3] J E Lynn and B B Back. "Sub-barrier fission probability for a double-humped barrier". In: *Journal of Physics A: Mathematical, Nuclear and General* 7.3 (1974), p. 395. URL: http://stacks.iop.org/0301-0015/7/i=3/a=011.

[4] *Settlement deal over MAPLE cancellation*. http://www.world-nuclear-news.org/C-Settlement_deal_in_MAPLE_cancellation-2108134.html. Accessed: 2017-10-10.

[5] A. Schiller et. al. "Level densities in ^{56,57}Fe and ^{96,97}Mo". In: *Phys. Rev. C* 68 (5 2003), p. 054326. DOI: 10.1103/PhysRevC.68.054326.

[6] A. C. Larsen and S. Goriely. "Impact of a low-energy enhancement in the γ-ray strength function on the neutron-capture cross section". In: *Phys. Rev. C* 82 (1 2010), p. 014318. DOI: 10.1103/PhysRevC.82.014318.

[7] M Guttormsen et al. "Statistical Gamma-Decay at Low Angular Momentum". In: *Physica Scripta* 1990.T32 (1990), p. 54. URL: http://stacks.iop.org/1402-4896/1990/i=T32/a=010.

[8] M. Guttormsen et al. "The SiRi particle-telescope system". In: *Nuc. Instrum. Meth. A* 648.1 (2011), pp. 168 –173. ISSN: 0168-9002. DOI: 10.1016/j.nima.2011.05.055.

[9] A.C. Larson et. al. "Analysis of possible systematic errors in the Oslo method". In: *Phys. Rev. C* 83 (3 2011), p. 034315. DOI: 10.1103/PhysRevC.83.034315.

[10] J. L. Ullmann et. al. "Cross section and γ-ray spectra for ^{238}U(n,γ) measured with the DANCE detector array at the Los Alamos Neutron Science Center". In: *Phys. Rev. C* 89 (3 2014), p. 034603. DOI: 10.1103/PhysRevC.89.034603.

[11] P. E. Koehler et al. "Spin measurements for ^{147}Sm+n resonances: Further evidence for nonstatistical effects". In: *Phys. Rev. C* 76 (2 2007), p. 025804. DOI: 10.1103/PhysRevC.76.025804.

[12] M Heil et al. "A 4BaF2 detector for (n,) cross-section measurements at a spallation neutron source". In: *Nuc. Instrum. Meth. A* 459.1 (2001), pp. 229 –246. ISSN: 0168-9002. DOI: 10.1016/S0168-9002(00)00993-1.

[13] C. Guerrero et. al. "The n_TOF Total Absorption Calorimeter for neutron capture measurements at CERN". In: *Nuc. Instrum. Meth. A* 608.3 (2009), pp. 424 –433. ISSN: 0168-9002. DOI: 10.1016/j.nima.2009.07.025.

[14] S. Paschalis et al. "The performance of the Gamma-Ray Energy Tracking In-beam Nuclear Array GRETINA". In: *Nuc. Instrum. Meth. A* 709 (2013), pp. 44 –55. ISSN: 0168-9002. DOI: 10.1016/j.nima.2013.01.009.

[15] John Simpson. "The AGATA project". In: *Journal of Physics: Conference Series* 41.1 (2006), p. 72. URL: http://stacks.iop.org/1742-6596/41/i=1/a=006.

[16] D.G. Sarantites et al. "Phoswich Wall: A charged-particle detector array for inverse-kinematic reactions with the Gretina/GRETA gamma-ray arrays". In: *Nuc. Instrum. Meth. A* 790 (2015), pp. 42 –56. DOI: 10.1016/j.nima.2015.04.007.

[17] M.D. Jones et al. "Understanding the Low-Energy Enhancement of the Photon Strength Function of ^{56}Fe". In: *Submitted to Phys. Rev. Lett* (2017).

[18] L M Bollinger. "Superconducting Linear Accelerators for Heavy Ions". In: *Annual Review of Nuclear and Particle Science* 36.1 (1986), pp. 475–503. DOI: 10.1146/annurev.ns.36.120186.002355.

[19] *ATLAS Floorplan*. https://www.phy.anl.gov/atlas/facility/floorplan.html. Accessed: 2016-6-01.

[20] G. Savard et al. "Radioactive beams from gas catchers: The CARIBU facility". In: *Nuc. Instrum. Meth. B* 266.1920 (2008). Proceedings of the XVth International Conference on Electromagnetic Isotope Separators and Techniques Related to their Applications, pp. 4086 –4091. ISSN: 0168-583X. DOI: 10.1016/j.nimb.2008.05.091.

[21] J.C. Lighthall et al. "Commissioning of the HELIOS spectrometer". In: *Nuc. Instrum. Meth. A* 622.1 (2010), pp. 97 –106. ISSN: 0168-9002. DOI: 10.1016/j.nima.2010.06.220.

[22] Cary N. Davids and James D. Larson. "The argonne fragment mass analyzer". In: *Nuc. Instrum. Meth. B* 40 (1989), pp. 1224 –1228. ISSN: 0168-583X. DOI: 10.1016/0168-583X(89)90624-1.

[23] G. Savard et al. "Studies of neutron-rich isotopes with the CPT mass spectrometer and the CARIBU project". In: *International Journal of Mass Spectrometry* 251.23 (2006), pp. 252 –259. ISSN: 1387-3806. DOI: 10.1016/j.ijms.2006.01.047.

[24] L.M. Bollinger et al. "First operational experience with the positive-ion injector of ATLAS". In: *Nuc. Instrum. Meth. A* 328.1 (1993), pp. 221–230. ISSN: 0168-9002. DOI: 10.1016/0168-9002(93)90631-Q.

[25] M. Schlapp et al. "A New 14 GHz Electron-Cyclotron-Resonance Ion Source (ECRIS) for the Heavy Ion Accelerator Facility ATLAS". In: *Proceedings of the 1997 Particle Accelerator Conference, Vancouver B. C.* 1997, pp. 2702–2704.

[26] *Tours of the Women in Science and Technology program (TWIST)*. http://blogs.anl.gov/wist/activities/twist-tours-with-the-women-in-science-and-technology-program/dsc_2304/. Accessed: 2016-10-13.

[27] P.N. Ostroumov et al. "Development and beam test of a continuous wave radio frequency quadrupole accelerator". In: *Physical Review Accelerators and Beams* 15.110101 (2012), pp. 1–11.

[28] Lowell M. Bollinger. "Superconducting linacs some recent developments". In: *Nuc. Instrum. Meth. A* 244.1 (1986), pp. 246 –258. ISSN: 0168-9002. DOI: 10.1016/0168-9002(86)90774-6.

[29] *Accelerator Facilities*. http://www.phy.anl.gov/atlas/userbook/accelfacilities.html#Contents. Accessed: 2016-10-14.

[30] *Q-value Calculator (QCalc)*. http://www.nndc.bnl.gov/qcalc/. Accessed: 2016-10-17.

[31] *Chart of the Nuclides*. http://www.nndc.bnl.gov/chart/. Accessed: 2016-10-17.

[32] Hans Bethe and J. Ashkin. Ed. by E. Segre. New York: J. Wiley, 1953, p. 253.

[33] I-Yang Lee. "The GAMMASPHERE". In: *Nuclear Physics A* 520 (1990), pp. c641 –c655. ISSN: 0375-9474. DOI: 10.1016/0375-9474(90)91181-P.

[34] J. Simpson. "The Euroball Spectrometer". In: *Zeitschrift für Physik A Hadrons and Nuclei* 358.2 (1997), pp. 139–143. ISSN: 1431-5831. DOI: 10.1007/s002180050290.

[35] G. Duchne et al. "The Clover: a new generation of composite Ge detectors". In: *Nuc. Instrum. Meth. A* 432.1 (1999), pp. 90 –110. ISSN: 0168-9002. DOI: 10.1016/S0168-9002(99)00277-6.

[36] G.J. Schmid et al. "A -ray tracking algorithm for the GRETA spectrometer". In: *Nuc. Instrum. Meth. A* 430.1 (1999), pp. 69 –83. ISSN: 0168-9002. DOI: 10.1016/S0168-9002(99)00188-6.

[37] Th. Krll and D. Bazzacco. "Simulation and analysis of pulse shapes from highly segmented HPGe detectors for the -ray tracking array MARS". In: *Nuc. Instrum. Meth. A* 463.12 (2001), pp. 227 –249. ISSN: 0168-9002. DOI: 10.1016/S0168-9002(01)00208-X.

[38] S. Ramo. "Currents Induced by Electron Motion". In: *Proceedings of the IRE* 27.9 (1939), pp. 584–585. ISSN: 0096-8390. DOI: 10.1109/JRPROC.1939.228757.

[39] David Radford. *Proposal for Gretina*. http://radware.phy.ornl.gov/greta/Gretina_prop_partial.pdf. Accessed: 2017-4-14. 2003.

[40] K. Vetter et al. "Performance of the GRETA prototype detectors". In: *Nuc. Instrum. Meth. A* 452.12 (2000), pp. 105 –114. ISSN: 0168-9002. DOI: 10.1016/S0168-9002(00)00431-9.

[41] K. Vetter et al. "Three-dimensional position sensitivity in two-dimensionally segmented HP-Ge detectors". In: *Nuc. Instrum. Meth. A* 452.12 (2000), pp. 223 –238. ISSN: 0168-9002. DOI: 10.1016/S0168-9002(00)00430-7.

[42] O. Klein and Y. Nishina. "Über die Streuung von Strahlung durch freie Elektronen nach der neuen relativistischen Quantendynamik von Dirac". In: *Zeitschrift für Physik* 52.11 (1929), pp. 853–868. ISSN: 0044-3328. DOI: 10.1007/BF01366453.

[43] T. Lauritsen et al. "Characterization of a gamma-ray tracking array: A comparison of GRETINA and Gammasphere using a 60Co source". In: *Nuc. Instrum. Meth. A* 836 (2016), pp. 46 –56. ISSN: 0168-9002. DOI: 10.1016/j.nima.2016.07.027.

[44] J.H. Hubbell and S.M. Seltzer. *Tables of X-Ray Mass Attenuation Coefficients and Mass Energy-Absorption Coefficients (version 1.4)*. Tech. rep. Accessed: 2017-Jan-12. National Institute of Standards and Technology, Gaithersburg, MD, 2004. URL: http://physics.nist.gov/xaamdi.

[45] J.K. Tuli. "Evaluated nuclear structure data file". In: *Nuc. Instrum. Meth. A* 369.2 (1996), pp. 506 –510. ISSN: 0168-9002. DOI: 10.1016/S0168-9002(96)80040-4.

[46] Kenneth Krane. *Introductory Nuclear Physics*. Hoboken, New Jersey: John Wiley & Sons, Inc., 1988.

[47] J. Lindhard, M. Scharff, and H.E. Schioett. "Range Concepts and Heavy Ion Ranges (Notes on Atomic Collisions, II)". In: *Kgl. Danske Videnskab. Selskab. Mat. Fys. Medd.* Vol: 33: No. 14 (1963).

[48] J. A. Davies et al. "The Range of Alkali Metal Ions of keV Energies in Aluminum". In: *Canadian Journal of Chemistry* 38.9 (1960), pp. 1535–1546. DOI: 10.1139/v60-214.

[49] Peter Sigmund. "LSS and the Integral Equations of Transport Theory". In: *Physica Scripta* 28.3 (1983), p. 257. URL: http://stacks.iop.org/1402-4896/28/i=3/a=001.

[50] Don E. Harrison. "Theory of the Sputtering Process". In: *Phys. Rev.* 102 (6 1956), pp. 1473–1480. DOI: 10.1103/PhysRev.102.1473.

[51] N. Bohr. "Scattering and Stopping of Fission Fragments". In: *Phys. Rev.* 58 (7 1940), pp. 654–655. DOI: 10.1103/PhysRev.58.654.

[52] N. Bohr. "Velocity-Range Relation for Fission Fragments". In: *Phys. Rev.* 59 (3 1941), pp. 270–275. DOI: 10.1103/PhysRev.59.270.

[53] D. K. Holmes and G. Leibfried. "Range of Radiation Induced Primary KnockOns in the Hard Core Approximation". In: *Journal of Applied Physics* 31.6 (1960), pp. 1046–1056. DOI: 10.1063/1.1735743.

[54] Mark T. Robinson and Ordean S. Oen. "Computer Studies of the Slowing Down of Energetic Atoms in Crystals". In: *Phys. Rev.* 132 (6 1963), pp. 2385–2398. DOI: 10.1103/PhysRev.132.2385.

[55] L. H. Thomas. "The calculation of atomic fields". In: *Mathematical Proceedings of the Cambridge Philosophical Society* 23.5 (1927), 542548. DOI: 10.1017/S0305004100011683.

[56] J. Lindhard and M. Scharff. "Energy Dissipation by Ions in the kev Region". In: *Phys. Rev.* 124 (1 1961), pp. 128–130. DOI: 10.1103/PhysRev.124.128.

[57] James F. Ziegler, M.D. Ziegler, and J.P. Biersack. "SRIM The stopping and range of ions in matter (2010)". In: *Nucl. Instrum. and Meth. B* 268.11 (2010). 19th International Conference on Ion Beam Analysis, pp. 1818 –1823. ISSN: 0168-583X. DOI: 10.1016/j.nimb.2010.02.091.

[58] *The Stopping and Range of Ions in Matter 2,300+ Scientific Citations*. http://www.srim.org/PlotCit.htm. Accessed: 2017-09-27.

[59] *Ions Stopping in Fe Target*. http://www.srim.org/StopPlots/STOPxx26.gif. Accessed: 2017-09-27.

[60] *Ions Stopping in Ni Target*. http://www.srim.org/StopPlots/STOPxx28.gif. Accessed: 2017-09-27.

[61] A. Hennig et al. "Lifetime measurement of excited low-spin states via the (p,p) reaction". In: *Nuc. Instrum. Meth. A* 794.Supplement C (2015), pp. 171 –176. ISSN: 0168-9002. DOI: 10.1016/j.nima.2015.05.024.

[62] K. W. JONES et al. "Recoil-Distance Method for Nuclear Lifetime Measurements: States of Na^{22}, Ne^{22}, and F^{19}". In: *Phys. Rev.* 178 (4 1969), pp. 1773–1782. DOI: 10.1103/PhysRev.178.1773.

[63] J. H. Hamilton et al. "Lifetime Measurements to Test the Coexistence of Spherical and Deformed Shapes in ^{72}Se". In: *Phys. Rev. Lett.* 36 (6 1976), pp. 340–342. DOI: 10.1103/PhysRevLett.36.340.

[64] Roderick V Reid. "Local phenomenological nucleon-nucleon potentials". In: *Annals of Physics* 50.3 (1968), pp. 411 –448. ISSN: 0003-4916. DOI: 10.1016/0003-4916(68)90126-7.

[65] Roger D. Woods and David S. Saxon. "Diffuse Surface Optical Model for Nucleon-Nuclei Scattering". In: *Phys. Rev.* 95 (2 1954), pp. 577–578. DOI: 10.1103/PhysRev.95.577.

[66] Maria Goeppert Mayer. "Nuclear Configurations in the Spin-Orbit Coupling Model. I. Empirical Evidence". In: *Phys. Rev.* 78 (1 1950), pp. 16–21. DOI: 10.1103/PhysRev.78.16.

[67] Maria Goeppert Mayer. "Nuclear Configurations in the Spin-Orbit Coupling Model. II. Theoretical Considerations". In: *Phys. Rev.* 78 (1 1950), pp. 22–23. DOI: 10.1103/PhysRev.78.22.

[68] *Nuclear shell model*. https://en.wikipedia.org/wiki/Nuclear_shell_model. Accessed: 2017-10-02.

[69] C. F. v. Weizsäcker. "Zur Theorie der Kernmassen". In: *Zeitschrift für Physik* 96.7 (1935), pp. 431–458. ISSN: 0044-3328. DOI: 10.1007/BF01337700.

[70] *Nuclear Force*. https://en.wikipedia.org/wiki/Nuclear_force. Accessed: 2017-10-02.

[71] *Nuclear Shell Model*. https://en.wikipedia.org/wiki/Nuclear_shell_model. Accessed: 2017-11-28.

[72] *Semi-empirical mass formula*. https://en.wikipedia.org/wiki/Semi-empirical_mass_formula. Accessed: 2017-11-28.

[73] Torleif Ericson. "A statistical analysis of excited nuclear states". In: *Nuclear Physics* 11 (1959), pp. 481 –491. ISSN: 0029-5582. DOI: 10.1016/0029-5582(59)90291-3.

[74] T. D. Newton. "Shell Effects on the Spacing of Nuclear Levels". In: *Canadian Journal of Physics* 34.8 (1956), pp. 804–829. DOI: 10.1139/p56-090.

[75] W. Dilg et al. "Level density parameters for the back-shifted fermi gas model in the mass range $40 < A < 250$". In: *Nuclear Physics A* 217.2 (1973), pp. 269 –298. ISSN: 0375-9474. DOI: 10.1016/0375-9474(73)90196-6.

[76] A. Gilbert and A. G. W. Cameron. "A Composite Nuclear-Level Density Formula with Shell Corrections". In: *Canadian Journal of Physics* 43.8 (1965), pp. 1446–1496. DOI: 10.1139/p65-139.

[77] T. Kibdi et al. "Evaluation of theoretical conversion coefficients using BrIcc". In: *Nucl. Instrum. and Meth. A* 589.2 (2008), pp. 202 –229. ISSN: 0168-9002. DOI: 10.1016/j.nima.2008.02.051.

[78] C. E. Porter and R. G. Thomas. "Fluctuations of Nuclear Reaction Widths". In: *Phys. Rev.* 104 (2 1956), pp. 483–491. DOI: 10.1103/PhysRev.104.483.

[79] P. E. Koehler et al. "Anomalous Fluctuations of s-Wave Reduced Neutron Widths of ^{192,194}Pt Resonances". In: *Phys. Rev. Lett.* 105 (7 2010), p. 072502. DOI: 10.1103/PhysRevLett.105.072502.

[80] Peter Axel. "Electric Dipole Ground-State Transition Width Strength Function and 7-MeV Photon Interactions". In: *Phys. Rev.* 126 (2 1962), pp. 671–683. DOI: 10.1103/PhysRev.126.671.

[81] DM Brink. "PhD Thesis, Oxford University (1955)." In: (1955).

[82] Niels Bohr. "Neutron Capture and Nuclear Constitution". In: *Nature* 137 (1936), pp. 344–348. DOI: 10.1038/137344a0.

[83] G. A. Bartholomew et al. "Gamma-Ray Strength Functions". In: *Advances in Nuclear Physics: Volume 7*. Ed. by Michel Baranger and Erich Vogt. Boston, MA: Springer US, 1973, pp. 229–324. ISBN: 978-1-4615-9044-6. DOI: 10.1007/978-1-4615-9044-6_4.

[84] D.M. Brink. "Individual particle and collective aspects of the nuclear photoeffect". In: *Nuclear Physics* 4 (1957), pp. 215 –220. ISSN: 0029-5582. DOI: 10.1016/0029-5582(87)90021-6.

[85] J. Kopecky and M. Uhl. "Test of gamma-ray strength functions in nuclear reaction model calculations". In: *Phys. Rev. C* 41 (5 1990), pp. 1941–1955. DOI: 10.1103/PhysRevC.41.1941.

[86] S.G. Kadmenskij, V.P. Markushev, and V.I. Furman. In: *Yad. Fiz.* (277 1983), p. 37.

[87] J. Kopecky and R.E. Chrien. "Observation of the M1 giant resonance by resonance averaging in 106Pd". In: *Nuclear Physics A* 468.2 (1987), pp. 285 –300. ISSN: 0375-9474. DOI: 10.1016/0375-9474(87)90518-5.

[88] R. Capote and et. al. "RIPL Reference Input Parameter Library for Calculation of Nuclear Reactions and Nuclear Data Evaluations". In: *Nuclear Data Sheets* 110.12 (2009), pp. 3107 –3214. ISSN: 0090-3752. DOI: 10.1016/j.nds.2009.10.004.

[89] S. Joly, D. M. Drake, and L. Nilsson. "Gamma-ray strength functions for ^{104}Rh, ^{170}Tm, and ^{198}Au". In: *Phys. Rev. C* 20 (6 1979), pp. 2072–2083. DOI: 10.1103/PhysRevC.20.2072.

[90] D. Bohle et al. "New magnetic dipole excitation mode studied in the heavy deformed nucleus 156Gd by inelastic electron scattering". In: *Physics Letters B* 137.1 (1984), pp. 27 –31. ISSN: 0370-2693. DOI: 10.1016/0370-2693(84)91099-2.

[91] N. Lo Iudice and F. Palumbo. "New Isovector Collective Modes in Deformed Nuclei". In: *Phys. Rev. Lett.* 41 (22 1978), pp. 1532–1534. DOI: 10.1103/PhysRevLett.41.1532.

[92] M. Guttormsen, T. Ramsøy, and J. Rekstad. "The first generation of γ-rays from hot nuclei". In: *Nucl. Instrum. and Meth. A* 255.3 (1987), pp. 518 –523. ISSN: 0168-9002. DOI: 10.1016/0168-9002(87)91221-6.

[93] M Guttormsen et al. "The unfolding of continuum γ-ray spectra". In: *Nucl. Instrum. and Meth. A* 374.3 (1996), pp. 371 –376. ISSN: 0168-9002. DOI: 10.1016/0168-9002(96)00197-0.

[94] M. Wiedeking et. al. "Low-Energy Enhancement in the Photon Strength of ^{95}Mo". In: *Phys. Rev. Lett.* 108 (16 2012), p. 162503. DOI: 10.1103/PhysRevLett.108.162503.

[95] *Nuclear Reactions*. https://en.wikipedia.org/wiki/Nuclear_reaction. Accessed: 2017-10-04.

[96] M. Herman et al. "EMPIRE: Nuclear Reaction Model Code System for Data Evaluation". In: *Nuclear Data Sheets* 108.12 (2007), pp. 2655 –2715. ISSN: 0090-3752. DOI: 10.1016/j.nds.2007.11.003.

[97] M. Blann. "Recent Progress and Current Status of Preequilibrium Reaction Theories and Computer Code ALICE". In: *Computation and Analysis of Nuclear Data Relevant to Nuclear Energy and Safety: Proceedings of the Workshop*. Ed. by M.K. Mehta and J.J. Schmidt. Trieste, Italy: World Scientific, 1993, p. 622.

[98] P.G. Young and E.D. Arthur. *GNASH: a preequilibrium, statistical nuclear-model code for calculation of cross sections and emission spectra. [In FORTRAN for CDC 7600].* 1977. DOI: 10.2172/5224192.

[99] S. Hilaire A.J. Koning and M. Duijvestijn. "TALYS: A nuclear reaction program". In: (2004). NRG-report 21297/04.62741/P.

[100] J. Raynal. *Notes on ECIS94*. Tech. rep. CEA-N-2772, pp. 1–145. Commisariat 'a l'Energie Atomique, Saclay, France, 1994.

[101] L. E. Kirsch and L. A. Bernstein. "RAINIER: A Simulation Tool for Distributions of Excited Nuclear States and Cascade Fluctuations". In: *Sumbitted to Nuc. Instrum and Meth. A* (2017).

[102] F. Bečvář. "Simulation of γ cascades in complex nuclei with emphasis on assessment of uncertainties of cascade-related quantities". In: *Nucl. Instrum. and Meth. A* 417.23 (1998), pp. 434 –449. ISSN: 0168-9002. DOI: 10.1016/S0168-9002(98)00787-6.

[103] F.F. Russ Knapp, et. al. "Reactor-produced radioisotopes from ORNL for bone pain palliation". In: *Applied Radiation and Isotopes* 49.4 (1998), pp. 309 –315. ISSN: 0969-8043. DOI: 10.1016/S0969-8043(97)00043-2.

[104] Till von Egidy and Dorel Bucurescu. "Systematics of nuclear level density parameters". In: *Phys. Rev. C* 72 (4 2005), p. 044311. DOI: 10.1103/PhysRevC.72.044311.

[105] T. von Egidy and D. Bucurescu. "Experimental energy-dependent nuclear spin distributions". In: *Phys. Rev. C* 80 (5 2009), p. 054310. DOI: 10.1103/PhysRevC.80.054310.

[106] H. Derrien et al. "Evaluation of 238U Resonance Parameters from 0 to 20 keV". In: *AIP Conference Proceedings* 769.1 (2005), pp. 276–281. DOI: 10.1063/1.1945005.

[107] A. Spyrou and S. N. Liddick, et. al. "Novel technique for Constraining r-Process (n, γ) Reaction Rates". In: *Phys. Rev. Lett.* 113 (23 2014), p. 232502. DOI: 10.1103/PhysRevLett.113.232502.

[108] F. Bečvář et al. "E1 and M1 strengths studied from two-step gamma cascades following capture of thermal neutrons in 162Dy". In: *Phys. Rev. C* 52 (3 1995), pp. 1278–1294. DOI: 10.1103/PhysRevC.52.1278.

[109] B. Baramsai et al. "Neutron resonance parameters in ^{155}Gd measured with the DANCE γ-ray calorimeter array". In: *Phys. Rev. C* 85 (2 2012), p. 024622. DOI: 10.1103/PhysRevC.85.024622.

[110] T. K. Alexander and J. S. Forster. "Lifetime Measurements of Excited Nuclear Levels by Doppler-Shift Methods". In: *Advances in Nuclear Physics: Volume 10*. Ed. by Michel Baranger and Erich Vogt. Boston, MA: Springer US, 1978, pp. 197–331. ISBN: 978-1-4757-4401-9. DOI: 10.1007/978-1-4757-4401-9_3.

[111] E. Algin et al. "Thermodynamic properties of ^{56,57}Fe". In: *Phys. Rev. C* 78 (5 2008), p. 054321. DOI: 10.1103/PhysRevC.78.054321.

[112] *How errors are used in the χ^2 function*. https://root.cern.ch/root/html524/TGraph.html#TGraph:Fit. Accessed: 2017-10-19.

[113] D. Weisshaar et al. "The performance of the -ray tracking array GRETINA for -ray spectroscopy with fast beams of rare isotopes". In: *Nuc. Instrum. Meth. A* 847 (2017), pp. 187 –198. ISSN: 0168-9002. DOI: 10.1016/j.nima.2016.12.001.

[114] Till von Egidy and Dorel Bucurescu. "Erratum: Systematics of nuclear level density parameters [Phys. Rev. C 72, 044311 (2005)]". In: *Phys. Rev. C* 73 (4 2006), p. 049901. DOI: 10.1103/PhysRevC.73.049901.

[115] G. Audi, A.H. Wapstra, and C. Thibault. "The Ame2003 atomic mass evaluation". In: *Nuclear Physics A* 729.1 (2003). The 2003 NUBASE and Atomic Mass Evaluations, pp. 337 –676. ISSN: 0375-9474. DOI: 10.1016/j.nuclphysa.2003.11.003.

[116] H. Zhongfu et al. In: *Chin. J. Nucl. Phys.* 13 (1991), p. 147.

[117] M. Gholami, M. Kildir, and A. N. Behkami. "Microscopic study of spin cut-off factors of nuclear level densities". In: *Phys. Rev. C* 75 (4 2007), p. 044308. DOI: 10.1103/PhysRevC.75.044308.

[118] S. M. Grimes et al. "Level density and spin cutoff parameters from continuum (p, n) and (α, n) spectra". In: *Phys. Rev. C* 10 (6 1974), pp. 2373–2386. DOI: 10.1103/PhysRevC.10.2373.

[119] A. Gilbert and A. G. W. Cameron. "A Composite Nuclear-Level Density Formula with Shell Corrections". In: *Canadian Journal of Physics* 43.8 (1965), pp. 1446–1496. DOI: 10.1139/p65-139.

[120] A. C. Larsen et al. "Evidence for the Dipole Nature of the Low-Energy γ Enhancement in ^{56}Fe". In: *Phys. Rev. Lett.* 111 (24 2013), p. 242504. DOI: 10.1103/PhysRevLett.111.242504.

[121] A. Voinov et al. "Large Enhancement of Radiative Strength for Soft Transitions in the Quasicontinuum". In: *Phys. Rev. Lett.* 93 (14 2004), p. 142504. DOI: 10.1103/PhysRevLett.93.142504.

[122] L. Katz and A. G. W. Cameron. "The Solution of X-ray Activation Curves for Photonuclear Cross Sections". In: *Canadian Journal of Physics* 29.6 (1951), pp. 518–544. DOI: 10.1139/p51-056.

[123] P. Carlos et al. "A study of the photoneutron contribution to the giant dipole resonance of nuclei in the 64 A 86 mass region". In: *Nuclear Physics A* 258.2 (1976), pp. 365 –387. ISSN: 0375-9474. DOI: 10.1016/0375-9474(76)90012-9.

[124] J.W. Norbury et al. "Photoneutron Cross Section of 54Fe". In: *Austrailian Journal of Physics* 31.6 (1978), pp. 471–476. DOI: 10.1071/PH780471.

[125] R. A. Alvarez et al. "Photoneutron cross sections for ^{55}Mn and ^{59}Co". In: *Phys. Rev. C* 20 (1 1979), pp. 128–138. DOI: 10.1103/PhysRevC.20.128.

[126] G. G. Seaman et al. "Lifetimes of Excited States in ^{56}Fe". In: *Phys. Rev.* 188 (4 1969), pp. 1706–1710. DOI: 10.1103/PhysRev.188.1706.

[127] M. Guttormsen et al. "Gamma-widths, lifetimes and fluctuations in the nuclear quasi-continuum". In: *Proceedings of The 16th International Symposium on Capture Gamma-Ray Spectroscopy and Related Topics* (2016).

[128] F. Bauwens et al. "Dipole transitions to bound states in ^{56}Fe and ^{58}Ni". In: *Phys. Rev. C* 62 (2 2000), p. 024302. DOI: 10.1103/PhysRevC.62.024302.

[129] T. Shizuma et al. "Dipole strength distribution in ^{56}Fe". In: *Phys. Rev. C* 87 (2 2013), p. 024301. DOI: 10.1103/PhysRevC.87.024301.

[130] R. B. Firestone et al. "Thermal neutron capture cross section for ^{56}Fe(n,γ)". In: *Phys. Rev. C* 95 (1 2017), p. 014328. DOI: 10.1103/PhysRevC.95.014328.

[131] *Chart of the Nuclides*. http://people.physics.anu.edu.au/~ecs103/chart/. Accessed: 2017-11-19.

[132] F. Bečvář et al. "Test of photon strength functions by a method of two-step cascades". In: *Phys. Rev. C* 46 (4 1992), pp. 1276–1287. DOI: 10.1103/PhysRevC.46.1276.

[133] J.F. Ziegler. "I - Introduction". In: *The Stopping and Ranges of Ions in Matter*. Ed. by J.F. Ziegler. Pergamon, 1977, pp. 1 –. ISBN: 978-0-08-021605-8. DOI: 10.1016/B978-0-08-021605-8.50004-9.

[134] Mme. Pierre Curie. In: *Comptes Rendus* 130.76 (1900).

[135] W. H. Bragg M.A. and R. Kleeman B.Sc. "XXXIX. On the particles of radium, and their loss of range in passing through various atoms and molecules". In: *Philosophical Magazine* 10.57 (1905), pp. 318–340. DOI: 10.1080/14786440509463378.

[136] *Bragg Curves and Peaks*. https://www.bnl.gov/nsrl/userguide/bragg-curves-and-peaks.php. Accessed: 2017-9-16.

[137] H. Geiger and E. Marsden. "On a Diffuse Reflection of the α-Particles". In: *Proceedings of the Royal Society of London A: Mathematical, Physical and Engineering Sciences* 82.557 (1909), pp. 495–500. ISSN: 0950-1207. DOI: 10.1098/rspa.1909.0054.

[138] Professor E. Rutherford F.R.S. "LXXIX. The scattering of and particles by matter and the structure of the atom". In: *Philosophical Magazine* 21.125 (1911), pp. 669–688. DOI: 10.1080/14786440508637080.

[139] Sir J.J. Thomson O.M. F.R.S. "XIX. Further experiments on positive rays". In: *Philosophical Magazine* 24.140 (1912), pp. 209–253. DOI: 10.1080/14786440808637325.

[140] N. Bohr Dr. phil. "I. On the constitution of atoms and molecules". In: *Philosophical Magazine* 26.151 (1913), pp. 1–25. DOI: 10.1080/14786441308634955.

[141] H. Bethe. "Zur Theorie des Durchgangs schneller Korpuskularstrahlen durch Materie". In: *Annalen der Physik* 397.3 (1930), pp. 325–400. ISSN: 1521-3889. DOI: 10.1002/andp.19303970303.

[142] F. Bloch. "Zur Bremsung rasch bewegter Teilchen beim Durchgang durch Materie". In: *Annalen der Physik* 408.3 (1933), pp. 285–320. ISSN: 1521-3889. DOI: 10.1002/andp.19334080303.

[143] O. Hahn and F. Strassmann. "Über den Nachweis und das Verhalten der bei der Bestrahlung des Urans mittels Neutronen entstehenden Erdalkalimetalle". In: *Naturwissenschaften* 27.1 (1939), pp. 11–15. ISSN: 1432-1904. DOI: 10.1007/BF01488241.

[144] Lise Meitner and O. R. Frisch. "Disintegration of Uranium by Neutrons: a New Type of Nuclear Reaction". In: *Nature* 143.1 (1939), pp. 239–240. DOI: 10.1038/143239a0.

[145] Enrico Fermi. "The Ionization Loss of Energy in Gases and in Condensed Materials". In: *Phys. Rev.* 57 (6 1940), pp. 485–493. DOI: 10.1103/PhysRev.57.485.

[146] Julian Knipp and Edward Teller. "On the Energy Loss of Heavy Ions". In: *Phys. Rev.* 59 (8 1941), pp. 659–669. DOI: 10.1103/PhysRev.59.659.

[147] J. Lindhard. In: *Mat. Fys. Medd. Dan. Vid. Selsk.* 28 (1954), p. 8.

[148] O. B. Firsov. In: *Zh. Eksp. Teor. Fiz.* 34 (1958), p. 447.

[149] L C Northcliffe. "Passage of Heavy Ions Through Matter". In: *Annual Review of Nuclear Science* 13.1 (1963), pp. 67–102. DOI: 10.1146/annurev.ns.13.120163.000435.

[150] C. C. Rousseau, W. K. Chu, and D. Powers. "Calculations of Stopping Cross Sections for 0.8- to 2.0-MeV Alpha Particles". In: *Phys. Rev. A* 4 (3 1971), pp. 1066–1070. DOI: 10.1103/PhysRevA.4.1066.

[151] W. D. Wilson, L. G. Haggmark, and J. P. Biersack. "Calculations of nuclear stopping, ranges, and straggling in the low-energy region". In: *Phys. Rev. B* 15 (5 1977), pp. 2458–2468. DOI: 10.1103/PhysRevB.15.2458.

[152] P. Gombas. *Die Statistische Theorie des Atoms und ihre Anwendungen*. Wien: Springer Verlag, 1949.

[153] *The ThomasFermi equation*. https://en.wikipedia.org/wiki/Thomas%E2%80%93Fermi_model. Accessed: 2017-9-25.

[154] N. Bohr. In: *Mat. Fys. Medd. Dan. Vid. Selsk.* 8 (1948), p. 18.

Appendix A

Stopping Theoretical Development

The interaction of charged particles with matter is a complex problem that involves several different physical phenomena. Early scientists had to take into account the fact that new energy loss mechanisms arise as an ion's kinetic energy decreases. An explanation of all the different components of ion-material interactions are detailed by Ziegler [133]. Some of the first developments of the slowing down theory began soon after the discovery of radioactivity via the experimental work of Curie in 1900 [134]. Shortly thereafter in 1905, Bragg and Kleeman demonstrated the rapid increase of linear energy transfer with decreasing ion velocity [135]. Figure A.1 shows a modern example of the widely-recognized Bragg curve in which the maximum linear energy transfer of a charged particle occurs near the end of its path. However, the lack of a coherent description of the atom stifled theoretical descriptions of early experimental work.

After the pioneering work of Gieger in the study of α-particle penetration through thin foils in 1909 [137] and subsequent atomic theory by Rutherford in 1911 [138], many scientists

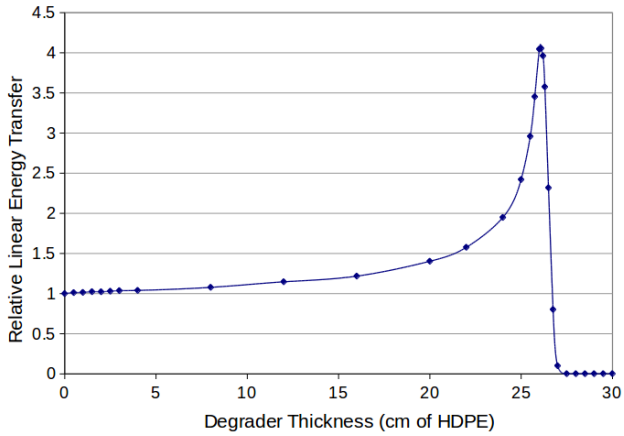

Figure A.1: Stopping of 205 MeV protons in High Density Polyethelene (HDPE) [136]. The peak in linear energy transfer at 26.1 cm is known as the Bragg peak.

including Thomson in 1912 [139] and Bohr in 1913 [140] attempted theoretical descriptions of the stopping of charged particles in matter. Bohr separated energy loss into two separate mechanisms: nuclear and electronic. The nuclear component of energy loss is the result of the Coulomb interaction between the positively charged nuclear cores of the target material and the incident ion. The electronic component is the result of the interaction between electrons in the target material and the nucleus of the incident ion. However, quantum mechanics was not well established at this time and there were many open questions impeding further development.

Bethe in 1930 [141] and Bloch in 1933 [142] applied relativistic quantum mechanics and perturbation theory to the slowing down of fully stripped charged particles traversing matter. Bethe's formula of the average stopping power of charged particles is

$$-\left\langle \frac{dE}{dx} \right\rangle = \frac{4\pi}{m_e c^2} \frac{nZ^2}{\beta^2} \left(\frac{e^2}{4\pi\epsilon_0} \right)^2 \left[\ln\left(\frac{2m_e c^2 \beta^2}{I(1-\beta^2)} \right) - \beta^2 \right], \tag{A.1}$$

where v and Z are the ion's velocity and charge, respectively, I is the mean excitation potential, $\beta = v/c$, m_e and e are the electron mass and charge, respectively, and

$$n = \frac{N_A Z_a \rho}{A M_u} \tag{A.2}$$

is the target material electron density where ρ is the density, Z_a is the atomic number, A is the atomic mass, and M_u is the molar mass of the material. Although this formula has excellent experimental confirmation at high energy, it breaks down at low energy in which the ion is not fully stripped of its orbital electrons. Therefore, this formula does not apply to many experimental scenarios nor is it of practical use to many industrial applications.

The observation of fission by Hahn and Strassman [143] and explanation by Meitner and Frisch [144] in 1939 brought about a resurgence in atomic collision theory. In the early 1940's, Bohr and others returned to the issue of low energy stopping of partially stripped heavy ions to describe fission fragment recoil. Bohr implemented Thomas-Fermi screening in which the incident ion is stripped of its electrons that have orbital velocities less than the ion velocity [51]. In 1941, the estimate of an ion's effective charge Z^* [52] was

$$Z^* = Z^{1/3} v / v_0, \tag{A.3}$$

where $v_0 = \alpha c$ is the Bohr velocity and α is the fine structure constant.

In 1940, Fermi helped quantify the degree of electric polarization of a charged particle within dielectric material [145], noting that the induced polarization from the incident ion alters the interaction with the sea of electrons in the target. In this work, Fermi also contributed a proportional scaling law that showed stopping powers were a function of the mass traversed by the ion. In 1941, Knipp and Teller applied Fermi's stopping power scaling law together with the effective charge in Equation (A.3) to relate H, He, C, N, O, F, and light fission fragment stopping powers [146]. These scaling laws gave experimentalists a basis for

interpolation and extrapolation of known stopping powers to unmeasured target materials and ion velocities.

Throughout the mid 1950's, Lindhard continued the work on the penetration of a charged particle into a quantized electron gas but focused on a non-relativistic approximation [147]. Linhard brought together the work of previous literature incorporating the assumptions that electrons are at zero temperature in the form of plane waves on a positive background for overall neutrality, that the electron density is constant before polarization, and that the ion provides a small perturbation to the target material. Lindhard's work provided the basis for a coherent theory of ions stopping in matter and deeply analyzed the energy transfer in screened Coulomb collisions. In screened Coulomb collisions, the mutual potential between ion and atom is

$$V(r) = \frac{Z^* Z_a e^2}{r} \exp(-r/a), \tag{A.4}$$

where r is the distance between ion and atom and a is known as the screening parameter which accounts for the shielding of nuclear charge by inner orbital electron. In 1958, Firsov implemented new numerical techniques to fit experimental data and obtained the following form for the screening parameter [148] and Northcliffe further refined the effective charge of Equation (A.3) in 1963 by fitting experimental data [149]. Their relations showed that ion and electron velocities were the important factors in determining the degree of ionization as opposed to electron binding energies. However, a fundamental derivation of effective charge was still lacking.

In the mid 1960's Lindhard, Scharff, and Schiott (LSS) compiled the existing theory on ion stopping power into a single unified theory [47]. With the introduction of LSS theory, experimentalists had the ability to calculate ion ranges with a single model that incorporated both electronic and nuclear stopping and applied to any element and energy. The Thomas-Fermi theory provided the backbone of LSS theory and is therefore accurate in the energy and ion range where there are many bound electrons, i.e. in the regime where ions are neither fully stripped nor almost neutral.

Further developments of stopping calculations included the employment of computers by Rousseau *et. al.* for the electronic component in 1970 [150] and Wilson *et. al.* for the nuclear component in 1977 [151]. These numerical methods complemented and advanced stopping theory and allowed a more realistic treatment of bound electrons using Hartree-Fock atoms. During the 1980's there were further modifications to the phenomenological models used to estimate effective charge, the screening parameter, and the mutual potential. More experimental data, fits, and evaluations helped guide the fine tuning of model parameters.

Section 3.2 gives a brief overview of the computer code `SRIM` [57] which encompasses the most up to date stopping power physics and model parameters to calculate ion trajectories. `SRIM` is the dominant software in the field of radiation material science and quotes stopping power accuracy to within 5% for the ions, targets, and energies of this experiment in this work.

Appendix B

Binet Equation

This Appendix derives the Binet equation of central force motion used in the Linhard Scharff Schiott Theory of atomic collisions.

The equations of motion in LSS theory begin with Newton's second law ($\mathbf{F} = m\mathbf{a}$) in polar coordinates for a purely centralized force in the center of mass system:

$$F(r) + F_{\rm c}(r) = \mu\ddot{r}, \tag{B.1}$$

where r is the distance of ion-atom separation, μ is the reduced mass, $F(r)$ is the interatomic repulsive force, and $F_{\rm c}(r)$ is the centrifugal force:

$$F_{\rm c}(r) = \mu r\dot{\phi}^2, \tag{B.2}$$

where ϕ is the polar angle. The substitution $u = 1/r$ makes the following algebra simpler. Taking the first derivative of u gives

$$\frac{du}{d\phi} = \frac{dt}{d\phi}\cdot\frac{d}{dt}\left(\frac{1}{r}\right) = -\frac{\dot{r}}{r^2\dot{\phi}} = -\frac{\dot{r}}{h}, \tag{B.3}$$

where

$$h = r^2\dot{\phi} = \frac{L}{\mu}, \tag{B.4}$$

is a constant by the conservation of angular momentum, L:

$$L = r^2\mu\dot{\phi} = \text{constant}. \tag{B.5}$$

Continuing with the derivatives of u,

$$\frac{d^2u}{d\phi^2} = \frac{d}{d\phi}\left(-\frac{\dot{r}}{h}\right) = -\frac{dt}{d\phi}\cdot\frac{d}{dt}\left(\frac{\dot{r}}{h}\right) = -\frac{\ddot{r}}{h\dot{\phi}} = -\frac{\ddot{r}}{hu^2r^2\dot{\phi}} = -\frac{\ddot{r}}{h^2u^2}, \tag{B.6}$$

where the inserted pair $ur = (ur)^2 = 1$. Substituting Equations (B.3), (B.6), and (B.2) into (B.1) yields the Binet equation:

$$F(r) = \mu(\ddot{r} - r\dot{\phi}^2) = \mu\left(-h^2u^2\frac{d^2u}{d\phi} - u^3h^2\right) = -\mu h^2u^2\left(\frac{d^2u}{d\phi} + u\right), \tag{B.7}$$

where rearranging the equality $(r^2\dot{\phi})^2 = h^2(ur)^3$ gives $r\dot{\phi}^2 = u^3h^2$. The initial condition $\phi \to 0$ gives $u \to 0$, $v \to v_\infty$, and $r\sin\phi \to b$, where b is the impact parameter and v_∞ is the initial center of mass velocity. Applying this initial condition gives

$$\mu h^2 = L^2/\mu = \mu(rv_\perp)^2 = \mu(v \cdot r\sin\phi)^2 \to \mu b^2 v_\infty^2 \tag{B.8}$$

where $v_\perp = r\dot{\phi} = v\sin\phi$.

Rearrangement of Equation (B.7) using (B.8) including the initial condition and its derivative gives the following set of differential equations for the center of mass motion:

$$\begin{cases} \frac{d^2u}{d\phi} + u + \frac{F(u)}{u^2\mu v_\infty^2 b^2} = 0 \\ u(\phi \to 0) = 0 \\ \frac{du}{d\phi}(\phi \to 0) = -\frac{1}{b}. \end{cases} \tag{B.9}$$

Appendix C

Similarity

This Appendix outlines the concept of similarity which allowed the work of Linhard Scharff Schiott Theory to be successful in the description of stopping power across a wide range of particle energies and species.

The first step toward similarity is the the reduction and approximation of the interaction potential, V:

$$V(u) = uZZ_a e^2 w, \tag{C.1}$$

where $F(r) = -dV(r)/dr$ and w is the reduced potential which has limits $w \to 1$ as $r \to 0$ (to restore the Coulomb potential) and $w \to 0$ as $r \to \infty$ (to achieve complete Coulomb screening at large distances). Unfortunately, a velocity independent potential,

$$w = w(Z, Z_a, r) \tag{C.2}$$

has $> 10^4$ possibilities for the various combinations of atoms and ions and therefore would require far too many experiments and evaluations to fully characterize a universal scattering equation. A potential resulting the Thomas-Fermi equations [55] has just two independent parameters and is a step closer to similarity:

$$w = w(Z/Z_a, r/a), \tag{C.3}$$

where a is the screening parameter as mentioned in (A.4). Here, the independent variable Z/Z_a has reduced the total number of independent parameters by one. The Thomas-Fermi potential is roughly independent of Z/Z_a and a further approximation reduces the number of independent parameters yet again at the cost of some precision:

$$w = w(r/a). \tag{C.4}$$

This potential gives a total deflection of only two parameters:

$$\theta = \theta(\epsilon, b/a), \tag{C.5}$$

where the reduced kinetic energy, ϵ, is

$$\epsilon = T_\mu \frac{a}{ZZ_a e^2}. \tag{C.6}$$

A further step in LSS theory is to encode the interaction potential's dependence on Z and Z_a into the yet unspecified screening parameter a.

In the limit of small deflection, a perturbation calculation of the transverse momentum transfer is

$$\theta \approx \frac{1}{\mu v_\infty^2} \int_{-\infty}^{\infty} K_\perp(b,z)dz = \frac{1}{\mu v_\infty^2} \frac{\partial}{\partial p} \int_{-\infty}^{\infty} V([b^2+z^2]^{1/2})dz, \tag{C.7}$$

where, $K_\perp$ denotes the force perpendicular to the path. For a screened Coulomb potential of the form of Equation (C.4),

$$\theta = \frac{2ZZ_a e^2}{\mu v_\infty b} g\left(\frac{b}{a}\right), \tag{C.8}$$

where $g(y)$ is a complicated mathematical function. Using the reduced energy of Equation (C.6), the number of independent variables shrinks to one:

$$\epsilon \cdot \theta = \frac{a}{b} \cdot g\left(\frac{b}{a}\right), \tag{C.9}$$

where the dependent variable characterizing the scattering is now $\epsilon\theta$. Thus, Equation (C.9) achieves similarity for small angles.

Appendix D

Thomas Fermi Model

This Appendix outlines the Thomas Fermi model of electron density distribution in atoms and molecules. The Linhard Scharff Schiott Theory of atomic stopping powers uses the Thomas Fermi model extensively to determine the Coulomb screening parameters in the interaction potential.

To obtain the functional dependence of the screening parameter a on Z and Z_a, LSS theory uses scaling laws of the Thomas-Fermi model. The Thomas-Fermi (TF) model [55] is a semiclassical theory developed in 1927 to approximate the distributions of electrons in atoms and molecules. The theory is a precursor to modern Density Functional Theory and is only valid in the limit of infinite nuclear charge, but it can reproduce general features in electron density.

The TF model begins with a small spatial volume element ΔV of an atom in its ground state with spherical momentum space volume V_f filled up to the Fermi momentum p_f:

$$V_f = \frac{4\pi p_f^3(\boldsymbol{x})}{3}, \tag{D.1}$$

where $\boldsymbol{x}$ is a spatial point in ΔV. The phase space volume of this spatial volume element is

$$\Delta V_{ph} = V_f \Delta V. \tag{D.2}$$

Considering that a maximum of 2 electrons can occupy a phase space volume of h^3, where h is Planck's constant, the number of electrons in ΔV_{ph} is

$$\Delta N_{ph} = \frac{2\Delta V_{ph}}{h^3}. \tag{D.3}$$

The total number of electrons in ΔV is

$$\Delta N = \rho_e(\boldsymbol{x})\Delta V, \tag{D.4}$$

where $\rho_e(\boldsymbol{x})$ is the electron density at point $\boldsymbol{x}$. Setting Equations (D.3) and (D.4) equal and solving for $\rho_e(\boldsymbol{x})$ gives the electron density in terms of the Fermi momentum:

$$\rho_e(\boldsymbol{x}) = \frac{8\pi}{3h^3} p_f^3(\boldsymbol{x}). \tag{D.5}$$

TF model uses the integral of Equation (D.5) to obtain kinetic and potential energies of the electrons in the system. At $\boldsymbol{x}$, the fraction of electrons with momentum between p and dp is the ratio of a shell of momentum space of radius p and thickness dp to the total momentum space volume:

$$F_{\boldsymbol{x}}(p)dp = \begin{cases} \frac{4\pi p^2 dp}{\frac{4}{3}\pi p_f^3(\boldsymbol{x})}, & p \leq p_f(\boldsymbol{x}) \\ 0, & \text{else} \end{cases} \tag{D.6}$$

The specific non-relativsitic, classical kinetic energy of the electrons is

$$t(\boldsymbol{x}) = \int \frac{p^2}{2m_e} \rho_e(\boldsymbol{x}) F_{\boldsymbol{x}}(p) dp \tag{D.7}$$

$$= \rho_e(\boldsymbol{x}) \int_0^{p_f(\boldsymbol{r})} \frac{p^2}{2m_e} \frac{4\pi p^2 dp}{\frac{4}{3}\pi p_f^3(\boldsymbol{x})} \tag{D.8}$$

$$= \frac{3h^2}{10m_e} \left(\frac{3}{8\pi}\right)^{2/3} [\rho_e(\boldsymbol{x})]^{5/3}, \tag{D.9}$$

with the implication that the total kinetic energy of the system is a function of only the electron density distribution. The specific potential energy of electrons in the field of the nuclear charge is

$$v_N = \rho_e(\boldsymbol{x}) V(\boldsymbol{x}), \tag{D.10}$$

where $V(\boldsymbol{x})$ is the potential energy of a single electron due to the nuclear electric field.

Extending the Thomas-Fermi treatment to interatomic potentials in ion scattering leads to the following dependence of the screening parameter:

$$a \propto Z^{-1/3} \quad \text{or} \quad \propto Z_a^{-1/3}, \tag{D.11}$$

where the "or" is due to the fact that the reduced potential w is symmetric in Z and Z_a. This $Z^{-1/3}$ proportionality is a result of scaling laws in the TF model described as follows. Consider a case where the TF equations are solved for Z, Z_a, and separation r; subsequent scaling of the nuclear charges by a factor of α results in a corresponding scaling in the separation by factor β:

$$\begin{aligned} Z' &= \alpha Z \\ Z'_a &= \alpha Z_a \\ r' &= \beta r. \end{aligned}$$

The scaling does not effect the relative distribution of electrons and therefore does not affect the ratio of local kinetic to potential energy:

$$\text{const} = \frac{t}{v_N} \propto \frac{\rho_e(\boldsymbol{x})^{5/3}}{\rho_e(\boldsymbol{x})V(\boldsymbol{x})}, \tag{D.12}$$

which scales as

$$\frac{\rho_e(\boldsymbol{x})^{2/3}}{V(\boldsymbol{x})} \propto \frac{(\alpha/\beta^3)^{2/3}}{\alpha/\beta} = \alpha^{-1/3}\beta^{-1} = \text{const}, \tag{D.13}$$

implying $\beta = \alpha^{-1/3}$. Thus a scaling of the reduced potential with $a \propto Z^{-1/3}$,

$$w\left(\frac{r}{a}\right) \to w\left(\frac{\beta r}{\alpha^{-1/3}Z^{-1/3}}\right), \tag{D.14}$$

is left unchanged, proving the assertion in Equation (D.11).

In the Lagrange minimization of the total kinetic and potential energy for the limit that $Z = 1$ and $Z_a \gg 1$, the reduced potential is approximately the TF potential of a single atom:

$$w = \varphi(r/a) \tag{D.15}$$

where $\varphi(y)$ is the Fermi function [152] and

$$a = \frac{a_0}{4}\left(\frac{9\pi^2}{2}\right)^{1/3} Z_a^{-1/3}, \tag{D.16}$$

where $a_0 = \hbar^2/m_e e^2$ is the Bohr radius. The details of the Lagrange minimization have been omitted for brevity [153]. This solution is consistent with $a \propto Z_a^{-1/3}$.

In the other extreme limit where $Z \approx Z_a$, LSS theory begins by using the Bohr approximation of the screening length dependent on both Z and Z_a [154]:

$$a = \frac{a_0}{4}\left(\frac{9\pi^2}{2}\right)^{1/3} (Z^{2/3} + Z_a^{2/3})^{-1/2}. \tag{D.17}$$

The numerical perturbation methods of Gombas [152] and Firsov [148] give more precise parameterizations of the screening length:

$$a = \frac{a_0}{4}\left(\frac{9\pi^2}{2}\right)^{1/3} (Z^{1/2} + Z_a^{1/2})^{-2/3}, \tag{D.18}$$

which do not differ from Equation (D.17) by more than 5% in most cases. These forms of the screening length deviate from more precise numerical estimates only for $r/a \gtrsim 5$, but additional modifications to the reduced potential provide a correction in the limit of large separation distances.